Dissertation zur Erlangung des Doktorgrades

der Fakultät für Chemie und Pharmazie

der Ludwig-Maximilians-Universität München

Generation and characterization of mouse and cell culture models to elucidate the function of Tet3 in neurons

Constanze Scheel

aus

Schwäbisch Gmünd, Deutschland

2020

Erklärung

Diese Dissertation wurde im Sinne von § 7 der Promotionsordnung vom 28. November 2011 von Herrn Prof. Dr. Stylianos Michalakis betreut.

Eidesstattliche Versicherung

Die Dissertation wurde eigenständig und ohne unerlaubte Hilfsmittel erarbeitet.

München, den 31.07.2020 _____

(Constanze Scheel)

Dissertation eingereicht am	30.06.2020
1. Gutachter:	Prof. Dr. Stylianos Michalakis
2. Gutachter:	Prof. Dr. Martin Biel
Mündliche Prüfung am	29.07.2020

Table of contents

List of Abbreviations

A	Ampere
Acadl	acyl-CoA dehydrogenase long chain
Acsa-2	astrocyte cell surface antigen - 2
Aldh1l1	aldehyde dehydrogenase-1 family member L1
a.m.	ante meridiem
AMD	age-related macular disease
AML	acute myeloid leukaemia
Anti-Anti	antibiotic-antimycotic
APC	Allophycocyanin
Arc	activity-regulated cytoskeleton-associated protein
Ascl1	achaete-scute family BHLH transcription factor 1
AuH	Au RNA binding methylglutaconyl-CoA hydratase
BER	base excision repair
Bdnf	brain-derived neurotrophic factor
BHT	butylated hydroxytoluene
BLAST	Basic Local Alignment Search Tool
bp	base pairs
BSA	bovine serum albumin
CA	*Cornu Ammonis*
$CaCl_2$	calcium chloride
Camk2a	calcium/calmodulin-dependent protein kinase II alpha
Cas9	CRISPR associated protein 9
C-C bond	carbon-carbon bond
cDNA	complementary DNA
Cirbp	cold-inducible RNA-binding protein
cKO	conditional knockout
Cngb1	cyclic nucleotide-gated channel beta 1
CNS	central nervous system
CRISPR	clustered regularly interspaced short palindromic repeats
crRNA	crispr RNA
C	cytosine
CFB	complement factor B
CFH	complement factor H
CpG	cytosine-guanine dinucleotide
CSF	cerebrospinal fluid
Ct	threshold cycle
CO_2	carbon dioxide
d	day
Darpp32	dopamine- and cAMP-regulated 32-kDa phosphoprotein
DG	dentate gyrus
dLGN	dorsal nucleus of lateral geniculate body
DMSO	dimethyl sulfoxide

DNA	deoxyribonucleic acid
DNMT	DNA methyltransferase
dNTP	deoxyribonucleotide triphosphate
DOX	doxycycline
DPBS	Dulbecco´s phosphate-buffered saline
DSB	double-strand break
DTT	dithiothreitol
E. coli	*Escherichia coli*
EDTA	ethylenediaminetetraacetic acid
Eif4g	eukaryotic translation initiation factor 4 G
e.g.	exempli gratia, for example
EMA	European Medicines Agency
EPPS	4-(2-Hydroxyethyl)-1-piperazinepropanesulfonic acid
et al.	et alia, and others
etc.	et cetera
EtOH	ethanol
FACS	fluorescence-activated cell sorting
floxed	loxP-flanked
fow	forward
g	gram
GABA	gamma-aminobutyric acid
Gadd45b	growth arrest and DNA damage inducible beta
GCL	ganglion cell layer
gDNA	genomic DNA
Gfap	glial fibrillary acidic protein
Glud1	glutamate dehydrogenase 1
GO	gene ontology
Gripap1	GRIP1(glutamate receptor interacting protein 1)-associated protein 1
Gua-Cl	guanidinium chloride
h	hour
HAT	histone acetyltransferase
HBSS (w)	Hank's Balanced Salt Solution with calcium and magnesium
HBSS (w/o)	Hank's Balanced Salt Solution without calcium and magnesium
HC	hippocampus
HCl	hydrochloric acid
HDAC	histone deacetylases
HDM	histone demethylases
HDR	homology-directed repair
HEs	homing endonucleases
HEK293T cells	human embryonic kidney cells
HEPES	N-2-hydroxyethylpiperazine-N-2-ethane sulfonic acid
HMT	histone methyltransferases
HPLC / MS	high liquid chromatography / mass spectrometry
HRP	horseradish peroxidase

Hz	Hertz
H3K36	histone 3 lysine 36
H_3PO_4	phosphoric acid
ICC	immunocytochemistry
IDT	Integrated DNA Technologies
IEG	immediate early gene
IHC	immunohistochemistry
IB	immuno blot
iNGN	inducible Neurogenin iPSC
INL	inner nuclear layer
IPL	inner plexiform layer
iPSC	induced pluripotent stem cell
ISH	*in situ* hybridisation
ITR	inverted terminal repeats
kb	kilobase
KCl	potassium chloride
kDa	kilodalton
Keap1	Kelch-like ECH-associated protein 1
KO	knockout
L	litre
LB	lysogeny broth
LV	lateral ventricle
M	molar
MBD1	methyl-CpG-binding domain protein 1
MeCN	acetonitrile
MECP2	methyl-CpG-binding protein 2
MeOH	methanol
$MgCl_2$	magnesium chloride
min	minute
mg	milligram
mL	millilitre
mM	millimolar
mRNA	messenger RNA
ms	milliseconds
mV	millivolt
NaCl	sodium chloride
$NaHCO_3$	sodium bicarbonate
NaH_2PO_4	sodium dihydrogen phosphate
NaOH	sodium hydroxide
NCBI	National Center for Biotechnology information
NEB	New England Biolabs
neg	negative
NeuN	neuronal nuclei
NeuroD1	neurogenic differentiation factor 1

NF	nerve fibre
ng	nanogram
NHEJ	non-homologous end joining
nm	nanometre
Npas4	neuronal per arnt sim domain 4
NPCs	neural progenitor cells
NSPCs	neural stem / progenitor cells
Nxf7	nuclear export factor 7
N_2	nitrogen
oB	olfactory bulb
ONL	outer nuclear layer
OS	outer segments
O_2	oxygen
Pafah1b3	platelet activating factor acetylhydrolase 1b catalytic subunit 3
PAGE	polyacrylamide gel electrophoresis
PAM	protospacer adjacent motif
Pax6	paired box 6
PBS	phosphate-buffered saline
PB	phosphate buffer
Pb	PiggyBac
PCR	polymerase chain reaction
PE	Phycoerythrin
PGP1 cell line	Personal Genome Project iPS cell line derived from Participant #1
PFA	paraformaldehyde
pH	potential hydrogen
Pik3c2a	phosphatidylinositol-4-phosphate 3-kinase catalytic subunit type 2 α
PNS	peripheral nervous system
pos	positive
PO_4	phosphate
ppm	parts per million
PVU	pellet volume units
qRT-PCR	real-time quantitative reverse transcription PCR
RACE	rapid amplification of cDNA ends
Rbfox3	RNA binding protein fox-1 homolog 3
RBM3	RNA-binding protein 3
REST	RE1 silencing transcription factor
rev	reverse
RGCs	retinal ganglion cells
RMS	rostral migratory stream
RNA	ribonucleic acid
RNP	ribonucleoprotein
ROB	Regierung von Oberbayern
RPE	retinal pigment epithelium
rpm	revolutions per minute

RT	room temperature
s	seconds
SAM	S-adenosyl-L-methionine
Sarm1	sterile alpha and TIR motif containing 1
SDS	sodium dodecyl sulphate
SEM	standard error of the mean
sgRNA	single guide RNA
Slc4a10	solute carrier family 4a member 10
Snrpn	small nuclear ribonucleoprotein-associated polypeptide N
Sox2	SRY (sex determining region Y)-box 2
Spata19	spermatogenesis associated protein 19
Stub1	STIP1 homology and U-box containing protein 1
SVZ	subventricular zone
TALENs	transcription activator-like effector nucleases
TDG	thymine DNA glycosylase
Tet	ten-eleven translocation
TMT	tandem mass tag
TNFα	tumour necrosis factor α
tracrRNA	trans-activating crRNA
TRE	tetracycline-responsive promoter element
Tris	tris(hydroxymethyl)aminomethane
Tspyl2	testis specific protein, Y-encoded-like 2
TSS	transcription starting site
UHRF1	ubiquitin-like with PHD and ring finger domains 1
UHPLC	ultra-high-performance liquid chromatography
UTR	untranslated region
V	Volt
vs.	versus
Wdr45	WD repeat domain 45
WT	wildtype
WHO	World Health Organization
ZFNs	zinc-finger nucleases
$ZnSO_4$	zinc sulphate
5mC	5-methylcytosine
5hmC	5-hydroxymethylcytosine
5fC	5-formylcytosine
5caC	5-carboxycytosine
8oxoG	8-oxoguanine
µg	microgram
µL	microlitre
µM	micromolar
µm	micrometre
°C	degree Celsius
x g	relative centrifugal force

List of Figures

List of Tables

Abstract

Epigenetics describes heritable changes of gene expression, which are independent from changes of the underlying DNA sequence. One major epigenetic mechanism involves DNA methylation and demethylation by the ten-eleven translocation (Tet) protein family of DNA dioxygenases. Tet enzymes (Tet1, Tet2, Tet3) catalyse the oxidation of 5-methylcytosine (5mC) to 5-hydroxymethylcytosine (5hmC) and further to 5-formylcytosine (5fC) and 5-carboxycytosine (5caC). Among the three variants, Tet3 is highly expressed in the central nervous system and thought to be involved in several physiological and pathophysiological processes such as neuronal development and differentiation.

To characterize the specific roles of Tet3 in neurons, tissue- and isoform-specific Tet3 knockout (KO) mouse models as well as human iPS cell lines overexpressing TET3 isoforms were generated and analysed.

Firstly, a conditional KO of Tet3 based on the Cre/loxP site recombination system was generated by crossing a loxP-flanked (floxed) Tet3 mouse line with a Nestin Cre driver mouse line. In this model, a genetic deletion of Tet3 was achieved in all cells expressing Nestin Cre recombinase including cells of the central and peripheral nervous system. Secondly, CRISPR-Cas9 technology was used to create mouse lines with a specific KO of Tet3 long (Tet3 L) and short (Tet3 S) isoforms. Thirdly, human iPS cells were genetically modified using PiggyBac transposon technology to overexpress TET3 isoforms upon doxycycline induction. Lastly, 5hmC dynamics in the brain and their connection to neuronal activity were examined by depolarization of mouse hippocampal slices.

The studies revealed that Tet3 depletion caused an abnormal phenotype in Tet3 conditional KO (cKO) animals displaying growth abnormalities, impaired brain size with smaller lateral ventricles and altered adult neurogenesis in the subventricular zone system of the brain. Transcriptome and proteome analyses of Tet3 cKO brains suggested that Tet3 deficiency caused impaired cell metabolism and stress-related conditions, resulting in pathological phenotype formation. Moreover, the study showed increased 5hmC levels in mouse hippocampus in response to depolarization, suggesting an influence of neuronal activity on 5hmC generation

and transcript levels of immediate early genes. Furthermore, the study demonstrated the successful generation of Tet3 L and Tet3 S KO mouse lines as well as the generation of TET3 isoform overexpressing cell lines. On the one hand, the Tet3 L and Tet3 S KO mouse lines can serve as a promising starting point to investigate Tet3 isoforms *in vivo*. On the other hand, the TET3 isoform overexpressing cell lines display a good basis for *in vitro* models such as organoids as well as for further investigations of cell-specific processes and their dependency on TET3 isoforms.

These models will help to elucidate the multifaceted roles of Tet3 in processes like neuronal plasticity or adult neurogenesis and form a promising basis for future investigations of the involvement of Tet3 in disease mechanisms.

1 Introduction

1.1 Epigenetics

The term "epigenetics" was first introduced around the 1940s by Conrad Hal Waddington, a leading British embryologist and geneticist, to describe interactions between the environment and genes leading to the development of a specific phenotype in organisms (Waddington, 1939; Waddington, 1942). The definition was further specified during the following decades proposing that epigenetics comprises all processes resulting in altered gene activity and function without changing the DNA sequence of the organism and includes the heritability of a phenotype to the next generation by either mitosis or miosis (Berger et al., 2009; Weinhold, 2006). Epigenetic mechanisms give explanations for the functioning of biological systems and they underline the importance of environmental effects on processes of cellular development and differentiation (Faulk and Dolinoy, 2011; Richards et al., 2010).

Essential aspects of epigenetic regulation are chromatin remodelling, post-translational histone modifications, DNA binding proteins and DNA as well as RNA modifications (Choudhuri et al., 2010; Szyf, 2009; Villota-Salazar et al., 2016; Weinhold, 2006).

Research in the field of epigenetics has become of high importance in the last decades, on the one hand, to fully understand epigenetic mechanisms and their physiological and pathophysiological role in biological systems, and, on the other hand, to find new therapeutic and diagnostic approaches for diseases triggered by epigenetic dysregulation (Egger et al., 2004; Sharma et al., 2010; Weinhold, 2006). Although many epigenetic aspects have not been investigated yet, their relevance in life sciences is undoubtedly clear. The increasing interest in the field and a constant development of new technologies and laboratory tools will lead to more knowledge about interactions among the environment, epigenome and genome as well as about their role in inheritance, adaption and evolution of organisms (Villota-Salazar et al., 2016).

1.1.1 From Histones to chromatin and chromosomes

The genomic DNA of each cell is organized into chromatin to fit into its nucleus. Chromatin exists in two forms, which show differences in their packing density and therefore in availability for transcription. Euchromatin is loosely packed, distributed throughout the nucleus and

transcriptionally active, while heterochromatin is highly condensed and therefore transcriptionally inactive (Cooper, 2000). Chromatin structure is mainly determined by repeating units of nucleosomes, which consist of approximately 147 base pairs (bp) of DNA wrapped around an octameric complex of two copies of each core histone protein (H2A, H2B, H3 and H4) (Kornberg, 1974; Kornberg and Thonmas, 1974; Luger et al., 1997). Histones are basic structure proteins and pack the DNA of approximately 2 m of length into the cell nucleus with a size of 10 - 100 µm (McGhee and Felsenfeld, 1980). The stable packing of DNA on histone surfaces is based on electrostatic interactions and hydrogen bonds between the DNA and the histone octamer (Luger et al., 1997). The nucleosome cores are further compacted into higher-order structures by the linker histone H1 and short free DNA segments of a varying size, called linker DNA (Widom, 1989), leading to a formation of a chromatin fibre of approximately 30 nm in diameter. This chromatin fibre subsequently forms large-scale tertiary structures, which build the entire chromosome (Figure 1) (Bednar et al., 1998).

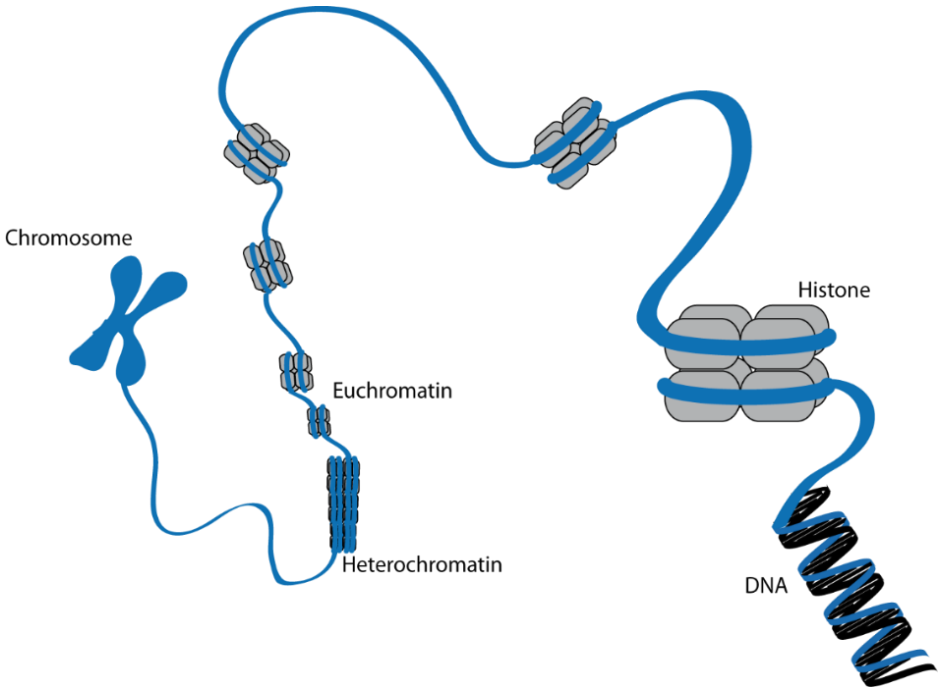

Figure 1: Histone - Chromatin - Chromosome

DNA is wrapped around octameric complexes of histones forming nucleosomes, which mainly determine the structure of chromatin. Large-scale tertiary structures of chromatin fibres finally build the chromosome. Figure adapted from (Wenzler and Jung, 2017).

Chromatin structure can be modified by the following main mechanisms: DNA methylation, covalent and non-covalent histone modifications as well as non-coding RNAs including microRNAs. By mainly influencing genome accessibility and compactness, these modifications create an "epigenetic landscape" that defines how the genome of an organism is read in different cell types, developmental stages and disease states (Jones and Baylin, 2007; Kouzarides, 2007; Sharma et al., 2010; Suzuki and Bird, 2008; Zhang et al., 2007).

As histones are the core basis of chromatin formation, their modification influences chromatin organization as well as function and therefore many biological processes (Bannister and Kouzarides, 2011; Cruickshank et al., 2010; Kouzarides, 2007; Strahl and Allis, 2000). The most investigated modifications are post-translational covalent histone modifications, comprising acetylation, methylation, phosphorylation, ubiquitinylation, sumolyation, deimination and ADP ribosylation of histone residues (Kouzarides, 2007; Strahl and Allis, 2000; Villota-Salazar et al., 2016). Among those, acetylation of lysine residues and methylation of lysine and arginine residues have been studied the most (Grunstein, 1997; Strahl and Allis, 2000).

Histone acetylation mainly occurs at free amino groups of lysine residues especially at the N - terminal end of histones and is regulated by the opposing actions of histone acetyltransferases (HATs) and histone deacetylases (HDACs) (Allfrey et al., 1964; Bannister and Kouzarides, 2011). Acetylation, which is catalysed by HATs using acetyl-CoA as a cofactor, neutralises the positive charge of lysine residues and therefore reduces the interaction of histones with the negatively charged DNA backbone, decreasing the packing density and finally causing a less compact chromatin structure, defined as euchromatin. Euchromatin is easily accessible for transcription factors, which generally leads to an increased gene transcription (Bannister and Kouzarides, 2011; Jenuwein and Allis, 2001; Yang and Seto, 2007). In contrast, desacetylation, which is catalysed by HDACs, restores the positive charge of lysine residues, resulting in compact and more stabilized chromatin, defined as heterochromatin. Heterochromatin is transcriptionally inactive, which is in line with the role of HDACs as transcriptional repressors (Bannister and Kouzarides, 2011; Jenuwein and Allis, 2001; Yang and Seto, 2007). Imbalance of acetylation and desacetylation plays an important role in cancer. For example, high HDAC activity leads to a decreased expression of different tumour suppressor

genes contributing to cancer development (Jones and Baylin, 2002; Jones and Baylin, 2007; Sharma et al., 2010; Villota-Salazar et al., 2016).

Histone methylation involves the transfer of a methyl group from S-adenosyl-L-methionine (SAM) to arginine and lysine residues. Instead of influencing their charge, histone methylation changes the hydrophobic and steric structures of histone proteins (An, 2007; Bannister and Kouzarides, 2011; Copeland et al., 2009; Fischle et al., 2003; Strahl and Allis, 2000; Upadhyay and Cheng, 2011). Arginine residues can carry one or two methyl groups, whereas lysine residues can carry up to three methyl groups, resulting in a high number of combinations and complex regulation mechanisms (An, 2007; Bannister and Kouzarides, 2011; Copeland et al., 2009; Fischle et al., 2003; Strahl and Allis, 2000). Histone methylation is catalysed by histone methyltransferases (HMTs), histone demethylation by histone demethylases (HDMs). Dependent on the position of the methylated amino acid, the amount of methylated amino acid residues as well as the position of further histone modifications, histone methylation either activates or represses transcription processes (Cruickshank et al., 2010; Upadhyay and Cheng, 2011; Villota-Salazar et al., 2016).

1.1.2 DNA methylation

In mammals, the most relevant form of DNA modification is DNA methylation, which controls many important processes and aspects in organisms such as gene transcription, genomic imprinting, X chromosome inactivation, maintenance of cell identity as well as tumorigenesis and therefore obtains crucial roles in development and disease (Greenberg and Bourc'his, 2019; Villota-Salazar et al., 2016; Wu and Zhang, 2017). 60 - 80 % of CpGs (cytosine-guanine dinucleotides) of mammalian genomes are methylated (Greenberg and Bourc'his, 2019; Li and Zhang, 2014). These high levels of methylation underline the importance of specific methylation patterns and DNA methylation processes for mammals.

As mentioned, mammalian gene expression is regulated by DNA methylation. In particular, DNA methylation of gene promotor regions is linked to repression of transcriptional processes. Different underlying mechanisms, summarised in (Li and Zhang, 2014), have been discussed. Firstly, methyl groups in the major groove of the DNA double-helix impair binding of

transcription factors, associated with transcription activation of specific genes. Secondly, proteins like MBD1 and MBD2 (methyl-CpG-binding domain protein 1 and 2) as well as MECP2 (methyl-CpG-binding protein 2), which themselves are attracted by methylated CpGs, are involved in the repression of gene transcription by associating with various corepressor complexes like mSin3a and SETDB1 (SET domain bifurcated histone lysine methyltransferase 1). Thirdly, interactions between DNA methylation and histone modifications are implicated in causing transcriptional suppression (Li and Zhang, 2014).

Those mechanisms are essential for the role of DNA methylation in neuronal plasticity, which describes the ability of the nervous system to structurally and functionally modify itself during development as well as adult stages in response to activity, experience or pathological events (von Bernhardi et al., 2017). Neuronal plasticity comprises stimulus-specific synaptic activation and membrane depolarization resulting in neurotransmitter release, receptor trafficking, neurotrophic factor synthesis as well as activation of various signalling pathways, affecting specific gene transcription in a long-term or activity dependent manner (Karpova et al., 2017). Consequently, impaired neuronal plasticity and connectivity cause misregulation of the transcription of neuronal plasticity-related genes (Karpova et al., 2017). Here, epigenetic processes and neuronal activity are tightly connected (Karpova et al., 2017; Santiago et al., 2014). Both DNA methylation and demethylation are induced by neuronal activity and required for proper functioning of the neuronal network (Karpova et al., 2017). For example, depolarization was demonstrated to cause loss of methylation at regulatory regions of the brain-derived neurotrophic factor gene (*Bdnf*) in post-mitotic neurons, correlating with higher transcript levels (Martinowich et al., 2003; Santiago et al., 2014). Moreover, it was described that neuronal activation leads to active demethylation or *de novo* methylation of approximately 3000 CpG sites, significantly enriched in low-CpG density regions associated with brain-specific and neuronal plasticity-related genes, in mouse dentate granule cells (Guo et al., 2011a; Santiago et al., 2014). Furthermore, *Gadd45b* (growth arrest and DNA damage inducible beta), a member of the *Gadd45* family involved in DNA repair mechanisms (Barreto et al., 2007; Tran et al., 2002), was reported to be important for activity-dependent DNA demethylation and neurotrophic factor expression (Ma et al., 2009).

5-methylcytosine (5mC) is the major form of mammalian DNA methylation (Smith and Meissner, 2013; Wu and Zhang, 2017), although N6-methyladenine was recently identified as another, but less frequent form of DNA modification in mouse embryonic stem cells (mESCs) (Wu et al., 2016b). 5mC is generated by DNA methyltransferases (DNMTs), DNMT1, DNMT3A and DNMT3B, which catalyse the transfer of a methyl group from SAM to the fifth carbon of cytosine residues of DNA (Figure 2) (Li and Zhang, 2014; Villota-Salazar et al., 2016). DNMT3A and DNMT3B are the major enzymes for *de novo* DNA methylation, whereas DNMT1 is mainly responsible for DNA methylation maintenance by copying DNA methylation patterns to the daughter strands during DNA replication (Holliday and Pugh, 1975; Li and Zhang, 2014; Riggs, 1975). These three DNMTs are additionally required for normal development, as their depletion in mice results in embryonic lethality in the case of DNMT1 and DNMT3B or in death at an age of four to eight weeks in the case of DNMT3A (Li et al., 1992; Okano et al., 1999).

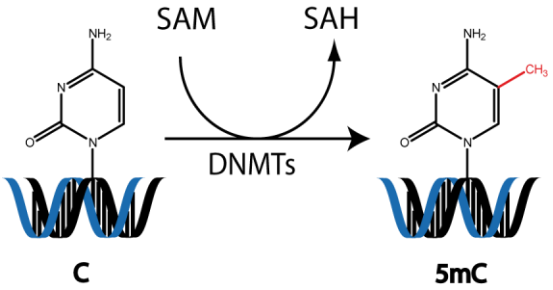

Figure 2: 5mC generation

S-adenosyl-L-methionine (SAM) - dependent DNA methyltransferases (DNMTs) generate 5-methylcytosine (5mC) by catalysing the transfer of a methyl group to cytosine residues of DNA.

In contrast to histone modifications, which are relatively instable and easily reversible, 5mC is an epigenetic mark, which is both chemically and genetically stable (Wu and Zhang, 2017). From a chemical point of view, the methyl group of 5mC is connected to the fifth carbon of cytosine residues through a stable carbon-carbon (C-C) bond, displaying a high chemical stability under physiological conditions and creating a barrier for direct removal of the methyl group (Wu and Zhang, 2017). From a genetic point of view, 5mC is maintained by DNMT1, which methylates hemi-methylated CpGs in the presence of its cofactor UHRF1 (ubiquitin-like with PHD and ring finger domains 1) (Bostick et al., 2007; Hermann et al., 2004; Holliday and

Pugh, 1975; Riggs, 1975). From a structural point of view, the methyl group of 5mC is localised in the major groove of double-helical DNA and therefore influences binding of many DNA-binding proteins such as MECP2 (Greenberg and Bourc'his, 2019; Li and Zhang, 2014).

For a long time, the methylation of cytosine was believed to be permanent. However, new mechanisms of DNA demethylation have been described since the discovery of the ten-eleven translocation (Tet) protein family of DNA dioxygenases in 2009, which convert 5mC into 5-hydroxymethylcytosine (5hmC), and further to 5-formylcytosine (5fC) and 5-caboxycytosine (5caC) (Ito et al., 2011; Iyer et al., 2009; Tahiliani et al., 2009).

1.1.3 DNA demethylation

Two mechanisms are known for DNA demethylation: passive demethylation and active demethylation (Figure 3) (Shi and Shen, 2017; Wu and Zhang, 2014; Wu and Zhang, 2017). On the one hand, passive demethylation, also described as replication-dependent dilution of 5mC, results in 5mC loss in the absence of the functional methylation maintenance machinery e.g. DNMT1 during replication (Shi and Shen, 2017). On the other hand, active DNA demethylation takes place either by the direct removal of the methyl group from 5mC or by an enzymatic process modifying 5mC with regeneration of unmodified cytosine. It involves the conversion of genomic 5mC to 5hmC, and further to 5fC and 5caC (Wu and Zhang, 2014; Wu and Zhang, 2017). For catalysing these oxidation processes, the Tet enzymes require oxygen (O_2) and α-ketoglutarate (αKG), one of the key metabolites of the organism (Wu et al., 2016a), as substrates and Fe(II) as a cofactor to generate carbon dioxide (CO_2) and succinate (Kaelin and McKnight, 2013; Lio and Rao, 2019; Wu and Zhang, 2017; Yang et al., 2016). This dependency of Tet enzymes on cofactors and substrates can influence the reaction kinetics e.g. due to altered availability. After 5mC oxidation to 5hmC, 5fC and 5caC, these oxidized forms can be converted to unmodified cytosine by multiple rounds of replication. This process is named active modification - passive dilution (AM-PD) (Shi and Shen, 2017; Wu and Zhang, 2017). Additionally, 5fC and 5caC can be converted to unmodified cytosine by thymine DNA glycosylase (TDG)-mediated excision coupled with base excision repair (BER) of the abasic site, which is independent from DNA replication and defined as active modification - active removal (AM-AR) (Shi and Shen, 2017; Wu and Zhang, 2017). For 5fC, an additional pathway of

conversion to unmodified cytosine is described. According to a recent study, cytosine can be regenerated from 5fC by C-C bond cleavage reaction (Iwan et al., 2018).

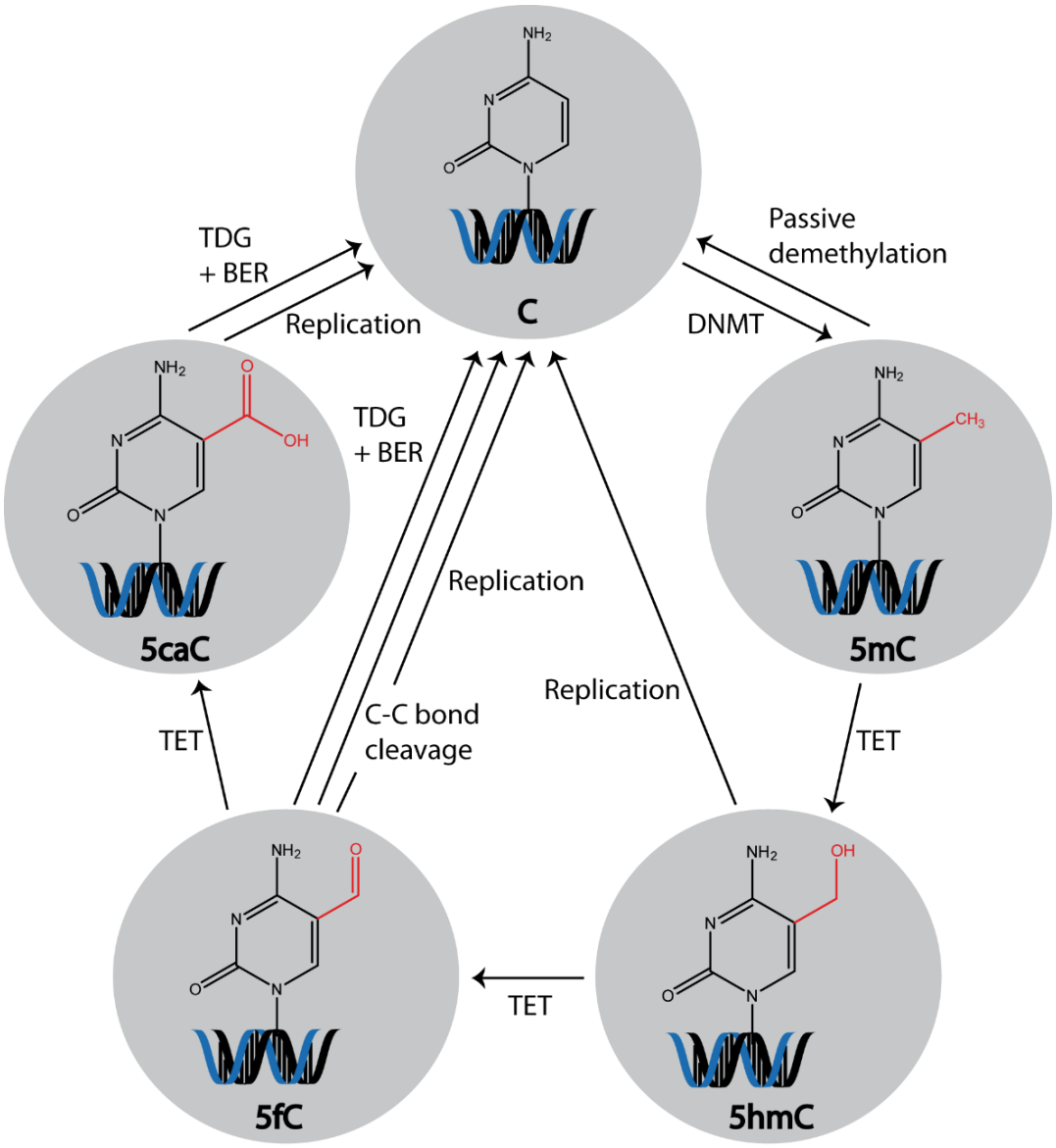

Figure 3: DNA methylation and demethylation

Unmodified cytosine is converted to 5-methylcytosine (5mC) by DNA methyltransferases (DNMTs). 5mC can be converted to unmodified cytosine either by passive or active DNA demethylation. Passive demethylation leads to 5mC loss due to an absent functional methylation maintenance machinery during replication. Active DNA demethylation comprises either a direct removal of the methyl group from 5mC or an enzymatic process modifying 5mC to regenerate unmodified cytosine. 5mC is oxidized to 5-hydroxymethylcytosine (5hmC), and further to 5-formylcytosine (5fC) and 5-carboxycytosine (5caC) by the Tet enzymes. Unmodified cytosine can be regenerated from 5hmC, 5fC and 5caC by multiple replication rounds. Additionally, it can be regenerated from 5fC and 5caC by thymine DNA glycosylase (TDG)-mediated excision coupled with base excision repair (BER) of the abasic site and from 5fC by C-C bond cleavage reaction.

DNA demethylation plays a crucial role in several biological contexts such as neuronal functions as well as ESC maintenance and differentiation. Furthermore, several publications report about the involvement of misregulated DNA methylation in diseases like cancer (Wu and Zhang, 2017).

1.1.4 5hmC - an important epigenetic mark

For decades, 5mC has been the only epigenetic mark in mammalian DNA. Hence, the process of 5mC formation is well characterized and its involvement in many biological processes was shown (Cheng et al., 2015). Since the discovery of the Tet enzymes and the detection of 5hmC in mouse Purkinje neurons and mESCs (Kriaucionis and Heintz, 2009; Tahiliani et al., 2009), 5hmC, as the sixth base in mammalian DNA, has become more and more a focus of current research.

5hmC is highly enriched in the brain (Globisch et al., 2010; Kriaucionis and Heintz, 2009; Münzel et al., 2010). Globisch et al. investigated the 5hmC distribution in different murine tissue types. The lowest amount of 5hmC was detected in liver, spleen and endocrine glands, medium levels were measured in kidney, bladder, heart, skeletal muscle and lung, whereas highest levels of 5hmC were detected in the central nervous system (CNS) (Globisch et al., 2010). These findings confirmed a first report by Münzel et al. regarding 5hmC levels in the mouse brain. Here, highest 5hmC levels were found in hippocampus and cerebral cortex, brain areas with higher cognitive function. Intermediate 5hmC levels were detected in brainstem and olfactory bulb, whereas cerebellum and retina contained the lowest 5hmC levels in comparison to the other neuronal tissue types (Münzel et al., 2010). Several studies additionally give evidence about the dependency of 5hmC levels on age. In mice, 5hmC levels in cerebral cortex tissue increase during postnatal development (Hahn et al., 2013; Münzel et al., 2010; Wagner et al., 2015), whereas in the human brain, global 5hmC levels vary during lifespan (Wagner et al., 2015).

Nowadays, 5hmC is recognized as an important epigenetic mark in mammals enriched within gene bodies, promotors and transcription factor binding sites (Hahn et al., 2013; Kaas et al., 2013). Regarding its molecular functions, 5hmC is an essential intermediate of the DNA

demethylation process and influences this process by three different mechanisms: passive demethylation, DNA repair-based demethylation and TET3-mediated demethylation (Cheng et al., 2015). Poor binding between 5hmC and UHRF1, an important DNMT1 partner, results in passive demethylation and leads to impaired maintenance of DNA methylation (Bostick et al., 2007; Cheng et al., 2015; Sharif et al., 2007). In addition to that, 5hmC mediates recruitment of chromatin binding proteins and gene expression by modulating the binding of protein complexes to chromatin (Cheng et al., 2015; Frauer et al., 2011; Hashimoto et al., 2012; Spruijt et al., 2013).

As 5hmC is very abundant in the brain, 5hmC patterns throughout the genome are essential for normal neurological development and function. Dysregulation of this epigenetic mark may lead to neurodevelopmental disorders such as Rett syndrome, Autism, schizophrenia or other psychiatric disorders, and neurodegenerative diseases such as Alzheimer's disease or Huntington's disease (Cheng et al., 2015). In addition to the involvement of 5hmC in those disorders, there are also reports about a role of 5hmC in acute stress and related diseases (Li et al., 2016b). Nevertheless, further research is necessary to fully understand the role of 5hmC-related disease mechanisms.

1.1.5 Tet variants and Tet3 isoforms

The Tet protein family of DNA dioxygenases includes three members: Tet1, Tet2, Tet3. The three Tet proteins are all dependent on Fe(II) and αKG and display the same catalytic activity containing a C-terminal catalytic domain, which is comprised of a double-stranded β-helix and a cysteine-rich domain (Wu and Zhang, 2017). Despite these similarities, the three Tet variants reveal differences in structure, expression pattern and function. Concerning structure, Tet1 and Tet3, in contrast to Tet2, harbour a N-terminal DNA-binding CXXC domain and exist in multiple isoforms generated by differential use of alternative exons encoding N-terminal portions of the protein. Regarding expression and function, Tet1 is highly present in ESCs (Gu et al., 2011; Huang et al., 2014; Ito et al., 2010), whereas Tet2 is more abundant in the hematopoietic system (Bowman and Levine, 2017; Feng et al., 2019; Figueroa et al., 2010; Moran-Crusio et al., 2011) and Tet3 represents the predominant Tet variant in oocytes and zygotes (Gu et al., 2011; Iqbal et al., 2011; Wossidlo et al., 2011). While all three Tet proteins are

expressed in the brain, Tet3 shows the highest levels in the CNS (Colquitt et al., 2013; Hahn et al., 2013)

As already mentioned, Tet3 exists in multiple isoforms (Figure 4), generated by alternative splicing and alternative promotor usage (Jin et al., 2016; Liu et al., 2013). The isoforms differ in their N-terminal sequence displaying a DNA-binding CXXC domain, which is composed of two Cys_4-type zinc finger motifs (Liu et al., 2013; Melamed et al., 2018). Tet3 long (Tet3 L) isoforms contain a CXXC domain at their N-terminal sequence, whereas the Tet3 short (Tet3 S) isoform lacks such a domain. Two Tet3 L isoforms are generated by alternative splicing, in which the CXXC domain is either spliced to exon 2 or exon 3. Tet3 S is expressed by an alternative promotor located upstream of exon 1, which represents the first unique exon of the Tet3 S isoform (Liu et al., 2013). In mouse oocytes, an additional isoform (Tet3 o), generated by alternative promotor usage, was identified (Jin et al., 2016). It contains an additional upstream exon coding for eleven unique amino acids but lacks the CXXC domain because of alternative splicing. The alternative promotor for Tet3 o isoform is located 5 kb upstream of the start codon of Tet3 L (Jin et al., 2016).

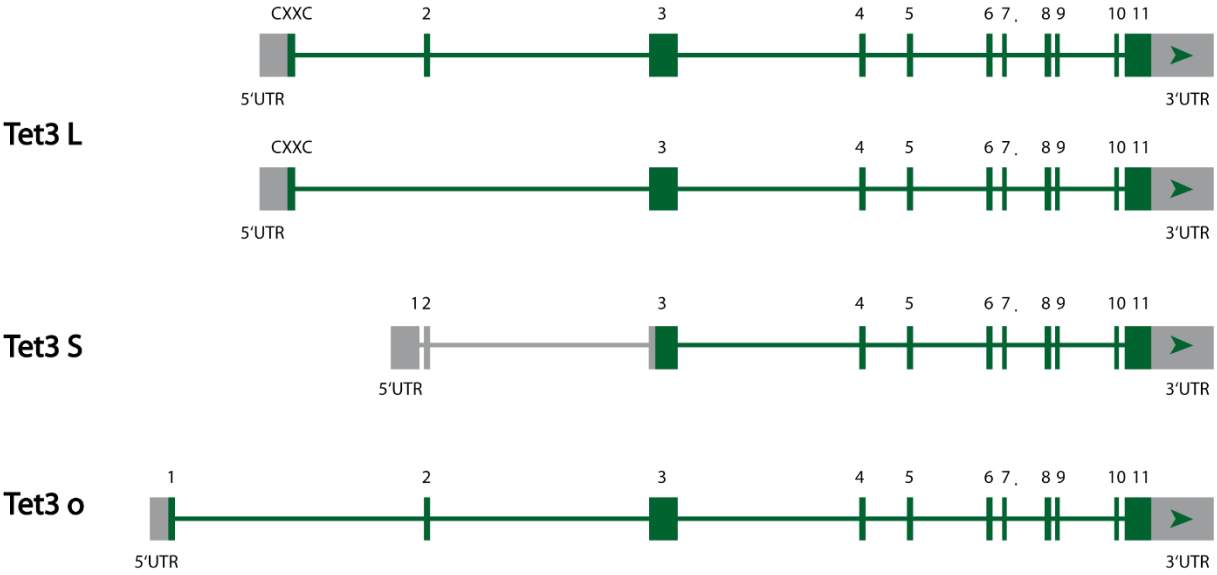

Figure 4: Tet3 isoforms

In mice, Tet3 exists in four main isoforms. Tet3 L isoforms contain a N-terminal CXXC domain and exist in two forms generated by alternative splicing. Tet3 S isoform lacks the N-terminal CXXC domain, being expressed by an alternative promotor. Tet3 o isoform, generated by alternative promotor usage, contains an additional N-terminal exon but lacks the CXXC domain due to alternative splicing. The coding sequence is marked in green, while grey regions mark the untranslated regions.

The TET3 isoforms annotated to date for human TET3 differ from those in mice regarding exon and intron size (Figure 5). Moreover, translation starts within the common exon 3 in the mouse Tet3 S isoform, while in the human TET3 S isoform translation is initiated in its unique exon 1, which is missing in mice. Finally, the existence of an oocyte-specific isoform has yet to be confirmed in humans.

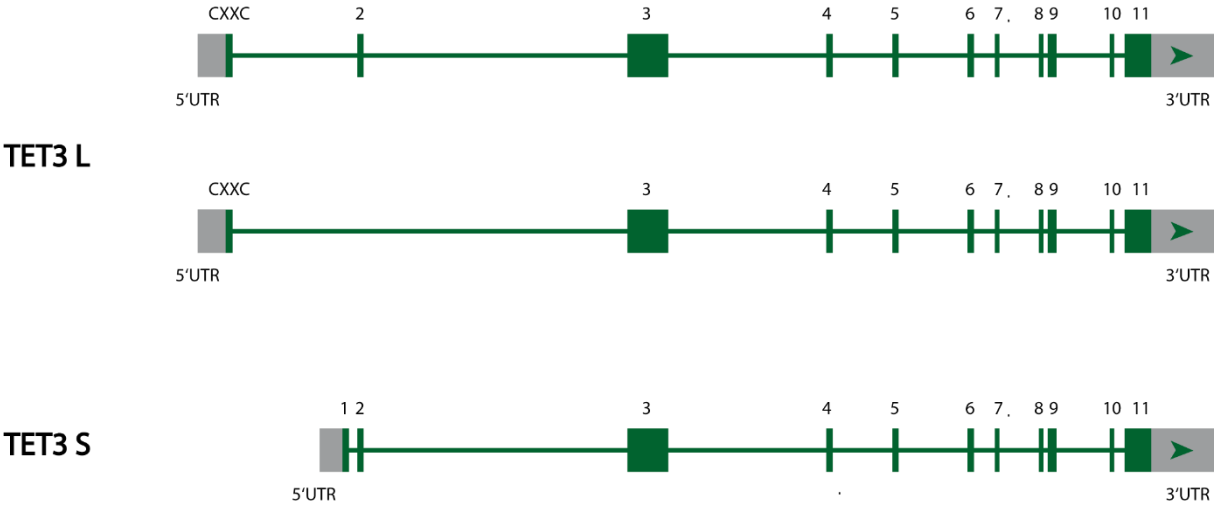

Figure 5: TET3 isoforms

In humans, TET3 exists in three main isoforms. TET3 L isoforms contain a N-terminal CXXC domain and exist in two forms generated by alternative splicing. Being expressed by an alternative promotor, TET3 S isoform lacks the N-terminal CXXC domain. The coding sequence is marked in green, while grey regions mark the untranslated regions.

The mechanisms regulating Tet expression and catalytic activity are still not fully understood. Various factors like substrate and cofactor availability or dynamic transcriptional control have been assumed to modulate Tet function (Lu et al., 2015). Notably, the DNA binding CXXC domain, exclusively present in Tet1 L and Tet3 L isoforms, was shown to play a key role for targeting Tet enzymes to genomic loci (Xu et al., 2011; Xu et al., 2012). Furthermore, the CXXC domain of Tet3 L isoforms was reported to more preferably bind carboxylated than unmethylated cytosines at CpG sequences, suggesting that the domain is a specific 5caC reader (Jin et al., 2016; Liu et al., 2013). Still, these findings do not explain how Tet DNA dioxygenases are targeted to their actual substrates 5mC, 5hmC and 5fC. Whereas, Tet3 L isoforms have a very restricted genomic localisation pattern at transcription start sites (TSS) of specific neuronal genes (Jin et al., 2016), the Tet3 S isoform is enriched in neuronal tissue, which is the reason

why it is also called neuronal Tet3 in literature (Liu et al., 2013). Additionally, Tet3 S is the major Tet3 isoform in the retina (Perera et al., 2015), where it plays an important role in development and maturation. As Tet3 S isoform lacks a DNA binding CXXC domain, it is probably targeted to the DNA by different mechanisms than Tet3 L isoforms (Melamed et al., 2018). In the retina, Tet3 S was shown to interact with the transcriptional factor REST (RE1 silencing transcription factor) to generate 5hmC and to induce histone 3 lysine 36 (H3K36) trimethylation, resulting in activation of neuronal gene transcription (Perera et al., 2015). Besides, multiple transcription factors like Nanog, Ebf1 and E2A have been reported to be involved in Tet targeting to specific genomic loci (Lio and Rao, 2019). In summary, this indicates that Tet enzymes are recruited to DNA cytosine modifications by additional DNA binding interaction partners.

Little is known, though, about the specific roles of Tet3 isoforms in biological systems, thus justifying further studies. To investigate function and importance of individual Tet3 isoforms, a specific knockout (KO) of each isoform *in vitro* and *in vivo* is necessary.

1.1.6 Relevance of Tet enzymes

Since the discovery of the Tet protein family by the group of Anjana Rao around ten years ago (Iyer et al., 2009; Tahiliani et al., 2009), research in the field of Tet enzymes has expanded in many different directions. For example, Tet enzymes are involved in gene expression (Kaas et al., 2013; Perera et al., 2015; Rudenko et al., 2013) as well as memory formation (Kaas et al., 2013). Since especially Tet3 is dependent on αKG (Kaelin and McKnight, 2013; Lio and Rao, 2019; Yang et al., 2016), Tet enzymes also play a role in metabolic processes and diseases (Da et al., 2020; Kaelin and McKnight, 2013). Furthermore, many publications report about an essential role of Tet enzymes in immune response (Lio and Rao, 2019), cell reprogramming (Bagci and Fisher, 2013; Singh et al., 2020), neurodegeneration (Gontier et al., 2018; Jin et al., 2016) as well as anxiety-like behaviour and cognitive function (Antunes et al., 2020).

Importantly, some more recent publications demonstrated the clinical relevance of TET enzymes and their involvement in several disease processes in humans. There have been reports about the role of TET2 in Parkinson Disease (Lee et al., 2019), TET involvement in ageing- and

injury-induced vision loss (Lu et al., 2019) and importantly about the identification of TET3 deficient human patients with neurodevelopmental disorders (Beck et al., 2020).

Beck et al. described the first Mendelian disorder in human patients caused by disruption of DNA demethylation, in which TET3 plays an important role. They identified and characterized eleven patients in eight different families with mutations in *TET3* and phenotypic features of intellectual disability and global developmental delay, hypotonia, autistic traits, movement disorders, growth abnormalities and facial dysmorphism. These phenotypic features show a big overlap with other disorders of the epigenetic machinery, including e.g. neurological manifestations and growth abnormalities. Inheritance processes of TET3 deficiency include both autosomal recessive and autosomal dominant mechanisms. These patients harboured either single frameshift or nonsense mutations in the *TET3* coding region. Some of the patients showed one or two missense variants within the coding region of the highly conserved catalytic domain of TET3 (Beck et al., 2020).

These recent publications revealed a physiological and pathophysiological role of Tet enzymes and doubtlessly showed their clinical relevance underlining the importance of research in the field of Tet enzymes.

1.1.7 Epigenetics in disease, therapy and diagnostics

A wide range of diseases from metabolic problems to neurological disorders and cancer is directly or indirectly related to epigenetic traits and regulation (Egger et al., 2004; Feinberg and Vogelstein, 1983; Rakyan et al., 2011; Sharma et al., 2010). Most known Mendelian disorders of the epigenetic machinery, resulting in e.g. intellectual disability and growth abnormalities, are caused by inherited conditions disrupting chromatin remodelling and post-translational histone modification (Fahrner and Bjornsson, 2014; Larizza and Finelli, 2019), whereas a smaller number of disorders are caused by defects in DNA methylation (Ehrlich et al., 2001; Mnatzakanian et al., 2004; Tatton-Brown et al., 2014) and in DNA demethylation processes (Beck et al., 2020). In cancer, the epigenomic landscape is extensively changed in comparison to the one of healthy cells. It is mainly characterized by global changes in DNA methylation and histone modification patterns as well as in expression profiles of chromatin-modifying

enzymes, leading to a global dysregulation of gene expression and finally to disease development by e.g. silencing of tumour suppressor genes or activating oncogenes (Egger et al., 2004; Esteller, 2008; Jones and Baylin, 2007; Sandoval et al., 2013; Sharma et al., 2010).

As disruption of the balance of epigenetic networks can cause several diseases, the development of therapies, interfering with epigenetic regulation processes, has great potential. In the last years, different "epigenetic" drugs, mainly for the therapy of different cancer types, were approved.

The nucleoside analogues azacitidine (Vidaza®) and decitabine (Dacogen®) were the first two drugs on the market, which target epigenetic regulation processes. They cause an irreversible inhibition of DNMTs after integration into the DNA and prevent hypermethylation of tumour suppressor genes (Constantinides et al., 1977; Egger et al., 2004; Jones and Taylor, 1980; Šorm et al., 1964). Azacitidine is indicated for the treatment of several haemato-oncological diseases like acute myeloid leukaemia (AML) and chronic myelomonocytic leukaemia under specific requirements (European Medicines Agency (EMA), 2009). Decitabine is also approved for AML therapy (European Medicines Agency (EMA), 2019).

The second group of drugs targeting epigenetic regulation processes are HDAC inhibitors. As a higher activity of HDACs reduces expression of tumour suppressor genes, contributing to cancer development. HDACs inhibitors consequently prevent the declining tumour suppressor gene expression (Marks et al., 2003; Marks et al., 2000; Xiao et al., 1999). HDAC inhibitors are e.g. vorinostat (Zolinza®), used in the therapy of cutaneous T-cell lymphoma (Mann et al., 2007), belinostat (Beleodaq®), approved for the therapy of peripheral T-cell lymphoma (Lee et al., 2015), and panabinostat (Farydak®), used for multiple myeloma treatment (European Medicines Agency (EMA), 2015).

Many more of such drug types have been waiting in the research and clinical study pipeline to gain a successful approval by the authorities.

Another common strategy to develop new options for therapy is drug repositioning, which describes the use of already approved drugs for new indications. A big advantage of this approach is that tolerability and side effects are already investigated (Langedijk et al., 2015;

Pushpakom et al., 2019). Examples for already approved drugs, which additionally interfere with epigenetic processes, are valproic acid, hydralazine and tranylcypromine. Valproic acid, originally used as an antiepileptic drug, inhibits HDACs in high dosage. Hydralazine, normally administered in antihypertensive therapy, is a DNMT inhibitor. The combination of both substances shows promising results in clinical studies for the therapy of myelodysplastic syndrome (Candelaria et al., 2017). Tranylcypromine, an antidepressant drug, inhibiting the enzyme monoamine oxidase, reveals an inhibitory effect on lysine specific histone demethylases. As their overexpression plays a role in leukaemia cells, it has been tested in clinical studies to treat AML (Luebbert, 2016).

Epigenetic mechanisms and patterns have not only served as a therapeutic target especially in different types of cancer but were also shown to have diagnostic as well as prognostic potential.

Epigenetic biomarkers display several advantages in comparison to genetic biomarkers, described in a review by García-Giménez et. al (García-Giménez et al., 2017). Firstly, epigenetic biomarkers contain information from an individual's environment and lifestyle, explaining e.g. how health and disease are affected by nutrition or sports. Secondly, they provide relevant information about the gene function in individual cell types, showing e.g. to which extent genetic programs are controlled or modified. Thirdly, many epigenetic biomarkers are extremely stable in fluids such as serum or urine as well as in primary types of tissue preparation like fresh frozen or formalin fixed tissue (García-Giménez et al., 2017).

As a key epigenetic modification, DNA methylation seems to be a suitable marker for disease diagnostics and monitoring (Schübeler, 2015; Smith and Meissner, 2013; Suzuki and Bird, 2008). The cytosine methylation patterns across the genome define the epigenetic state of the cell. When epigenetic reprogramming takes place, it leads to fundamental changes in cell biology, finally triggering diseases such as cancer. Epigenetic reprogramming in cancer simultaneously involves a loss of global DNA methylation and an increase of 5mC levels (hypermethylation) at regions, which are important for regulation processes (Sharma et al., 2010; Suzuki and Bird, 2008). Most cancer types display this methylation landscape, potentially serving as a universal cancer biomarker. Changes in the methylation landscape lead to changes

in physicochemical DNA properties such as solvation in aqueous solution and affinity to solid surfaces like gold, which can be utilised for cancer detection (Sina et al., 2018). Strategies for analysing DNA methylation patterns are affinity-enrichment based methods, methylation-sensitive restriction enzymes techniques, bisulfite-converted genomic DNA methods or next-generation sequencing technologies (Sandoval et al., 2013).

Epigenetic biomarkers show a high potential for clinical diagnostics, although several issues need to be solved until they fully access routine laboratory work. For example, standardised and high-throughput methods for epigenetic biomarkers need to be established as well as knowledge of clinicians and technicians regarding epigenetic mechanisms and technologies needs to be expanded for the correct interpretation of the obtained results (García-Giménez et al., 2017).

Together, the number of diseases, in which epigenetic mechanisms are involved, the routinely used drugs for epigenetic targets and the diagnostic potential of specific epigenetic patterns clearly reveal the general relevance of epigenetic research.

1.2 The Brain: an overview about structure, function and mechanisms

As one of the largest and most complex organs of the body, the brain consists of a large variety of cell types and fulfils an immense number of functions.

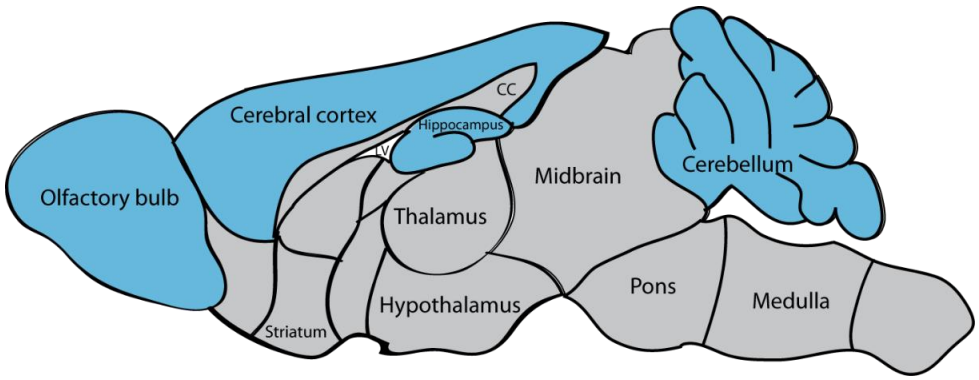

Figure 6: Mouse brain - sagittal section

Sagittal section of a mouse brain. The brain regions highlighted in blue are further described in the following.

As the study mainly focussed on four specific brain regions (cerebellum, cerebral cortex, hippocampus, and olfactory bulb), those are further described in the following (Figure 6). Bear et al. is used as basis (Bear et al., 2016). Additional references are indicated.

1.2.1 Cerebellum

The cerebellum plays an important role in coordination and regulation of motor actions, specifically in the maintenance of balance and posture, coordination of voluntary movements, motor learning and cognitive functions (Knierim, 1997; Schröder et al., 2020a). As most dorsal part of the brainstem, it consists of three different layers, the granular cell, Purkinje cell and molecular cell layer, as well as an extended white matter appearing as a treelike structure (Knierim, 1997; Schröder et al., 2020a). The granular layer, the innermost layer of the cerebellar cortex, consists of small, tightly packed granule cells, which comprise more than half of the neurons of the entire mammalian brain. Only one layer of parallel oriented Purkinje cells forms the Purkinje cell layer. The molecular cell layer, the outermost layer of the cerebellar cortex, is mainly composed of axons of granule cells and dendrites of Purkinje cells. In addition to those two main cell types, the cerebellum contains various other types like interneurons. The major target structures of the cerebellum are the motor nuclei of the thalamus and the mesencephalic red nucleus. The cerebellum receives its main direct input from precerebellar nuclei reaching the Purkinje cells of the cerebellum via different fibres (Knierim, 1997; Schröder et al., 2020a).

1.2.2 Cerebral cortex

The cerebral cortex, which develops from the forebrain region of the neural tube, is from a hierarchical point of view the highest unit of the mammalian brain and occupies the largest area of the mammalian brain as its grey matter covers the hemispheres (Schröder et al., 2020b; Swenson, 2006). The cerebral cortex is composed of four different lobes: the frontal, parietal, temporal and occipital lobes, being responsible for specific functions in the mammalian body, respectively (Schröder et al., 2020b; Swenson, 2006). In addition, the cerebral cortex can be divided into primary and association cortices (Schröder et al., 2020b). Primary cortices take over simpler functions such as the reception of sensory input from e.g. vision or eye movements. In contrast, association cortices occupy more complex functions like computing signals from the primary cortices and linking different qualities (Schröder et al., 2020b). The cerebral cortex

consists of various neuronal cell types such as pyramidal cells, stellate cells, granule cells and small populations of e.g. horizontal cells (Swenson, 2006).

1.2.3 Hippocampus

From a phylogenetic point of view, the hippocampus is the second oldest part of the telencephalon after the olfactory system. In rodents, the continuous hippocampal structure is located in a cranial dorsal to lateroventral position, finally reaching the ventral brain surface (Schröder et al., 2020c). The hippocampus is mainly composed of three layers: dentate gyrus (DG), *Cornu Ammonis* (CA, Ammon's horn), consisting of three sub-fields (CA1, CA2, CA3) and the subicular complex (Figure 7) (Schröder et al., 2020c).

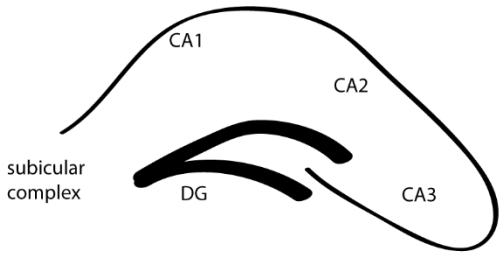

Figure 7: Hippocampal formation

Sagittal view of a mouse hippocampus. The hippocampus is divided into the dentate gyrus (DG), *Cornu Ammonis* (CA), consisting of three sub-fields (CA1, CA2, CA3) and the subicular complex.

The hippocampus is part of the classical trisynaptic circuit, the major signalling circuit for memory formation, spatiotemporal orientation and learning, which is based on synaptic transmissions between the different hippocampal regions. The circuit starts in the entorhinal cortex, the major interface between neocortex and hippocampus, and leads to the DG and CA, finally returning to the entorhinal cortex (Schröder et al., 2020c).

1.2.4 Olfactory bulbs

The olfactory bulbs are a bulb-shaped nervous structure, which is responsible for the sense of smell (Schröder et al., 2020d; Scott et al., 1993). The tissue is histologically divided into five layers: the glomerular layer, the external plexiform layer, the mitral cell layer, the internal plexiform layer and the granule cell layer. In the glomerular layer, first synaptic processing of olfactory impulses takes place. The mitral cell layer forwards information received from

olfactory neurons to other areas of the brain, whereat the inner plexiform layer only serves as a passage to the nerve fibres (Scott et al., 1993). For rodents, the olfactory system is highly essential for reproduction and exploration of the environment. The system is composed of two parts, the main olfactory bulb system and the vomeronasal system, which differ in type and location of primary sensory neurons, in connectivity patterns and in function. The main olfactory bulb system receives and transmits olfactory stimuli, whereas the vomeronasal system connects olfactory perception to reproductive activity (Schröder et al., 2020d).

1.2.5 Adult neurogenesis in the brain: function, regulation and relevance

Adult neurogenesis, a highly complex and polygenic process, is defined as the generation of new neurons from neural stem / progenitor cells (NSPCs) in the adult brain (Braun and Jessberger, 2014; Kempermann, 2015; Zhao et al., 2008). While it is a common process in several species like fish and birds, adult neurogenesis is an exceptional process in mammals (Kempermann, 2015). In mammals, it mainly takes place in the hippocampal region as well as in the subventricular zone (SVZ) - olfactory bulb (oB) system (Figure 8) (Braun and Jessberger, 2014; Kempermann, 2015; Lim and Alvarez-Buylla, 2016). However, in the striatum of humans and rabbits, adult neurogenesis is normal, whereas, in the striatum of mice and rats, it only occurs after ischemic states (Arvidsson et al., 2002; Lindvall and Kokaia, 2015; Parent et al., 2002).

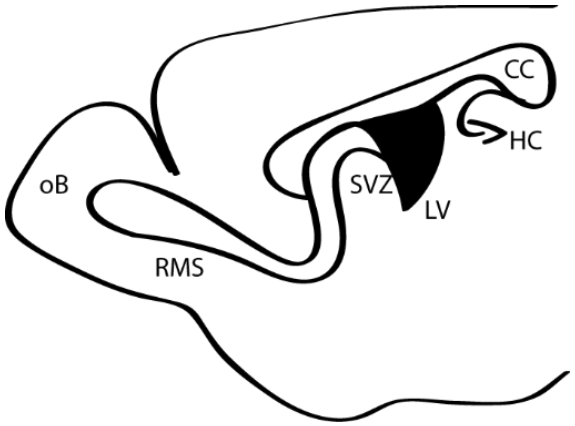

Figure 8: HC - SVZ - RMS - oB

Sagittal view of a mouse brain. Mammalian adult neurogenesis mainly takes place in hippocampus (HC) and the subventricular zone (SVZ) - olfactory bulb (oB) system. The newly generated cells migrate in chains from the SVZ neurogenic niche towards the olfactory bulb via the rostral migratory stream (RMS). Figure adapted from (Sun et al., 2010).

The subgranular zone in the DG of the hippocampus and the SVZ, located in the lateral wall of the lateral ventricle (LV), provide a niche of NSPCs (Braun and Jessberger, 2014; Kaneko et al., 2017). In those niches, the NSPCs stay in a largely inactive and quiescent state until activation by niche-derived and / or intrinsic signals leads to differentiation and finally to the birth of new neurons (Braun and Jessberger, 2014; Zhao et al., 2008).

In the DG, adult NPCs transform into excitatory glutamatergic granule cells, the major type of neurons in the DG, via the following process. After activation, radial glia-like NPCs enter the cell cycle and produce proliferating non-radial glia cells. These cells form neuroblasts, which migrate into the granule cell layer and mature into newborn granule cell neurons over a time period of several weeks. Typical granule cell neurons display a large dendritic arbour and axons reaching the adjacent molecular layers and innervating target cells (Braun and Jessberger, 2014; Kempermann et al., 2015).

In the SVZ, adult NSPCs are located below an ependymal cell layer in the lateral wall of the lateral ventricles. They produce more proliferating, non-radial transit-amplifying Type-C-progenitors, which then generate few glia cells and neuroblasts. Those neuroblasts migrate in chains through the RMS to the olfactory bulb, where neurogenesis continues. In the olfactory bulb, neuroblasts subsequently locate in the granule and glomerular cell layer, mature and differentiate either into dopaminergic periglomerular neurons or gamma-aminobutyric acid-(GABA)ergic granule neurons over a time period of several weeks (Braun and Jessberger, 2014; Lim and Alvarez-Buylla, 2016; Zhao et al., 2008).

The RMS is a highly specialised migratory route, in which one of the longest migrations in CNS development takes places (Lim and Alvarez-Buylla, 2016; Nam et al., 2007; Sun et al., 2010). It is organized as a tubular extension of the lateral ventricle, which reaches the corpus callosum via a vertical descending tract, and then orients horizontally in the elbow of the RMS and finally enters the olfactory bulb (Figure 8) (Sun et al., 2010). The RMS consists of several cell types, among which migrating neuroblasts are the most common ones. Neuroblasts form chains via their homophilic interactions and are surrounded by specialised glia cells, which form a tube-like-structure, the so-called glial tube (Lois and Alvarez-Buylla, 1994; Lois et al., 1996; Sun et

al., 2010). Neuroblast migration through the RMS is regulated by multiple factors in different steps (Sun et al., 2010). In brief, RMS migration is initiated by newborn neuroblasts in the SVZ spontaneously and autonomously forming chains by homophilic aggregation. Those chains migrate towards the olfactory bulb with a certain speed and direction, which can be influenced by cell-cell adhesion and extracellular matrix effects, chemoattractive and chemorepulsive signals and local factors from other cell types within the RMS. Neuroblast migration in the RMS is finally terminated, when neuroblasts reach the olfactory bulb, detach from the chains and migrate to their final positions in a radial way (Sun et al., 2010).

The different steps and the rate of adult neurogenesis are regulated by a variety of molecular as well as environmental factors (Braun and Jessberger, 2014; Zhao et al., 2008) such as transcriptional regulators like Sox2 (SRY (sex determining region Y)-box 2), Pax6 (paired box 6), NeuroD1 (neurogenic differentiation factor 1) and Ascl1 (achaete-scute family BHLH transcription factor 1) (Zhao et al., 2008). Furthermore, niche-derived morphogens, neurotransmitters such as GABA and glutamate, growth factors like Bdnf and epidermal growth factor (Egf) and cytokines including interleukin 6 (IL-6) or tumour necrosis factor α (TNFα) are essential for controlling the different neurogenic processes (Zhao et al., 2008). Additionally, extrinsic environmental factors like physical activity, environmental enrichment and olfactory- or hippocampus-dependent learning can impact adult neurogenesis in the brain (Braun and Jessberger, 2014). Moreover, epigenetic mechanisms play a role in its regulation. For example, Tet3 is reported to have a critical role in neural progenitor cell maintenance and terminal differentiation (Li et al., 2015; Montalbán-Loro et al., 2019). Furthermore, Tet3 was shown to be involved in the correct regulation of the imprinted gene small nuclear ribonucleoprotein-associated polypeptide N (*Snrpn*) in the neurogenic niche (Montalbán-Loro et al., 2019). In addition to that, Tet1 is involved in neural progenitor cell proliferation. In general, functional DNA methylation and demethylation is necessary for normal neural cell differentiation (Santiago et al., 2019). Furthermore, small non-coding RNAs and histone modifications recognized by the transcriptional repressor MBD1 are important to control levels of neurogenesis (Jobe et al., 2017; Zhao et al., 2008; Zhao et al., 2003).

In general, adult neurogenesis is essential for brain homeostasis and disease. On the one hand, adult neurogenesis is important for olfactory- and hippocampus-dependent learning and memory (Deng et al., 2010). On the other hand, impaired neurogenesis has been associated with different neuropsychiatric diseases like epilepsy and depression (Parent and Murphy, 2008; Sahay and Hen, 2007; Scharfman and Hen, 2007; Zhao et al., 2008). Moreover, adult neurogenesis may have therapeutic potential for the treatment of chronic diseases of the CNS or acute lesions e.g. caused by stroke, as it offers cell sources for brain repair (Braun and Jessberger, 2014; Lindvall and Kokaia, 2015).

1.3 Retina and Visual system

1.3.1 Structure and basic functioning

The retina is located on the inner surface of the posterior eye and is part of the CNS. The adult retina consists of six different types of neurons, which are rod and cone photoreceptors, bipolar cells, amacrine cells, horizontal cells, and ganglion cells as well as one type of glia cells, the Müller glia cells (Figure 9 - A). These different cell types are organized into different cellular layers: the outer nuclear, the inner nuclear and the ganglion cell layers, where the cell bodies are located, and the outer and inner plexiform layers, where the processes and synaptic contacts of the retinal cells are located (Figure 9 - A) (Bassett and Wallace, 2012; Bear et al., 2016; Purves et al., 2001c). Retinal cell types are generated at different time points during embryogenesis. In mouse embryogenesis, ganglion cells are produced first, followed by cone photoreceptors, horizontal cells and a major part of amacrine cells, whereas bipolar cells, the remaining amacrine cells, most rod photoreceptors and Müller glia cells are generated postnatally (Bassett and Wallace, 2012; Bear et al., 2016).

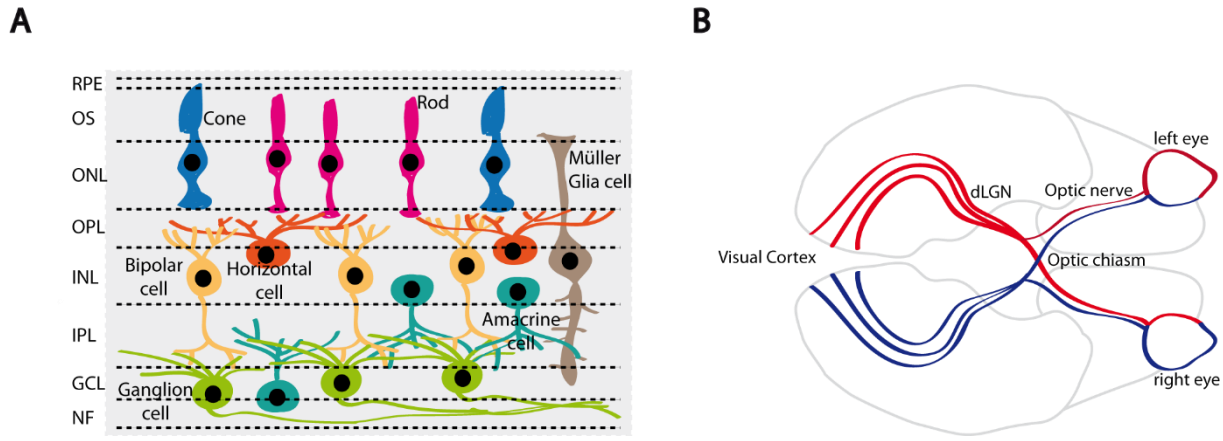

Figure 9: Visual system

(A) The adult retina consists of different cell types: rod and cone photoreceptors, bipolar cells, amacrine cells, horizontal cells, ganglion cells and the Müller glia cells. They are organized into different cellular layers: the outer and inner nuclear layers (INL and ONL), the ganglion cell layer (GCL), the outer and inner plexiform layers (IPL and OPL) and the nerve fibre layer (NF). The outer segments (OS) of the photoreceptors reach the retinal pigment epithelium (RPE). Figure adapted from (Bassett and Wallace, 2012). **(B)** The retina converts photonic energy from light into neural signal, which reaches the visual cortex of the brain via the optic nerve and the retinogeniculate pathway passing the dorsal lateral geniculate nucleus (dLGN) of the thalamus. Most axons of retinal ganglion cells (RGCs) cross sides in the optic chiasm. Figure adapted from (Euroform Healthcare, 2020).

Rod and cone photoreceptors are the two light-sensitive elements of the retina. Their essential function is to initiate the phototransduction cascade (Bear et al., 2016; Purves et al., 2001b) by light absorption with the photopigment in their outer segments. The complex network of bipolar, amacrine, horizontal and ganglion cells and their interactions are mainly responsible for the sensitivity of the visual system to contrast over a broad range of light intensities, whereas Müller glia cells mainly contribute to retinal structure and homeostasis (Goldman, 2014; Grosche et al., 2016).

Being part of the CNS and consisting of a neural network, the retina converts photonic energy from light via photoreceptors into a neural signal, which finally reaches the visual cortex of the brain via the optic nerve and the retinogeniculate pathway (Figure 9 - B). This pathway is responsible for the transmission of visual information from the retina to the visual cortex, which are connected by the dorsal lateral geniculate nucleus (dLGN) of the thalamus (Bear et al., 2016; Kerschensteiner and Guido, 2017; Purves et al., 2001a). The retina sends signals to the dLGN through the axons of retinal ganglion cells (RGCs), of which the terminations are organized

into overlapping maps according to origin, topographic position within the retina and cell type (Bear et al., 2016; Kerschensteiner and Guido, 2017; Purves et al., 2001a). The dLGN consists of two major cell types: thalamocortical relay cells and interneurons. They both receive input from the retina via RGCs, although only thalamocortical neurons project to the visual cortex via axons leaving the dLGN (Bear et al., 2016; Kerschensteiner and Guido, 2017; Purves et al., 2001a). The visual cortex of each hemisphere receives information from the contralateral eye. Based on structural and functional properties, it is divided up into five different areas (V1 to V5). V1, the primary visual cortex, receives information from the dLGN. Afterwards, the processed information is sent to other brain regions to be further used. This highly specialized mechanism enables the brain to quickly recognize any object without much conscious effort (Bear et al., 2016).

1.3.2 Epigenetics in the eye

Complex biological systems and processes such as organogenesis, homeostasis but also the visual system, are regulated by genetic programs and fine-tuned by epigenetic mechanisms. Environmental factors, lifestyle, drugs or inflammatory processes impact healthy and diseased states of the visual system by epigenetic factors (Alkozi et al., 2017; Corso-Díaz et al., 2018). Concerning eye and visual system, an increasing number of reports suggests influence of epigenetic factors on ocular diseases (Alkozi et al., 2017; Busanello et al., 2017; Corso-Díaz et al., 2018; Hewitt et al., 2017; Wei et al., 2012).

In the following, the impact of epigenetic changes and mechanisms on important ocular diseases such as cataracts, age-related macular degeneration (AMD) and diabetic retinopathy is described in detail.

Cataract is the number one leading cause of reversible vision loss according to the World Health Organization (WHO). Opacity in the crystalline lens leads to blocked transmission of light to the retina (Alkozi et al., 2017; World Health Organization (WHO)). Three altered epigenetic factors have been reported in the context of cataracts. Firstly, hypermethylation of the *Klotho* gene promotor appears to be involved in development of the disease. The expression of the *Klotho* gene family generally shows correlation to the progression of age-related and chronic

diseases in mammals (Jin et al., 2015). Secondly, hypermethylation of the CpG island in the *CRYAA* gene promotor is correlated with the reduction of α-crystallin expression in age-related cataracts, which represents 35 % of all crystalline in the ocular lens. Application of inhibitors of DNA methylation results in restoring *CRYAA* gene expression, which opens new therapeutic options in cataract treatment (Zhou et al., 2012a; Zhou et al., 2012b). Thirdly, demethylation of Kelch-like ECH-associated protein 1 (Keap1), which suppresses antioxidant protection of the lens, is reported to be involved in development of cataracts (Gao et al., 2015).

AMD is a common disease of age affecting the macula, the part of the retina for central vision (Bear et al., 2016), and finally leading to loss of central vision. Aging is generally associated with many epigenetic alterations in cells such as changes in histone modifications, global loss of core histones, exchange of histone variants, global reduction of DNA methylation and loss of heterochromatin (Benayoun et al., 2015; Pal and Tyler, 2016). For AMD, not much is described about epigenetic factors contributing to disease development, as it is highly heterogenous and most likely guided by environmental factors such as diet or smoking. However, there are reports about hypermethylation on AMD susceptibility genes, e.g. Complement Factor H (CFH) or Complement Factor B (CFB) (Hutchinson et al., 2014), and about decreased expression of HDACs in AMD retina and retinal pigment epithelium (RPE) (Anderson et al., 2015).

The pathophysiology of diabetic retinopathy, a common complication of diabetes, has been frequently connected to epigenetic changes in the complex system of the retina (Corso-Díaz et al., 2018). Many studies reported global alterations in histone acetylation and impaired expression of HDACs and lysine acetyltransferases, suggesting an epigenetic imbalance (Kadiyala et al., 2012; Zhong and Kowluru, 2010). Moreover, several studies link dysregulation of histone and DNA modifying enzymes to changes in the epigenetic environment and expression of genes involved in disease progression (Corso-Díaz et al., 2018; Kowluru, 2017). For example, impaired activity of epigenetic writers and erasers caused changes in the epigenetic landscape of matrix metalloproteinase-9 *(MMP9)* and mitochondrial superoxide dismutase 2 *(SOD2)* promotors, both important for mitochondrial homeostasis in retina, fitting to the involvement of oxidative stress and mitochondrial dysfunction in diabetic retinopathy (Kowluru et al., 2015).

To conclude, epigenetic factors play an important role in ocular diseases, offering new therapeutic options in addition to standard treatments. Moreover, further investigation of epigenetic influence on retinal disease development might help to detect diseases in early stages to stop the irreversible effect of vision loss as early as possible.

1.4 Generation of genetically modified mouse models

1.4.1 Historical view

The use of animal models in life sciences dates back to the ancient Greek, when animal models primarily were used in observational studies to understand human anatomy, physiology and behaviour. With the beginning of the 20th century, the use of animal models highly increased and became more experimental than only observational. Later, advances in genetics as well as technologies and the ability to manipulate the genome enabled the creation of animal models for specific research questions. Especially in the 1980s, the number of technologies to create genetically modified mice exploded (Ericsson et al., 2013).

The laboratory mouse (*Mus musculus*) has remained the most important research animal to study human biology, pathology and disease because of several advantages and biological characteristics required for modelling of human physiology and pathophysiology (Gurumurthy and Lloyd, 2019; Rosenthal and Brown, 2007). The key advantage is the highly conserved genetic homology, which exists between mice and humans (Justice and Dhillon, 2016). Furthermore, mice display a short life cycle as well as a short gestation period and lifespan. They additionally have a high breeding efficiency, which is especially important for fast expansion of experimental research for statistical reasons (Doyle et al., 2012; Gurumurthy and Lloyd, 2019). In addition to those characteristics, the ability to manipulate the genome of mice in a Mendelian-inheritable way has been essential for their widespread use to study human diseases (Doyle et al., 2012). The technologies for the generation of genetically modified mouse models have developed over the last decades from first approaches using chemical agents for genetic manipulation to genome editing with programmable endonucleases, which is state of the art nowadays.

First research in mouse genetics was based on directly visible phenotypes caused by spontaneous or induced mutations. This approach is called “forward genetics” and describes the process of observing a phenotype and subsequently searching for the underlying genetic mechanism. Chemicals, radiation and viruses were e.g. used to damage genes in mice to identify their functions and associated diseases (Gurumurthy and Lloyd, 2019; Justice et al., 2011). With the development of molecular cloning techniques and the usage of recombinant DNA, this approach was more and more replaced by “reverse genetics”, in which the resulting phenotype from a known specific genetic manipulation is investigated (Gurumurthy and Lloyd, 2019; Justice et al., 2011). The first strategy in the 1980s to generate gene KO mouse models was gene-targeting in mESCs (Gordon and Ruddle, 1981; Gordon et al., 1980). Here, the genome of mESCs is genetically modified, the targeted cells are injected into blastocysts, which are subsequently transferred into pseudo-pregnant female mice. The offspring contains the desired gene manipulation. Another similar technique, developed in that decade, was the generation of transgenic mice by introducing an exogenous gene via microinjection into one-cell-embryos, which are then transferred into pseudo-pregnant female mice (Palmiter and Brinster, 1985; Palmiter et al., 1982). Those initially developed technologies have been improved overcoming limitations concerning specificity, reproducibility and efficiency. Those next-generation technologies comprise conditional mutagenesis strategies in mESCs, gene function knockdown using RNA interference, targeted transgenesis in zygotes via homologous recombination in mESCs and usage of programmable endonucleases in zygotes for genome editing (Gurumurthy and Lloyd, 2019; Justice et al., 2011).

In the following, creation of KO models using tissue-specific conditional mutagenesis and genome editing via CRISPR-Cas9 is further described, as they were used in this study to generate specific mouse models.

1.4.2 Cre-loxP-recombination system

Conditional mutagenesis can solve e.g. the problem of embryonic lethality resulting from the deletion of specific genes, such as Tet3, in animal models. The system is based on the ability to efficiently convert a functional allele either in a specific cell type and / or at a specific time point into a mutant allele and vice versa. Those two possibilities are called tissue-specific and time-specific or inducible conditional mutagenesis (Gurumurthy and Lloyd, 2019).

In this context, the most commonly used strategy in mouse models is the Cre-loxP-recombination system (Kim et al., 2018; Nagy, 2000; Sauer, 1998). In this system, the target region of a specific gene is flanked by loxP sites, which are short palindromic target sequences of Cre recombinase (Gurumurthy and Lloyd, 2019). Cre recombinase, a 38-kDa DNA recombinase, belongs - together with flipase (Flp) and D6 specific recombinase (Dre) - to the family of tyrosine site-specific recombinases (Meinke et al., 2016). In the absence of Cre recombinase, the loxP-flanked (floxed) sequences do not affect gene transcription. However, depending on their position and orientation, the loxP sites recombine to excise or invert the target gene region, when exposed to Cre recombinase (Gurumurthy and Lloyd, 2019). When Cre recombinase recognizes two loxP sites of the same orientation, the intervening floxed gene sequence is finally excised (Figure 10). By contrast, when the loxP sites are symmetrically oriented, they recombine to invert the intervening gene sequence (Gurumurthy and Lloyd, 2019; Kim et al., 2018; Nagy, 2000; Sauer and Henderson, 1988). By mating a Cre driver line, in which Cre recombinase is expressed by a specific promotor targeting a specific cell or tissue type, with a mouse line, containing a loxP-flanked gene sequence, their offspring displays expression of the recombined allele and a mouse line with e.g. a KO in a specific cell or tissue type is generated (Kim et al., 2018; McLellan et al., 2017). The respective originating mouse lines are generated by gene targeting in mESCs followed by injection of selected clones into mouse blastocytes and oocytes, respectively (Hall et al., 2009; McLellan et al., 2017).

In an inducible Cre-loxP system, Cre recombinase activity is additionally controlled by an exogenously inducible promotor. The most common exogenous inducers are tamoxifen (CreERT system) and tetracycline (Tet-on/off-system) (Kim et al., 2018; McLellan et al., 2017; Metzger and Chambon, 2001; Nagy, 2000).

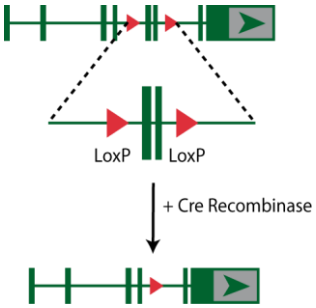

Figure 10: Cre-loxP-recombination system

Cre recombinase recognizes two repeated asymmetrically oriented loxP sites leading to an excision of the loxP-flanked (floxed) DNA sequence. A mouse line with a KO in a specific cell or tissue type is generated by simply breeding a Cre driver line, in which Cre recombinase is expressed by a specific promotor targeting a specific cell or tissue type, with a floxed mouse line.

A huge variety of cell- and tissue-specific Cre and/or inducible Cre driver lines, summarised in (Kim et al., 2018), have been generated, as this system is a very useful technology for genetical manipulation in research models.

1.4.3 Genome editing using CRISPR-Cas9 technology

Programmable and targeted endonucleases are a powerful tool for genome editing and the generation of genetically modified animal models, displaying several advantages like higher efficiency and much faster workflows in comparison to the classical strategies like ESC-based gene-targeting (Gurumurthy and Lloyd, 2019). Four major systems of programmable endonucleases exist: homing endonucleases (HEs) (Rouet et al., 1994), zinc-finger nucleases (ZFNs) (Carroll, 2011; Urnov et al., 2010), transcription activator-like effector nucleases (TALENs) (Sung et al., 2013) and the clustered regularly interspaced short palindromic repeats (CRISPR)-Cas9 system (CRISPR-Cas9) (Cong et al., 2013; Jinek et al., 2012; Mali et al., 2013). They all have in common that the nucleases introduce a DNA double-strand break (DSB) at a specific target locus, which is subsequently repaired by one of two major pathways for DNA damage repair: the error-prone and imprecise pathway of non-homologous end joining (NHEJ) or the precise and high-fidelity pathway of homology-directed repair (HDR) (Gurumurthy and Lloyd, 2019; Ran et al., 2013).

CRISPR-Cas9 technology has revolutionized the field of genome editing, due to several advantages compared to the other nuclease-based genome engineering systems, HEs, ZFNs and TALENs. Those advantages are e.g. an easier design, low costs, higher efficiency as well as the ability to use the system for high-throughput and multiplexed editing in various cell types and organisms (Ran et al., 2013; Sander and Joung, 2014).

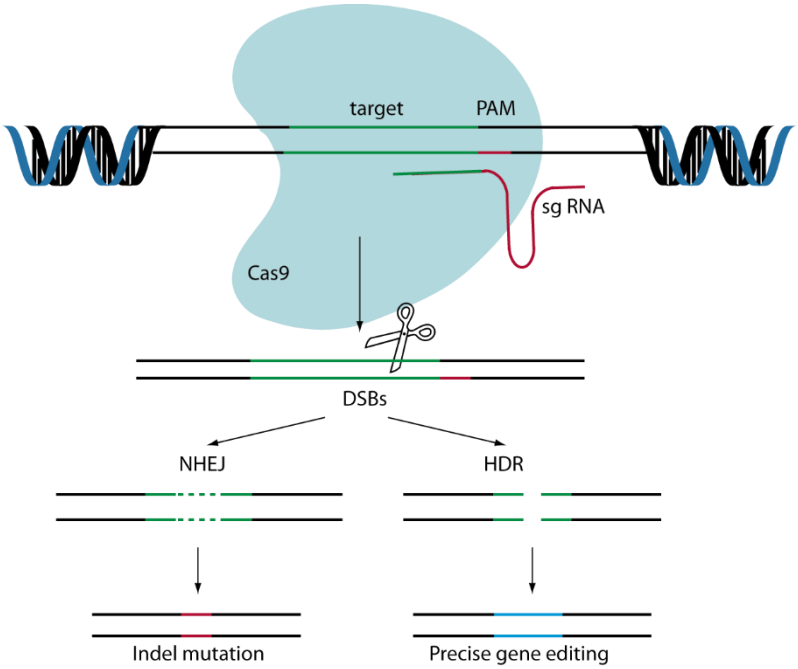

Figure 11: Genome editing using CRISPR-Cas9

CRISPR-Cas9 system comprises the Cas9 nuclease, which is guided by a single guide RNA (sgRNA) to a complementary target DNA followed by a 5'-NGG protospacer adjacent motif (PAM). The Cas9 nuclease introduces a DNA double-strand break (DSB) at a specific target locus, which is repaired by either the error-prone imprecise pathway of non-homologous end joining (NHEJ) or the precise high-fidelity pathway of homology-directed repair (HDR). Figure adapted from (Horii and Hatada, 2014).

CRISPR-Cas9 system originally functions as microbial adaptive immune system in a wide range of bacteria and archaeal hosts using RNA-guided nucleases to damage foreign genetic elements (Bhaya et al., 2011; Garneau et al., 2010; Horvath and Barrangou, 2010; Makarova et al., 2011). The most used CRISPR Cas system derives from *Streptococcus pyogenes*, while further systems derive from *Staphylococcus aureus* (Ran et al., 2015), *Streptococcus thermophilus* (Cong et al., 2013; Esvelt et al., 2013) or *Neisseria meningiditis* (Esvelt et al., 2013).

In brief, the Cas9 endonuclease from *S. pyogenes* is targeted to genomic DNA by a single guide RNA (sgRNA). The targeting mechanism is based on sequence complementarity between the sgRNA and the genomic locus. The only requirement for the selection of Cas9 target sites is the presence of a 5'-NGG protospacer adjacent motif (PAM) sequence directly 3' of the 20-bp target sequence. The Cas9 endonuclease binds the sgRNA and is then directed to the target locus in the genome, where it introduces a specific DNA DSB 3 - 4 bp upstream of the PAM sequence (Figure 11) (Garneau et al., 2010; Gasiunas et al., 2012; Jinek et al., 2012; Ran et al., 2013). Direct injection of the required components, crispr RNA (crRNA), trans-activating crRNA (tracrRNA) and recombinant Cas9 protein, forming the active ribonucleoprotein (RNP) complex, into embryos and their transfer to pseudo-pregnant mice allows very fast and efficient generation of genetically modified mouse models with multiple modified alleles (Ran et al., 2013; Shen et al., 2013; Wang et al., 2013).

Although challenges in the context of mosaicism (Mehravar et al., 2019; Yen et al., 2014) as well as Cas9 off-target (Zhang et al., 2015) effects remain and some optimization regarding the generation of knock-in mouse models is necessary, CRISPR-Cas9 technology has mostly replaced the classical techniques in the field of genetic manipulation and genome editing.

2 Aim of the Study

The major aim of the study was to facilitate the elucidation of the multifaceted functions and roles of Tet3 and its isoforms in neurons and the CNS by generating and characterizing tissue- and isoform-specific Tet3 KO mouse models as well as TET3 isoform overexpressing human iPS cell lines. These mouse and cell culture models shall form the basis for future investigations to gain more knowledge about Tet3 involvement in disease mechanisms, as TET3 was recently reported to be a disease gene of the epigenetic machinery in humans.

As the focus of this study lies on Tet3 and its catalytic products, a further aim was to examine 5hmC dynamics in the brain and their connection to neuronal activity by depolarizing acute mouse hippocampal slices. 5hmC is a highly enriched in the mammalian brain and serves as an important epigenetic mark for normal neuronal development and function. Therefore, these investigations shall lead to a better understanding of the influence of neuronal activity on Tet3 action and hydroxymethylation of genes under physiological and pathophysiological conditions. This work should thus offer novel options for the treatment of neurological disorders of epigenetic aetiology.

3 Material and Methods

3.1 Animals

For this thesis, different genetically modified mouse lines and BL/6 wildtype (WT) mice were used. C57BL/6J or C57BL/6N males and females were obtained from Charles River (Sulzbach, Germany). Conditional Tet3 KO mice (Amouroux et al., 2016), in the following named as Tet3 L2/L2 mouse line, were kindly provided by Prof. Dr. Petra Hajkova's research group at the Imperial College in London. Nestin Cre mice (Tronche et al., 1999) were obtained from Prof. Dr. Rüdiger Klein at the Max Plank Institute of Neurobiology in Munich. Both mouse lines were bred to generate the Tet3 L2 + Nestin Cre mouse line (Figure 12).

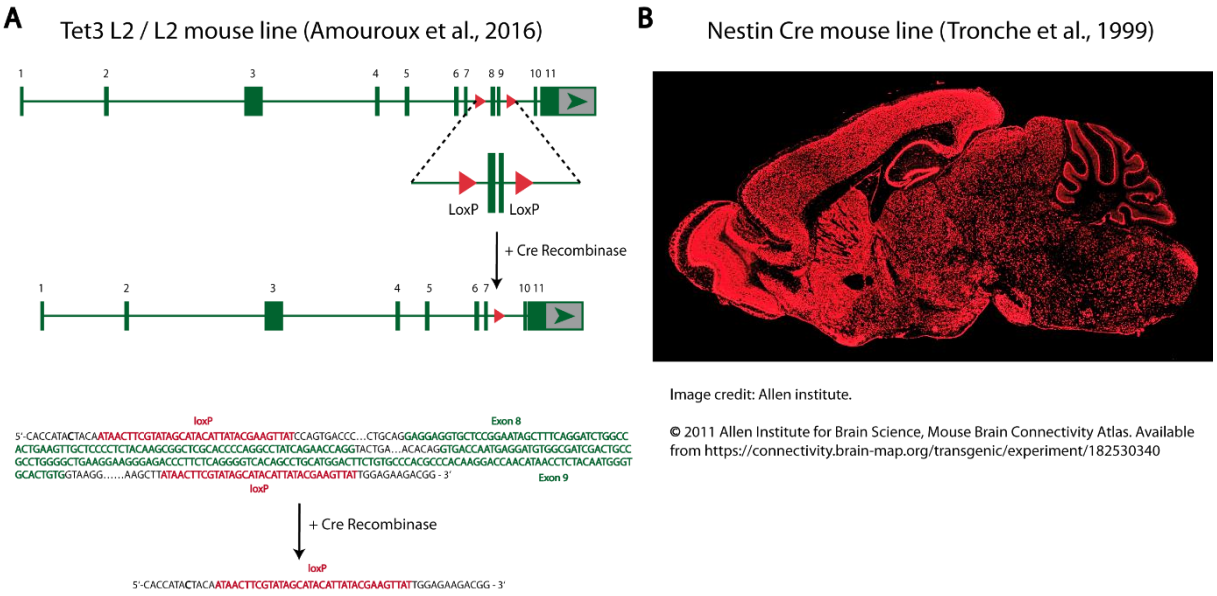

Figure 12: Mouse lines used for generation of the Tet3 L2 + Nestin Cre mouse model

(A) The conditional Tet3 KO in the Tet3 L2/L2 mouse line is based on the Cre/loxP site specific recombination system. After crossing this line with a Cre driver line, exon 8 and 9 of the Tet3 gene flanked by loxP sites are excised in those cells, in which the specific promotor driven Cre recombinase is active. **(B)** Regarding the nervous system, Nestin promotor driven Cre recombinase is present in the central nervous system (CNS) and peripheral nervous system (PNS) as well as in Müller glia cells of the retina by embryonic day 11 (E11). The image of a brain sagittal section of a Nestin Cre mouse (male, P56) crossed with a TdTomato reporter line visualises that all TdTomato positive red cells were affected by Nestin Cre activity during the period from E11 to adult age. The image is available from https://connectivity.brain-map.org/transgenic/experiment/182530340 (Allen Institute for Brain Science, Mouse Brain Connectivity Atlas and (Oh et al., 2014)).

Tet3 short KO (Tet3 S KO) and Tet3 long KO (Tet3 L KO) mouse lines were generated in collaboration with Dr. Florian Giesert from Prof. Dr. Wolfgang Wurst's research group at the Helmholtz Zentrum in Munich. The generation strategy of Tet3 S and Tet3 L KO mouse lines is described under chapter 3.3. All procedures concerning animals conform to the German animal protection laws and were approved by the local authority (ROB - Regierung von Oberbayern). Mice were housed under a 12 h light/dark cycle (lights on at 7 a.m.) with ad libitum access to food (Ssniff; regular feed: R/M-H; breeding feed: M-Z Extrudat) and water.

3.2 Chemicals and solutions

All used chemicals were obtained from Bio-Rad, Merck, Roth, Sigma-Adrich or VWR unless stated otherwise. Their quality was either "pro analysi" or "for molecular biology". For the preparation of all solutions, high pure and deionized water from the Milli-Q Plus System (Merck Millipore) was used.

3.3 Generation of Tet3 isoform-specific KO mouse lines

Tet3 S KO and Tet3 L KO mouse lines were generated using CRISPR-Cas9 technology.

3.3.1 Single guide RNAs

Genomic DNA and transcript sequences of the mouse reference genome (Dec.2011, GRCm38/mm10) were downloaded from NCBI gene, Ensembl Genome Browser or UCSC Genome Browser. To design single guide RNA (sgRNA) sequences in the target region, the CRISPOR website was used. For *Sp*Cas9, a 20 bp-NGG PAM setting was applied (Haeussler et al., 2016). The elimination of sgRNAs was set at a specificity score (Hsu et al., 2013) lower than 50. For the generation of the Tet3 S KO and Tet3 L KO mouse lines, the listed gene specific sgRNAs were used (Table 1).

Table 1: sgRNA sequences

The listed gene specific sgRNA were used to generate Tet3 S KO and Tet3 L KO mouse lines.

Mouse Line	sgRNA sequence (5' - 3')
Tet3 S KO	GCGCCAGCCAATCCCGCGCC TGCTGGGCAGGTCCTTGGCG AGATCCCCGGGACCCGCTCG GCCGGCCGAGGTAGAGCGCT
Tet3 L KO	GGCAAGAAGTGGGTGCCCGA TGAGGCCGTTGTCATCACGA

3.3.2 Off-target analysis

The CRISPOR website predicted off-targets which were ranked by CFD off-target score (Doench et al., 2016). For experimental off-target analysis, top three global and top two exonic off-targets were chosen.

Primers for off-target analysis, which are listed in the appendix, were designed using the NCBI primer-BLAST tool (National Center for Biotechnology information, U.S. National Library of Medicine) and synthesised by Eurofins Genomics. For PCR amplification, Q5® High-Fidelity DNA Polymerase (NEB) was used following manufacturer's instructions (Table 2). PCRs were run in a ProFlex™ 3x32-well PCR System (Applied Biosystems, Thermo Fisher Scientific).

DNA	150	ng
Primer forward (10 mM)	1.25	µL
Primer reverse (10 mM)	1.25	µL
dNTPs (1 mM)	5	µL
5x Q5® Reaction Buffer	5	µL
Q5® High Fidelity DNA Polymerase	0.2	µL
Water	ad 25	µL

Table 2: Q5® High Fidelity DNA Polymerase - PCR cycling parameters

*1 Annealing temperature was optimised for each primer pair based on the primer melting temperature estimated using NEB T_m Calculator online tool. *2 Extension time was optimised based on the specific length of the PCR products.

Step	Temperature	Time	Number of cycles
Initial denaturation	98 °C	30 s	1
Denaturation	98 °C	5 - 10 s	25 - 35
Annealing *1	50 – 72 °C	10 - 30 s	
Extension *2	72 °C	20 - 30 s / kb	
Final extension	72 °C	2 min	1
Soak	4 -10 °C	indefinite	1

Extraction of PCR products from 1 % agarose gels was performed using the QIAquick gel extraction kit (Qiagen) following the manufacturer´s instructions. DNA was sent to Eurofins Genomics for Sanger sequencing.

3.3.3 Microinjection of CRISPR Cas9 components

Microinjection procedure was carried out by Dr. Florian Giesert from Prof. Dr. Wolfgang Wurst's research group at the Helmholtz Zentrum in Munich.

100 µM of the respective synthetic Alt-R™ CRISPR crRNAs were mixed with 100 µM of Alt-R™ CRISPR-Cas9 tracrRNA (Integrated DNA Technologies Inc., Coralville, IA, USA). The mixture was incubated for 5 minutes (min) at 95 °C and cooled down to room temperature (RT) to form a crRNA/tracrRNA duplex. The duplex and recombinant Cas9 protein (IDT, Coralville, USA) were then diluted in microinjection buffer (5 mM Tris, 0.1 mM EDTA, pH 7.2) to working concentrations of 11 ng/µL for crRNA, 22 ng/µL for tracrRNA and 50 ng/µL for Cas9 protein. The injection mix was incubated for 10 min at RT and 10 min at 37 °C to form the active ribonucleoprotein (RNP) complex. One-cell embryos were obtained by mating C57BL/6N males with C57BL/6N females, which were superovulated with 7.5 units PMSG (Pregnant Mare`s Serum Gonadotropin) and 7.5 units Human Chorionic Gonadotropin (HCG). For microinjections, one-cell embryos were injected into the larger pronucleus. After the injection, zygotes were transferred into pseudo-pregnant CD1 female mice to obtain live pups. All mice showed normal development and appeared healthy.

3.4 Genotyping

For genotyping analysis, genomic DNA (gDNA) was isolated from mouse ear biopsies. Gene-specific regions of the isolated gDNA were amplified by PCR and visualised via agarose gel electrophoresis to obtain the genotype.

To isolate gDNA, the mouse tissue sample was incubated in 600 µL 50 mM NaOH at 95 °C for 10 min on a heating block and then mixed well by vortexing. The sample was neutralised by adding 50 µL Tris-HCl pH 8 and centrifuged for 6 min at 13,000 rpm and RT.

For PCR amplification, gene-specific primers and GoTaq® DNA Polymerase (Promega, M300) were used following manufacturer's instructions (Table 3). PCRs were run in a ProFlex™ 3x32-well PCR System (Applied Biosystems, Thermo Fisher Scientific).

gDNA	2	µL
Primer forward (10 mM)	1.25	µL
Primer reverse (10 mM)	1.25	µL
dNTPs (1 mM)	5	µL
Green GoTaq® Reaction Buffer	5	µL
GoTaq® G2 DNA Polymerase	0.2	µL
Water	ad 25	µL

Table 3: GoTaq® G2 DNA Polymerase - PCR cycling parameters

*1 Annealing temperature was optimised for each primer pair based on the primer melting temperature.
*2 Extension time was optimised based on the specific length of the PCR products.

Step	Temperature	Time	Number of cycles
Initial denaturation	95 °C	2 min	1
Denaturation	95 °C	0.5 – 1 min	25 - 35
Annealing *1	42 – 65 °C	0.5 – 1 min	
Extension *2	72 °C	1 min / kb	
Final extension	72 °C	5 min	1
Soak	4 °C	indefinite	1

PCR primers were designed using the NCBI Primer-BLAST online tool (National Center for Biotechnology information, U.S. National Library of Medicine) and synthesised by Eurofins Genomics. The primer pairs used for genotyping PCRs and PCR programs for specific genes are listed in the appendix.

3.5 Generation of TET3 isoform overexpressing cell lines

3.5.1 Cell culture

If not stated otherwise, all cell culture media, supplements and solutions were supplied by Gibco™ (Thermo Fisher Scientific). Materials used for cell culture experiments were either ordered in cell culture grade or sterilized by autoclaving (Sterilisator, Münchener Medizin Mechanik).

PGP1 cells and inducible Neurogenin iPS cells (iNGN) were a kind gift of the laboratory of Prof. Dr. Volker Busskamp (DFG-Center for Regenerative Therapies Dresden / Department of Ophthalmology, University of Bonn).

PGP1 cells and iNGNs were cultured in StemFlex Medium + 1 % Antibiotic-Antimycotic (Anti-Anti) at 37 °C and 5 % CO_2 in an incubator (Heraeus, Thermo Scientific). Cell culture plates were pre-coated with Geltrex™ LDEV-free, hESC-qualified reduced growth factor basement membrane matrix 1:50 diluted in Dulbecco´s modified eagle medium (DMEM)/F-12 (1:1) + L-Glutamine + 15 mM HEPES + 1 % Anti-Anti. For passaging, cells were first washed with Dulbecco´s phosphate-buffered saline (DPBS), then detached from the plates using TrypLE™ Express, washed again with DPBS and centrifuged for 5 min at 300 x g and RT. Finally, the cells were resuspended and seeded in StemFlex + 1 % Anti-Anti + 1 % RevitaCell™ Supplement. Medium was changed after 18 - 24 h to StemFlex + 1 % Anti-Anti, which was then changed every two days.

To induce iNGN differentiation and overexpression of TET3 isoforms, doxycycline (DOX) hyclate was added to StemFlex + 1 % Anti-Anti + 1 % RevitaCell™ Supplement to a final concentration of 0.5 µg/mL, when the cells were seeded. The day of DOX addition to the cells was considered as day 0 (d0). On d1, medium was changed to StemFlex + 1 % Anti-Anti supplemented with DOX and afterwards changed every two days.

3.5.2 Cloning of PiggyBac constructs

For cloning, either classical restriction digest and ligation or restriction enzyme independent methods such as Gibson cloning (Gibson et al., 2009) were applied. All enzymes used for restriction and ligation were obtained from Thermo Fisher Scientific.

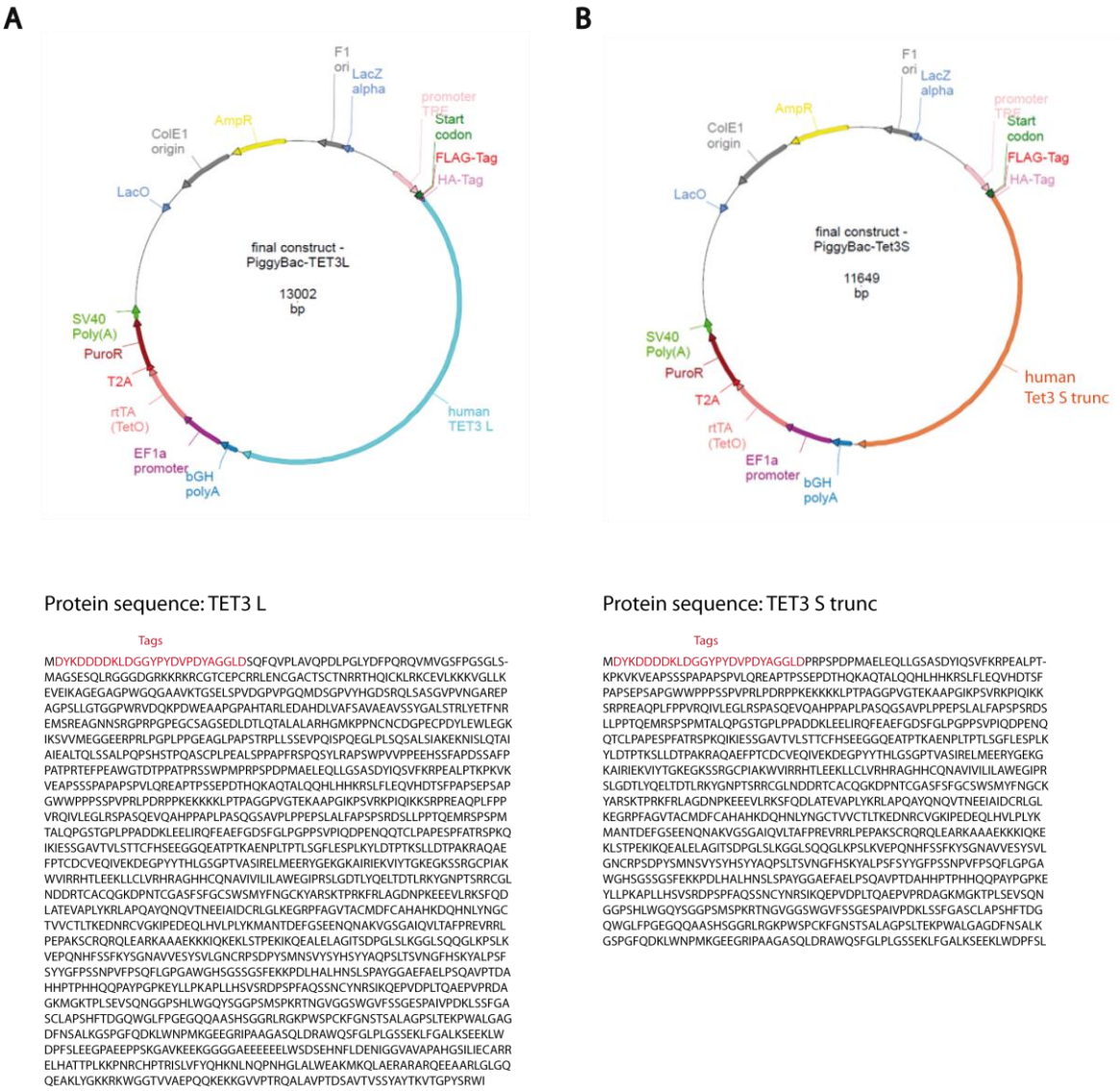

Figure 13: Cloned PiggyBac constructs

A PiggyBac transposon vector containing the coding sequence for human TET3 L and S isoforms under the control of the tetracycline-responsive promoter element (TRE), an expression cassette consisting of the reverse tetracycline-controlled transactivator and the puromycin resistance gene (rtTA-T2A-PuroR) as well as sequences encoding HA- and FLAG-Tags was cloned, respectively **(A+B)**. TET3 S trunc is a shortened version of TET3 S isoform, lacking the exon, which is specific for TET3 S. The coding sequence starts within exon 3, which is common for all TET3 isoforms **(B)**.

For cloning of the constructs for the generation of TET3 isoform overexpressing cells lines, the Addgene plasmid FH-TET3-pEF (order number 49446, depositor Anjana Rao, (Ko et al., 2013)) was used for amplification of the TET3 coding sequence. The TET3 L coding sequence was inserted into a PiggyBac plasmid (System Biosciences) downstream of a DOX inducible promotor (Tet-on-system) (Figure 13 - A). For the TET3 S construct, an at the 5' shortened

coding sequence as well as a commercially synthesized gene fragment encoding FLAG- and HA-tags were assembled downstream of the promotor (Figure 13 - B).

Used cloning oligos and gene fragments, which are listed in Table 14 in the appendix, were designed using the NCBI primer-BLAST tool and the NEBuilder® Assembly tool and synthesised by Eurofins Genomics. For PCR amplification, Q5® High-Fidelity DNA Polymerase (NEB) was used following manufacturer's instructions (Table 4). PCRs were run in a ProFlex™ 3x32-well PCR System (Applied Biosystems, Thermo Fisher Scientific).

DNA	1 - 150	ng
Primer forward (10 mM)	1.25	µL
Primer reverse (10 mM)	1.25	µL
dNTPs (1 mM)	5	µL
5x Q5® Reaction Buffer	5	µL
Q5® High Fidelity DNA Polymerase	0.2	µL
Water	ad 25	µL

Table 4: Q5® High Fidelity DNA Polymerase - PCR cycling parameters

* The insert sequence for TET3 S was PCR amplified with an extension time of 2 min 20 s per cycle. The insert sequence for TET3 L was PCR amplified with an extension time of 3 min 10 s per cycle.

Step	Temperature	Time	Number of cycles
Initial denaturation	98 °C	30 s	1
Denaturation	98 °C	10 s	30
Annealing	72 °C	20 s	
Extension	72 °C	2 min 20 s / 3 min 10 s *	
Final extension	72 °C	2 min	1
Soak	4 -10 °C	indefinite	1

Extraction of PCR products from agarose gels was performed using the QIAquick gel extraction kit (Qiagen) following the manufacturer´s instructions. Purification of DNA sequences from PCR reaction mixes was performed using the QIAquick PCR purification kit (Qiagen) following the manufacturer's instructions.

Transformation of chemically competent bacteria was carried out as described (Cosloy and Oishi, 1973; Mandel and Higa, 1970). In brief, 3 µL of ligation products were added to chemically competent 10-beta *Escherichia coli* (*E. coli*) K12 bacterial cells (NEB) thawed on ice.

After mixing gently with the pipette tip and incubating for 30 min on ice, a heat shock was applied to the mixture by putting it into a 42 °C ThermoMixer® C (Eppendorf) for 30 - 45 s and incubating it again on ice for 2 min. Then, the bacteria cells were plated onto lysogeny broth (LB) agar plates containing 50 µg/mL ampicillin. Finally, the plates were incubated at 37 °C overnight.

For plasmid preparations, the PureLink™ HiPure Plasmid Midiprep or Maxiprep Kit (Invitrogen, Thermo Fisher Scientific) following the manufacturer's instructions were used. To check the sequence of the cloned plasmid, plasmid DNA was sent to Eurofins Genomics for Sanger sequencing.

3.5.3 Generation of stable cell lines using PiggyBac technology

To generate human TET3 isoform overexpressing PGP1 and iNGN cell lines, the coding sequences for human TET3 isoforms were inserted into the cell genome using PiggyBac transposon technology (System Biosciences). Therefore, a PiggyBac transposon vector containing the coding sequence for human TET3 isoforms under the control of the tetracycline-responsive promoter element (TRE) and a bicistronic expression cassette consisting of the reverse tetracycline-controlled transactivator and the puromycin resistance gene (rtTA-T2A-PuroR) was cloned. To insert the sequence encoded between the ITRs (inverted terminal repeats) of the transposon vector into random TTAA sites in the genome, PGP1 and iNGN cells were co-transfected with a PiggyBac transposase expression vector and the cloned PiggyBac transposon vector in a 1:2.5 DNA mass ratio. For the 24-well format, approximately 143 ng PiggyBac transposase vector and approximately 357 ng PiggyBac transposon vector (in total 500 ng vector DNA) were mixed and used for cell transfection with Lipofectamine ™ Stem Transfection Reagent. After 24 h, successfully transfected PGP1 and iNGN cells were selected by addition of puromycin dihydrochloride (0.75 µg/mL, Gibco, Thermo Fisher Scientific) for approximately one week. TET3 isoform overexpression as well as iNGN differentiation were induced by adding DOX to the cells.

3.6 Dissection, preparation and slicing of mouse tissue

3.6.1 Retina dissection for DNA, RNA and protein isolation

Mice were anaesthetized with isoflurane and sacrificed. The eyes were taken out from the orbit and fixed with curved forceps. The cornea was carefully cut with a sharp scalpel and the curved forceps were moved upwards to remove the retina form the eye. The retina was isolated from residual compartments like lens or vitreous body in cold 0.1 M phosphate buffer (PB) pH 7.4 under a microscope (Stemi 2000, Zeiss), transferred to a 2 mL safe-lock reaction tube (Order no. 0030120.094, Eppendorf) and snap frozen in liquid nitrogen. The tissue was stored at -80 °C until further use.

3.6.2 Preparation of retina for cryosections

Mice were anaesthetized with isoflurane and sacrificed. The eyeballs were marked temporally using a glowing needle. This mark was essential for tracking the retina's orientation during the whole procedure. The eyes were collected and transferred into 0.1 M PB. Using a stereomicroscope (Stemi 2000, Zeiss) the eyes were punctured at the ora serrata using a cannula (FINE-JECT®, 30G, Ref. 4710003012, Henke-Sass-Wolf) and prefixed for 5 min in 4 % PFA in 0.1 M PB on ice. Afterwards, the cornea, lens and vitreous body were removed by cutting along the ora serrata with micro-scissors (Vannas Spring Scissor, order no. 15001-01, Fine Science Tools). The temporal mark at the ora serrata was conserved by a small cut in the retina. The remaining eyecup containing the retina was fixed for 45 min in 4 % PFA on ice. Afterwards, the eyecups were washed three times in 0.1 M PB for 5 min and dehydrated in 30 % sucrose in 0.1 M PB overnight at 4 °C. Finally, the eyecups were embedded in embedding medium (Richard-Allan Scientific ™ Neg-50 ™, cat. no. 6502, Thermo Fisher Scientific) and frozen on dry ice. The embedded tissue was stored at -80 °C until further use.

3.6.3 Cryosectioning of mouse retina

Before cryosectioning, embedded retina tissue was adapted to the sectioning temperature (approximately -20 °C) in the cryostat (CM3050 S, Leica) and mounted onto a cutting plate with embedding medium (Richard-Allan Scientific ™ Neg-50 ™, cat. no. 6502, Thermo Fisher Scientific). Three to four serial retina slices (10 µm) were placed onto one microscope slide

(Menzel-Gläser Superfrost® Plus, Ref. J1800AMNZ, Thermo Scientific). After air drying the slides were stored at -20 °C or - 80 °C until further usage.

3.6.4 Dissection of mouse brain for DNA, RNA and protein isolation

Mice were anaesthetized with isoflurane and sacrificed. The brains were carefully removed and put into cold phosphate-buffered saline (PBS) pH 7.4. The brain regions of interest were isolated from other compartments in cold PBS pH 7.4 under a microscope (Stemi 2000, Zeiss) using forceps and spatula (Fine Science tools), transferred to a 2 mL safe-lock reaction tube (Order no. 0030120.094, Eppendorf) and snap frozen in liquid nitrogen. The tissue was stored at -80 °C until further use.

3.6.5 Perfusion

Mice were anaesthetized via an intraperitoneal injection of ketamine/xylazine solution (100 mg ketamine per kg body weight + 15 mg xylazine per kg body weight). After reaching the tolerance state, the mice were fixed to expose the abdomen. Abdomen and thorax were opened until the heart was visible making sure not to injure other organs during the process. At the same time, an isotonic PBS solution was loaded by a pump system and released through a cannula (FINE-JECT®, 30G, Ref. 4710003012, Henke-Sass-Wolf). Subsequently, the cannula connected to the pump system was inserted into the left ventricle of the heart and the venae cavae were cut through. Then, PBS was continuously circulated through the vascular system for 3 min to remove the blood from the organism. Afterwards, a 4 % PFA in PBS solution was pumped through the vascular system for 5 min for fixation. Finally, the brain was carefully removed from the skull and stored in PBS or 30 % sucrose in PBS until further use.

3.6.6 Cryosectioning of mouse brains

Animals were anaesthetized with isoflurane and sacrificed. The brains were carefully removed and submerged into cold isopentane at a temperature between -20 °C and -30 °C to remove any liquid from the brain and freeze the brain. Brains were put on dry ice to freeze completely, before storing at -80 °C until further use. Before cryo-sectioning, brains adapted to the sectioning temperature (approximately -20 °C) in the cryostat (CM3050 S, Leica) and were mounted onto a cutting plate with embedding medium (Richard-Allan Scientific ™ Neg-50 ™,

cat. no. 6502, Thermo Fisher Scientific). Three to four serial coronal or sagittal brain slices (12 µm) were placed onto one microscope slide (Menzel-Gläser Superfrost® Plus, Ref. J1800AMNZ, Thermo Scientific). After air drying the slides were stored at -20 °C or -80 °C until further use.

3.6.7 Vibratome sectioning of mouse brains

PFA-fixed brains were washed twice in PBS before further use. The brain was placed into a plastic embedding mould and residual liquid was completely removed using a pipette. For coronal sections, the cerebellum was removed, and the brain was placed vertically into the embedding mould. For sagittal sections, the two brain hemispheres were separated and placed in the embedding mould with the medial side to the bottom. A mix of 4 % agarose in water was then poured into the mould and polymerized at RT. The block of agarose was either directly used for vibratome sectioning or was stored at 4 °C with a few drops of PBS on top and covered with parafilm. For sectioning, a vibratome VT1200S (Leica) was used. The agarose block was placed onto the vibratome slicing platform. 60 µm thick sagittal or coronal sections were collected in a 24-well plate filled with PBS. For long-term storage, the slices were stored in a 24-well plate (surrounded by parafilm) in 600 µL storing solution (30 % glycerol, 30 % ethylene glycol, 10 % PO_4 buffer 0.25 M pH 7.2 - 7.4 in water) at -20 °C.

3.6.8 Preparation of hippocampal slices for UHPLC-MS and qRT-PCR analysis

Acute transverse hippocampal slices (400 µm thick) were prepared as described previously (Kleppisch et al., 1999; Michalakis et al., 2011). In brief, 4 – 5-week-old C57BL/6J WT mice were anaesthetized with isoflurane and sacrificed, the brain was removed, the hippocampi of each hemisphere were dissected and cut using a MX-TS tissue slicer (Siskiyou Cooperation, OR). The slices were collected in an oxygenated (95 % O_2, 5 % CO_2) physiological solution (118 mM NaCl, 3 mM KCl, 1 mM NaH_2PO_4, 25 mM $NaHCO_3$, 10 mM Glucose, 1.5 mM $CaCl_2$, 1 mM $MgCl_2$, 0.1 % DMSO) at 37 °C until the hippocampi of all biological replicates were processed. Then, the slices were distributed to two different conditions: oxygenated physiological solution and oxygenated 25 mM KCl solution (118 mM NaCl, 25 mM KCl, 1 mM NaH_2PO_4, 25 mM $NaHCO_3$, 10 mM Glucose, 1.5 mM $CaCl_2$, 1 mM $MgCl_2$). 6 – 10 slices were pooled for each biological replicate per condition. After an incubation time of 6 hours (h), the

slices were transferred into reaction tubes, snap frozen in liquid nitrogen and stored at -80 °C until further use. Three mice (biological replicates) were processed in one experiment.

3.6.9 SVZ explants

The protocol was set up according to (Andrade et al., 2007) and (Petricca, 2015). Animals were anaesthetized with isoflurane and sacrificed. The brains were carefully removed, collected in cold Hank's Balanced Salt Solution without calcium and magnesium (HBSS (w/o)) supplemented with 10 mM HEPES and 1 % penicillin/streptomycin (Biochrom) and divided at the optic chiasm. The rostral piece of the brain was placed vertically into a plastic embedding mould with the most caudal side to the bottom. Residual liquid was removed using a pipette. A mix of 4 % agarose in water was then poured into the mould and polymerized at RT. Afterwards, the piece of the brain was cut coronally into 350 µm thick slices in cold HBBS (w/o) supplemented with 10 mM HEPES and 1 % penicillin/streptomycin (Biochrom) using a vibratome (VT1200S, Leica). From those coronal slices, the SVZ was punched out using a sample corer (1 mm in diameter, # 18035-01, Fine Science tools). The tissue pieces were collected in 200 µL Matrigel® (Corning® Matrigel® Basement Membrane Matrix, phenol red-free, #356237, Corning) in a Petri dish (6 cm in diameter) on ice, until all slices were processed. Afterwards, the tissue pieces were incubated for 5 min at RT, subsequently transferred (one piece per well) into a µ-Slide Angiogenesis ibiTreat (Cat. No. 81506, Ibidi), to which 8 µl Matrigel® were added in advance, and incubated at 37 °C and 5 % CO_2 for 15 min. Finally, 50 µL of culturing medium (0.45 % Glucose, 1 % B-27 Supplement, 1 % GlutaMax™, 10 mM HEPES, 1 % penicillin/streptomycin (Biochrom) in Neurobasal A) was added. The explants were cultured under 5 % CO_2 at 37 °C. The medium was changed every day. On day 4 (d4) of culturing, the explants were fixed for 45 min using pre-warmed 4 % PFA in PBS. After washing once with PBS, the slide was kept at RT until further use for immunohistochemistry. During culturing, images of the explants were taken with the EVOS® FL cell imaging system (Life Technologies, Thermo Fisher Scientific).

3.7 Cell sorting of neurons and astrocytes from mouse cortex

To sort neurons and astrocytes from mouse cortex, cortical tissue was dissected from mouse brain and manually dissociated. During tissue dissociation, a lot of myelin debris was generated

which impacts further applications like immunostainings (Pfenninger et al., 2007; Simons and Trotter, 2007; Tham et al., 2003). To remove the myelin debris, the debris was magnetically labelled with beads and separated from unlabelled cells by applying it onto a column in a magnetic field. To increase antibody specificity to their target cells, the samples were incubated with a FcR Blocking Reagent and were then labelled with fluorescently tagged neuron- and astrocyte-specific antibodies. Finally, the cortical neuron and astrocyte population, respectively, was isolated by fluorescence-activated cell sorting (FACS).

3.7.1 Tissue dissociation

Brain tissue was dissociated manually using the Neural Tissue Dissociation Kit (P) (Miltenyi, order number 130-092-628) following the manufacturer's instructions. Animals were anaesthetized with isoflurane and sacrificed. The brains were carefully removed, and the brain regions of interest, in this case mouse cortex, were isolated from other compartments in cold HBSS (w/o). The weight of the tissue was determined in 1 mL HBSS (w/o) to make sure to not exceed the 400 mg limit per digestion. The brain was cut into small pieces in HBSS (w/o) using a scalpel. The pieces in HBSS (w/o) were transferred with a pipette into a 2 mL reaction tube. The tube was centrifuged for 2 min at 400 x g and 4 °C. The supernatant was carefully removed. 1950 µL enzyme mix 1 (50 µL Enzyme P + 1900 µL Buffer X), which was pre-heated at 37 °C for 15 min, was added to the tissue.

The sample was incubated for 1 h at 37 °C under slow, continuous rotation in a ThermoMixer C (Eppendorf). After 15 min of incubation, enzyme mix 2 (10 µL Enzyme A + 20 µL Buffer Y) was added to the tube. The tube was inverted gently to mix several times during incubation.

After incubation, the tissue was dissociated mechanically firstly by using a 1 mL pipet and pipetting 10 times up and down, and secondly by using a 200 µL pipet and pipetting 10 times up and down. The cell suspension was then applied to a strainer (70 µm in diameter, VWR) placed over a 50 mL tube. 10 mL HBSS with calcium and magnesium (HBSS (w)) was applied through the strainer. The cell suspension was centrifuged for 10 min at 400 x g and 4 °C, the supernatant was aspirated completely. The cell pellet was resuspended in 10 mL HBSS (w) and again centrifuged for 10 min at 400 x g and 4 °C. The supernatant was aspirated completely, and

the cells were immediately resuspended with the buffer (PBS containing 0.5 % BSA) to the required volume for further applications.

3.7.2 Myelin Removal

For myelin removal from the dissociated tissue samples, Myelin Removal Beads II (Miltenyi, order number 130-096-733) were used following the manufacturer's instructions.

After the dissociation procedure described above, the cells were resuspended in 1,800 µL buffer (PBS containing 0.5 % BSA). Then, 200 µL of beads were added to the cell suspension. The cell suspension was mixed well by pipetting and incubated for 15 min at 4 °C.

After the incubation, the cells were washed by adding 10 times the labelling volume of buffer and centrifuged for 10 min at 400 × g. The supernatant was aspirated completely. The cell pellet was resuspended in the 3,000 µL buffer volume (1,000 µL of buffer per column). Then 1,000 µL of cell suspension was applied onto the column, which was prepared by rinsing with 3 mL of buffer. The unlabelled cells, which passed through the columns, were collected and washed two times with 1 mL of buffer. The cell suspension was centrifuged for 10 min at 400 x g and 4 °C, the supernatant was aspirated completely. The cell pellet was immediately resuspended with the buffer to the required volume for further applications.

3.7.3 FcR blocking

First, the cell number was determined using a Countess II FL (Invitrogen, Thermo Fisher Scientific). Then, the cell suspension was centrifuged at 400 x g for 5 min. The supernatant was aspirated completely. The cell pellet (< 10^7 nucleated cells) was resuspended in 90 µL buffer (PBS containing 0.5 % BSA). 10 µL FcR Blocking Reagent (Order no. 130-092-575, Miltenyi) was added to the cell suspension. The suspension was mixed well and incubated for 20 min at 4 °C. After the incubation time, the required amount of antibody can be directly added to the mix following the corresponding protocol.

3.7.4 Surface staining

After blocking, the antibodies (Appendix - Table 21) for surface staining were directly added. Depending on the antibody, the required amount of antibody solution is added to the cell suspension. The suspension was mixed well and incubated in the dark for 20 min at 4 °C.

Afterwards, the cell suspension was centrifuged at 400 x g for 5 min and washed once with 500 µL buffer after removing the supernatant completely. After centrifuging the cell suspension for 5 min at 400 x g and 4 °C, the supernatant was aspirated completely, and the cell pellet was resuspended in PBS containing the viability dye (eBioscience™ Fixable Viability Dye eFluor™ 450, order no. 65-0863, Thermo Fisher Scientific) in a dilution of 1:500. The cell suspension was incubated in the dark for 20 min. Afterwards, the cell suspension was centrifuged at 400 x g for 5 min and washed once with 500 µL buffer after removing the supernatant completely. Finally, the cell pellet was resuspended in the required amount of buffer for further applications.

3.7.5 Nuclear staining

After blocking, the cell suspension was centrifuged for 5min at 400 x g and 4 °C. The supernatant was completely removed. To fix, the cell suspension was incubated for 20 min at 4 °C with BD Phosflow™ fix buffer 1 (order no. 557870, BD Biosciences) and then centrifuged for 5 min at 400 x g and 4 °C. To permeabilise, the cell suspension was incubated for 20 min at 4 °C with BD Phosflow™ Perm/Was Buffer 1 (order no. 557885, BD Biosciences) and then centrifuged for 5min at 400 x g and 4 °C. The supernatant was aspirated completely, and the primary antibody diluted in buffer was added. The cell suspension was incubated in the dark for 20 min at 4 °C. The same step was repeated with the secondary antibody. After washing, the cell pellet was resuspended in the required amount of buffer for further applications.

3.7.6 FACS

FACS was carried out by Dr. Lisa Richter at the Core Facility Flow Cytometry at the Biomedical Center, LMU Munich.

Among single, live (Fixable Viability Dye eFluor 450-negative) cells, neurons were sorted as CD11b negative and CD90.2hi positive cells, astrocytes were sorted as CD11b negative and Acsa-2hi positive cells, and microglia as CD11b positive cells. It was confirmed in advance that CD90.2hi cells were NeuN positive and Acsa-2 negative, while Acsa-2hi cells were GFAP positive. The cell populations were sorted directly into PBS in 4-way-purity mode using a 100 µm Nozzle at 20 psi on a FACS AriaIIIu (Becton Dickinson) with BD FACSDiva software v8.0. Data was analysed with FlowJo v10.

3.8 gDNA isolation

For gDNA isolation from mouse tissue, 800 µL - 3.2 mL (depending on the amount of tissue) of RLT Lysis Buffer (Qiagen) containing 1 % β-mercaptoethanol, 0.4 mM Desferal® and 0.4 mM butylated hydroxytoluene (BHT) were added to the sample. After vortexing, the tissue was homogenized by adding one stainless steel bead (0.5 mm in diameter) to each tube and using a mixer mill (MM400, Retsch) first at 30 Hz for 1 min and then at 20 Hz for 4 min. After removing the steel bead using a strong magnet, the samples were centrifuged for 5 min at 21,000 x g and RT. Subsequently, up to 800 µL lysate were transferred to a Zymo-Spin IIC-XL column placed into a 2 mL collection tube and centrifuged for 4 min at 1,500 x g and RT and afterwards for 1 min at 10,000 x g and RT. This step was repeated until all lysate was centrifuged. The flow through containing RNA as well as proteins was pooled and stored at -80 °C until further use. Next, 400 µL RNase wash buffer (Genomic Lysis Buffer (Zymo research) containing 0.2 mg/mL RNase A (Qiagen), 0.4 mM BHT and 0.4 mM Desferal) were added to the columns. After incubating for 10 - 15 min at RT, the columns were centrifuged for 2 min at 10,000 x g and RT. Then, the columns were washed by adding 600 µL DNA Pre-Wash Buffer (Zymo research) and centrifuging for 1 min at 10,000 x g and RT. The columns were washed a second time by adding 600 µL gDNA wash Buffer (Zymo Research) and centrifuging for 1 min at 10,000 x g and RT. Finally, the columns were washed a third time by adding again 600 µL gDNA wash Buffer (Zymo Research) and centrifuging for 2 min at 10,000 x g and RT. After all centrifugation steps the flow through was discarded. To eliminate residual wash buffer, the columns were transferred into new 2 mL collection tubes and centrifuged for 1 min at 10,000 x g and RT. Subsequently, the columns were transferred into fresh 1.5 mL reaction tubes. To elute the gDNA from the columns, they were incubated with 100 µL water + 20 µM BHT for 10 min at RT and centrifuged for 2 min at 10,000 x g and RT. The DNA concentration was measured using a NanoDrop 2000c spectrophotometer (Thermo Fisher Scientific). The DNA was stored at -80 °C until further use.

3.9 Quantification of cytosine modifications using mass spectrometry

Quantification of cytosine modifications in murine tissue samples and human iPSC cells was carried out by Dr. Franziska Traube from Prof. Dr. Thomas Carell's research group at LMU

Munich as described previously (Traube et al., 2019). In brief, quantification of cytosine modifications was carried out using an ultra-high-performance liquid chromatography tandem mass spectrometry (UHPLC-MS/MS) system and analysing three technical replicates per biological replicate. For each technical replicate, 3 µg of genomic DNA in 35 µL water were digested (depending on the amount and sort of original sample). In detail, 7.5 µL of a 480 µM ZnSO4 aqueous solution, containing 18.4 U nuclease S1 (Aspergillus oryzae, Sigma-Aldrich), 5 U Antarctic phosphatase (New England BioLabs) and labelled internal standards ([15N2]-5caC 0.04301 pmol, [15N2,D2]-5hmC 7.7 pmol, [D3]-5mC 51.0 pmol, [15N5]-8-oxo-dG 0.109 pmol, [15N2]-5fC 0.04557 pmol) were mixed with the sample DNA. Afterwards, the mixture was incubated at 37 °C for 3 h. Then, 7.5 µL of a 520 µM [Na]2-EDTA solution, containing 0.2 U snake venom phosphodiesterase I (Crotalus adamanteus, USB corporation) were added. The mixture was incubated again for 3 h at 37 °C and then stored at −20 °C. Before using for UHPLC-MS/MS analysis, samples were filtered using an AcroPrep Advance 96 filter plate 0.2 µm Supor (Pall Life Sciences). Quantitative UHPLC-MS/MS analysis was performed using an Agilent 1290 UHPLC system equipped with a UV detector and an Agilent 6490 triple quadrupole mass spectrometer. Natural nucleosides were quantified with the stable isotope dilution technique, which allowed the concurrent analysis of all nucleosides in one single analytical run. The following source-dependent parameters were set: gas temperature 80 °C, gas flow 15 L/min (N_2), nebulizer 30 psi, sheath gas heater 275 °C, sheath gas flow 15 L/min (N_2), capillary voltage 2,500 V in the positive ion mode, capillary voltage −2,250 V in the negative ion mode, nozzle voltage 500 V, fragmentor voltage 380 V/ 250 V and for the positive mode Delta EMV 500 V. Chromatography was performed by a Poroshell 120 SB-C8 column (Agilent, 2.7 µm, 2.1 mm × 150 mm) at 35 °C using a gradient of water and MeCN, each containing 0.0085 % (v/v) formic acid, at a flow rate of 0.35 mL/min: 0 → 4 min; 0 → 3.5% (v/v) MeCN; 4 → 6.9 min; 3.5 → 5 % MeCN; 6.9 → 7.2 min; 5 → 80 % MeCN; 7.2 → 10.5 min; 80 % MeCN; 10.5 → 11.3 min; 80 → 0 % MeCN; 11.3 → 14 min; 0 % MeCN. The effluent before 1.5 min and after 9 min was diverted to waste by a Valco valve. The autosampler was cooled to 4 °C. The injection volume was 39 µL.

3.10 RNA isolation

3.10.1 RNA isolation from mouse tissue

For RNA isolation from mouse tissue, the flow-through containing RNA and proteins from the first column centrifugation step of the gDNA isolation protocol (chapter 3.8) was mixed with 300 µL of 95 % EtOH. 400 µL of the mixture were transferred to Zymo-Spin IIC columns placed into a 2 mL collection tube and centrifuged first for 5 min at 1,000 x g and RT and then for 1 min at 10,000 x g and RT. This step was repeated until all lysate was centrifuged. The columns were washed by applying 800 µL RNA Wash buffer (Zymo Research) and followed by centrifuging for 1 min at 10,000 x g and RT. For on-column digestion of DNA, a mixture of 73.5 µL Digest Buffer (Qiagen) and 1.5 µL DNase I (Qiagen) was applied to the columns and incubated for 15 min at 24 °C. Afterwards, the columns were centrifuged for 1 min at 10,000 x g and RT. Subsequently, the columns were washed by applying first 800 µL Pre-Wash RNA Buffer and then 800 µL RNA Wash buffer followed by centrifugation for 1 min at 10,000 x g and RT in each case. To eliminate residual wash buffer, the columns were transferred into new 2 mL collection tubes and centrifuged for 1 min at 10,000 x g and RT. Subsequently, the columns were transferred into fresh 1.5 mL reaction tubes. To elute the RNA from the columns, they were incubated with 50 µL water for 5 min at RT and centrifuged for 2 min at 10,000 x g and RT. The RNA concentration was measured using a NanoDrop 2000c spectrophotometer (Thermo Fisher Scientific). The RNA was stored at -80 °C until further use.

3.10.2 RNA isolation from human iPSC cells

For RNA isolation from human iPSC cells, RNeasy® Plus Mini Kit (Qiagen) was used following the manufacturer's instructions. After washing with DPBS, cells were harvested in the cell culture plate by adding RLT Plus buffer (Qiagen) + 1 % β-mercaptoethanol. Plates were placed on an orbital shaker for 5 min and cell suspension was transferred to a 2 mL safe-lock tube (order no. 0030120.094, Eppendorf). The cells were homogenized by adding one stainless steel bead (0.5 mm in diameter) to each tube and using a mixer mill (MM400, Retsch) at 30 Hz for 1 min. After removing the steel bead using a strong magnet, the samples were centrifuged for 5 min at 21,000 x g and RT. The homogenate was transferred to a gDNA Eliminator spin column placed in a 2 mL collection tube. The column was centrifuged for 30 s at ≥ 8,000 x g and RT and

discarded afterwards. The RNA containing flow-through was mixed with an equal volume of 70 % ethanol and transferred to a RNeasy spin column placed in a 2 mL collection tube. The column was centrifuged for 15 s at ≥ 8,000 x g and RT, the flow-through was discarded. This step was repeated until all homogenate was applied to the column. Next, 700 µL Buffer RW1 were added to the column. It was centrifuged for 15 s at ≥ 8,000 x g and RT to wash the spin column membrane, the flow-through was discarded. This washing step was repeated twice with 500 µL Buffer RPE. After the second application of Buffer RPE, the column was centrifuged for 2 min at ≥ 8,000 x g and RT. The flow-through was discarded, the column was placed in a new 2 mL collection tube and centrifuged at full speed for 1 min to eliminate residual wash buffer. Finally, the RNeasy spin column was transferred in a new 1.5 mL collection tube and 30 µl RNase-free water were directly added to the spin column membrane. The column was centrifuged for 1 min at ≥ 8,000 x g and RT to elute the RNA. The RNA concentration was measured using a NanoDrop 2000c spectrophotometer (Thermo Fisher Scientific). The RNA was stored at -80 °C until further use.

3.10.3 RNA isolation from FACS-sorted cells

For RNA isolation from FACS-sorted cells for RNA sequencing, RNeasy® Plus Micro Kit (Qiagen) in combination with an additional on-column-digest using RNase-free DNase set (Qiagen) was applied following the manufacturer's instructions. After FACS sorting the cells, the cells were centrifuged for 5 min at 400 x g and RT. After centrifugation, cells were resuspended in 350 µL RLT Plus buffer+ 1 % β-mercaptoethanol and cell suspension was transferred to a 2 mL safe-lock tube (Order no. 0030120.094, Eppendorf). The cells were homogenized by adding one stainless steel bead (0.5 mm in diameter) to each tube and using a mixer mill (MM400, Retsch) at 30 Hz for 20 s. After removing the steel bead using a strong magnet, the samples were centrifuged for 5 min at 21,000 x g and RT. The homogenate was transferred to a gDNA Eliminator spin column placed in a 2 mL collection tube. The column was centrifuged for 30 s at ≥ 8,000 x g and RT and discarded afterwards. The RNA containing flow-through was mixed with an equal volume of 70 % ethanol and transferred to a RNeasy MinElute spin column placed in a 2 mL collection tube. The column was centrifuged for 15 s at ≥ 8,000 x g and RT, the flow-through was discarded. This step was repeated until all homogenate

was applied to the column. Next, 350 µL Buffer RW1 were added to the column. It was centrifuged for 15 s at ≥ 8,000 x g and RT to wash the spin column membrane, the flow-through was discarded. Then, 80 µL of the DNase I incubation mix was added to the column and incubated for 15 min at RT. Next, 350 µL Buffer RW1 were added to the column. It was centrifuged for 15 s at ≥ 8,000 x g and RT to wash the spin column membrane, the flow-through was discarded. This washing step was repeated first with 500 µL Buffer RPE and then with 500 µL of 80 % ethanol. After the application of 80 % ethanol, the column was centrifuged for 2 min at ≥ 8,000 x g and RT. The flow-through was discarded, the column was placed in a new 2 mL collection tube and centrifuged with an open lid at full speed for 5 min to eliminate residual wash buffer. Finally, the RNeasy MinElute spin column was transferred into a new 1.5 mL collection tube and 14 µL RNase-free water were directly added to the spin column membrane. The column was centrifuged for 1 min at ≥ 8,000 x g and RT to elute the RNA. The RNA concentration was measured using a NanoDrop 2000c spectrophotometer (Thermo Fisher Scientific). The RNA was stored at -80 °C until further use.

3.11 cDNA synthesis

For cDNA synthesis, the RevertAid First Strand cDNA Synthesis Kit (#K1621, Thermo Fisher Scientific) was used following the manufacturer's instructions.

The lab bench and equipment (pipets, racks, etc.) were cleaned with RNase Away to get rid of RNase which might destroy RNA. The kit components were thawed, mixed, briefly centrifuged and stored on ice until use.

The following reagents were pipetted into sterile, nuclease-free tubes on ice:

RNA	0.1 – 1	µg
Radom Hexamer Primer	1	µL
Oligo $(dT)_{18}$ Primer	1	µL
Nuclease-free water	ad 12	µL

The sample was mixed gently by pipetting up and down, centrifuged briefly and incubated at 65 °C for 5 min. Afterwards, it was cooled to 10 °C, spun down and placed back on ice.

Then the following kit components were added:

5X Reaction Buffer	4	µL
RiboLock RNase Inhibitor (20 U/µL)	1	µL
10 mM dNTP Mix	2	µL
RevertAid M-MuLV RT (200 U/µl)	1	µL

The sample was gently mixed by pipetting up and down, centrifuged briefly and incubated for 5 min at 25 °C followed by 60 min at 42 °C. The reaction was terminated by heating the sample at 70 °C for 5 min and then cooling down to 10 °C.

cDNA was kept either at -20 °C for short-term storage (one week) or at -80 °C for long-term storage. For application in qRT-PCR, cDNA was diluted 1:5 with 80 µL nuclease-free water.

3.12 qRT-PCR

Real-time quantitative Reverse Transcription PCR (qRT-PCR) was performed on a StepOnePlus Real-Time PCR system (Applied Biosystems, Thermo Fisher Scientific) using PowerUp™ SYBR™ Green qPCR Master Mix (cat. no. A25742, Applied Biosystems, Thermo Fisher Scientific) for quantification of the PCR products. Reaction mixtures were pipetted in MicroAmp Fast 96-well reaction plates (cat. no. 4346907, Applied Biosystems, Thermo Fisher Scientific) according to the following scheme:

cDNA (1:5 diluted)	5	µL
PowerUp™ SYBR™ Green Master Mix (2x)	10	µL
Primer forward (10 µM)	0.8	µL
Primer reverse (10 µM)	0.8	µL
RNase-free water	ad 20	µL

C_T values of each sample were determined by the StepOne™ Software (Applied Biosystems, Thermo Fisher Scientific) using the fast cycle protocol (Table 5) and detected in at least technical duplicates.

Table 5: Fast-mode real time PCR parameters

The asterisks * mark the points of data collection.

Step	Temperature	Time	Number of cycles
Uracil-DNA-glycosylase activation	95 °C	2 min	1
DNA polymerase activation	95 °C	2 min	1
Denaturation	95 °C	3 s	40
Annealing	58 °C	10 s	
Extension	60 °C *	25 s	
Melt curve acquisition	95 °C	15 s	1
	60 °C	1 min	1
	95 °C Ramp + 0.3 °C/s *	15 s	1

Expression levels of biological replicates were analysed and normalized to the expression levels of a housekeeping gene. The relative quantification was determined according to Pfaffl et al. (Pfaffl, 2001; Pfaffl et al., 2002).

The primer pairs used for housekeeping and target genes are listed in Table 12 in the appendix.

3.13 RNA sequencing

RNA sequencing was carried out by Dr. Gilles Gasparoni from Prof. Dr. Jörn Walter's research group at Saarland University in Saarbrücken.

mRNA library was produced according to a scaled-up version of the SMARTseq2 protocol (Picelli et al., 2013). In brief, mRNA from a total amount of approximately 7 to 25 ng of total RNA was captured with a mixture of 0.5 µL of 20 µM oligo dT primer and 0.5 µL of 20 mM dNTPs followed by heating up to 72 °C for 3 min and immediately putting into an ice-water bath afterwards. Then, double stranded cDNA was synthesised in a 10 µL reaction mixture by adding 2 µL of 5x Superscript II first-strand buffer (Thermo Fisher Scientific), 2 µL of 5 M Betaine, 0.6 µL of 100 mM $MgCl_2$, 0.5 µL of 100 mM DTT, 0.4 µL of RNAsin (Promega), 0.5 µL of 20 µM template-switch oligo as well as 0.5 µL of SuperScript II reverse transcriptase (200 U/µL, Thermo Fisher) and incubating at 42 °C for 90 min. This incubation step was followed by 14 cycles at 50 °C and 42 °C for 2 min respectively and a final heat inactivation at

70 °C for 15 min. Subsequently, pre-amplification was carried out by adding 12.5 µL of 2x KAPA HiFi HotStart Ready mix, 0.25 µL of 10 µM IS PCR primers and 2.25 µL of nuclease-free water using a cycling protocol of 98 °C for 3 min, 10 pre-amp cycles (98 °C for 20 s, 67 °C for 15 s, 72 °C for 6 min), followed by 5 min at 72 °C and hold at 4 °C. Synthesised cDNA was purified using AMPure XP beads (Beckman Coulter), quantified via Qubit (Thermo Fisher) and checked for fragment length distribution using Agilent Bioanalyzer. Next, 7 ng of cDNA were fragmented in a 20 µL reaction mixture by incubating with 1 µL of Tn5 enzyme (Illumina Nextera library preparation kit) and 10 µL of 2x tagmentation DNA buffer at 55 °C for 10 min. Tagmented cDNA was then purified using MinElute columns (Qiagen) and PCR amplified by adding NEBNext High-Fidelity 2x PCR Mastermix, 1 µL of each 10 µM Nextera index 1 and Nextera index 2 primer (Illumina) using a cycling protocol of 72 °C for 5 min, 98 °C for 30 s, 7 cycles (98 °C for 10 s, 63 °C for 30 s, 72 °C for 1 min), 72 °C for 5 min and hold at 4 °C. The final library was purified using AMPure beads, quantified by Qubit and sequenced for 100 bp using a V3 single read flow cell on a HiSeq 2500 (Illumina).

The generated data was trimmed for quality and adapter reads with TrimGalore (https://www.bioinformatics.brabraham.ac.uk/projects/trim_galore/) and mapped with STAR aligner (Dobin et al., 2013). Duplicates were marked using the MarkDuplicates function from Picard tools (https://boradinstitute.github.io/picard/). Reads were summarised with RSEM (Li and Dewey, 2011). FPM count matrix was generated with DESeq2 (Love et al., 2014).

3.14 Protein isolation

3.14.1 Protein isolation from whole cell lysate

The tissue samples, which were stored at -80 °C, were thawed on ice. 200 µL - 1,000 µL (depending on the amount of tissue) of RIPA buffer (10 mM Tris pH = 7.75, 150 mM NaCl, 0.5 mM EDTA, 0.1 % SDS, 1 % Triton X-100, 1 % Deoxycholate, Protease inhibitor (order no. 11873580001, Roche)) were added to each sample. Brain and Cortex samples were minced before adding the buffer. After adding the buffer to the tissue samples, the tissue was homogenized using a glass douncer. Then, the samples were incubated for 30 to 60 min at 4 °C under rotation in a wheel. Afterwards, the samples were centrifuged for 10 min at 15,000 x g and 4 °C. The supernatant was transferred into a fresh tube and stored on ice until measuring

the protein concentration via a Bradford Assay. Finally, the samples were snap frozen in liquid nitrogen and stored at -80 °C until further use.

3.14.2 Bradford assay

Protein Assay Dye Reagent Concentrate (order no. 5000006, Bio-Rad) was used for the determination of protein concentration. First, the concentrate was diluted with a ratio of 1:5 in water. Then, 1 µL of protein lysate was directly mixed with 49 µL water in a PMMA cuvette (VWR) and 950 µL of diluted Protein Assay Dye Reagent Concentrate were added. The mixture was incubated for 2 min at RT. The absorption was measured and compared to a blank solution containing only resuspension buffer using a BioPhotometer (Eppendorf).

3.15 Western Blotting

20 µg protein were mixed with 4x SDS loading buffer (500 mg Tri pH = 6.8, 5 mL glycerol, 1 g SDS, 1.25 mg Bromophenol Blue, 2.5 mL 2-Mercaptoethanol, H_2O up to 50 mL) and incubated at 92 °C for 5 min. For SDS-Page, a 4 - 15 % polyacrylamide gradient gel (cat. no. 456-1083, Bio-Rad) was used. Protein samples and a PageRuler Prestained Protein Ladder (Thermo Fisher Scientific) to determine the protein size were loaded on the gel. Electrophoresis was run for approximately 1 h at 150 V in SDS running buffer (25 mM Tris, 192 mM glycine, 0.1 % (w/v) SDS). Afterwards, proteins were blotted on a polyvinylidene fluoride membrane (GE Healthcare) using a pre-cooled transfer buffer (25 mM Tris, 192 mM glycine, 20% (v/v) MeOH, 0.038% (w/v) SDS). Here, the membrane was activated in MeOH for 1 min and the filter paper was equilibrated in transfer buffer for 5 min. Western blotting was performed at 50 V for 1.5 h and at 45 V for 3.5 h under stirring in the Mini Trans-Blot cell (Bio-Rad) at 4 °C. After blotting, the membrane was incubated in blocking solution (5 % (w/v) milk powder in TBS-T (20 mM Tris pH = 7.5, 150 mM NaCl, 0.1 % (v/v) Tween-20)) for 30 min at RT under rotation. Then, the membrane was incubated in a primary antibody solution (antibody diluted in 5 % (w/v) milk powder in TBS-T) overnight at 4 °C under rotation. The next day, the membrane was washed three times in TBS-T and then incubated with a secondary antibody solution (antibody diluted in 5 % (w/v) milk powder in TBS-T) for 1 h at RT. Afterwards, the membrane was washed three times with TBS-T and once with water, before signal detection was performed. For detection, the membrane was incubated with SuperSignal West Pico Chemiluminescent

Substrate (order no. 34077, Thermo Fisher Scientific) according to the manufacturer´s instructions. The chemiluminescence signal was detected using the Chemidoc MP Imaging system (Bio-Rad) including Image Lab software (Bio-Rad).

3.16 Proteomics

Proteomic analysis of tissue samples from mouse brain and retina was carried out by Dr. Michael Stadlmeier from Prof. Dr. Thomas Carell's research group at LMU Munich.

3.16.1 Sample preparation

First, the protein concentration was measured by performing a Bradford assay (chapter 3.14.2). The same amount of protein was used for each condition. Each sample volume was adjusted to 125 µL with a HEPES solution (100 mM, pH 7.4). For reduction of disulfides, an aqueous solution of 500 mM DTT was added to the samples to obtain a final concentration of 5 mM. Then, the samples were incubated for 20 min at 60 °C while shaking at 750 rpm and cooled down to RT. Subsequently, N-ethylmaleimide (1 M in MeCN) was added to the samples to a final concentration of 20 mM. After shaking for 20 min at 750 rpm and RT, additional aqueous solution of 500 mM DTT was added to a final concentration of 10 mM. The samples were again shaken for 10 min at 750 rpm and RT. For protein precipitation, a volume of 4.1 times the sample volume of cold acetone (-20 °C) was added to the samples which were then incubated overnight at -20 °C. The next day, the samples were centrifugated for 10 min at 15,000 × g and 4 °C, the supernatant was removed, and the samples were dried on air. The obtained protein pellets were resuspended in resuspension buffer (6 M guanidinium chloride (Gua-Cl), 10 mM EPPS pH 8.5) to a final protein concentration of 5 µg/uL and incubated for 15 min at 60 °C while shaking at 750 rpm. The samples were diluted by adding slowly an EPPS (10 mM pH 8.5) containing buffer to a final Gua-Cl-concentration of 0.486 mM. The resulting protein concentrations of the samples were determined by using the Pierce ™ BCA protein assay kit (Thermo Fisher Scientific). For protein digestion, the same protein amount was used for each condition. Each sample was adjusted with a buffer containing 0.486 mM Gua-Cl and 10 mM EPPS pH 8.5 to the same volume. Afterwards, Sequence Grade Modified Trypsin (Promega) was used in a ratio of 1:13.3 (trypsin : protein weight) to digest the proteins overnight at 37 °C under mild shaking at 350 rpm. For isobaric labelling, TMTsixplex ™ Isobaric Label Reagent

(Thermo Fisher Scientific) set was used. Then, the samples were concentrated by vacuum concentration and resuspended in EPPS buffer (200 mM, pH 8) to a final concentration of 1 µg/µL. After resuspension of the samples, one isotopomer of the TMT-reagent set was added per condition (0.8 mg solved in 40 µL dry MeCN, 4 µg TMT per 1 µg peptides). Labelling was carried out for 2 h at RT while shaking at 750 rpm. For quenching of the TMT reagents, 50 % aqueous hydroxylamine solution (Thermo Fisher Scientific) was diluted to 5 % with water. 1 µL of that solution was added per 12 µL sample. The samples were incubated for 10 min at RT while shaking at 750 rpm. For relative quantification, the same sample amount of the respective samples was combined, and the samples were acidified with H_3PO_4 (aq., 5 %). Afterwards, the samples were concentrated by vacuum concentration and desalted with ZipTips (0.6 µL material, C18, Merck) for measurement without fractionation or were fractionated with Pierce™ High pH Reverse-Phase Peptide Fractionation Kit (Thermo Fisher Scientific) according to manufacturer's recommendations. The resulting desalted peptides were resuspended in MS-solvent (0.1 % formic acid, 2 % MeCN in water). Finally, approximately 2 µg of peptides were analysed by HPLC-MS^2.

3.16.2 HPLC-MS^2 analysis

For identification and quantification, the samples were analysed on a Q Exactive HF mass spectrometer (Thermo Fisher Scientific), coupled to an Ultimate 3000 nano-HPLC-system (Thermo Fisher Scientific). First, peptides were loaded with 0.1 % formic acid (aq) onto an Acclaim PepMap 100 µ-precolumn cartridge (5 µm, 100 Å, 300 µm ID × 5 mm, Thermo Fisher Scientific). For separation of the peptides, a PicoTip emitter (noncoated, 15 cm, 75 µm ID, 8 µm tip, New Objective), packed in house with Reprosil-Pur 120 C18-AQ material (1.9 µm, 120 Å, Dr. A. Maisch GmbH), was used. The flowrate was set to 300 nL/min and the 120 min gradient was programmed with percentages B as follows: 1 % for 5 min; 1 % – 8 % in 3 min; 8 % – 36 % in 90 min; 36 % – 85 % in 2 min; 85 % for 5 min; 85 % – 1 % in 5 min; 1 % for 10 min. For fractionated samples, the gradient for fractions 1 – 4 was modified as follows: 1 % for 5 min; 1 % – 5 % in 3 min; 5 % – 30 % in 90 min; 30 % – 85 % in 2 min; 85 % for 5 min; 85 % – 1 % in 5 min; 1 % for 10 min. MS-grade water (Sigma-Aldrich) with 0.1 % (v/v) formic acid (Thermo Fisher Scientific) was used as solvent A, MS-grade MeCN with 0.1 % (v/v) (Carl Roth) as solvent

B. The Pico-Tip emitter was positioned in front of the MS-inlet using a modified Nanospray Flex ion source (Thermo Fisher Scientific). Then, a voltage of 2.2 kV in respect to the mass spectrometer was applied through a T-junction. The column was heated to a constant temperature of 30 °C by a column oven (Sonation GmbH). The Q Exactive HF was operated in dd-MS^2 mode with the following settings: polarity: positive; MS1 resolution: 120k; MS1 AGC target: 3e6 charges; MS1 maximum IT: 35 ms; MS1 scan range: m/z 350 – 1,400; MS^2 resolution: 60k; MS^2 AGC target: 1e5 charges; MS^2 maximum IT: 120 ms; Top N: 20; isolation window: m/z 0.8; isolation offset: m/z 0.0; HCD normalised collision energy: 32 %; Fixed first mass: m/z 120; Minimum AGC target: 4.5e4 charges; charge exclusion: unassigned, 1, 7, 8, > 8; peptide match: off; exclude isotopes: on; dynamic exclusion: 60 s.

3.16.3 Data analysis

Proteome Discoverer 2.2 (Thermo Fisher Scientific) was used for data analysis. For identification, Sequest was set to the following parameters: Max. Missed Cleavages: 2; Precursor Mass Tolerance: 20 ppm; Fragment Mass Tolerance: 0.02 Da; Dynamic Modifications: +15.995 Da (M, oxidation), +42.011 Da (protein N-terminus, acetylation); Static Modifications: +125.048 Da (C, NEM-protection), +229.163 Da (K, peptide N-terminus, TMTsixplex). Additionally, organism-wide, recent.FASTA-files from SwissProt and UniProt were used. PSM FDR was controlled by the Percolator node and PSMs were filtered strictly to 1 % FDR. TMT reporter ion integrals were extracted after mass recalibration of the spectral files and the integration tolerance was set to 10 ppm. For ratio generation and calculation of adjusted p-values, the “Reporter Ions Quantifier”-consensus node of the Proteome Discoverer 2.2 was used. No quan value correction was applied due to the used TMT6e-reagents. Normalization mode was set to “Total Peptide Amount”, while the Scaling Mode was set to “On All Average”. For hypothesis testing, the “ANOVA (Background Based)” setting was used. The ratio calculation was performed using the “Summed Abundance Based” setting.

3.17 Immunohistochemistry

3.17.1 Mouse retina cryosections

Slices previously stored at -20 °C were thawed and adapted to RT. The slices were surrounded by a hydrophobic barrier using a liquid blocker (PAP-Pen Mini - Liquid-Repellent Slide Marker

Pen, order no. N71312, Science Services). Then, the slices were rehydrated with 0.1 M PB for 5 min and post-fixed by adding 4 % PFA in PBS for 10 min. The slices were washed three times with 0.1 M PB for 5 min and then incubated with the primary antibodies diluted in 0.1 M PB containing 5 % ChemiBlocker™ (order no. 2170, Merck Millipore) and 0.3 % Triton X-100 overnight at 4 °C. Then, the cryosections were washed three times with 0.1 M PB for 5 min after removing the primary antibody solutions. The slices were then incubated with appropriate secondary antibodies diluted in 0.1 M PB containing 2 % ChemiBlocker™ (order no. 2170, Merck Millipore) for 1.5 h at RT. After washing three times with 0.1 M PB for 5 min, the cell nuclei were stained by applying 5 µg/mL Hoechst 33342 (Invitrogen, Thermo Fisher Scientific, diluted in 0.1 M PB) or DAPI (Invitrogen, Thermo Fisher Scientific, diluted in PB, 1:1,500) for 5 min to the slices. The slices were then washed again two times with 0.1 M PB for 5 min. Coverslips (Menzel-Gläser, order no. 630-2108, VWR) were mounted onto the brain slices using Aqua-Poly/Mount mounting medium (order no. 18606-5, Polysciences). The slides were dried and stored protected from light at RT until use for microscopy.

3.17.2 Mouse brain cryosections

Slices previously stored at -20 °C were thawed and adapted to RT. The slices were surrounded by a hydrophobic barrier using a liquid blocker (PAP-Pen Mini - Liquid-Repellent Slide Marker Pen, order no. N71312, Science Services). Then, the slices were rehydrated with PBS for 5 min and then post-fixed by adding 4 % PFA in PBS for 5 min. The slices were washed twice with PBS for 5 min and then in one step permeabilised and blocked incubating them with a solution containing 10% ChemiBlocker™ (order no. 2170, Merck Millipore), 0.3% Triton X-100 in PBS for 1 h. The blocking and permeabilization solution was carefully removed. The slices were then incubated with the primary antibodies diluted in PBS containing 5 % ChemiBlocker™ (order no. 2170, Merck Millipore) overnight at 4 °C. Then, the slices were washed three times with PBS after removing the primary antibody solutions. The slices were then incubated with appropriate secondary antibodies diluted in PBS containing 2 % ChemiBlocker™ (order no. 2170, Merck Millipore) for at least 1 h at RT. After washing two times with PBS for 5 min, the cell nuclei were stained by applying 5 µg/mL Hoechst 33342 (Invitrogen, Thermo Fisher Scientific) or DAPI (Invitrogen, Thermo Fisher Scientific, diluted in PBS, 1:1,500) for 5 min to the slices. The

slices were then washed again two times with PBS for 5 min. Coverslips (Menzel-Gläser, order no. 630-2108, VWR) were mounted onto the brain slices using Aqua-Poly/Mount mounting medium (order no. 18606-5, Polysciences). The slides were dried and stored protected from light at RT until microscopy.

3.17.3 Mouse brain vibratome sections

The slices were stored in a 24-well plate (surrounded by parafilm) in 700 µL storing solution (30 % water, 30 % glycerol, 30 % ethylene glycol, 10 % PO_4 buffer 10x, 0.25 M, pH 7.2 - 7.4) at -20 °C. The slices were transferred into a petri dish (diameter 10 cm) containing PBS to wash. Then, they were transferred into a 24-well plate containing PBS and washed again with PBS for 5 min. The free-floating sections were incubated for 1 h in blocking solution (2 % Bovine Serum Albumin (BSA) in water, 0.5 % Triton X-100 in PBS) under shaking at RT. The slices were then incubated with the primary antibodies diluted in blocking solution overnight at 4 °C. The next day the slices were washed two times with PBS after removing the primary antibody solutions. The slices were then incubated with appropriate secondary antibodies diluted in blocking solution for 2 h at RT. After washing two times with PBS for 5 min, the cell nuclei were stained using DAPI (Invitrogen, Thermo Fisher Scientific, diluted in PBS, 1:1,500) for 5 min. The slices were then washed again two times with PBS for 5 min. The slices were finally transferred on microscope slides (order no. 631-1551, VWR). Coverslips (Menzel-Gläser, order no. 630-2108, VWR) were mounted onto the brain slices using Aqua-Poly/Mount mounting medium (order no. 18606-5, Polysciences). The slides were stored protected from light at RT until microscopy.

3.17.4 Nissl staining

For Nissl staining of mouse brain cryosections and vibratome sections, NeuroTrace red fluorescent Nissl stain (order no. N-21482, Thermo Fisher Scientific) was used. The staining was carried out following the manufacturer's instructions. When combined with an antibody staining, the antibody was performed first followed by the staining with the fluorescent Nissl dye. For blocking, standard solution containing e.g. BSA quench the signal of the Nissl dye. Instead, no blocking at all was carried out or PBS plus 0.5 % fish skin gelatine was used.

On the one hand, cryosections previously stored at -20 °C were thawed and adapted to RT. The slices were surrounded by a hydrophobic barrier using a liquid blocker (PAP-Pen Mini - Liquid-Repellent Slide Marker Pen, order no. N71312, Science Services). On the other hand, vibratome sections were stored in a 24-well plate (surrounded by parafilm) in 700 µL storing solution (30 % water, 30 % glycerol, 30 % ethylene glycol, 10 % PO_4 buffer 10x, 0.25 M, pH 7.2 - 7.4) at -20 °C. The slices were transferred into a petri dish (diameter 10 cm) containing PBS to wash. Then, they were transferred into a 24-well plate containing PBS. The slices were rehydrated in PBS for 40 min. For permeabilization, the sections were washed in PBS plus 0.1 % Triton X-100 for 10 min. Then, the sections were washed two times with PBS for 5 min. The NeuroTrace fluorescent Nissl dye was diluted 1:150 in PBS and applied on the sections. Cryosections were incubated with the dye for 30 min, whereas vibratome sections were incubated with the dye for 1 h at RT. Afterwards, the stain was removed and the sections were washed with PBS plus 0.1 % Triton X-100 for 10 min. Then, the sections were washed again two times with PBS for 5 min. An additional washing step with PBS for 2 h at RT followed. Afterwards, the cell nuclei were counterstained using DAPI (Invitrogen, Thermo Fisher Scientific, diluted in PBS, 1:1,500) for 5 min. The slices were then washed two times with PBS for 5 min. Finally, the slices were mounted onto the brain slices using Aqua-Poly/Mount mounting medium (order no. 18606-5, Polysciences). The slides were stored protected from light at RT until microscopy.

3.17.5 SVZ explants

On day 4 (d4) of culturing, the explants were fixed for 45 min using pre-warmed 4 % PFA in PBS. After washing once with PBS, the slide was kept in PBS at RT until further use for immunohistochemistry. Then, the fixed explants were washed again twice with PBS for 5 min under rotation and incubated in blocking solution (2 % BSA in water, 0.5 % Triton X-100 in PBS) for 2 h under rotation at RT. The explants were then incubated with the primary antibodies diluted in blocking solution overnight under rotation at RT. The next day, the explants were washed two times with PBS after removing the primary antibody solutions. The explants were then incubated with appropriate secondary antibodies diluted in blocking solution for 3 h under rotation at RT. After washing two times with PBS for 5 min, the cell nuclei were stained using DAPI (Invitrogen, Thermo Fisher Scientific, diluted in PBS, 1:1,500)

for 10 min under rotation. The explants were then washed again two times with PBS for 5 min. After removing the whole liquid, each well was filled with Aqua-Poly/Mount mounting medium (order no. 18606-5, Polysciences). The slides containing the explants were properly closed using parafilm and were stored protected from light at 4 °C until microscopy.

3.18 RNAscope®

The RNAscope® technology by ACD (a biotechne brand) is a novel variation of *in situ* hybridization (ISH) to simultaneously visualise up to three different RNA targets per cell in sample slides. The method is based on multiplexed signal amplification systems and a background suppression technology. In brief, tissue sections were first treated with different solutions to allow access to target RNA. Then, gene-specific probes were hybridized to target mRNAs and then to fluorescent dyes to amplify the signal. Finally, the target RNA is visualised using a fluorescent microscope (ACD (Biotechne), 2017). The specific *Tet3* probe, used in this study, is synthesised by ACD Biotechne. It binds to *Tet3* mRNA in exon 3 (NCBI reference sequence: NM_183138.2 - target region 814 - 1866), with the exact sequence being not available for the public.

In this study, the RNAscope® Multiplex Fluorescent Reagent Kit v2 Assay was used following the manufacturer's instructions. Some incubation times and volumes were optimized during establishing the assay. Per slide, a volume of 50 µL was used.

First, fresh frozen tissue sections were prepared. Animals were anaesthetized with isoflurane and sacrificed. The brains were carefully removed and frozen on dry ice within 5 min. The frozen tissue was placed into a cryomold and embedded in cryo-embedding medium. The cryomold was put on dry ice to let the cryo-embedding medium surrounding the brain tissue freeze completely. The frozen block was stored in an air-tight container at -80 °C until sectioning.

The frozen tissue block was equilibrated to -20 °C in a cryostat (CM3050 S, Leica) for 1 h. 20 µm thick brain sagittal or coronal sections were cut and mounted onto microscope slides (Menzel-Gläser Superfrost® Plus, Ref. J1800AMNZ, Thermo Scientific). The sections were dried for 60 to 120 min at -20 °C and stored at -80 °C until further use.

After removing the slides from -80 °C, the slices were immediately fixed with on 4 °C pre-chilled 4 % PFA in PBS for 1 h at 4 °C. Afterwards, the slices were washed two times with PBS for 5 min to remove excess PFA. The sections were then dehydrated with 50 % ethanol for 5 min, then with 70 % ethanol for 5 min and finally two times in 100 % ethanol for 5 min at RT. The slides were then air dried for 5 min at RT. Using the ImmEdge™ hydrophobic barrier pen, a hydrophobic barrier was drawn around each section. Next, the slices were incubated with hydrogen peroxide for 10 min at RT in the included humidity chamber and then washed two times with distilled water. Afterwards, the slices were incubated with Protease III (1:2 diluted in PBS) for 15 min at RT and then washed two times with PBS.

Before proceeding with the probe hybridisation, 1x Wash Buffer, the probes and different reagents had to be prepared and equilibrated according to the manufacturer's manual.

After removing excess liquid from the slides, Tet3 probe mix (dilution 1:50) as well as positive and negative control probes were added to the slices. The slides were incubated for 2 h at 40 °C in the HybEZ™ Oven and then washed two times with 1x Wash Buffer for 2 min at RT. Then, RNAscope® Multiplex FL v2 Amp 1 solution was added to the slices. The slides were inserted into the HybEZ™ Oven for 30 min at 40 °C and then washed two times with 1x Wash Buffer for 2 min at RT. Then, RNAscope® Multiplex FL v2 Amp 2 solution was added to the slices. The slides were inserted into the HybEZ™ Oven for 30 min at 40 °C and then washed two times with 1x Wash Buffer for 2 min at RT. Finally, RNAscope® Multiplex FL v2 Amp 3 solution was added to the slices. The slides were inserted into the HybEZ™ Oven for 15 min at 40 °C and then washed two times with 1x Wash Buffer for 2 min at RT. Next, the HRP-C3 signal was developed. RNAscope® Multiplex FL v2 HRP-C3 solution was added to slices. The slides were incubated for 15 min at 40 °C in the HybEZ™ Oven and then washed two times with 1x Wash Buffer for 2 min at RT. Then, 1:1,500 diluted Opal™ 690 dye was added to each slice. The slides were incubated for 30 min at 40 °C in the HybEZ™ Oven and washed two times with 1x Wash Buffer for 2 min at RT. RNAscope® Multiplex FL v2 HRP blocker solution was added to each slice. The slides were incubated for 15 min at 40 °C in the HybEZ™ Oven and washed two times with 1x Wash Buffer for 2 min at RT.

Finally, the slides were counterstained with DAPI (Invitrogen, Thermo Fisher Scientific, diluted in PBS, 1:1,000) for 10 min at RT and mounted. A glass coverslip (Menzel-Gläser, order no. 630-2108, VWR) was carefully placed over the tissue section after adding two drops of Aqua-Poly/Mount mounting medium (order no. 18606-5, Polysciences). The slides were dried protected from light at RT and then stored at 4 °C for microscopy analysis.

3.19 Immunocytochemistry of transfected HEK293T cells

Human embryonic kidney (HEK293T) cells were grown and maintained in DMEM + GlutaMAX medium - pyruvate + 4.5 g/l glucose + 10 % fetal bovine serum (Biochrom) + 1 % penicillin/streptomycin (Biochrom) at 37 °C and 10 % CO_2 in an incubator (Heraeus, Thermo Scientific).

The transfection was performed in µ-slide 8 Well plates (Cat. no. 80826, Ibidi). $3 \cdot 10^4$ cells were seeded per well in 200 µL medium. 24 h after seeding, the cells were transfected using 150 ng of DNA per expression plasmid, 0.5 µL of jetPRIME® and 15 µL of jetPRIME® buffer (Polyplus transfection). The used GFP-Tet3 and GFP constructs were described in (Liu et al., 2013). 24 h after transfection, the cells were washed with DPBS + $MgCl_2$ / $CaCl_2$.

Subsequently, immunocytochemistry (ICC) was performed. If not stated otherwise, all steps were carried out in a humidity chamber at RT. The cells were fixed by adding 4 % PFA in DPBS + $MgCl_2$ / $CaCl_2$ for 15 min and washed three times with DPBS + $MgCl_2$ / $CaCl_2$ for 5 min. Then, the cells were permeabilised and blocked with 0.3 % Triton X-100 and 5 % ChemiBlocker™ (order no. 2170, Merck Millipore) for 30 min. Afterwards the cell were incubated with the primary antibodies diluted in DPBS + $MgCl_2$ / $CaCl_2$ containing 5 % ChemiBlocker™ (order no. 2170, Merck Millipore) and 0.3 % Triton X-100 overnight at 4 °C. After removing the primary antibody solutions, the cells were washed three times with DPBS + $MgCl_2$ / $CaCl_2$ for 5 min and then incubated with appropriate secondary antibodies diluted in DPBS + $MgCl_2$ / $CaCl_2$ containing 3 % ChemiBlocker™ (order no. 2170, Merck Millipore) for 1 h at RT. After washing three times, the cell nuclei were stained by applying 5 µg/mL Hoechst 33342 (Invitrogen, Thermo Fisher Scientific, diluted in 0.1 M PB) for 10 min. The cells were then washed again two times with PBS for 5 min. Then, a few drops of Aqua-Poly/Mount mounting

medium (order no. 18606-5, Polysciences) were added to the wells. Finally, the plates were stored protected from light at RT until further use for microscopy.

3.20 Confocal microscopy

Immunohistochemical stainings of mouse brain slices, mouse retina slices and SVZ explants were analysed using the Leica TCS SP8 spectral confocal laser scanning microscope (Leica Microsystems) equipped with 405 nm, 488 nm, 552 nm and 638 nm lasers. All images were acquired with a HC PL FLUOTAR 10x/0.30 Dry objective, 20x HC PL APO CS2 20x/0.75 IMM or HC PL APO 40x/1.30 Oil CS2 objective (Leica Microsystems) using Z-Stack mode. The generated files were processed with LAS X software and the open-source software Fiji (Preibisch et al., 2009; Schindelin et al., 2012).

3.21 Statistics

For statistical analysis and graphing of data, GraphPad Prism software version 8.4.2 was used. The statistical tests applied on each data set are described in the respective figure legends.

4 Results

4.1 5hmC dynamics in mouse hippocampus

The focus of this study lies on Tet enzymes and the products, they generate by oxidation processes. Thus, the first step was to examine the connection between neuronal activity and DNA demethylation in mouse hippocampus. To determine whether 5hmC levels in mouse hippocampus are regulated by neuronal activity, acute mouse hippocampal slices were prepared and depolarized using 25 mM potassium chloride (KCl) (Figure 14). Global cytosine modification levels as well as relative mRNA expression levels of several neuronal activity-related genes were measured in KCl treated and control samples.

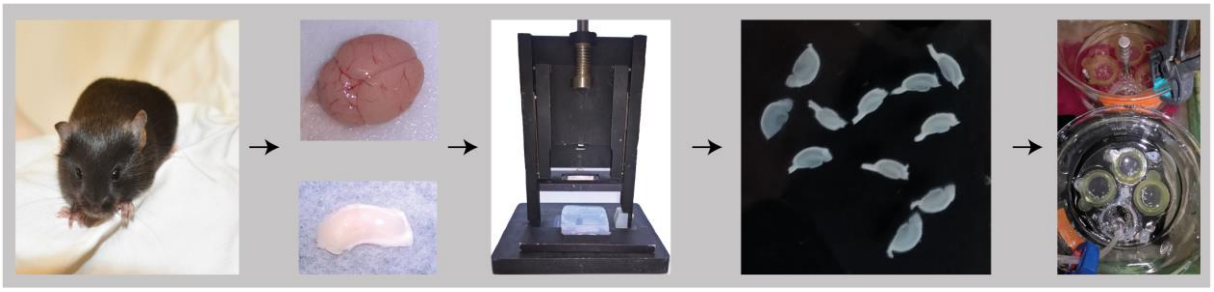

Figure 14: Preparation of mouse hippocampal slices

C57BL/6J WT mice (4 - 5 weeks old) were sacrificed and brains were removed. The hippocampi of each hemisphere were dissected and cut using a guillotine-type tissue slicer. The slices were collected in an oxygenated physiological solution at 37 °C until the hippocampi of all biological replicates were processed. The slices were then distributed to two different conditions: oxygenated physiological solution and oxygenated 25 mM KCl solution. After an incubation time of 6 h, the slices were transferred into reaction tubes and snap frozen in liquid nitrogen until further use for quantification of global levels of cytosine modifications as well as relative mRNA expression levels of relevant genes.

Depolarization of hippocampal slices using 25 mM KCl resulted in significantly increased global 5hmC levels (Figure 15 - B). In contrast, 5mC levels did not change, indicating that depolarization substantially affects 5mC to 5hmC oxidation but not 5mC formation (Figure 15 - A). 8-oxoguanine (8oxoG) levels, serving as a control and representing the number of oxidative damages in the gDNA caused during the whole procedure or by biological influences, stayed under the estimated background level of $5 \cdot 10^{-6}$ 8oxoG per dN (Traube et al., 2019), hinting at predominantly Tet3-mediated oxidation processes (Figure 15 - C).

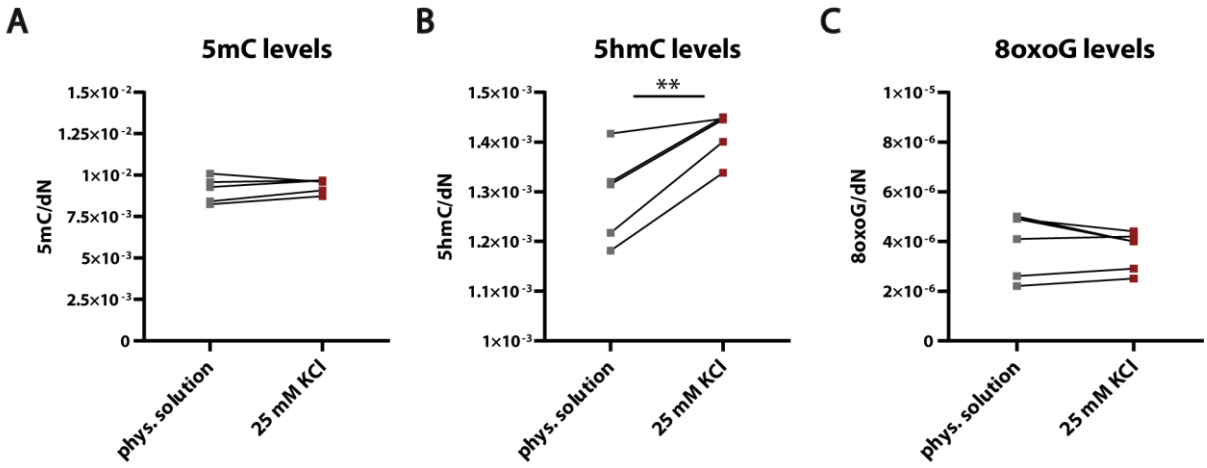

Figure 15: Levels of cytosine modifications after depolarization of hippocampal tissue

(A) Global 5mC levels did not change between the different conditions. **(B)** Global 5hmC levels increased after depolarization of mouse hippocampal slices using 25 mM KCl. **(C)** 8oxoG levels stayed low, representing only little oxidative damage during the procedure. Statistics: ** $p \leq 0.01$ (paired t-test, two tailed), n = 6.

Tet1, *Tet2* and *Tet3* mRNA expression levels stayed stable after depolarization, meaning that the effect of 5hmC increase is mainly based on an increased Tet activity and not on increased Tet transcript levels (Figure 16 - A).

As a consequence of neuronal stimulation, several neuronal activity-dependent genes or immediate early genes (IEGs) modulating the response of neurons towards stimuli are activated by DNA demethylation (Sun and Lin, 2016). Such genes are e.g. *Npas4* (neuronal per arnt sim domain 4), *Bdnf* (brain-derived neurotrophic factor) and *Arc (*activity-regulated cytoskeleton-associated protein), which play essential roles in synaptic homeostasis, learning and memory formation (Dieni et al., 2012; Kaas et al., 2013; Sun and Lin, 2016). 25 mM KCl-induced cell depolarization in hippocampal slices resulted in increased *Npas4* mRNA expression levels, suggesting a direct effect of 5hmC increase on *Npas4* transcript levels. However, no consistent effect on *Bdnf total* and *Arc* transcript levels was detected (Figure 16 - B).

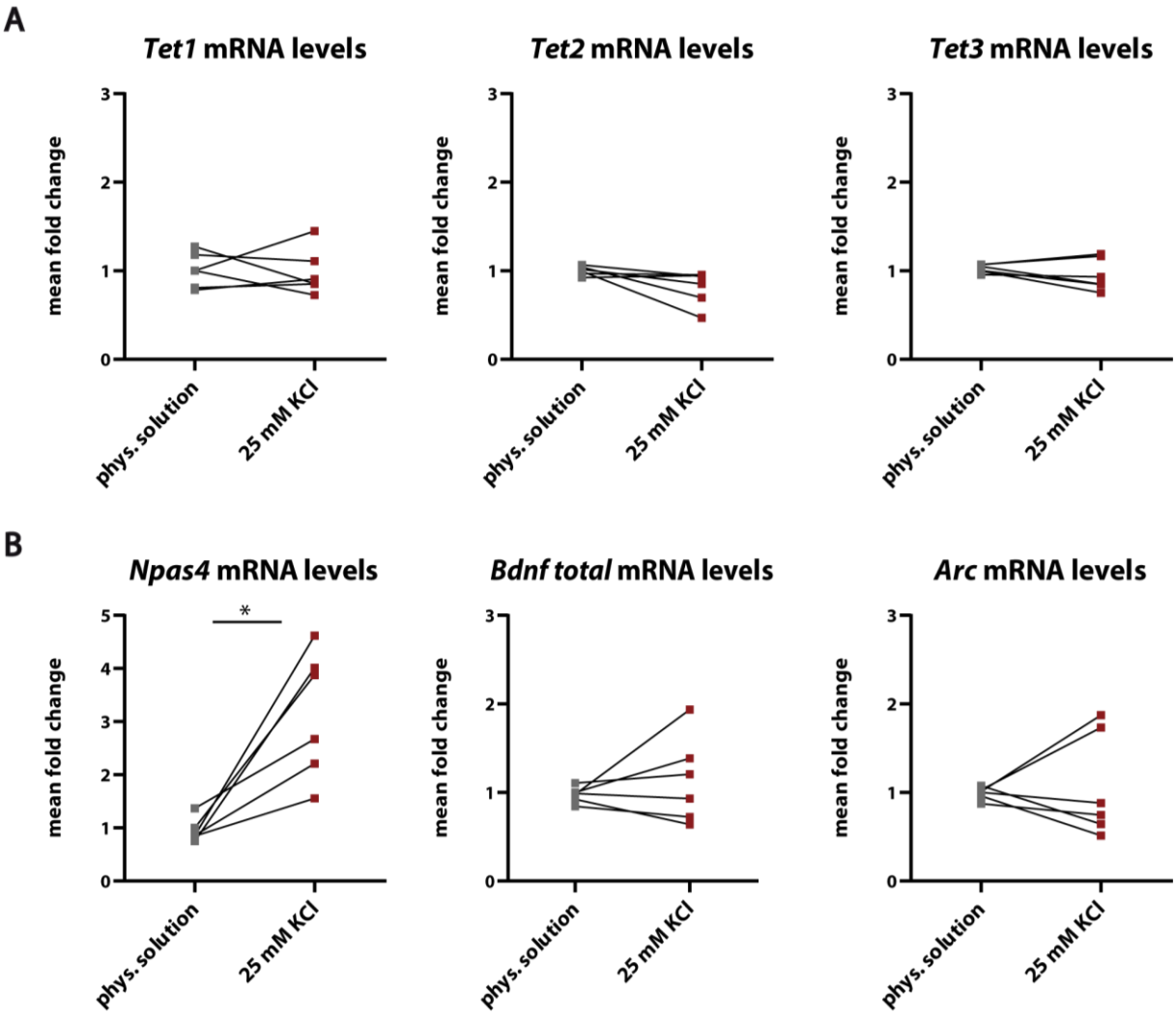

Figure 16: Transcript levels after depolarization of hippocampal tissue

(A) *Tet1, Tet2* and *Tet3* mRNA expression levels remained stable after depolarization of mouse hippocampal slices using 25 mM KCl. **(B)** *Npas4* mRNA expression levels significantly increased after depolarization, whereas *Bdnf total* and *Arc* mRNA expression levels did not show significant changes. Statistics: * $p \leq 0.05$ (paired t-test, two tailed), n = 6.

To conclude, 5hmC levels increased as a direct response to 25 mM KCl induced depolarization, accompanied by changes in expression levels of selected IEGs. The study of 5hmC dynamics in mouse hippocampus raised the question about the mechanisms generating the cytosine modifications. Tet enzymes play an essential role in these DNA demethylation processes, whereat Tet3, the most abundant Tet variant in the CNS, is in the focus of interest in this study. *In vivo* and *in vitro* models are necessary to fully understand the role and functions of Tet3 in neurons.

4.2 Tet3 L2 + Nestin Cre mouse model

Since a general Tet3 KO is embryonically lethal (Gu et al., 2011), only mouse models can be used, in which the KO of Tet3 is limited to specific cell types or specific regions of the body. In this study, a mouse model was chosen, in which a conditional Tet3 KO is based on the Cre/loxP site recombination system.

To generate the Tet3 L2 + Nestin Cre mouse model, a conditional Tet3 KO mouse line (Amouroux et al., 2016) and a Nestin Cre mouse line (Tronche et al., 1999) were utilised (Figure 12). After crossing those two lines, Cre recombinase excises the loxP-flanked DNA, in this case exons 8 and 9 of the *Tet3* gene encoding for large parts of the Tet3 enzyme's catalytic domain (Figure 12 - A), finally leading to a functional KO of Tet3 in all cells, in which Cre recombinase is expressed. Within the nervous system, the Nestin promotor driven Cre recombinase expression is found in the CNS and peripheral nervous system (PNS), including neuronal and glia cell precursors, and in Müller glia cells of the retina by embryonic day 11 (E11) (Ivanova et al., 2010; Tronche et al., 1999). Nestin is additionally expressed in the heart, muscle, kidney and testis tissue during development (Chen et al., 2006; Kachinsky et al., 1995; Wilhelmsson et al., 2019). In general, Nestin, a class VI intermediate filament protein, is a marker for neural stem cells (Korzhevskii et al., 2015; Lendahl et al., 1990; Matsuda et al., 2013). It was reported to be essential for the regulation of cellular processes, including stemness, cell cycle and neurogenesis (Matsuda et al., 2013; Wilhelmsson et al., 2019). The image from Allen Brain Atlas shows a brain sagittal section of a Nestin Cre positive mouse crossed with a TdTomato reporter mouse line (Figure 12 - B) (Ai14 (RCL-tdT)) (https://connectivity.brain-map.org/transgenic/experiment/182530340, Allen Institute for Brain Science, Mouse Brain Connectivity Atlas and (Oh et al., 2014)). All TdTomato positive red cells were affected by Nestin Cre activity at some time point during the period between E11 and adult stages. Transferred to the Tet3 L2 + Nestin Cre mouse model, this means that those cells are affected by Nestin Cre recombinase activity during that time period resulting in a loss of Tet3 catalytic activity.

4.2.1 Basic characterization of the Tet3 L2 + Nestin Cre mouse model

First, a basic characterization of the Tet3 L2 + Nestin Cre mouse model regarding body size, brain size and morphology was performed to identify a possible effect of the functional Tet3 KO on those parameters (Figure 17).

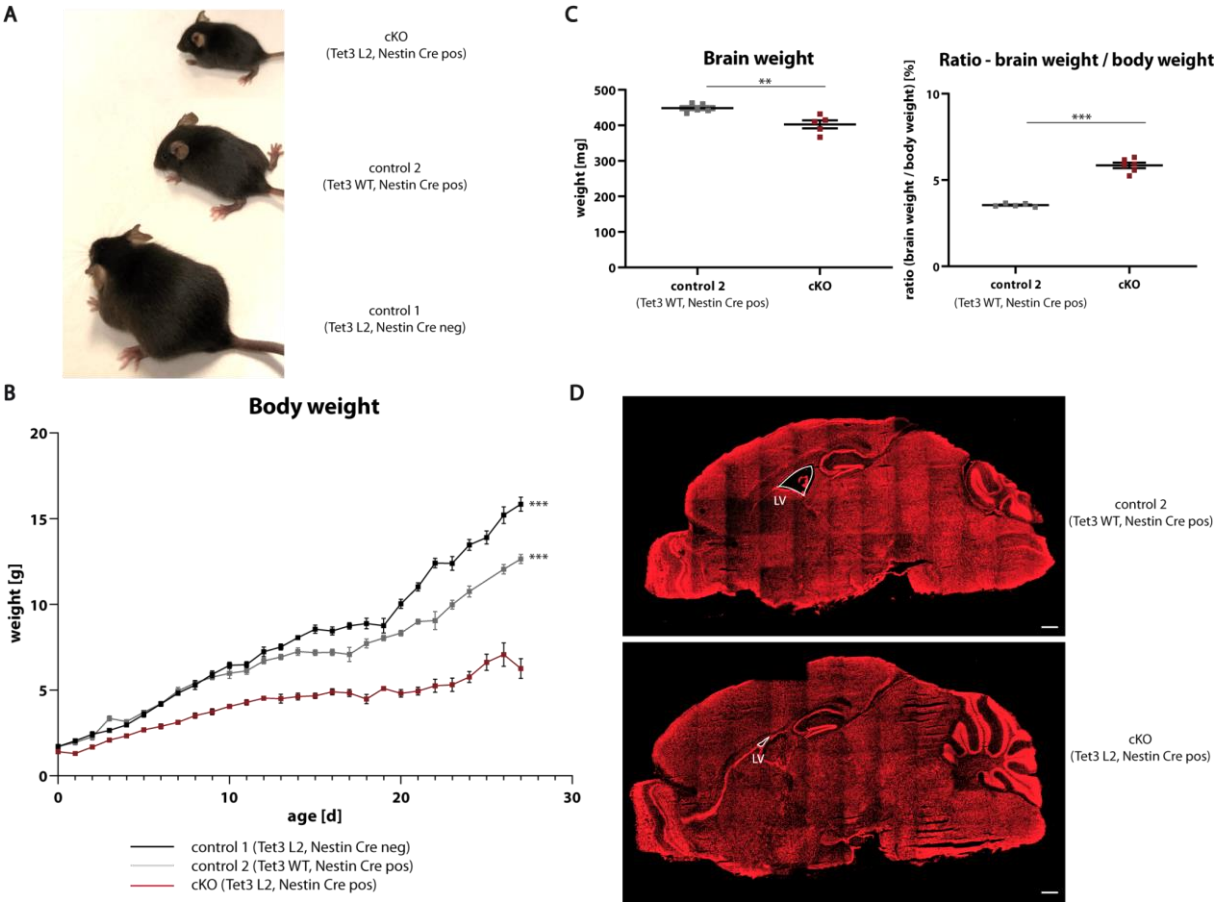

Figure 17: Basic characterization of the Tet3 L2 + Nestin Cre mouse model

(A) Representative images of mice of the different genotypes (controls and cKO) at an age of 4 weeks: control 1 (Tet3 L2, Nestin Cre neg), control 2 (Tet3 WT, Nestin Cre pos), cKO (Tet3 L2, Nestin Cre pos). **(B)** Body weight comparison between controls and cKO over a period of 28 days. Means are plotted for a certain number of replicates (control 1: n = 23, control 2: n = 12, cKO: n = 13) per genotype. Statistics: Error bars (SEM = standard error of the mean) are shown. *** $p \leq 0.001$ (Two-Way ANOVA with Tukey´s multiple comparisons test). Stars indicate statistical difference of each control line in comparison to cKO. **(C)** Brain weight comparison between different genotypes after brain removal from mice at an age of 4 weeks. Absolute values and the ratio of brain to body weight are shown. Statistics: ** $p \leq 0.01$ and *** $p \leq 0.001$ (unpaired t-test, two tailed), n = 5. **(D)** Nissl staining on sagittal cryosections of brains removed from cKO and control mice at an age of 4 weeks. Scale bar 500 µm.

An abnormal phenotype regarding body size and body weight was observed. Tet3 L2 homozygous and Nestin Cre positive mice, named cKO (conditional KO) in the following, were much smaller than their Tet3 L2 homozygous, Nestin Cre negative (control 1) and Tet3 WT, Nestin Cre positive (control 2) siblings. A representative picture of mice with the three different genotypes was taken at the age of four weeks (Figure 17 - A) and clearly shows the growth abnormalities in cKO animals. In addition to that, the body weight of mice with the three different genotypes was measured over a period of 28 days (Figure 17 - B). Importantly, the Nestin Cre mouse line, which was used in this study, itself displays a growth retardation phenotype (https://www.jax.org/strain/003771). For that reason, this genotype (control 2 - Tet3 L2 WT, Nestin Cre positive), named CTR (control) in the following, served as control group for all experiments. Furthermore, the weight of CTR and cKO brains were measured. The absolute values of the brain weight and the ratio of brain to body weight were analysed (Figure 17 - C). Concerning the absolute brain weight values in mg, the brains of cKO animals were smaller. Regarding the ratio of brain to body weight, it was reversed, indicating that the brain of cKO mice are abnormally large in comparison to CTR. Furthermore, a Nissl staining was performed in CTR and cKO sagittal brain sections to study morphology and pathology of neurons in mouse brain tissue as well as to understand the cytoarchitecture of different brain areas (Kádár et al., 2009) (Figure 17 - D). A preliminary analysis of the sections seemed to indicate that neuronal morphology does not differ between cKO and CTR animals. However, closer morphological analysis regarding brain structure revealed a smaller lateral ventricle (LV) size in brains of cKO in comparison to CTR animals, which needs to be further confirmed by quantitative analysis.

In conclusion, the characterization of the Tet3 L2 + Nestin Cre mouse model regarding body size, brain size and morphology revealed an abnormal phenotype in cKO animals displaying growth abnormalities and smaller brains with smaller lateral ventricles, suggesting an effect of depletion of functional Tet3 on those parameters.

4.2.2 Detection of Tet3 on protein and transcript level

To visualise Tet3 protein in mouse brain slices of CTR and cKO animals, immunohistochemical analysis was performed using a Tet3 antibody, specifically recognizing the C-terminal part of the Tet3 protein (Figure 18).

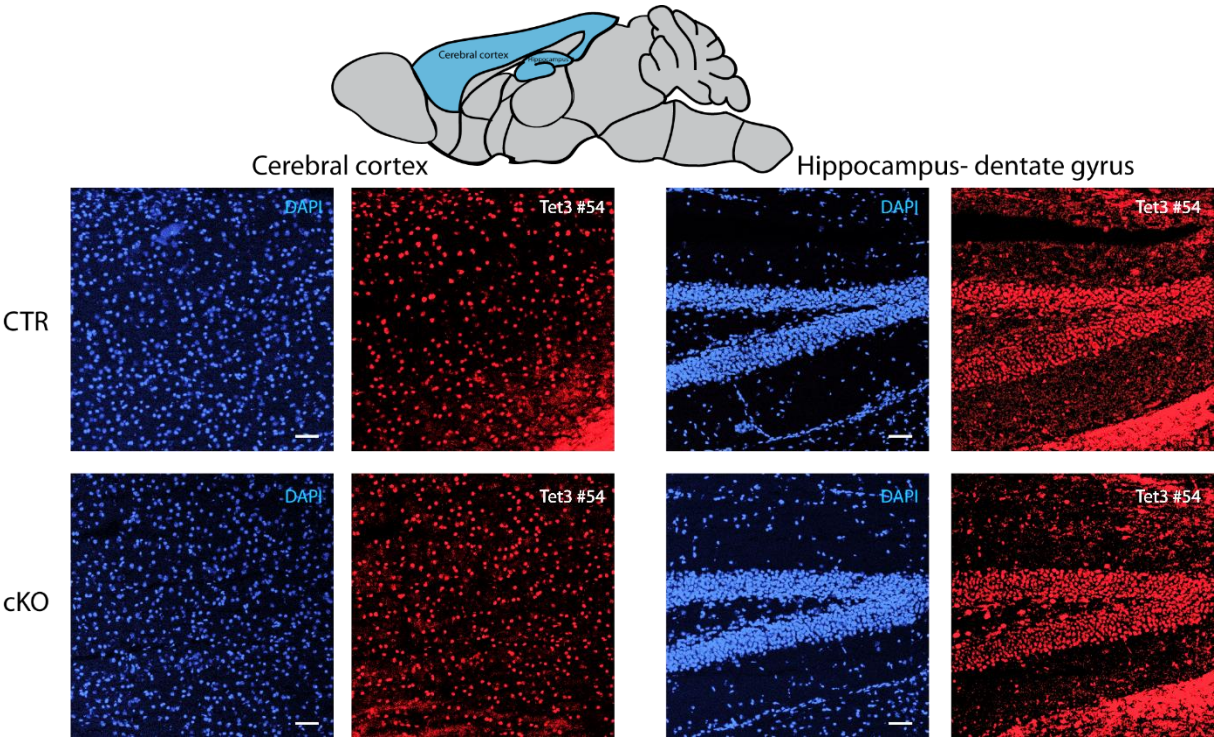

Figure 18: Visualisation of Tet3 protein using immunohistochemistry

Immunohistochemistry in cerebral cortex and hippocampus of mouse sagittal brain slices of CTR and cKO animals: DAPI (blue), Tet3 #54 (red). Images were taken using a confocal microscope. Scale bar 50 µm.

Surprisingly, Tet3 protein signal was detected in mouse brain slices of both CTR and cKO animals.

Moreover, a custom RNAscope® *in situ* hybridisation probe was generated to visualise *Tet3* transcript localisation in brain slices. The specific probe, used in this study, binds to *Tet3* mRNA in exon 3 (NCBI reference sequence: NM_183138.2 - target region 814 - 1866).

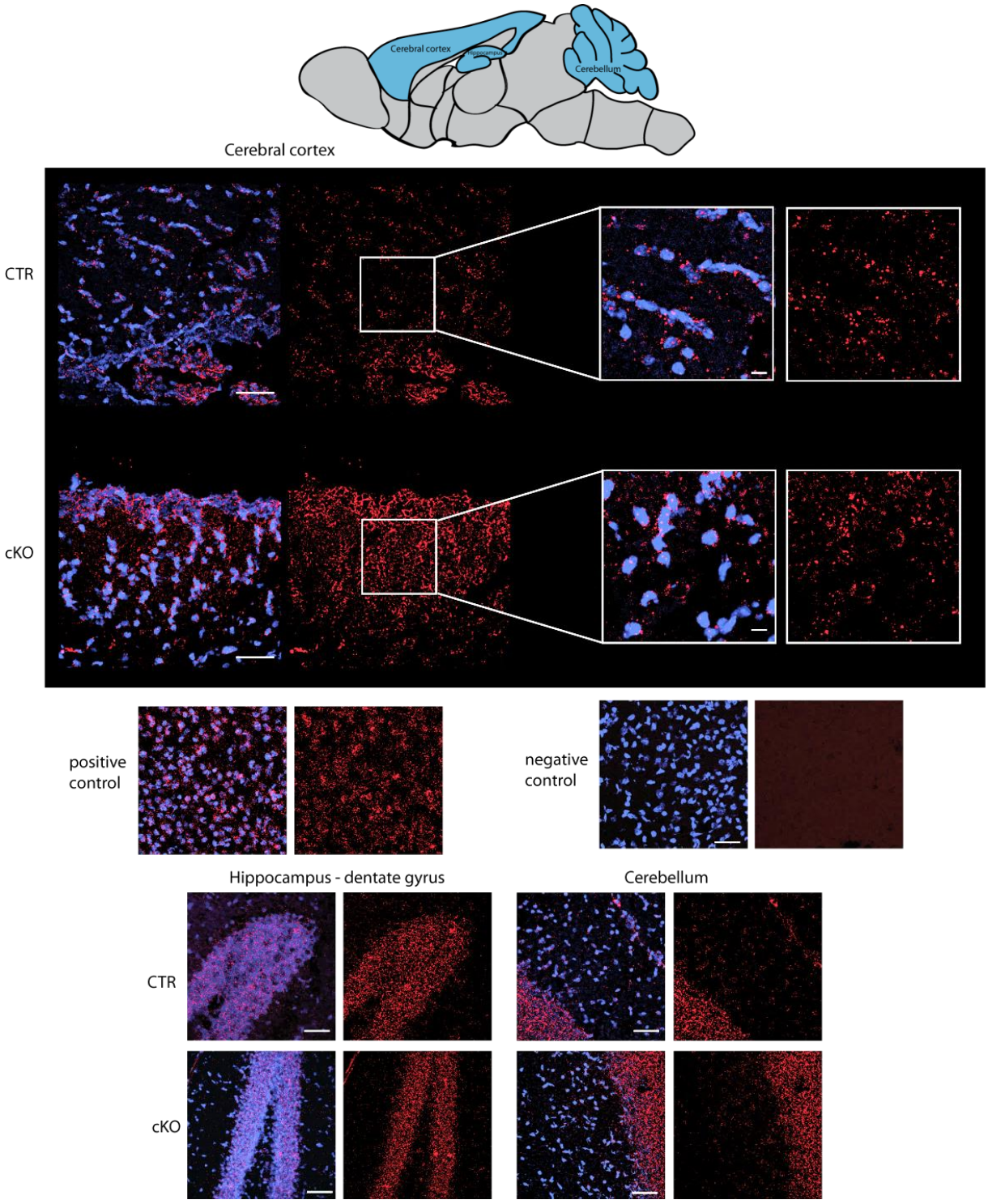

Figure 19: Visualisation of *Tet3* transcript using RNAscope® technology

Confocal images of brain sagittal slices: DAPI (blue), *Tet3* (red dots). Images of different brain regions (cerebral cortex, hippocampus and cerebellum - highlighted in blue) as well as positive and negative controls are shown. Scale bars 10 µm and 50 µm.

Confocal microscopy analysis showed *Tet3* localisation in a dotty, for RNAscope® technology typical way, but did not reveal any obvious differences between CTR and cKO (Figure 19). Positive and negative controls confirmed the specificity of the *Tet3* signal in the tissue.

To further validate the Tet3 L2 + Nestin Cre mouse line and to quantify mRNA expression levels of all Tet enzymes, qRT-PCR experiments were performed for different brain regions (cerebral cortex, cerebellum, hippocampus, olfactory bulb) of CTR and cKO animals at an age of four weeks (Figure 20). For *Tet3* mRNA levels, two different primer pairs were used, which bind either in the 5' part of the *Tet3* transcript (*total Tet3*) or in exon 9 and 10 (*Tet3 del*). Exon 9 is deleted after a successful excision by Cre recombinase. Hence, this qRT-PCR assay only generates a signal from the WT *Tet3* locus and is thus used to confirm the efficient Cre-mediated excision of Exon 9.

In cerebral cortex, mRNA levels of *total Tet3* transcript did not change in CTR and cKO animals, whereas mRNA levels of *Tet3 del* were significantly reduced in cKO animals (Figure 20 - A). This indicates that, on the one hand, the excision of the loxP-flanked *Tet3* exons by Cre recombinase was successful and, on the other hand, that *Tet3* transcript was still existent, as not all cortical cells express Nestin or Cre recombinase, respectively. Additionally, *Tet1* and *Tet2* mRNA expression levels did not change significantly in cKO. However, there was a slight tendency for an increase of *Tet2* transcript levels in cKO in comparison to CTR animals, suggesting minimal compensation mechanisms by *Tet1* and *Tet2* after Tet3 depletion (Figure 20 - B). Furthermore, transcript levels of *Npas4* were analysed, because reports suggested changing expression of neuronal-activity regulated genes like *Npas4* after Tet3 depletion in brain tissue (Antunes et al., 2020). *Npas4* mRNA expression levels showed a tendency to increase suggesting that Tet3 might regulate mRNA expression levels of *Npas4* in Nestin positive neurons (Figure 20 - B).

Figure 20 - C summarises the data obtained for relative transcript levels of *Tet1*, *Tet2*, *Tet3* and *NPas4* in all analysed brain regions in cKO compared to CTR animals. In all tissues, transcript levels of *total Tet3*, *Tet1* and *Npas4* did not show significant changes between the cKO and CTR animals, with *Npas4* transcript levels showing a tendency to increase. *Tet3 del* transcript levels

were significantly reduced in all analysed tissues of cKO animals. *Tet2* transcript levels were increased in cerebellum und olfactory bulb tissue in cKO compared to CTR animals.

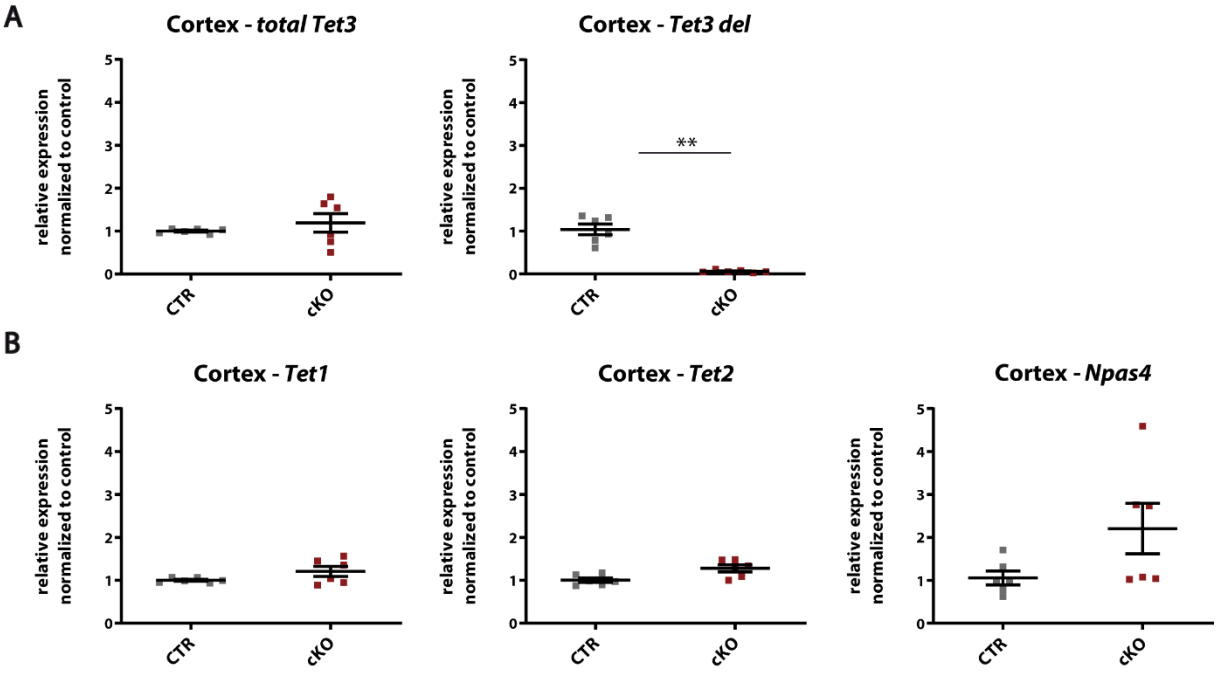

C

Region	*Tet3 total*	*Tet3 del*	*Tet1*	*Tet2*	*Npas4*
Cerebral cortex	ns	** ↓	ns	ns	ns
Olfactory bulb	ns	** ↓	ns	*** ↑	ns
Cerebellum	ns	*** ↓	ns	** ↑	ns
Hippocampus	ns	*** ↓	ns	ns	ns

Figure 20: Analysis of relative mRNA expression levels in different brain regions

(A + B) Relative mRNA expression levels of *Tet1*, *Tet2*, *Tet3* and *Npas4* in cerebral cortex tissue of cKO and CTR animals at an age of four weeks were analysed by qRT-PCR. Expression was normalized to the respective levels in CTR animals. **(C)** Summary of all qRT-PCR experiments to analyse relative mRNA expression levels of *Tet1*, *Tet2*, *Tet3* and *Npas4* in specific brain tissue (cerebral cortex, olfactory bulb, cerebellum, hippocampus) of cKO and CTR animals at an age of four weeks. Expression was normalized to the respective levels in CTR animals. Statistics: Error bars (SEM) are shown. ** $p \leq 0.01$, *** $p \leq 0.001$ (Unpaired t-test, two-tailed), n = 6.

To conclude, qRT-PCR analysis of *Tet3* transcript in different brain regions of cKO and CTR animals indicated that the loxP-flanked *Tet3* sequence was successfully excised by Nestin Cre recombinase in cKO mice. However, *Tet3* transcript was still detectable, as not all brain cells express Nestin or Cre recombinase, respectively, and are affected by the Tet3 depletion.

Furthermore, it suggested that the excision of Exon 8 and 9 of *Tet3* caused by Nestin Cre recombinase does not lead to substantial nonsense-mediated mRNA decay. *Tet3* transcript as well as Tet3 protein remained detectable at largely unchanged levels. Analysis of *Tet1* and *Tet2* transcript levels indicated minimal and brain region specific compensation mechanisms resulting from Tet3 depletion. Moreover, *Npas4* mRNA expression levels might be regulated by Tet3, but high variability did not allow to obtain conclusive data.

4.2.3 Quantification of global 5mC and 5hmC levels

Tet enzymes catalyse the oxidation of 5mC to 5hmC and further to 5fC and 5caC. To assess whether the deletion of a part of the Tet3 catalytic domain leads to a loss of Tet3 oxidative function in the Tet3 L2 + Nestin Cre mouse model influencing the levels of cytosine modifications in different brain regions, immunohistochemical analysis of mouse sagittal brain slices using specific antibodies for 5mC and 5hmC was performed (Figure 21).

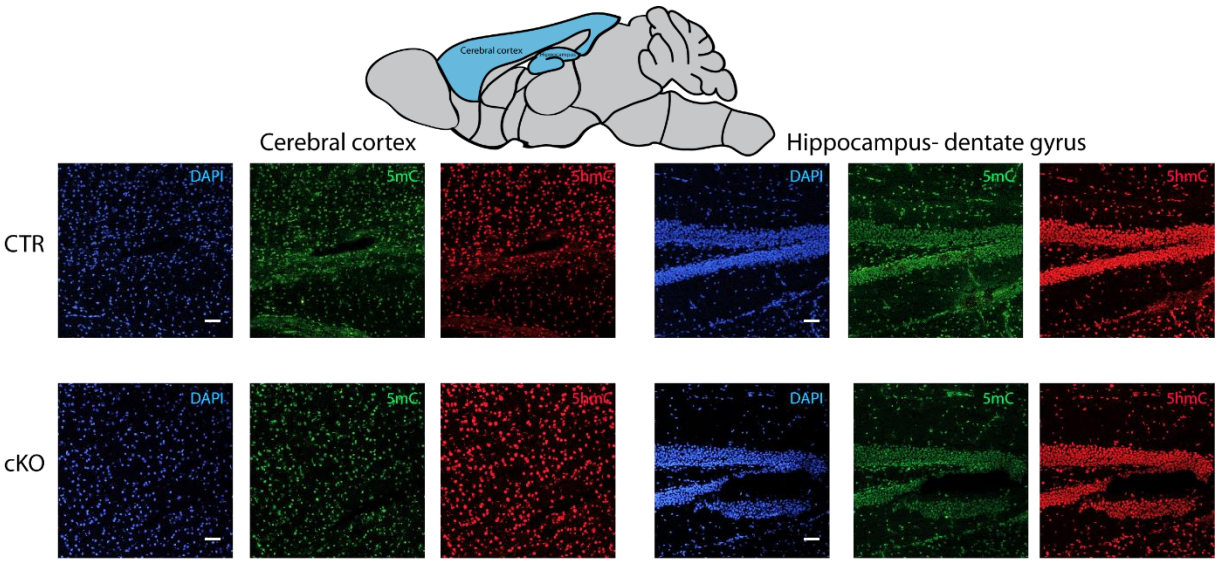

Figure 21: Visualisation of 5mC and 5hmC

Immunohistochemistry in cerebral cortex and hippocampus of mouse sagittal brain slices of CTR and cKO animals: DAPI (blue), 5mC (green), 5hmC (red). Images were taken using a confocal microscope. Scale bar 50 µm.

5mC and 5hmC were detected in mouse brain slices of both CTR and cKO animals. No obvious differences between the genotypes were observed.

To quantitatively assess global 5mC and 5hmC levels in gDNA samples of mouse hippocampus, cerebral cortex, cerebellum and olfactory bulb of CTR and Tet3 cKO animals, UHPLC-MS/MS analysis was used (Figure 22).

5mC levels stayed stable in all analysed tissue, indicating that Tet3 depletion does not influence 5mC levels (Figure 22 - A). 5hmC levels significantly decreased in cerebellum samples of cKO animals. In hippocampus, cerebral cortex, and olfactory bulb, 5hmC levels did not change between CTR and cKO animals (Figure 22 - B).

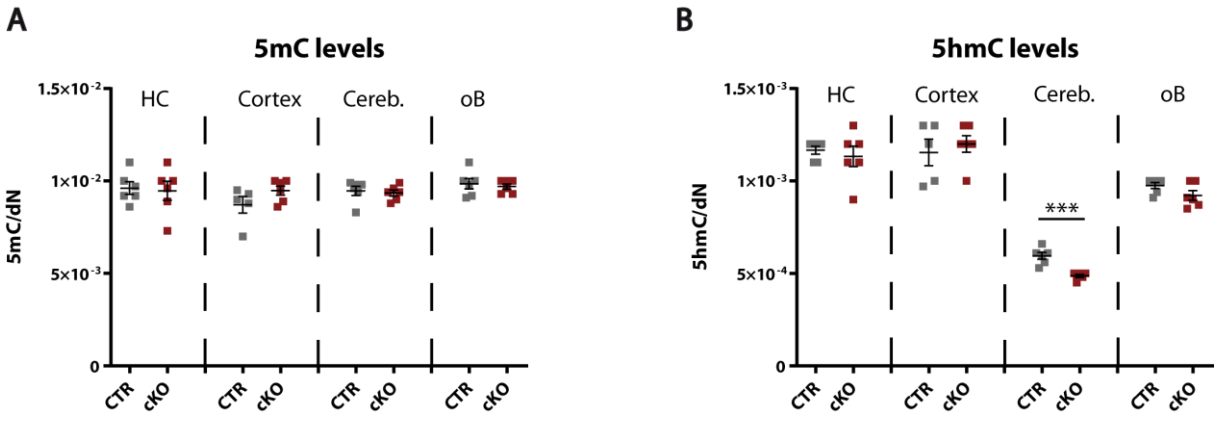

Figure 22: Quantification of global 5mC and 5hmC levels in different tissues

Global 5mC **(A)** and 5hmC **(B)** levels were measured by UHPLC-MS/MS in gDNA samples of hippocampus, cerebral cortex, cerebellum and olfactory bulb tissue of CTR and Tet3 cKO animals. Statistics: Error bars (SEM) are shown. *** $p \leq 0.001$ (Unpaired t-test, two-tailed), $n = 6$.

From these results, it can be concluded that there is less Tet3 activity in cerebellum tissue of cKO animals compared to CTR animals represented by the decrease of 5hmCs levels, which is generated by Tet3. In hippocampus, cerebral cortex and olfactory bulb samples, 5hmC levels did not change, which might reflect Tet1 and Tet2 action, as their transcript expression was not affected or even increased after Tet3 deletion.

4.2.4 Proteomics

Next, the proteome of mouse cerebral cortex, cerebellum, hippocampus and olfactory bulb of CTR and Tet3 cKO animals was analysed by mass spectrometry to investigate how protein expression in those tissues is changed by Tet3 catalytic deficiency.

Differences between cKO and CTR proteome in different tissues were visualised using volcano plots (Figure 23). Significantly enriched proteins in cKO tissue in comparison to CTR are located in the upper right quadrant, whereas significantly depleted proteins in cKO tissue are located in the upper left quadrant of the graphs. Histones and keratins, which were also significantly enriched or depleted in all analysed tissue samples, are considered as technical impurities and therefore excluded from the analysis.

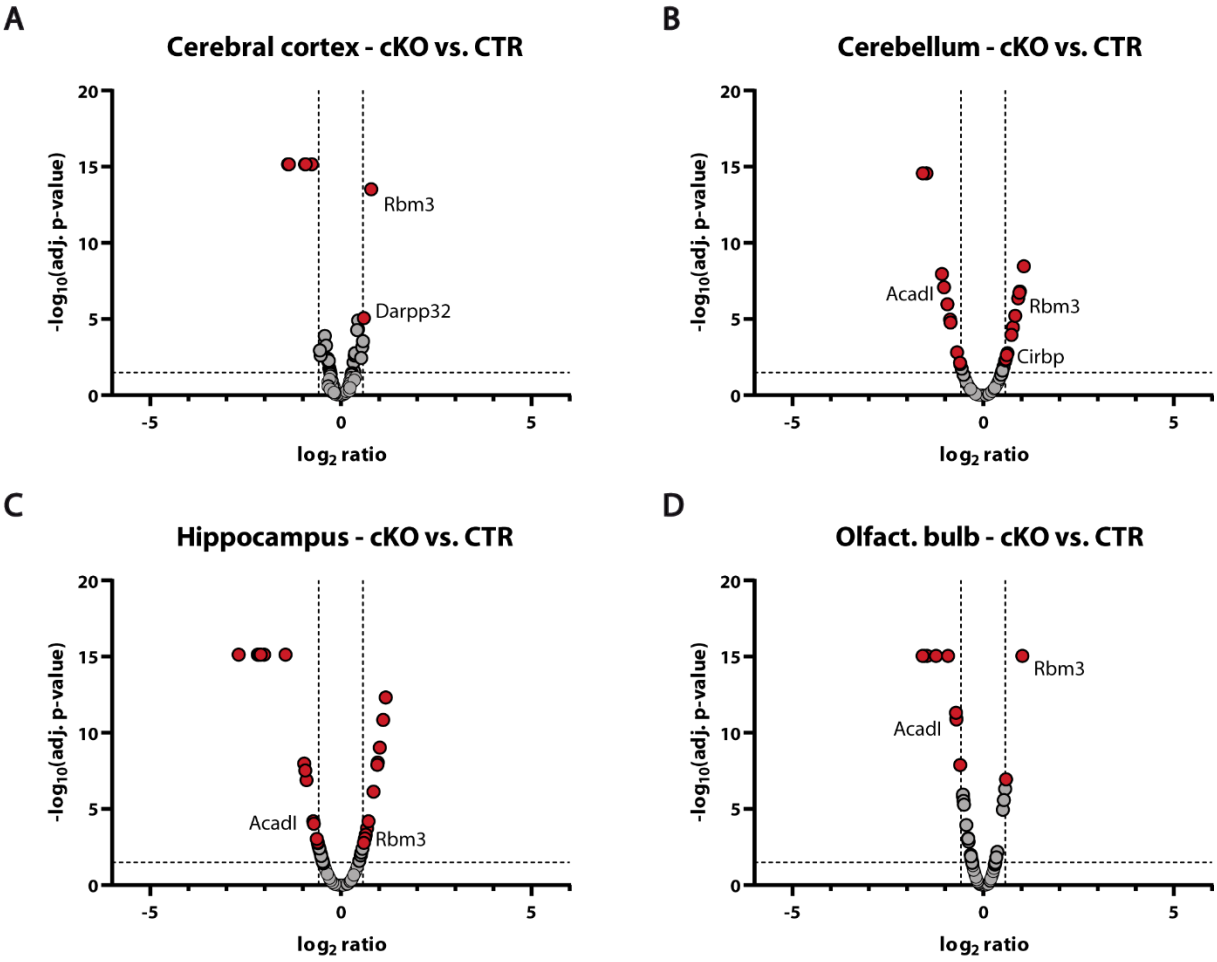

Figure 23: Proteome analysis in different tissues

Comparisons for cKO and CTR animals in different tissues were visualised using volcano plots **(A - D)**. Proteins, detected in at least three replicates, were plotted according to their expression ratio between cKO and CTR (log_2 ratio) and adjusted p-value ($-log_{10}p_{adj}$). The threshold value for the expression ratio was set to log_2 ratio ≥ 0.584 and ≤ -0.584 (equivalent to a ratio of 1.5). The cut-off value for the significance level was set to $-log_{10}p_{adj} \geq 1.3$ (equivalent to $p_{adj} \leq 0.05$). Relevant differentially expressed proteins are marked with their name.

The volcano plots did not reveal major differences between cKO and CTR animals regarding the proteome in all analysed tissues. Relevant significantly enriched and depleted proteins in different tissue types of cKO in comparison to CTR animals are summarised in Table 6.

Table 6: Summary of proteome analysis - Tet3 L2 + Nestin Cre mouse model

The table summarises all significantly enriched and depleted proteins in different tissue types of cKO compared to CTR animals. Histones and keratins were excluded from the analysis.

Brain regions	sign. enriched proteins in cKO	sign. depleted proteins in cKO
Cerebral cortex	Rbm3, Darpp32	Timm10, Ndufa2, Atp2a
Cerebellum	Rbm3, Cirbp, Vdac2, Vdac3, Cox7c, Ndufa5	Acadl, Mpc2
Hippocampus	Rbm3, Ndufa5	Acadl, Cox7b
Olfactory bulb	Rbm3	Acadl, Timm10, Ndufa2

In all analysed tissue samples, cold-inducible RNA-binding protein 3 (Rbm3) was significantly enriched in cKO in comparison to CTR animals. It is reported to be in involved in neurodegeneration, cell migration and neurogenesis (Jackson et al., 2015; Yan et al., 2019; Zhu et al., 2016; Zhu et al., 2019). Moreover, long-chain acyl-CoA dehydrogenase (Acdal), a mitochondrial protein and a member of the acyl-CoA dehydrogenase family, was significantly depleted in all analysed cKO tissues except cerebral cortex. Its main function is the β-oxidation of fatty acids within the mitochondria.

Furthermore, in cerebellum samples, cold-inducible RNA-binding protein (Cirbp) was enriched in cKO in comparison to CTR animals. In addition to that, especially in cerebellum samples, proteins related to metabolism were significantly enriched and depleted. Those were Vdac2 and Vdac3 (voltage dependent anion-selective channel 2 and 3), Cox7c (cytochrome c oxidase subunit 7C), Ndufa5 (NADH dehydrogenase 1 alpha subcomplex subunit 5), Timm10 (translocase of inner mitochondrial membrane 10), Mpc2 (mitochondrial pyruvate carrier 2) and Atp2a (sarcoplasmic/endoplasmic reticulum calcium ATPase 1).

In samples of the cerebral cortex, additionally, Darpp32 (dopamine- and cAMP-regulated neuronal phosphoprotein, also known as protein phosphatase 1 regulatory subunit

1B (PPP1R1B)), was significantly enriched in cKO in comparison to CTR animals. It is a specific marker for mature striatal neurons (Bibb et al., 2000; Jin et al., 2005).

To conclude, the proteomics data might contribute to explanations for the mechanisms behind the observed abnormalities in cKO compared to CTR animals.

4.2.5 Transcriptome analysis of sorted neurons and astrocytes

To further complement the proteomics analysis of bulk protein samples of different brain tissues and to have a distinct look on neurons and astrocytes, as they are both produced by Nestin amongst others, cell sorting from cerebral cortex tissue was performed. Subsequently, the transcriptome of sorted cortical neurons and astrocytes of cKO and CTR animals was analysed by RNA sequencing.

After removing and dissociating cerebral cortex tissue from cKO and CTR animals, different cell fractions were stained with surface marker specific antibodies and sorted via FACS. Neurons were detected using an anti-CD90.2-APC (Allophycocyanin) antibody, astrocytes were sorted using an anti-Acsa-2-(astrocyte cell surface antigen-2)-PE (Phycoerythrin) antibody and microglia were labelled using an anti-CD11b-PE-Cy7 antibody (Figure 24). Dead and live cells were distinguished using a fluorescent viability dye.

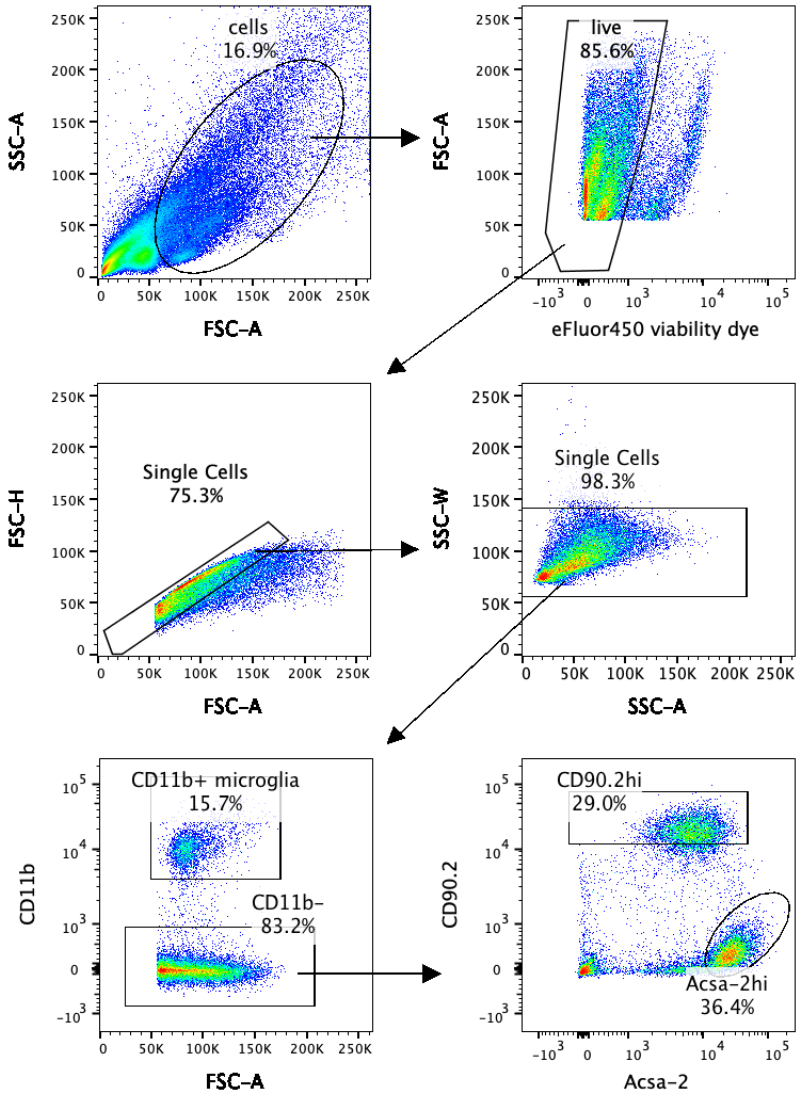

Figure 24: FACS gating strategy using specific antibodies for cell surface markers

Different cell types were separated using FACS. Microglia were sorted using an anti-CD11b-PE-Cy7 antibody, neurons using an anti-CD90.2-APC antibody, while astrocytes were detected using an anti-Acsa-2-PE antibody. Among single live cells, neurons were sorted as CD11b neg, CD90.2hi pos cells, astrocytes were sorted as CD11b neg, Acsa-2hi pos cells, and microglia as CD11b pos cells.

The gating was confirmed, on the one hand, by additional staining of the cell populations with antibodies against CD11b for microglia, NeuN (neuronal nuclei) for neurons and Gfap for astrocytes (Figure 25) and, on the other hand, by qRT-PCR to determine mRNA expression levels of typical markers for neurons as well as astrocytes. (Figure 26). Visualisation of *Gfap* and *NeuN* (*Rbfox3* (RNA binding protein fox-1 homolog 3)) transcript using IGV software additionally confirmed the purity of the obtained cell populations (Appendix - Figure 51).

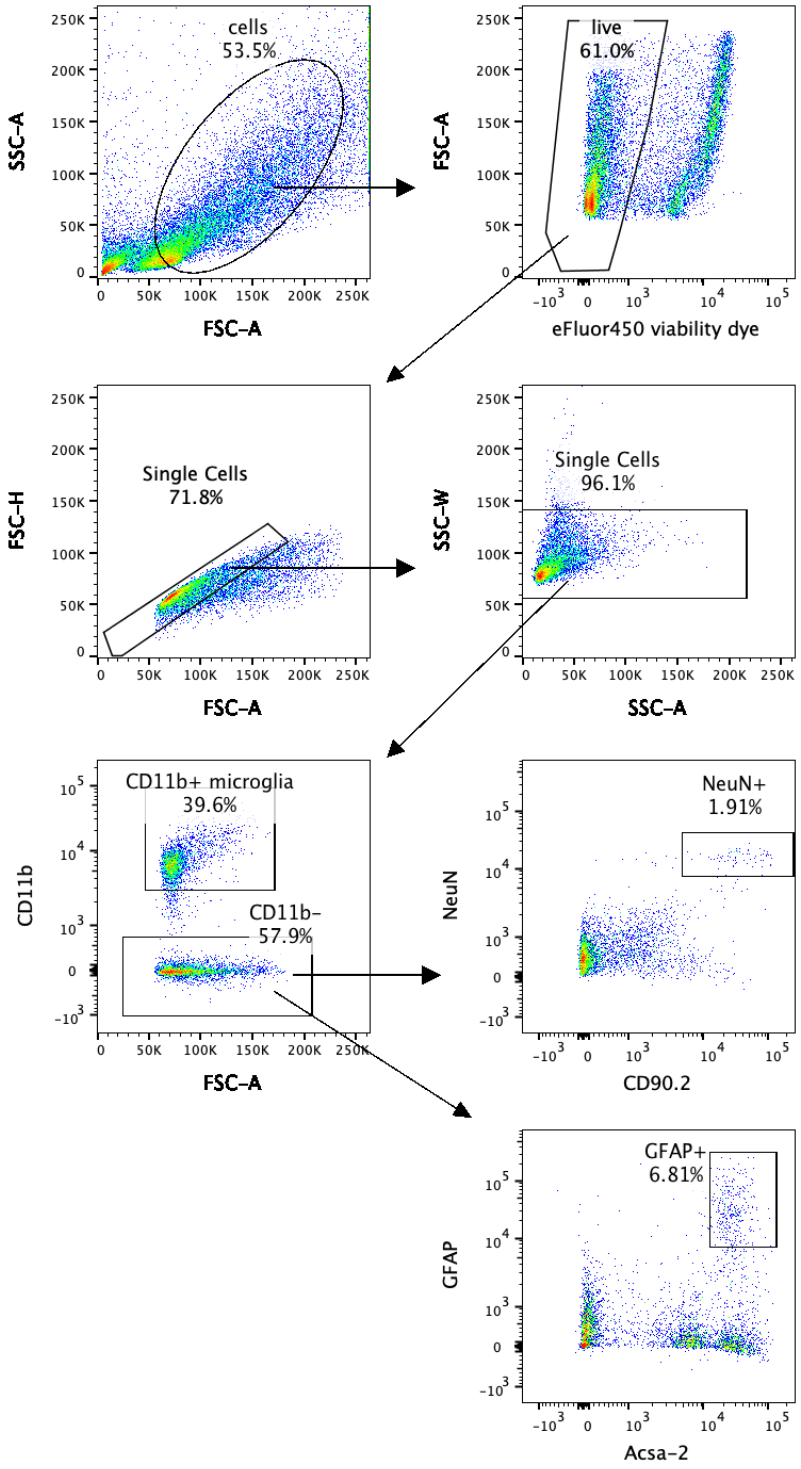

Figure 25: Confirmation of FACS gating strategy

The FACS gating strategy using specific antibodies for cell surface markers was confirmed using an anti-NeuN-antibody to detect neurons and an anti-Gfap-antibody to detect astrocytes. CD90.2hi cells (neurons) were detected as NeuN pos, Acsa-2 neg, while Acsa-2hi cells (astrocytes) were detected as Gfap pos.

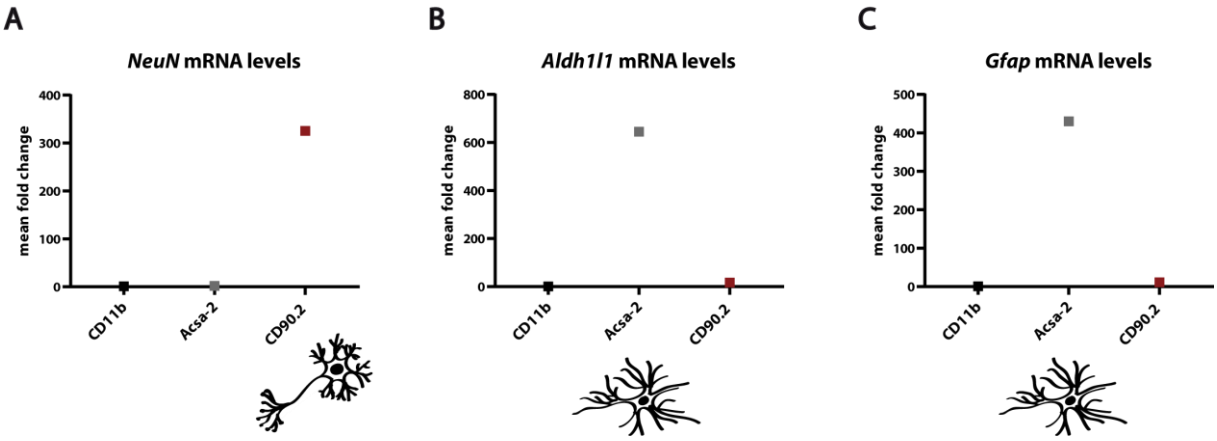

Figure 26: qRT-PCR analysis of different cell fractions

Relative mRNA expression levels of specific neuron and astrocyte markers were determined to confirm the gating strategy and the purity of the sorted populations. qRT-PCR analysis of *NeuN* **(A)** as well as *Aldh1l1* **(B)** and *Gfap* **(C)** transcript levels in the sorted fractions were quantified. mRNA expression levels were normalized to expression levels of the CD11b-PE-Cy7 positive fraction.

qRT-PCR analysis of neuron and astrocyte markers revealed that the obtained sorted fractions showed a high purity and no contamination with other cell types. mRNA expression levels were normalized to expression levels of the CD11b fraction. In the CD90.2-APC positive fraction, which should contain only neurons, a high level of *NeuN* transcript was detected, whereas the other fractions did not show any *NeuN* mRNA expression (Figure 26 - A). Similar results were obtained for common astrocyte markers *Gfap* (glial fibrillary acidic protein) and *Aldh1l1* (aldehyde dehydrogenase-1 family member L1). The CD90.2-APC positive fraction, which should contain only neurons, and the CD11b-PE-Cy7 fraction, which should only contain microglia, did not display any *Gfap* and *Aldh1l1* expression, whereas in the Acsa-2-PE positive fraction, which should contain only astrocytes, high levels of *Gfap* and *Aldh1l1* mRNA expression were detected (Figure 26 - B + C). To conclude, the gating strategy for the different cell types and the purity of the sorted fractions were confirmed.

Four replicates of each genotype were used for cell sorting. The obtained number of events in each FACS experiment, which correspond to the respective number of sorted cells, are listed in Table 7. For the neuron fractions, cell numbers in a range from 650 to 16,630 were obtained, whereas for the astrocyte fraction cell numbers ranged from 75,863 to 252,916. Microglia fractions mostly reached the set maximum of 150,000 cells.

Table 7: Cell numbers obtained by FACS for different cell types

The cell numbers varied between the different fractions. Neuron numbers ranged from 650 to 16,630, astrocyte numbers from 75,863 to 252,916. Microglia fractions mostly reached the set maximum of 150,000 cells.

		Neurons (Cd90.2-APC pos)	**Astrocytes** (Acsa-2-PE pos)	**Microglia** (Cd11b-PE-Cy7 pos)
CTR Cortex	Replicate 1	650	75,863	105,000
	Replicate 2	2,524	112,848	150,000
	Replicate 3	16,630	252,916	150,000
	Replicate 4	16,241	160,488	134,429
cKO Cortex	Replicate 1	3,023	146,572	150,000
	Replicate 2	2,144	179,519	150,000
	Replicate 3	11,438	135,382	110,844
	Replicate 4	918	175,206	150,000

After cell sorting, total RNA was isolated from the different fractions of each replicate. RNA from neurons and astrocytes were analysed by RNA sequencing to reveal changes on transcriptome level after depletion of functional Tet3.

Different comparisons were visualised using volcano plots. Significantly upregulated transcripts are located on the right side and significantly downregulated transcripts on the left side of the graphs.

Firstly, the comparisons CTR astrocytes versus (vs.) CTR neurons (Figure 27 - A) and cKO astrocytes vs. cKO neurons (Figure 28 - A) were analysed. The volcano plots showed many differences between the two cell populations in CTR and cKO animals. Those findings were in line with the expectations, as astrocytes and neurons as different cell types were expected to display different gene expression patterns. A high number of genes were differentially expressed in CTR astrocytes compared to CTR neurons as well as in cKO astrocytes compared to cKO neurons. Comparison CTR astrocytes vs. CTR neurons revealed that more transcripts were upregulated (3,182 genes) than downregulated (1,633 genes) in CTR astrocytes (Figure 27 - A). Similarly, in the comparison cKO astrocytes vs. cKO neurons, more transcripts were upregulated (4,242 genes) than downregulated (1,700 genes) in cKO astrocytes (Figure 28 - A).

To analyse in which processes upregulated and downregulated transcripts were involved, gene ontology (GO) analysis was performed using the GOrilla tool. The top 15 GO processes for significantly up- and downregulated genes in CTR astrocytes in comparison to CTR neurons (Figure 27 - B) as well as in cKO astrocytes in comparison to cKO neurons were visualised in bar graphs (Figure 28 - B).

GO analysis revealed similar processes for significantly up- and downregulated genes in both comparisons. It demonstrated that a statistically significant percentage of the genes that were upregulated in CTR and cKO astrocytes in comparison to CTR and cKO neurons were associated with metabolic processes and that a statistically significant percentage of the genes that were downregulated in CTR and cKO astrocytes in comparison to CTR and cKO neurons were associated with cell and synaptic signalling as well as transport mechanisms in cells (Figure 27 - B, Figure 28 - B).

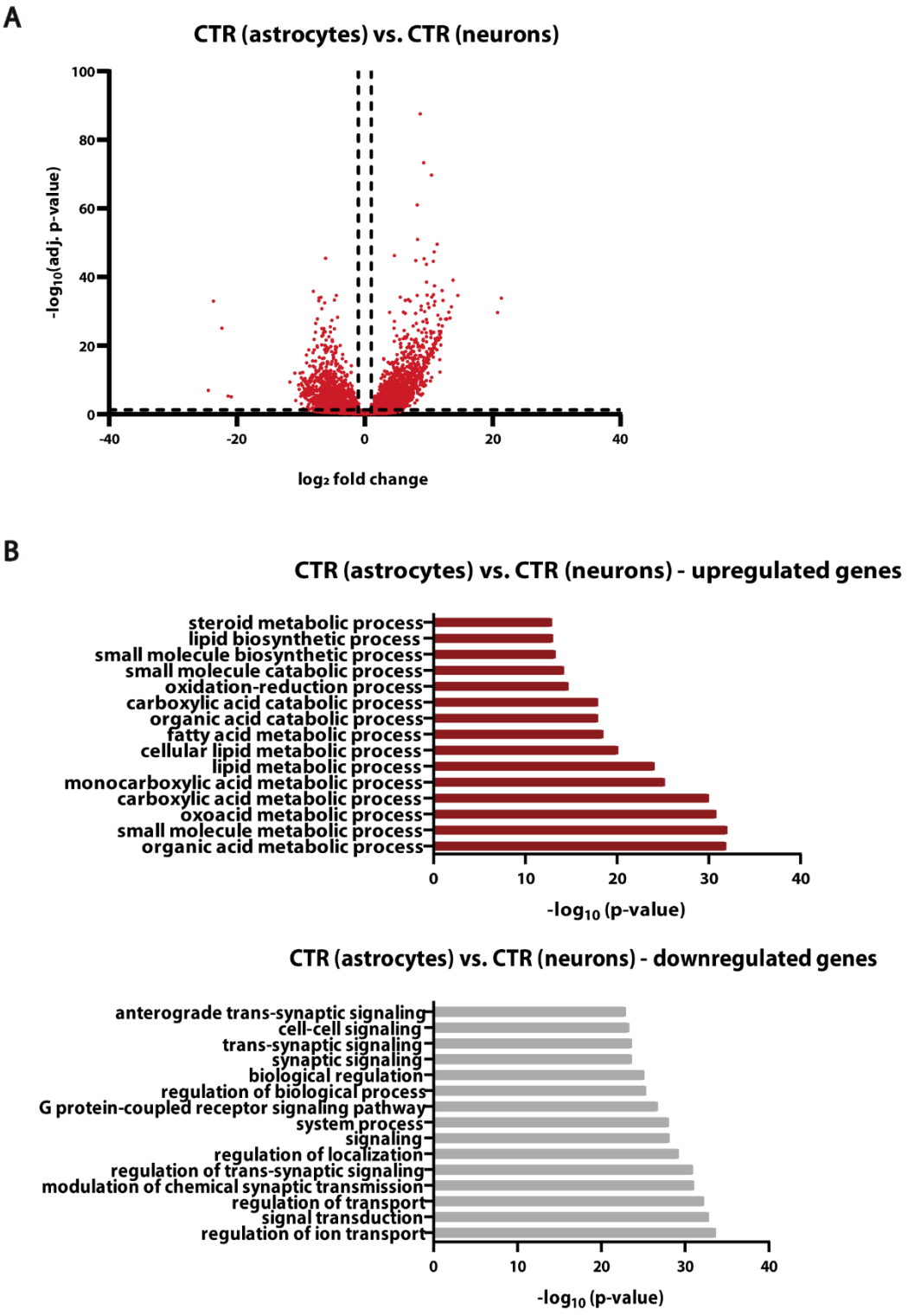

Figure 27: Transcriptome analysis - CTR (astrocytes) vs. CTR (neurons)

(A) Transcripts were plotted according to their expression fold change between CTR (astrocytes) and CTR (neurons) (log_2 fold change) and adjusted p-value ($-log_{10}p_{adj}$). The threshold value for the expression fold change was set to log_2 fold change ≥ 1 and ≤ -1 (equivalent to a fold change of 2 and 0.5). The cut-off value for the significance level was set to $-log_{10}padj \geq 1.3$ (equivalent to $p_{adj} \leq 0.05$). **(B)** Gene Ontology (GO) terms were ranked according to the significance of their enrichment ($-log_{10}$(p-value)). The top 15 GO processes were visualised in a list of significantly up- or downregulated genes in CTR (astrocytes) in comparison to CTR (neurons).

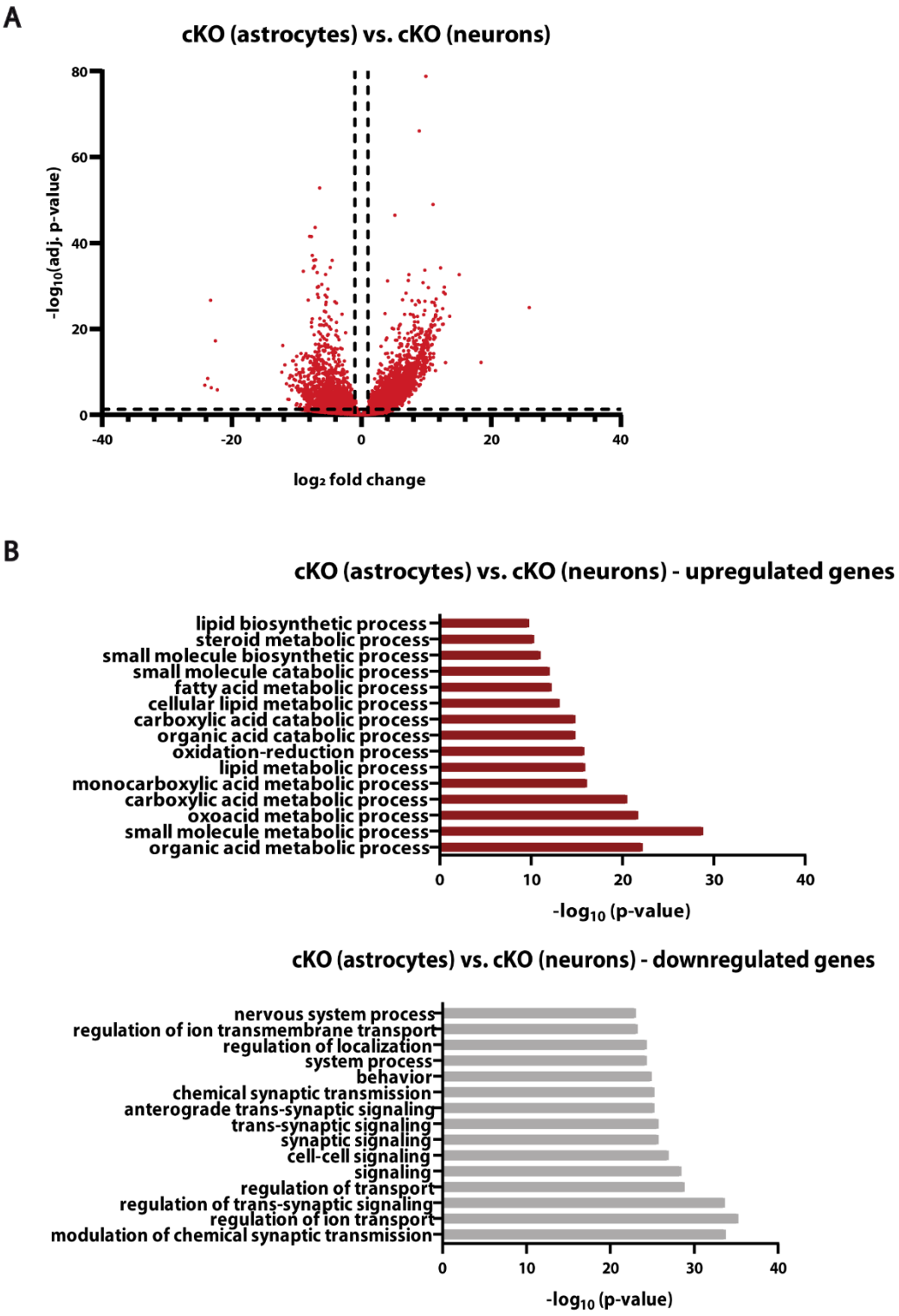

Figure 28: Transcriptome analysis - cKO (astrocytes) vs. cKO (neurons)

(A) Transcripts were plotted according to their expression fold change between cKO (astrocytes) and cKO (neurons) (log_2 fold change) and adjusted p-value ($-log_{10}p_{adj}$). The threshold value for the expression fold change was set to log_2 fold change ≥ 1 and ≤ -1 (equivalent to a fold change of 2 and 0.5). The cut-off value for the significance level was set to $-log_{10}padj \geq 1.3$ (equivalent to $p_{adj} \leq 0.05$). **(B)** Gene Ontology (GO) terms were ranked according to the significance of their enrichment ($- log_{10}$(p-value)). The top 15 GO processes were visualised in a list of significantly up- or downregulated genes in cKO (astrocytes) in comparison to cKO (neurons).

To conclude, transcriptome analyses and comparisons between cortical astrocytes and neurons of CTR and cKO animals revealed many differences between the two cell types, which meets the expectations, because, independently from their genotype, astrocytes and neurons are different cell types. Additionally, GO analysis displayed general differences between developmental processes, metabolism, signalling and function between these major cell types.

Secondly, the transcriptomic differences between cKO vs. CTR neurons or astrocytes, respectively, were analysed (Figure 29, Figure 30).

For the comparison cKO neurons vs. CTR neurons, the volcano plot showed many differences between the two populations (Figure 29 - A). Tet3 is highly present in neurons, which leads to the assumption that the differences are caused by depletion of Tet3 function. A high number of genes were differentially expressed in cKO neurons compared to CTR neurons. In this case, more transcripts were downregulated (1,267 genes) than upregulated (366 genes) in cKO neurons when compared to CTR neurons, suggesting that a functional Tet3 KO in neurons influences neuronal gene expression patterns and, preferentially, leads to a suppression of gene expression.

GO analysis showed that a statistically significant percentage of the genes that were upregulated in cKO neurons in comparison to CTR neurons were associated with chromosome and chromatin organization and in general cell cycle and that a statistically significant percentage of the genes that were downregulated in cKO neurons were associated with immune response and connected signalling pathways (Figure 29 - B).

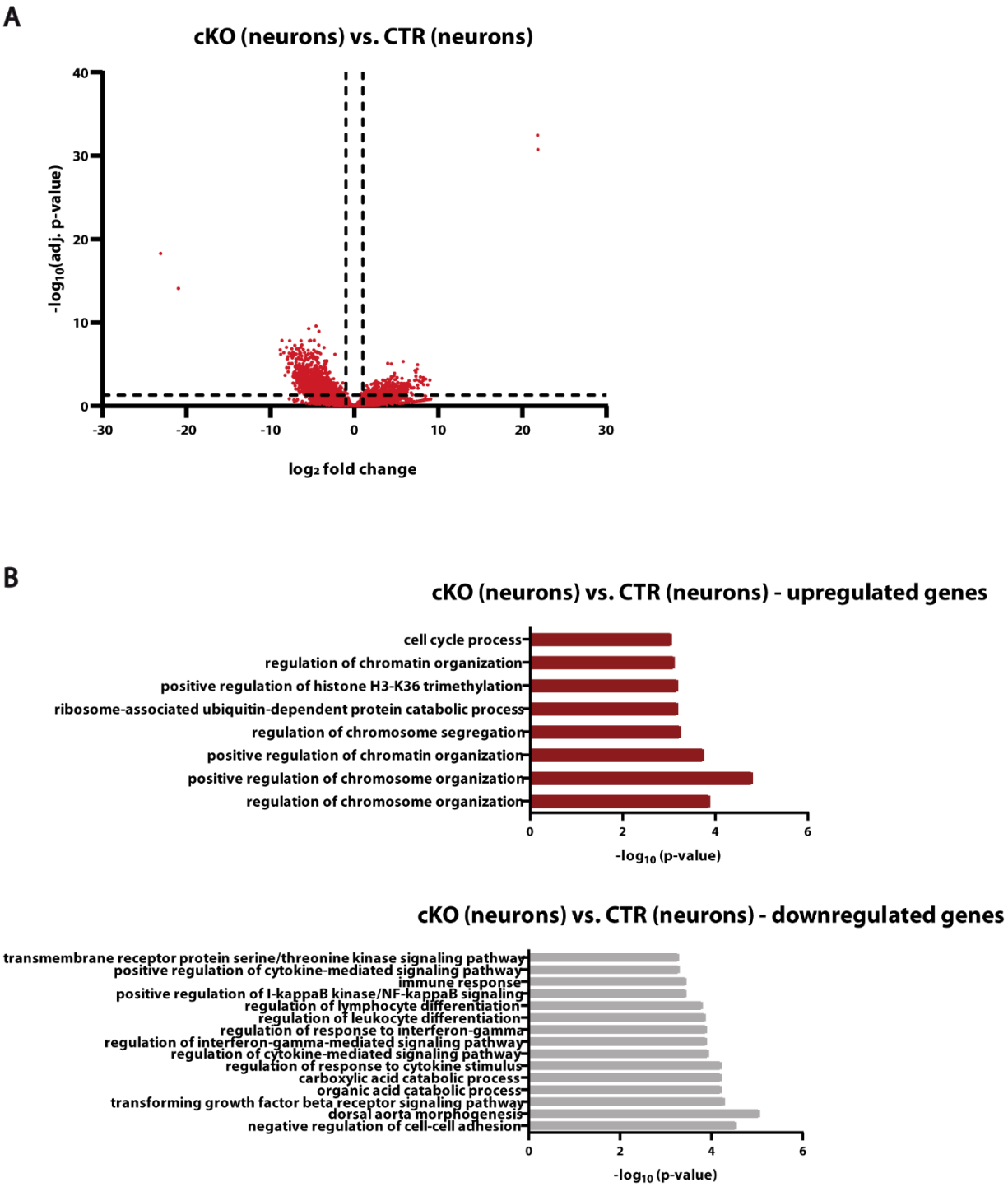

Figure 29: Transcriptome analysis - cKO (neurons) vs. CTR (neurons)

(A) Transcripts were plotted according to their expression fold change between cKO (neurons) and CTR (neurons) (log_2 fold change) and adjusted p-value ($-log_{10}p_{adj}$). The threshold value for the expression fold change was set to log_2 fold change ≥ 1 and ≤ -1 (equivalent to a fold change of 2 and 0.5). The cut-off value for the significance level was set to $-log_{10}padj \geq 1.3$ (equivalent to $p_{adj} \leq 0.05$). **(B)** Gene Ontology (GO) terms were ranked according to the significance of their enrichment ($- log_{10}$(p-value)). The top 15 GO processes were visualised in a list of significantly up- or downregulated genes in cKO (neurons) in comparison to CTR (neurons).

For the comparison cKO astrocytes vs. CTR astrocytes, the volcano plot displayed no differences between the two populations (Figure 30). Since Tet3 was shown not to be expressed and of relevance in astrocytes (Antunes et al., 2020), the partial genomic and resulting functional deletion of Tet3 did not show any effect on the transcriptome of astrocytes. A GO analysis was not possible here. Further analysis of the namely marked transcripts, *St18* (suppression of tumorigenicity 18), *Fam78a* (family with sequence similarity 78 member A), *Fam220a* (family with sequence similarity 220 member A) using IGV software was not conclusive and indicated them being deviants probably due to data quality issues.

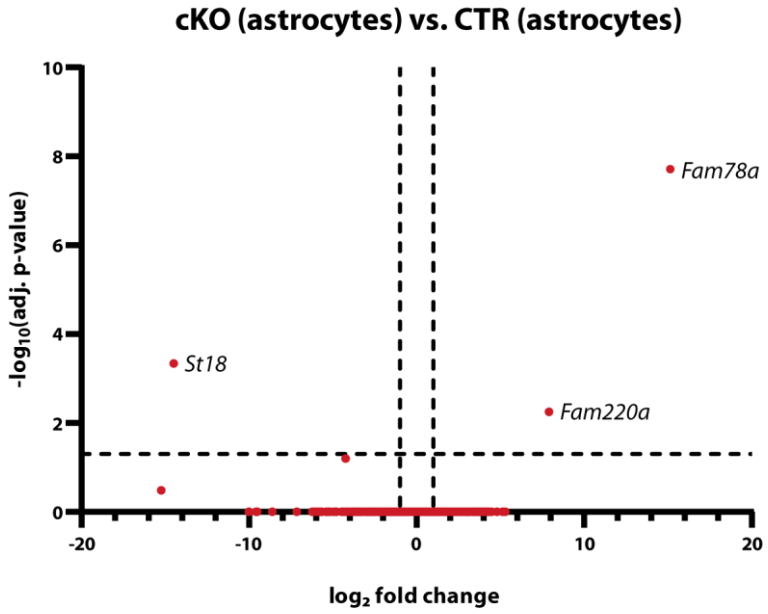

Figure 30: Transcriptome analysis - cKO (astrocytes) vs. CTR (astrocytes)

Transcripts were plotted according to their expression fold change between cKO (astrocytes) and CTR (astrocytes) (log_2 fold change) and adjusted p-value ($-log_{10}p_{adj}$). The threshold value for the expression fold change was set to log_2 fold change ≥ 1 and ≤ -1 (equivalent to a fold change of 2 and 0.5). The cut-off value for the significance level was set to $-log_{10}padj \geq 1.3$ (equivalent to $p_{adj} \leq 0.05$).

To conclude, transcriptome analyses of cortical neurons in cKO and CTR revealed many differences between the two populations, meeting the expectations. The differences were based on the different genotype of the two populations and consequently on the functional Tet3 KO. Cortical cKO and CTR astrocytes did not show changes on transcriptome level suggesting Tet3 not to play a major role in astrocytes.

4.2.6 Analysis of adult neurogenesis

Since in this study a Nestin Cre driver line was used to functionally knock out Tet3, impairment all over the brain and, specifically, effects connected to neurogenesis may be expected. Furthermore, the observed abnormal phenotype in cKO animals regarding brain and body size supported the assumption that the generation of neurons, the main cell type in the brain, may be altered after deletion of catalytically active Tet3. For that reason, neuroblast migration in the brain was analysed, among others.

Neuroblasts migrate in one direction and in organized chains from the subventricular zone (SVZ) along the rostral migratory stream (RMS) to the olfactory bulb, as described in chapter 1.2.5. The typical marker for migrating neuroblasts during CNS development as well as adulthood is the microtubule binding protein Doublecortin (Dcx) (Gleeson et al., 1999). The typical marker for proliferating cells is Ki67. It is a nuclear protein, which is expressed during the whole cell cycle except the resting phase (Kee et al., 2002).

Using a DAPI + Dcx co-staining (Figure 31 - A, Figure 32 - B), migrating neuroblasts (Dcx positive) were visualised in brain sagittal slices of CTR and cKO animals. Although the RMS was detected in cKO animals indicating that neurogenesis and neuroblast migration in principle take place, the immunohistochemical analysis revealed a disorganization of the neuroblast chains in the RMS in cKO compared to CTR animals (Figure 31 - A). In addition, migrating neuroblasts were detected in the dorsal SVZ of cKO animals, displaying diffuse neuroblast migration in brain regions, into which neuroblasts normally do not migrate (Figure 32 - B).

To investigate cell proliferation, a DAPI + Ki67 co-staining (Figure 31 - C, Figure 32 - A) was performed. Proliferating cells (Ki67 positive) leaving the RMS were detected in cKO in comparison to CTR animals, which supports the observed diffuse neuroblast migration. Furthermore, proliferating cells were detected in the dorsal SVZ of cKO animals, further indicating abnormalities concerning adult neurogenesis.

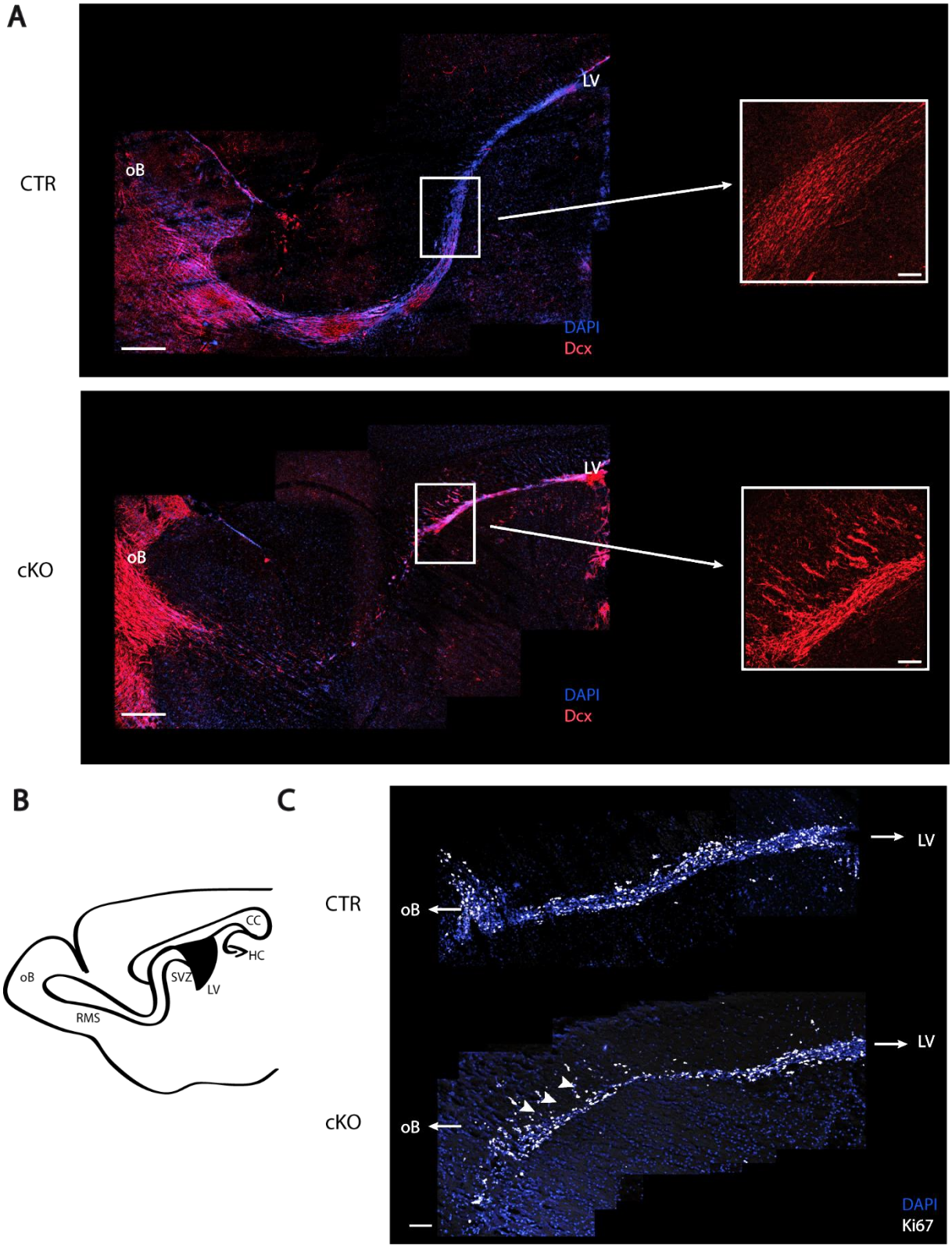

Figure 31: Analysis of SVZ-RMS-oB system

(A + C) Immunohistochemistry of vibratome sagittal brain sections of CTR and cKO mice to visualise neuroblast migration and cell proliferation in the SVZ-RMS-oB system **(B)**: DAPI (blue), Dcx (red), Ki67 (white). Images were taken using a confocal microscope and stitched using ImageJ Software. Scale bars 50 µm and 1 mm.

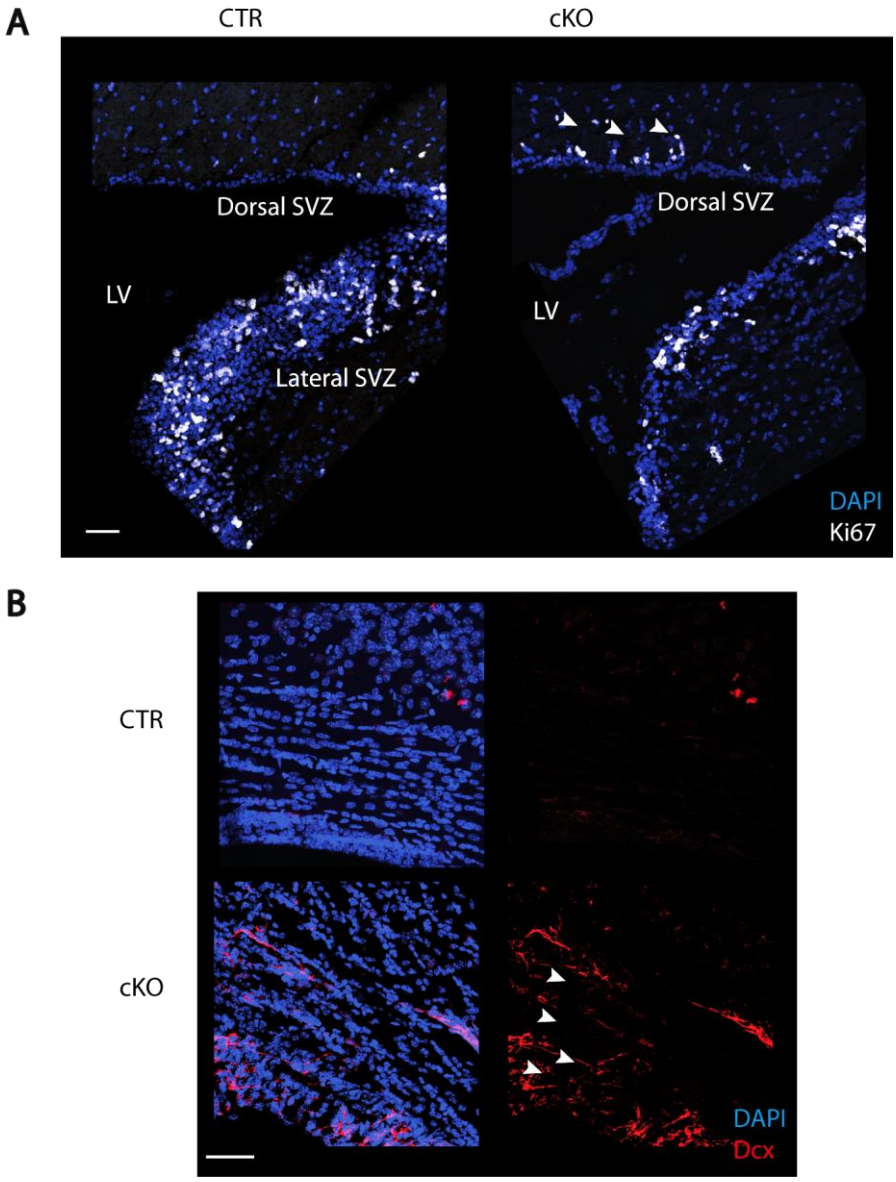

Figure 32: Analysis of the dorsal SVZ

(A + B) Immunohistochemistry of vibratome sagittal brain sections of CTR and cKO mice to visualise proliferating cells in the dorsal SVZ: DAPI (blue), Ki67 (white), Dcx (red). Images were taken using a confocal microscope and stitched using ImageJ Software. Scale bar 50 µm.

To conclude, an abnormal phenotype in neuroblast migration of adult neurogenesis resulting from Tet3 depletion was detected by immunohistochemical experiments in the brain of Tet3 cKO mice, which needs to be further investigated.

4.2.7 *In vitro* analysis of neuroblast migration from SVZ to olfactory bulb

To visualise cell migration *in vitro* and to further analyse adult neurogenesis and neuroblast migration from the SVZ to the olfactory bulb, SVZ explants were prepared (Figure 33).

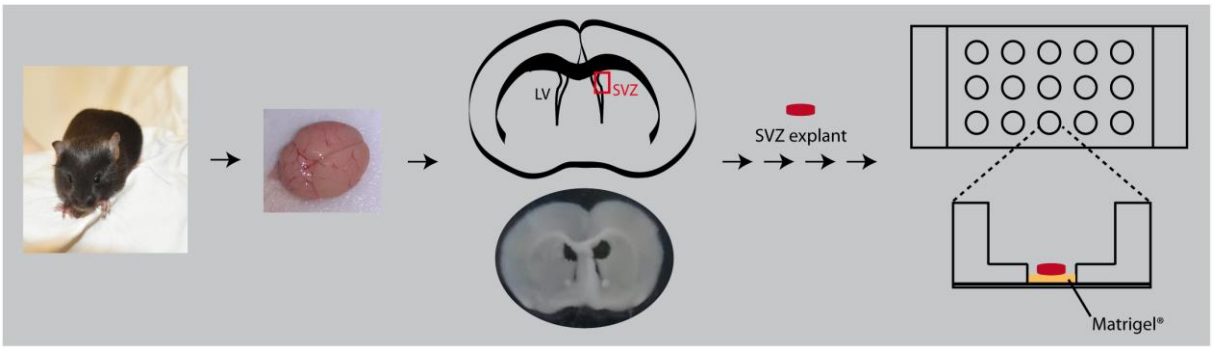

Figure 33: Preparation of SVZ explants

After removing the brain, coronal sections (350 µm) were prepared using a vibratome. From those coronal slices, the SVZ was punched out. After a few processing steps, the tissue pieces were transferred into a µ-Slide Angiogenesis ibiTreat (one explant per well) and embedded in Matrigel®. The explants were cultured for four days at 5 % CO_2 and 37 °C.

To establish and validate the protocol, experiments using BL/6J WT animals were performed (Figure 34). The bright field images (Figure 34 - A) taken at d3 of the explant culture clearly show migrating cells as well as cell chains, identified as neuroblasts by immunohistochemistry (IHC), starting in the SVZ explant of WT mouse. The IHC (Figure 34 - B), performed after fixing the cells at d5 of the culture, confirmed the presence of the different cell types existing in the SVZ and the lateral ventricle of WT mice using specific markers (Figure 34 - C). Dcx positive neuroblasts started to migrate in the SVZ explant and formed chains finally migrating in one direction. Gfap positive astrocytes were also detected in the explant culture confirming their presence in the SVZ. Ki67 positive cells were rarely detected in the SVZ explants, meaning that only little cell proliferation takes place. As Figure 34 - C shows more Ki67 positive cells are normally present in the SVZ *in vivo*. Since the explant conditions imitate but do not completely reach natural conditions, neuroblasts stop proliferating during migration in SVZ explants, whereat in the core and at the border of the explant tissue, more proliferating cells can be detected.

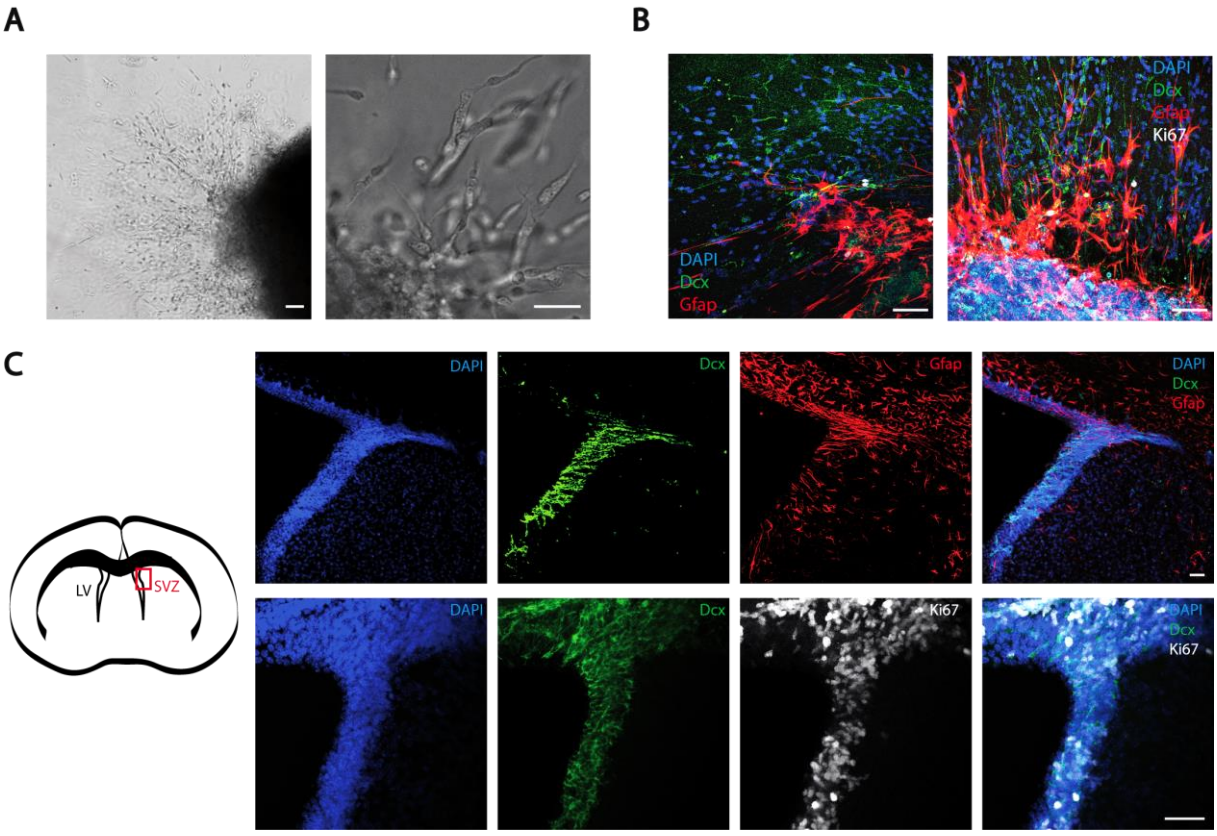

Figure 34: Validation of SVZ explants

(A) Bright field images of SVZ explants from WT animals, taken with EVOS® FL cell imaging system, show cell migration starting in SVZ explants. Scale bar 50 µm and 100 µm. **(B)** Immunohistochemistry of SVZ explants from WT animals to visualise different cell types starting in SVZ explant: DAPI (blue), Dcx (green), Gfap (red), Ki67 (white). Images were taken using a confocal microscope. Scale bar 50 µm. **(C)** Immunohistochemistry of mouse coronal brain slices from 4-week-old WT animals to visualise the different cell types in the SVZ *in vivo*: DAPI (blue), Dcx (green), Gfap (red), Ki67 (white). The images show a DAPI-Dcx-Gfap-staining (upper row) and a DAPI-Dcx-Ki67-staining (bottom row) of the SVZ of WT mice, respectively. Images were taken using a confocal microscope. Scale bar 50 µm.

From theses test and validation experiments, it was concluded that the established protocol was successfully implemented. In the SVZ explants, all cell types were detected as they were expected from *in vivo* experiments and literature, which confirmed the protocol. For that reason, it was used for further experiments with tissue from Tet3 CTR and cKO animals.

SVZ explants of CTR and cKO confirmed the observations of immunohistochemical experiments on brain sagittal sections. Confocal images (Figure 35 - A) show DAPI stained cells of explants of CTR and cKO. For the CTR, neuroblast migration started only from one side of the explant, which is expected, as in the mouse brain neuroblast migration starts in the SVZ and

leads into one direction to the olfactory bulb. For the cKO, cells were detected, which started to migrate from several points of the explant. Neuroblast migration was existent, but seemed to be more diffuse, confirming the observations from the IHC in mouse brain in chapter 4.2.9. A DAPI + Dcx co-staining (Figure 35 - B) revealed that, in cKO SVZ explants, neuroblasts migrated in a more chaotic way compared to CTR and into different direction. Furthermore, the typical chains of neuroblasts were not detected in cKO SVZ explants, whereas they were found in CTR SVZ explants.

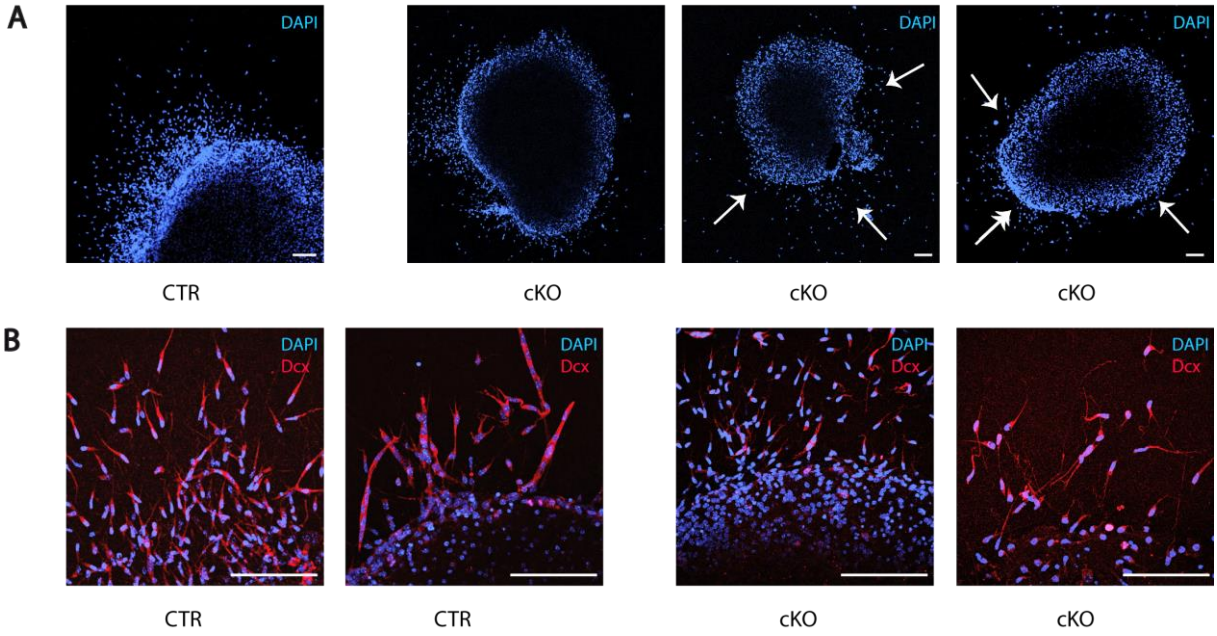

Figure 35: SVZ explants of CTR and cKO animals

(A) Immunohistochemistry of SVZ explants from CTR and cKO animals: DAPI (blue). Images were taken using a confocal microscope. **(B)** Immunohistochemistry of SVZ explants from CTR and cKO animals: DAPI (blue), Dcx (red). Images were taken using a confocal microscope. Scale bar 100 µm.

To conclude, altered neuroblast migration was detected in cKO SVZ explants. Neuroblasts migrated, but in a more chaotic and disorganized way in comparison to CTR, indicating an effect of Tet3 depletion on neuroblast migration starting in the SVZ and generally on adult neurogenesis and confirming *in vivo* observations.

4.3 Analysis of Tet3 isoforms

Mammalian Tet3 exists in various isoforms, generated by alternative splicing and alternative promotor usage, and differ at their N-terminal sequence. Not much has been known about

specific functions and roles of the different Tet3 isoforms. For that reason, isoform-specific Tet3 KO mouse models as well as TET3 isoform overexpressing human iPS cell lines were generated in this study to examine Tet3 isoforms *in vivo* and *in vitro*.

4.3.1 Tet3 L KO and Tet3 S KO mouse models

To investigate different functions of Tet3 isoforms *in vivo*, mouse lines with a specific KO of respective Tet3 isoforms were generated using CRISPR-Cas9 technology. In the Tet3 L KO mouse line, long Tet3 isoforms were deleted. In the Tet3 S KO mouse line, the short Tet3 isoform was deleted.

4.3.1.1 Generation of Tet3 L KO and Tet3 S KO mouse lines

To generate a Tet3 L KO mouse line, the exon encoding the CXXC domain, which is specific for the Tet3 L isoforms, and the corresponding putative promotor were deleted from the mouse genome (Figure 36 - A). To generate a Tet3 S KO mouse line, the putative alternative promotor located upstream of exon 1, which is unique for the Tet3 S isoform, and exon 1 itself were deleted (Figure 37 - A). For the generation of the Tet3 L KO mouse line, two sgRNAs, one upstream of the promotor and one downstream of the CXXC domain, were designed for the KO approach, while for the generation of the Tet3 S KO mouse line, four sgRNAs, two upstream and two downstream of the alternative promotor and the unique exon of the Tet3 S isoform, were designed. The sgRNAs were assembled into an RNP complex with recombinant SpCas9 protein and subsequently injected into one-cell embryos of pseudo-pregnant female mice.

After screening of approximately 20 animals, in case of the Tet3 L KO mouse line generation, one mouse with a successful deletion of the CXXC exon was identified, which was used to expand the genotype and bred to homozygosity. In case of the Tet3 S KO mouse line generation, approximately 25 animals were screened. Four mice with a successful deletion of the alternative promotor and exon 1 were identified. All four founder lines, showing a different size of genomic deletion, were used for genotype expansion and bred to homozygosity. The designed genotyping assay uses three primers (one forward (fow) and two reverse (rev) primers) (Figure 36 - B, Figure 37 - B). Reverse 1 primer is located in the deleted region, whereas the reverse 2 primer is located downstream of the deleted region. Primer pair 1 (forward and reverse 1

primers) amplifies the WT band (Tet3 L: 306 bp, Tet3 S: 340 bp) in case of no deletion. Primer pair 2 (forward and reverse 2 primers) amplifies the KO band (Tet3 L: 470 bp, Tet3 S: 498 bp / 474 bp / 315 bp) in case of deletion. Sanger sequencing of the obtained PCR products confirmed the deletion and displayed exact information about the edited genomic sequence. In the Tet3 L KO mouse line, a genomic deletion of 2,375 bp was detected (Figure 36 - C). In Tet3 S KO founder lines 1 and 3, a genomic deletion of 203 bp was identified, whereas, in the Tet3 S KO founder line 2, the genomic deletion was 228 bp and, in the Tet3 S KO founder line 4, 387 bp of length (Figure 37 - C).

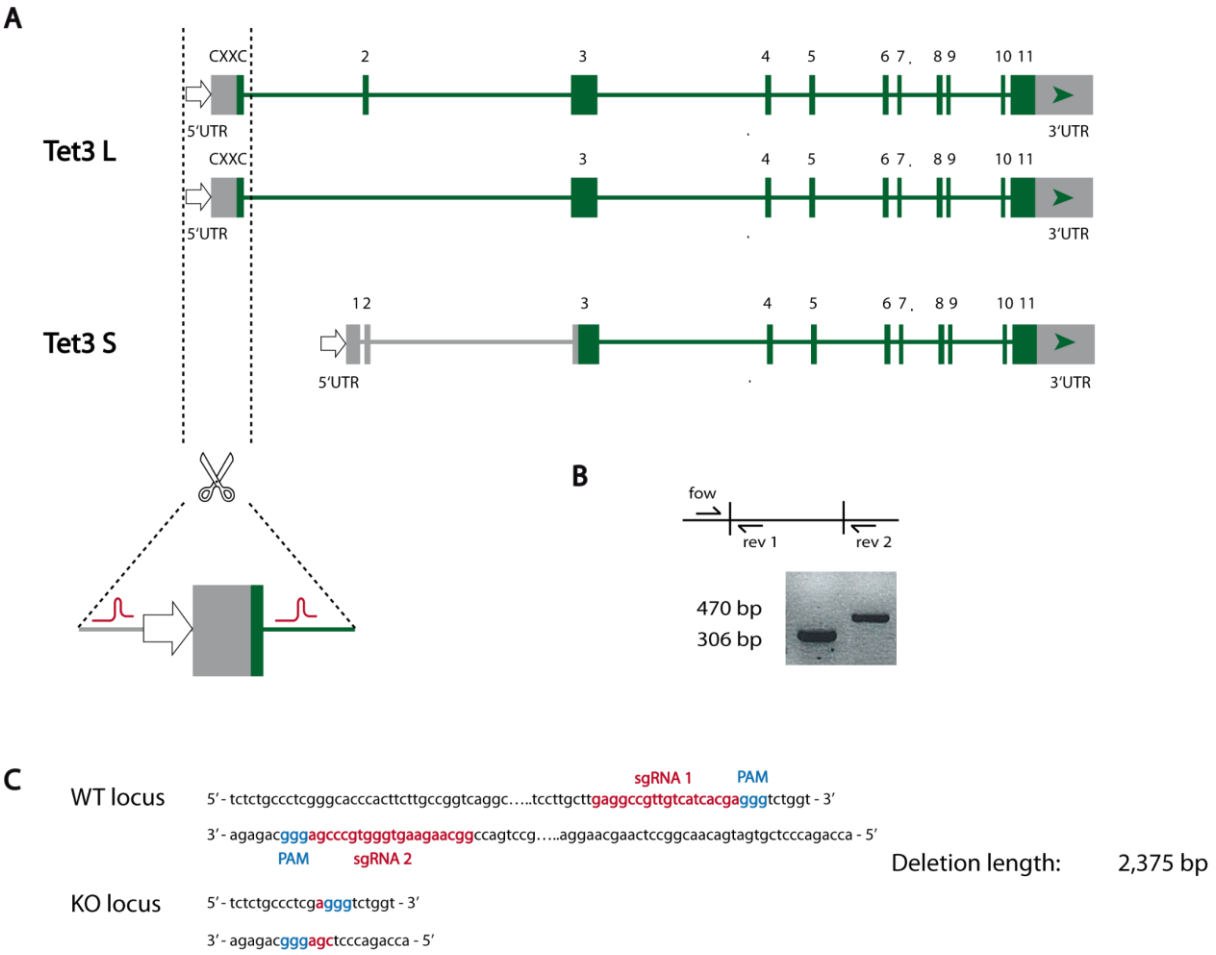

Figure 36: Generation of Tet3 L KO mouse line

(A) For the generation of the Tet3 L KO mouse line, the Tet3 L specific promotor and the exon encoding the CXXC domain were deleted using CRISPR-Cas9 technology. Two sgRNAs (marked in red), one upstream of the promotor and one downstream of the CXXC domain, were designed. **(B)** The scheme of the genotyping assay shows the position of the primer binding sites on the genomic locus in relation to the deleted region marked by two vertical lines. PCR amplification of WT alleles results in a band at 306 bp, whereas PCR amplification of KO alleles results in a band at 470 bp. **(C)** A deletion of 2,375 bp was detected by Sanger sequencing in the edited genomic sequence. The target sequences of used sgRNAs are marked in red, the corresponding PAM sequence is marked in blue.

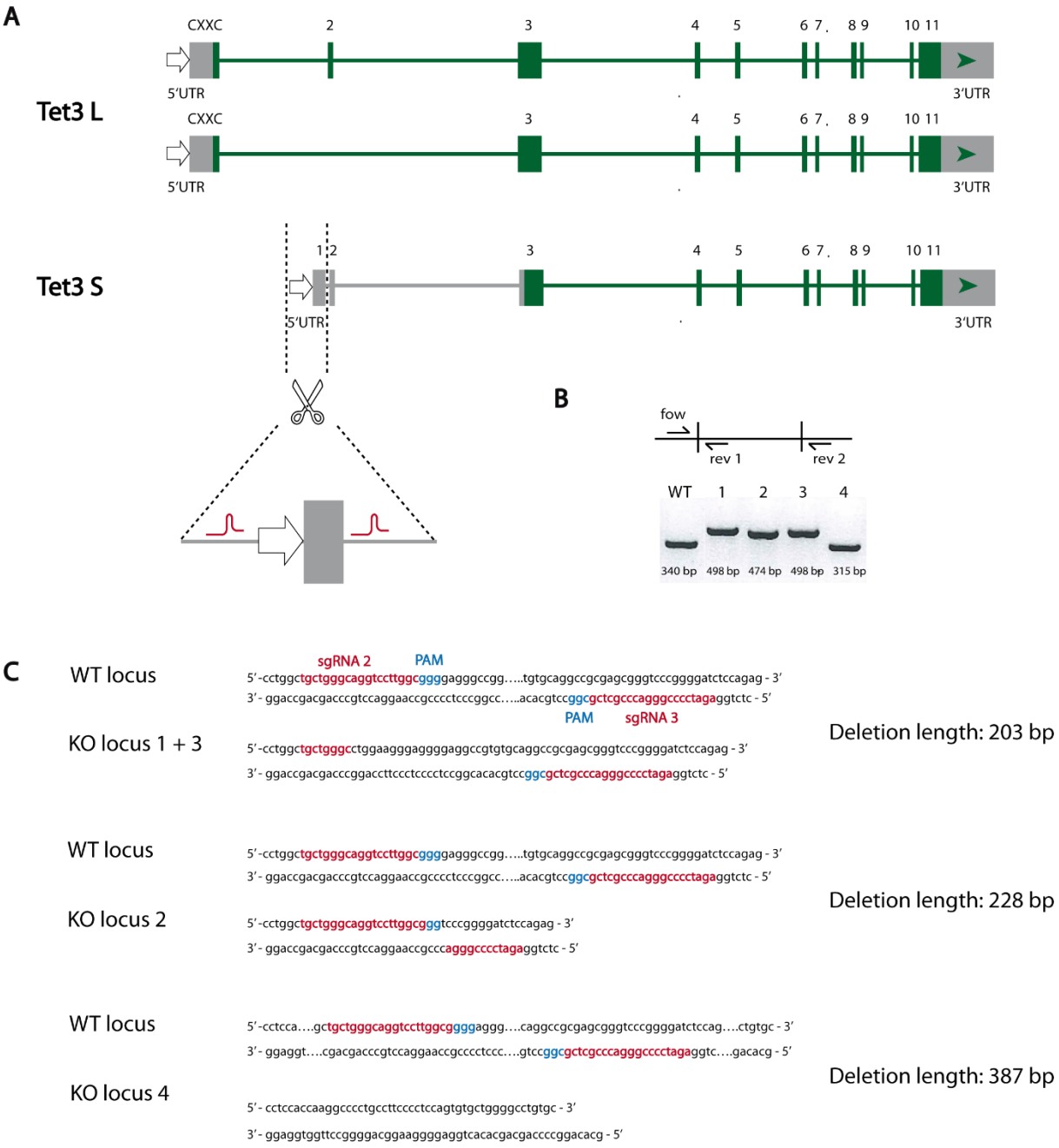

Figure 37: Generation of Tet3 S KO mouse line

(A) For the generation of the Tet3 S KO mouse line, the alternative promotor and exon 1, which are unique for Tet3 S, were deleted using CRISPR-Cas9 technology. Four sgRNAs (marked in red), two upstream and two downstream of the alternative promotor and exon 1, were designed. Four founder lines with a successful deletion, but different deletion sizes, were identified. **(B)** The scheme of the genotyping assay shows the position of the primer binding sites on the genomic locus in relation to the deleted region marked by two vertical lines. PCR amplification of WT alleles results in a band at 306 bp, whereas PCR amplification of KO alleles results in bands with different size for each founder line (498 bp, 474 bp, 315 bp). **(C)** Sanger sequencing displayed a deletion length of 203 bp in founder lines 1 and 3, of 228 bp in founder line 2 and of 387 bp in founder line 4. The target sequences of used sgRNAs are marked in red, the corresponding PAM sequence is marked in blue.

4.3.1.2 Off-target analysis in Tet3 L KO and Tet3 S KO mouse lines

As frequently reported, Cas9 endonuclease is able to cleave off-target DNA sequences in the genome, which can be a problem when using CRISPR-Cas9 technology (Zhang et al., 2015). Off-target effects are defined as mutations induced by the endonuclease at genomic sequences differing from the intended target sequence (Zhang et al., 2015). The extent, to which a sgRNA sequence shows off-target activity, depends on multiple factors such as enzyme concentration and the existing number of similar sequences in the target genome (Ran et al., 2013; Zhang et al., 2015). Therefore, the five most probable exonic off-target regions in the Tet3 L KO and Tet3 S KO mouse genome per used sgRNA were predicted using the CRISPOR website (Haeussler et al., 2016) and analysed to investigate potential mutations resulting from Cas9-mediated DSB generation and following incorrect repair. Off-target sequences and corresponding genomic loci are listed for both Tet3 L KO and Tet3 S KO mouse lines (Table 8). Regarding the Tet3 S KO mouse line, all four different founder lines were analysed.

Table 8: Off-target analysis - Tet3 L KO and Tet S KO mouse lines

sgRNA sequences and respective five off-target sequences in the mouse genome are listed together with genomic location and gene position. Mismatches of the off-target sequence in comparison to the sgRNA sequence are marked in red. A tick indicates no changes in the off-target sequence in the Tet3 L KO and Tet3 S KO mouse lines.

sgRNA sequence	off-target sequence	genomic location	position in gene	intact?
Tet3L 1	TGCAGGAAGTGGGTGACTGAAGG	chr19 : 58791266 - 58791288	intergenic:Gm17150-1700019N19Rik	✓
GGCAAGAAGTGGGTGCCCGAGGG	GGCAGGAAGTGAGTGACAGATGG	chr6 : 119882476 - 119882498	intergenic:3110021A11Rik-Gm15532	✓
	GGCAAGGAGTGGATGACAGACGG	chr4 : 131324764 - 131324786	intergenic:Gm25261-Gm831	✓
	GGCAAGAGGTGGATGCCCTGAGG	chr16 : 11447430 - 11447452	exon:Snx29	✓
	GGGAAGAAGTGGGTCACTGAAGG	chr1 : 119481920 - 119481942	exon:Ralb	✓
Tet3L 2	GAAGGTCATTGTCATCACGAAGG	chr2 : 75458147 - 75458169	intergenic:Gm13658-Gm13660	✓
TGAGGCCGTTGTCATCACGAGGG	TAAAGCCATTGTTATCACGATGG	chr6 : 117329205 - 117329227	intergenic:Rpl28-ps4-Gm9946	✓
	AGAGGCCCAAGTCATCACGAGGG	chr8 : 83647038 - 83647060	intergenic:Dnajb1-Gipc1	✓
	GGTGCCCGTTGACATCACGAAGG	chr11 : 106287537 - 106287559	exon:Tcam1	✓
	TCAGTCCATTGTCATCATGATGG	chr5 : 148925883 - 148925905	exon:Katnal1	✓
Tet3S 1	GAGCCTGCCCACCCCGCGCCAGG	chr12 : 91891275 - 91891297	intergenic:Rpl31-ps1-Gm21614	✓
GCGCCAGCCAATCCCGCGCCCGG	GAGCCTGCCCGTCCCGCGCCGGG	chr1 : 39367983 - 39368005	exon:Rpl31	✓
	GCACCACCCCGTCCCGCGCCCGG	chr7 : 66388124 - 66388146	intergenic:Gm10974-Lrrk1	✓
	CTGCCAGCCCATCCCGTGCCCGG	chr3 : 135697468 - 135697490	intergenic:Nfkb1-Gm9799	✓
	TGGCCAGCCCCTCCCGCGCCAGG	chr7 : 44604452 - 44604474	exon:Kcnc3	✓
Tet3S 2	TGTTGGACAGATCCTTGGCAGGG	chr10 : 21560751 - 21560773	intergenic:1700021A07Rik-1700020N01Rik	✓
TGCTGGGCAGGTCCTTGGCGGGG	AGCTGGGCAGGTCTTTGTCAAGG	chr2 : 142162861 - 142162883	intergenic:Fau-ps1-Macrod2	✓
	AGCTGGGTAGATCCTTGGTGGGG	chr1 : 182551043 - 182551065	intergenic:Capn2-Capn8	✓
	GGCTGGGCAGCCCCTTGGCTTGG	chr17 : 12210704 - 12210726	exon:Agpat4	✓
	TATGGGGCAGGTCCTTGGCCAGG	chr11 : 115801700 - 115801722	exon:Caskin2	✓
Tet3S 3	AGACCTCCGAGACCCGCTCTTGG	chr13 : 48091183 - 48091205	intron:A330033J07Rik	✓
AGATCCCCGGGACCCGCTCGCGG	AGATCCCAGGGATCCACACGTGG	chr6 : 79887477 - 79887499	intergenic:Gm20594-Gm4409	✓
	TGATCCCCAGGACCCACTTGAGG	chr2 : 103813901 - 103813923	intergenic:Gm13878-Gm13880	✓
	AGATACCTGGAACCCGCTCCAGG	chr8 : 105702876 - 105702898	exon:Pard6a	✓
	AGCTCCCCGGGTGCCGCGCGGGG	chr12 : 3366119 - 3366141	exon:Kif3c	✓
Tet3S 4	CCAGGCAGAGGCAGAGCGCTGGG	chr11 : 101167752 - 101167774	exon:Plekhh3	✓
GCCGGCCGAGGTAGAGCGCTGGG	GCAGGCAGAGGAAGAGCACTAGG	chr18 : 82654214 - 82654236	intron:Zfp236	✓
	GCCGGCCGTAGCAGAGCTCTGGG	chr6 : 89644412 - 89644434	intron:Txnrd3	✓
	GCAGGCAGAGGAAGAGCTCTGGG	chr16 : 8567792 - 8567814	intron:Abat	✓
	CGGGGCCGAGGAAGAGCGCTCGG	chr4 : 123342936 - 123342958	exon:Bmp8a	✓

For both Tet3 L KO and Tet3 S KO mouse lines, all tested loci did not show any differences in the sequence compared to the mouse reference genome, which is shown in Table 8 by a tick in the right column, indicating low off-target activity by the used RNP complexes.

4.3.1.3 Detection of Tet3 isoforms on protein and transcript level

To determine mRNA expression levels of *total Tet3* and *Tet3* isoforms in retina and different brain regions and to confirm the KO of *Tet3* isoforms on mRNA level in these tissues, qRT-PCR experiments were performed. 4-week-old Tet3 L KO, Tet3 S KO (all founder lines) as well as BL/6J, referred to as WT in the following, animals were analysed.

Total Tet3 transcript levels in retina decreased in Tet3 L and Tet3 S KO animals, although statistical significance was only reached in the Tet3 S KO founder lines (Figure 38 - A). In contrast, there were only minimal differences in *total Tet3* transcript levels in cerebral cortex in Tet3 L KO and Tet3 S KO mouse lines in comparison to WT (Figure 38 - B). *Tet3 L* transcript levels significantly increased in all Tet3 S KO founder lines in retina and cerebral cortex in comparison to WT, whereas no *Tet3 L* transcript was detectable in Tet3 L KO animals. *Tet3 S* transcript was not detected in all Tet3 S KO founder lines, but in both retina and cerebral cortex of WT and Tet3 L KO animals (Figure 38 - A + B).

The obtained data indicated compensation between the different Tet3 isoforms. In Tet3 S KO mice, *Tet3 L* transcript levels increased in retina and cortex. In Tet3 L KO animals, *Tet3 S* transcript levels significantly increased in cortex, whereas they did not change in retina.

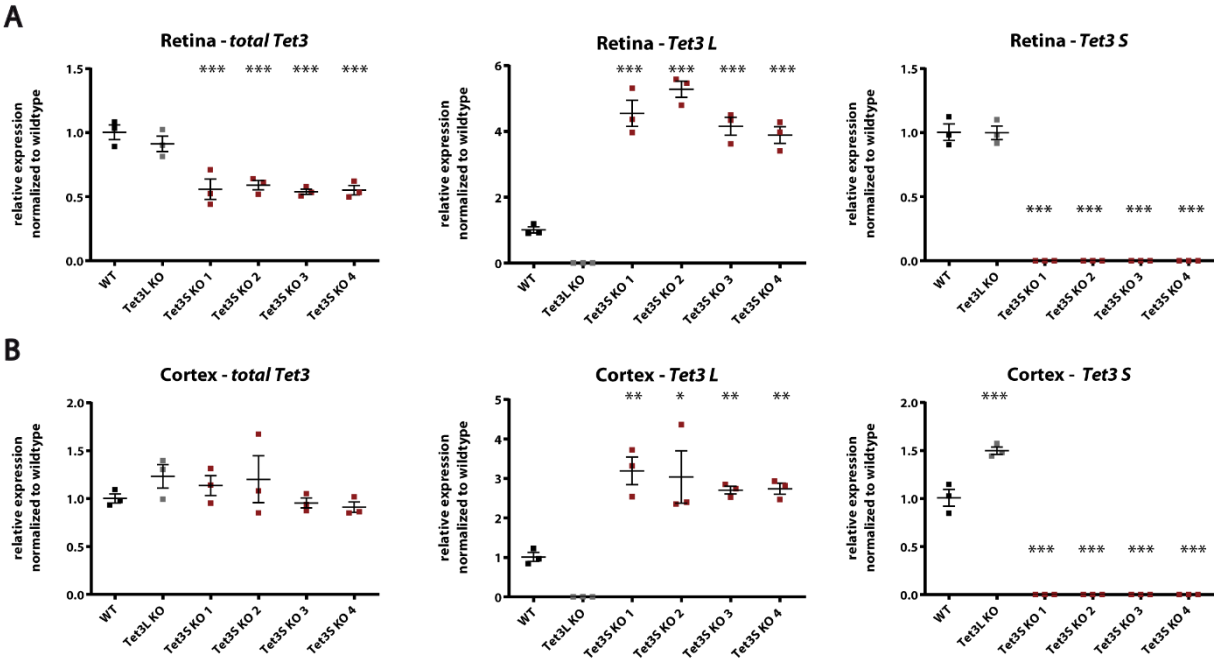

Figure 38: Analysis of relative mRNA expression of *total Tet3* and *Tet3* isoforms

Relative mRNA expression levels of *total Tet3* and *Tet3* isoforms (*Tet3 L* and *Tet3 S*) in retina **(A)** and cerebral cortex **(B)** were determined by qRT-PCR. 4-week-old Tet3 L KO, Tet3 S KO (all founder lines) as well as WT animals were analysed. Relative mRNA expression levels normalized to WT are shown. Statistics: Error bars (SEM) are shown. * $p \leq 0.05$, ** $p \leq 0.01$, *** $p \leq 0.001$ (Ordinary one-way ANOVA with Dunnett's multiple comparisons test), n = 3. Stars indicate statistical difference of each mouse line in comparison to WT.

To conclude, the results of the qRT-PCR analysis of *total Tet3* and *Tet3* isoforms transcript levels suggest compensation mechanisms between the different *Tet3* isoforms.

To visualise Tet3 isoforms in mouse retina and brain slices of WT, Tet3 L KO and Tet3 S KO animals, immunohistochemical analysis was performed (Figure 39) using Tet3 antibodies, specifically recognizing the common C-terminal part of all isoforms as well as the Tet3 L specific N-terminal part of the Tet3 protein (Appendix - Figure 52). The antibody, which specifically binds to the C-terminal part of the Tet3 protein (Tet3 #54), is expected to recognize all Tet3 isoforms, because this part is common for all Tet3 isoforms. The antibody, which specifically binds to the N-terminal part of the Tet3 protein (Tet3 #55), is expected to recognize Tet3 L isoforms only, because this CXXC domain containing part is specific for Tet3 L isoforms. Consequently, an absence of Tet3 S isoform cannot be detected.

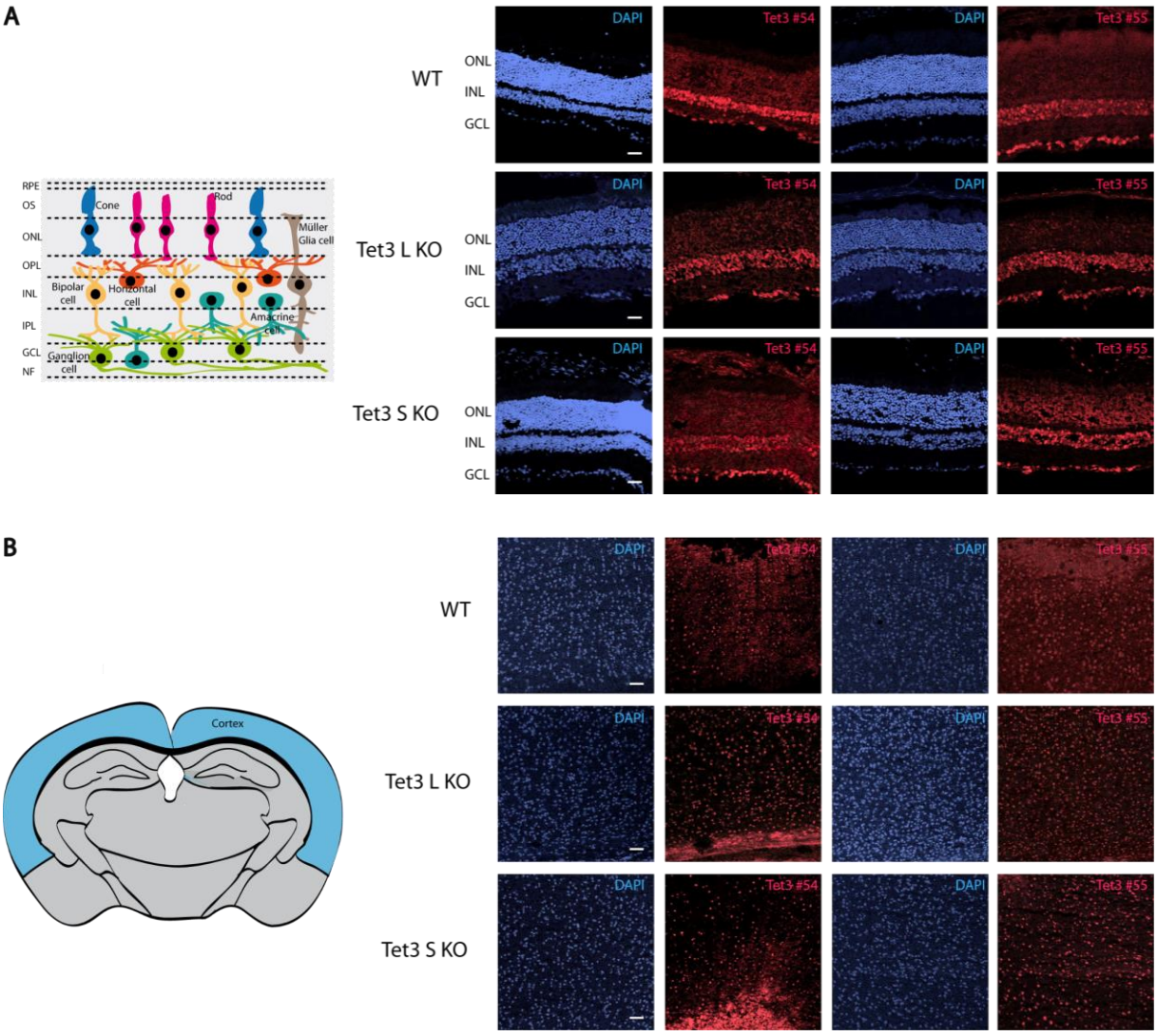

Figure 39: Visualisation of Tet3 by immunohistochemistry

Immunohistochemistry of mouse retina **(A)** and coronal brain **(B)** slices from WT, Tet3 L KO and Tet3 S KO animals: DAPI (blue), Tet3 #54 (red), Tet3 #55 (red). Images were taken using a confocal microscope. Scale bar 50 µm.

To conclude, Tet3 signal was detected in mouse retina as well as brain slices of WT, Tet3 L KO and Tet3 S KO animals by IHC (Figure 39), matching the mRNA expression analysis of *Tet3* and its isoforms, in which compensation mechanisms between the isoforms were observed in all mouse lines (Figure 38).

In Tet3 L KO retina and brain slices, Tet3 L signal appeared not to be different than in the control and Tet3 S KO slices. In those Tet3 L KO samples, the Tet3 N-terminus-specific antibody should not bind any protein, questioning the success of the KO, but also the specificity of the antibodies in mouse tissue.

4.3.1.4 Quantification of global 5mC and 5hmC levels

To assess whether a KO of specific Tet3 isoforms influences global levels of cytosine modifications in retina and different brain regions, immunohistochemical analysis of mouse retina and sagittal brain slices of WT, Tet3 L KO and Tet3 S KO animals using specific antibodies for 5mC and 5hmC was performed (Figure 40, Figure 41).

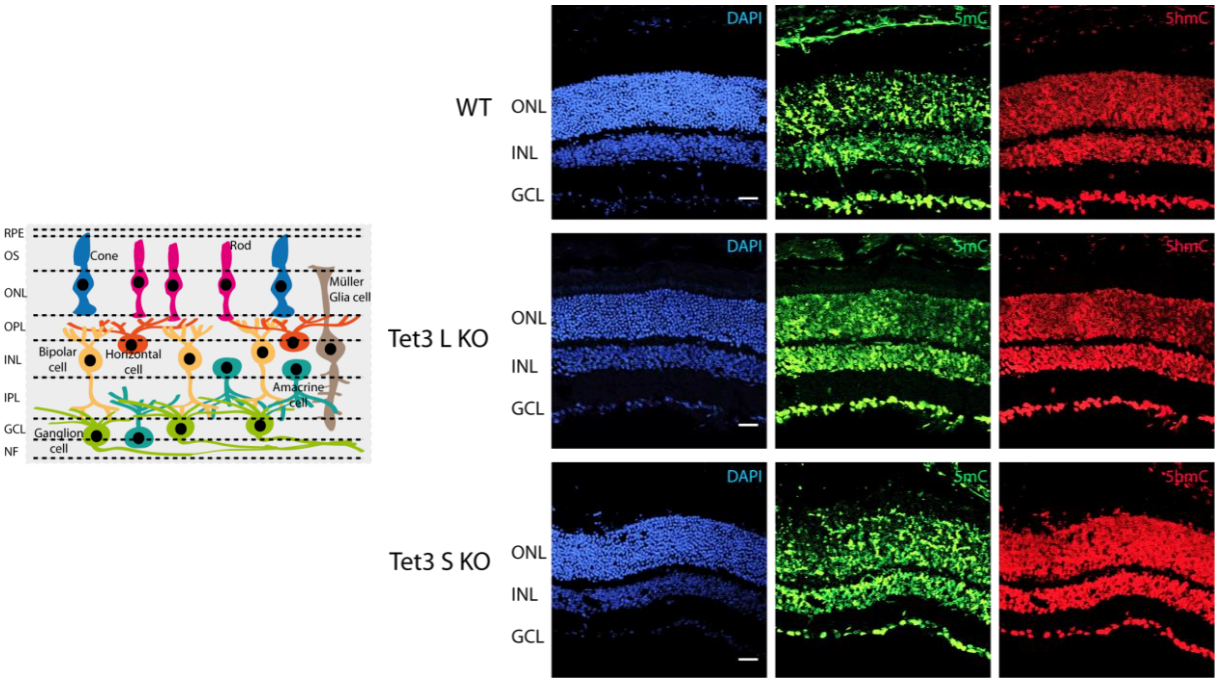

Figure 40: Visualisation of 5mC and 5hmC in the retina

Immunohistochemistry of mouse retina slices from WT, Tet3 L KO and Tet3 S KO animals: DAPI (blue), 5mC (green), 5hmC (red). Images were taken using a confocal microscope. Scale bar 50 µm.

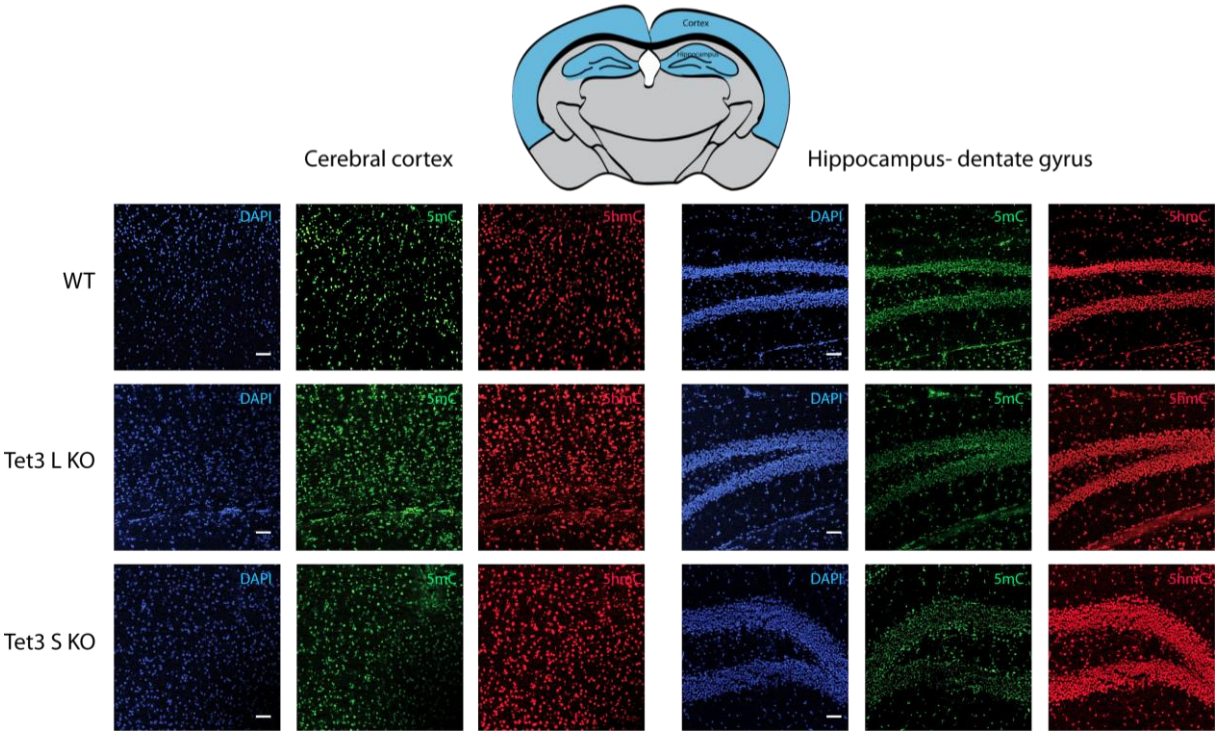

Figure 41: Visualisation of 5mC and 5hmC in the brain

Immunohistochemistry of mouse coronal brain slices from WT, Tet3 L KO and Tet3 S KO animals: DAPI (blue), 5mC (green), 5hmC (red). Images were taken using a confocal microscope. Scale bar 50 µm.

5mC and 5hmC were detected in retina and brain slices of WT, Tet3 S KO, and Tet3 L KO animals (Figure 40, Figure 41). No obvious differences were observed between the genotypes in both tissue types.

Next, global levels of 5mC and 5hmC in gDNA of retina and cerebral cortex tissue of WT, Tet3 L KO and Tet3 S KO animals were quantified by UHPLC-MS/MS analysis (Figure 42).

5mC levels did not change significantly in retina and cerebral cortex between all analysed genotypes. In retina, 5hmC levels decreased slightly, but significantly, in all Tet3 S KO founder lines compared to WT, whereas there was no significant change in 5hmC levels of Tet3 L KO animals (Figure 42 - A). In cerebral cortex, 5hmC levels did not change significantly between the three genotypes (Figure 42 - B), which was also observed for hippocampus und cerebellum tissue samples (data not shown).

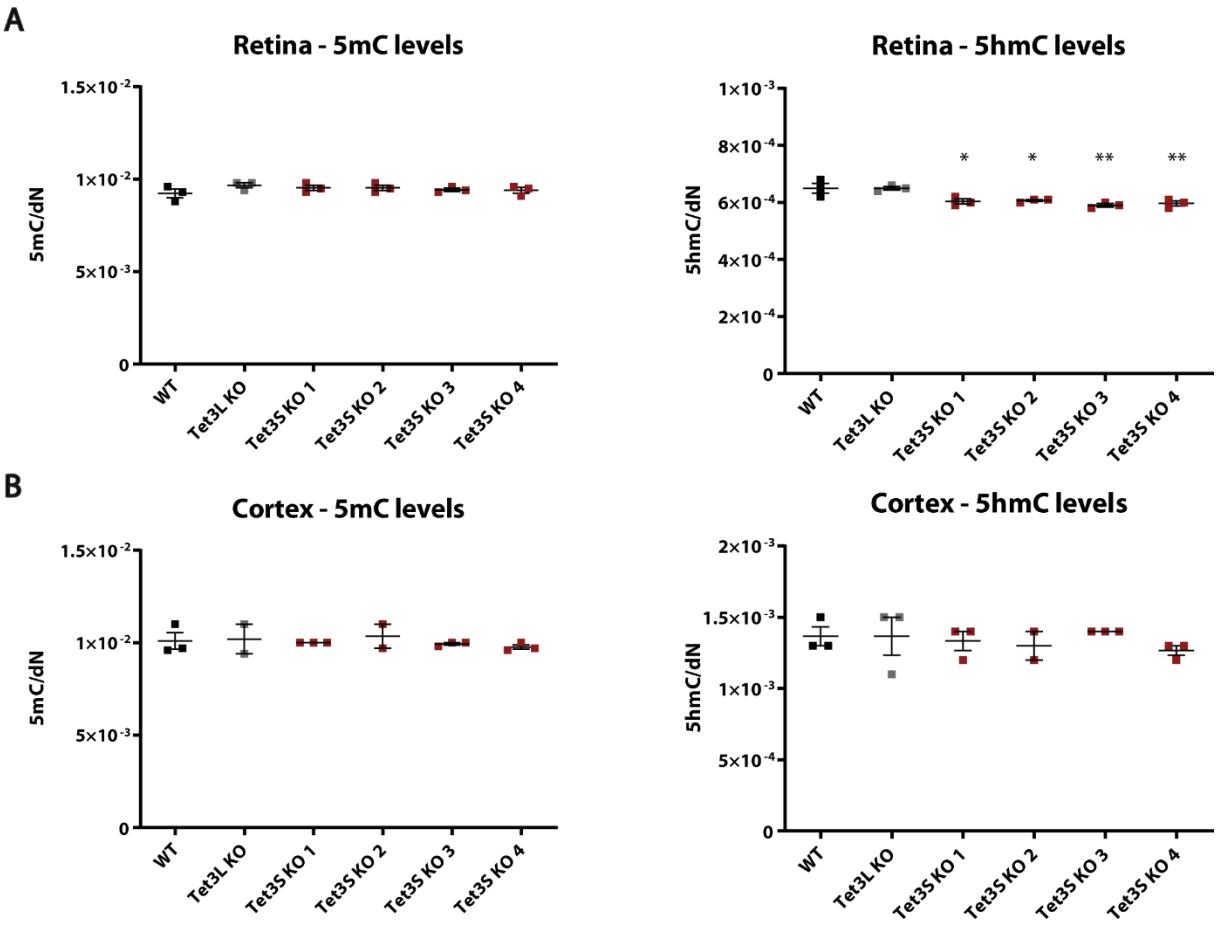

Figure 42: Quantification of global 5mC and 5hmC levels in different tissues

Global 5mC and 5hmC levels were measured by UHPLC-MS/MS in gDNA samples of retina **(A)** and cerebral cortex **(B)** of WT, Tet3 L KO and Tet3 S KO animals. Statistics: Error bars (SEM) are shown. * $p \leq 0.05$, ** $p \leq 0.01$ (Ordinary one-way ANOVA with Dunnett's multiple comparisons test), n = 3. Stars indicate statistical difference of each mouse line in comparison to WT.

To conclude, data obtained from the quantification of global 5mC and 5hmC levels in retina and different brain tissues fits to the results of the qRT-PCR experiments. In retina, *total Tet3* transcript levels significantly decreased in Tet3 S KO founder lines in comparison to WT as well as 5hmC levels were reduced. This suggests that the general amount of catalytically active Tet3 protein is reduced and therefore less 5hmC is generated in retina tissue. In cerebral cortex, *total Tet3* transcript levels did not change in any of the analysed genotypes, matching to unchanged 5hmC levels and suggesting compensation mechanisms between the different Tet3 isoforms.

4.3.1.5 Proteomics

Next, the proteome of whole brain and retina of WT, Tet3 L KO and Tet3 S KO animals was analysed by mass spectrometry to assess, if a KO of Tet3 isoforms influences protein expression in the respective tissues. Comparisons of the proteome of Tet3 L KO or Tet3 S KO vs. WT animals in retina and brain were visualised using volcano plots (Figure 43). Significantly enriched or depleted histones, crystallins and keratins were considered as technical impurities and excluded from the analysis.

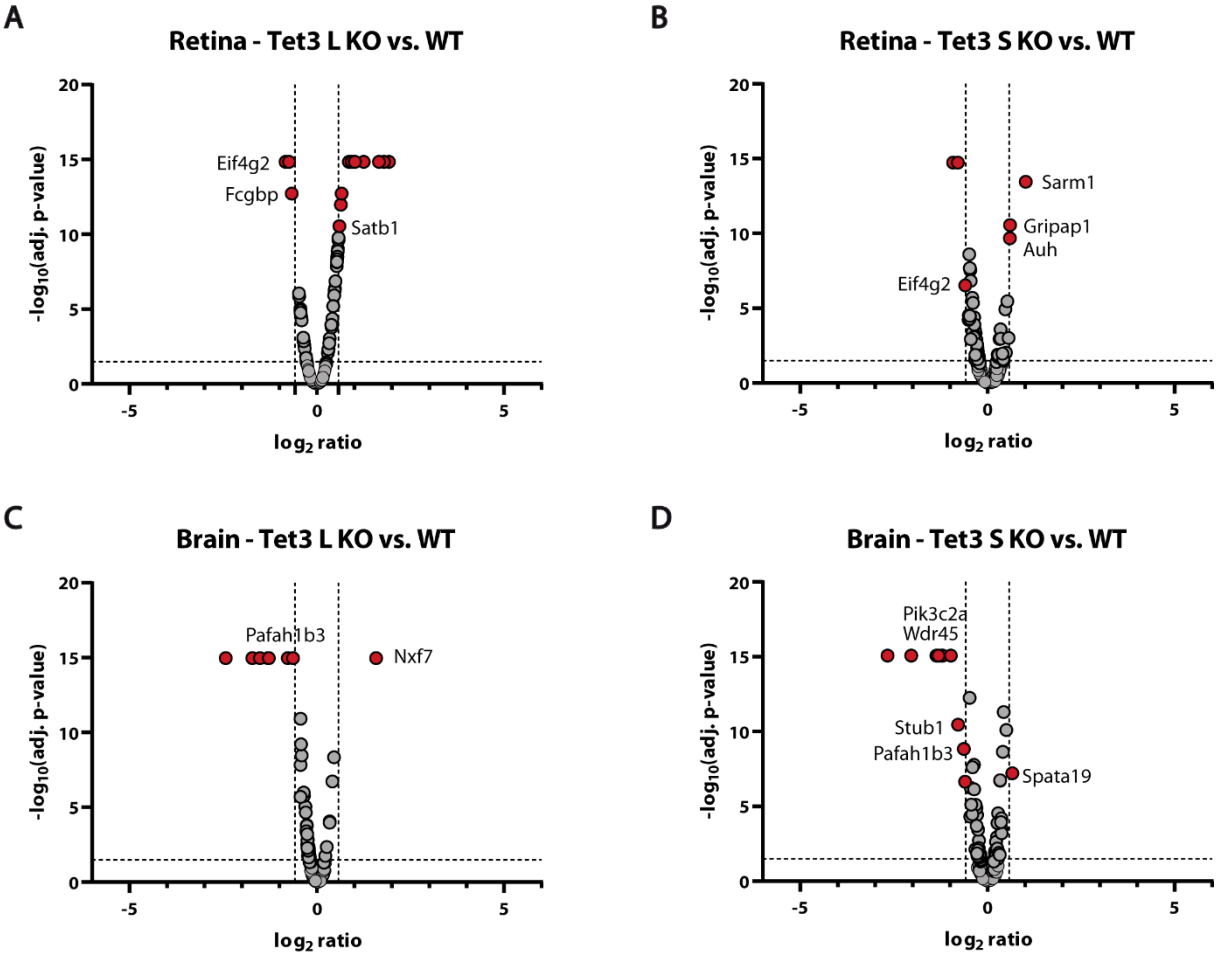

Figure 43: Proteome analysis in retina and brain

Comparisons of the proteome of Tet3 L KO or Tet3 S KO vs. WT animals in retina **(A + B)** and brain **(C + D)** were visualised using volcano plots. Proteins, detected in at least three replicates, were plotted according to their expression ratio between Tet3 L KO or Tet3 S KO and WT (log_2 ratio) and adjusted p-value ($-log_{10}p_{adj}$). The threshold value for the expression ratio was set to log_2 ratio ≥ 0.584 and ≤ -0.584 (equivalent to a ratio of 1.5). The cut-off value for the significance level was set to $-log_{10}p_{adj} \geq 1.3$ (equivalent to $p_{adj} \leq 0.05$). Relevant differentially expressed proteins are marked with their name.

The volcano plots did not display major differences between Tet3 L KO or Tet3 S KO and WT animals regarding the proteome in retina and brain tissue. The major findings are summarised in Table 9 and Table 10 and further described in the following.

Table 9: Summary of proteome analysis - Tet3 L KO mouse model

The table summarises significantly enriched and depleted proteins in different tissue types of Tet3 L KO compared to WT animals. Histones and keratins were excluded from the analysis.

Tissue type	sign. enriched proteins in Tet3 L KO	sign. depleted proteins in Tet3 L KO
Retina	Satb1	Eif4g
Brain	Nxf7	Pafah1b3

Table 10: Summary of proteome analysis - Tet3 S KO mouse model

The table summarises significantly enriched and depleted proteins in different tissue types of Tet3 S KO compared to WT animals. Histones and keratins were excluded from the analysis.

Tissue type	sign. enriched proteins in Tet3 S KO	sign. depleted proteins in Tet3 S KO
Retina	Sarm1, Gripap1, Auh	Eif4g
Brain	Spata19	Pafah1b3, Stub1, Wdr45, Pik3c2a

In Tet3 L KO retina tissue, Satb1 (special AT-rich sequence binding protein 1), a chromatin organizer involved in cancer development and essential for proper functioning of RGCs (Payne et al., 2017; Peng et al., 2017), was significantly enriched in comparison to WT. In Tet3 S KO retina tissue, Sarm1 (sterile alpha and TIR motif containing 1), which plays a role in axonal degeneration in general and in degeneration of retinal ganglion cells and photoreceptors in particular (Fernandes et al., 2018; Ozaki et al., 2020), Gripap1 (GRIP1-(glutamate receptor interacting protein 1)-associated protein 1) and Auh (Au RNA binding methylglutaconyl-CoA hydratase) were significantly enriched compared to WT. In both Tet3 L and Tet3 S KO retina tissue, Eif4g (eukaryotic translation initiation factor 4 G), which plays a major role in translation initiation, was significantly depleted compared to WT.

In Tet3 L KO brain tissue, Nxf7 (nuclear export factor 7), involved in transport of cytoplasmic mRNA (Vanmarsenille et al., 2013), was significantly enriched compared to WT. In Tet3 S KO brain tissue, Spata19 (spermatogenesis associated protein 19), critical for sperm mitochondrial

function and male fertility (Mi et al., 2015), was significantly enriched compared to WT. In Tet3 L KO brain tissue, Pafah1b3 (platelet activating factor acetylhydrolase 1b catalytic subunit 3), which plays a role in cancer development (Mulvihill et al., 2014), was significantly depleted compared to WT. In Tet3 S KO brain tissue, Pafah1b3, E3 ubiquitin ligase Stub1 (STIP1 homology and U-box containing protein 1), Wdr45 (WD repeat domain 45), essential for neurodegeneration in the brain (Abidi et al., 2016; Wan et al., 2020), and Pik3c2a (phosphatidylinositol-4-phosphate 3-kinase catalytic subunit type 2 alpha), which if mutated cause various syndromes like short stature, skeletal abnormalities, and cataracts associated with ciliary dysfunction (Tiosano et al., 2019), were significantly depleted compared to WT.

To summarise, from the obtained results no major conclusion can be drawn to connect Tet3 isoforms with specific enriched or depleted proteins and biological processes or disease mechanisms. GO analysis cannot be performed due to the low number of significant findings. Other more specific and sensitive approaches, e.g. transcriptome analysis of sorted cell populations, are necessary to assess the role of Tet3 isoforms in the organisms.

4.3.2 TET3 isoform overexpressing cell lines

To have a complementary model to the Tet3 L KO and Tet3 S mouse lines, TET3 isoform overexpressing cell lines were generated using human induced pluripotent stem cells (iPS cells), namely PGP1 and iNGN cells. iNGNs are modified PGP1 cells, in which a DOX inducible neurogenin expression cassette was integrated into the genome by lentiviral transduction. Here, DOX application triggers neuronal differentiation (Busskamp et al., 2014).

4.3.2.1 Generation of cell lines

TET3 isoform overexpressing cell lines were generated by inserting the coding sequences for human TET3 isoforms into the iPS cell genome using PiggyBac transposon technology (Figure 44 - A). Human iPS cells were co-transfected with a PiggyBac transposase expression vector and a PiggyBac transposon vector containing the coding sequence for human TET3 isoforms under the control of the tetracycline-responsive promoter element (TRE) and an expression cassette consisting of the reverse tetracycline-controlled transactivator and the puromycin resistance gene (rtTA-T2A-PuroR). The coding sequence for human TET3 isoforms localised between the

ITRs of the transposon vector was inserted into random TTAA sites of the host cell genome. The addition of DOX to the system enables binding of the rtTA to the TRE, leading to the overexpression of human TET3 isoforms in the cells. In iNGNs, application of DOX induces both TET3 isoform overexpression and cell differentiation.

TET3 S isoform, used in this study and called TET3 S trunc, is a truncated version of TET3 S. The isoform lacks the exon, which is specific for TET3 S isoform. The sequence starts within Exon 3, which is common for all TET3 isoforms (Figure 13 - B).

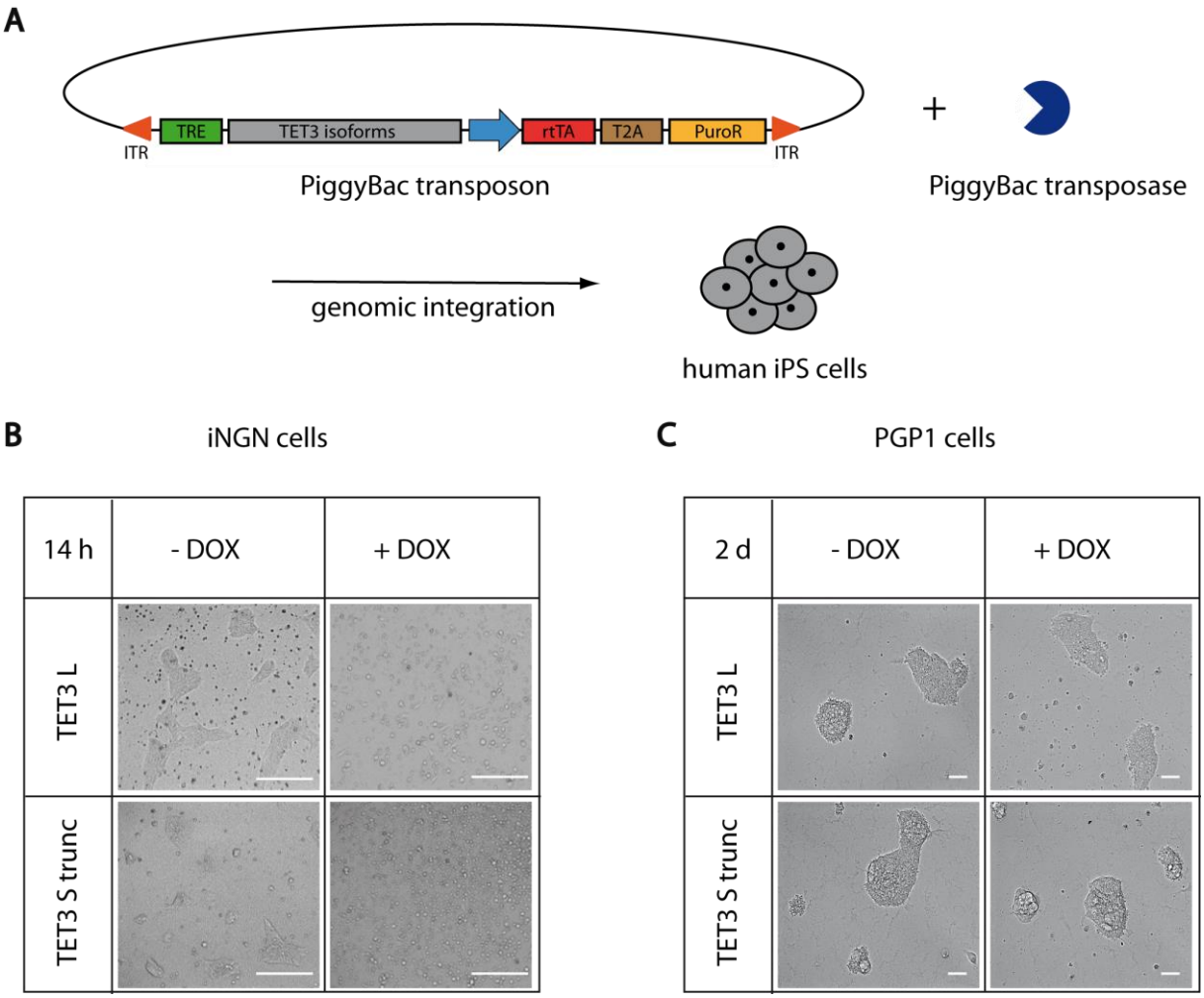

Figure 44: TET3 isoform overexpressing cell lines

(A) TET3 isoforms overexpressing cell lines were generated using PiggyBac transposon technology. A PiggyBac transposon vector and a PiggyBac transposase expression vector were co-transfected into human iPS cells to insert the coding sequence for human TET3 isoforms localised between the ITRs of the transposon vector into random TTAA sites of the cell genome. The addition of DOX to the system enables binding of the rtTA to the TRE, leading to the overexpression of human TET3 isoforms in the cells. **(B + C)** Bright field images of iNGNs and PGP1 cells after DOX application show cell death of iNGN cells and normal cell growth of PGP1 cells. Scale bar 10 mm.

Interestingly, iNGNs died when TET3 isoforms were overexpressed during differentiation (Figure 44 - B). Bright field images were taken after 14 h of DOX incubation. Cells cultured without DOX (-DOX) served as a control. The images of cells incubated with DOX show dead cells floating at the surface of the medium, whereas the images of cells without DOX display normal growth. A range of different DOX concentrations (from 0.05 µg/mL to 0.5 µg/mL) was tested, revealing no differences between the concentrations.

In contrast to the iNGNs, the PGP1 cells show normal growth and development after DOX induced TET3 isoform overexpression. The bright field images do not reveal any differences between the cells with or without DOX (Figure 44 - C).

4.3.2.2 mRNA expression levels of TET enzymes

To validate the generated TET3 isoforms overexpressing cell lines, qRT-PCR analysis was performed to determine mRNA expression levels of *total TET3*, *TET3* isoforms at d3 and d8 of DOX incubation.

Expression levels of *total TET3* transcript increased after induction of TET3 isoform overexpression (Figure 45 - A). At d3 of incubation with DOX, there were higher transcript levels in comparison to d8 of DOX incubation. As expected, mRNA expression levels of *TET3 L* increased in TET3 L overexpressing cells. At d3 of DOX incubation, again higher *TET3 L* transcript levels in comparison d8 of DOX incubation were detected. In contrast to that, *TET3 L* mRNA expression levels did not increase in TET3 S trunc overexpressing cells, as expected. *TET3 S* levels were not measured, because TET3 S trunc lacks the TET3 S specific exon 1 and therefore cannot be distinguished from TET3 L and total TET3. Nevertheless, *total TET3* transcript levels detected in the TET3 S trunc overexpressing cell line represent *TET3 S trunc* transcript levels in addition to any natively expressed *TET3*, since the primer set binds in the common C-terminal part of the transcript. Regarding expression levels of *TET1* and *TET2*, no significant changes of the mRNA expression levels were observed, meaning that overexpression of TET3 L and TET3 S trunc isoforms did not influence mRNA expression levels of the other *TET* variants (Figure 45 - B). To conclude, PGP1 cells, which overexpress TET3 L and TET3 S trunc isoforms, were successfully generated.

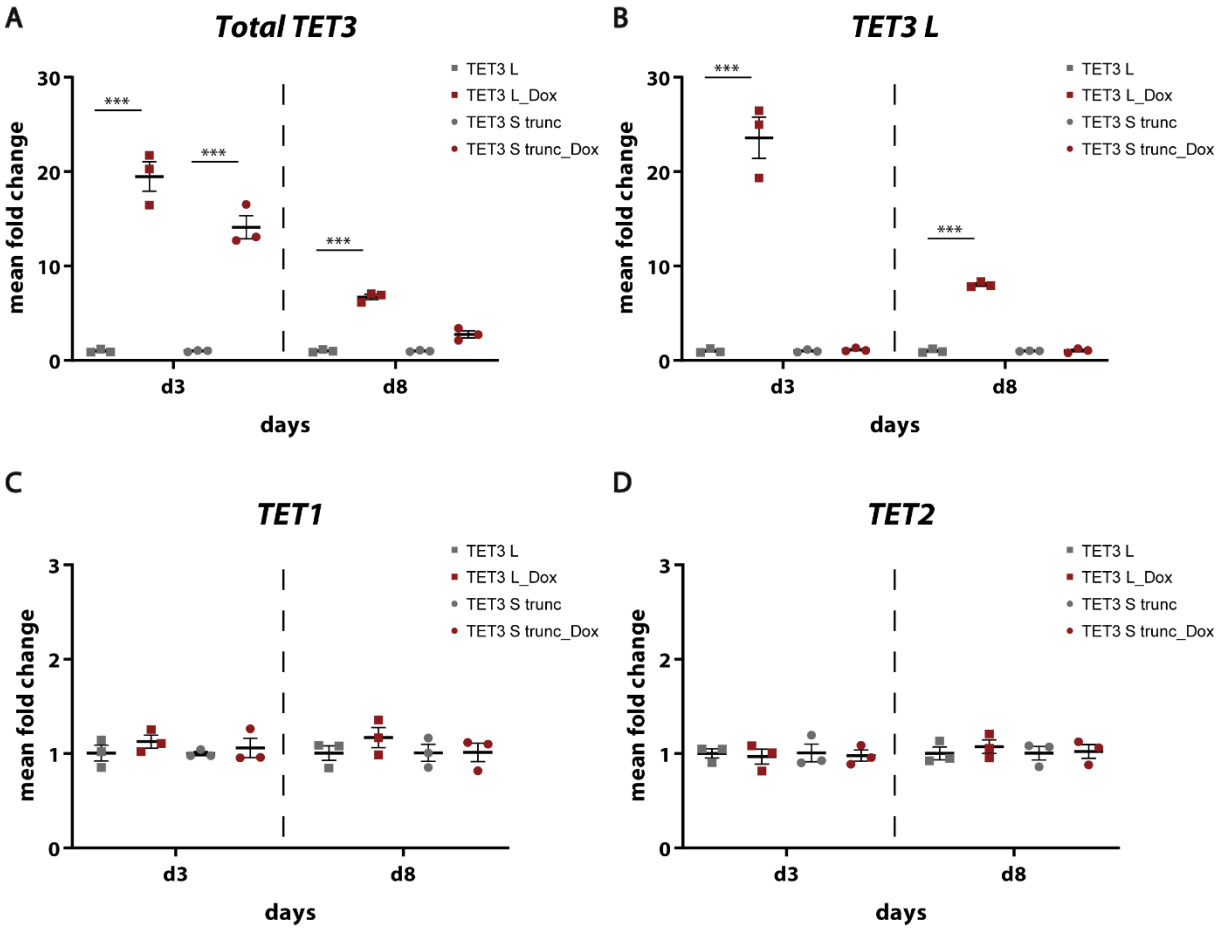

Figure 45: Relative mRNA expression levels of *TET* enzymes

Relative mRNA expression levels of *TET* variants **(A, C, D)** and *TET3 L* isoforms **(B)** were determined by qRT-PCR after isolating RNA from cells harvested at d3 and d8 of DOX incubation. Three replicates for each condition and timepoint were analysed. Statistics: Error bars (SEM) are shown. *** $p \leq 0.001$ (Two-way ANOVA with Sidak´s multiple comparisons test), n = 3. Stars indicate the statistical difference of each condition at respective time points to its control (-DOX). Expression levels are normalized to the controls, respectively.

4.3.2.3 Quantification of global levels of cytosine modifications

To quantitatively assess whether overexpression of TET3 isoforms influences global levels of cytosine modifications, gDNA samples of TET3 L and TET3 S trunc overexpressing PGP1 cells, harvested at d3 and d8 of DOX incubation, were analysed by UHPLC-MS/MS (Figure 46). In contrast to other experiments (Figure 15, Figure 22, Figure 42), 5fC levels were detectable in all conditions. Hence, in this experiment, it was possible to directly assess how the cytosine oxidation continues further on from 5hmC. 8oxoG levels, representing the number of oxidative damages in the gDNA caused during the experiment, stayed under the estimated background level of $5 \cdot 10^{-6}$ 8oxoG/dN (Traube et al., 2019), indicating predominantly Tet3-mediated

oxidation processes (Figure 46 - A). 5mC levels did not change significantly in TET3 L and TET3 S trunc overexpressing cells harvested at d3 of DOX incubation, whereas 5mC levels significantly decreased for TET3 L overexpressing cells compared to the control at d8 (Figure 46 - B). 5hmC levels significantly increased for TET3 L and TET3 S trunc overexpressing cells in comparison to control at d3 of DOX incubation. In contrast, no changes in 5hmC levels were detectable for the cells harvested at d8 of DOX incubation. 5hmC levels even seemed to decrease at this time point, although an increase was expected (Figure 46 - C). 5fC levels significantly increased for TET3 L and TET3 S trunc overexpressing cells in comparison to control at d3 of DOX incubation. For the TET3 S conditions, the increase was highly significant for the cells harvested at d3 and even at d8 of DOX incubation. Again, 5fC levels in cells harvested at d8 of DOX incubation were lower than 5fC levels in cells harvested at d3 (Figure 46 - D).

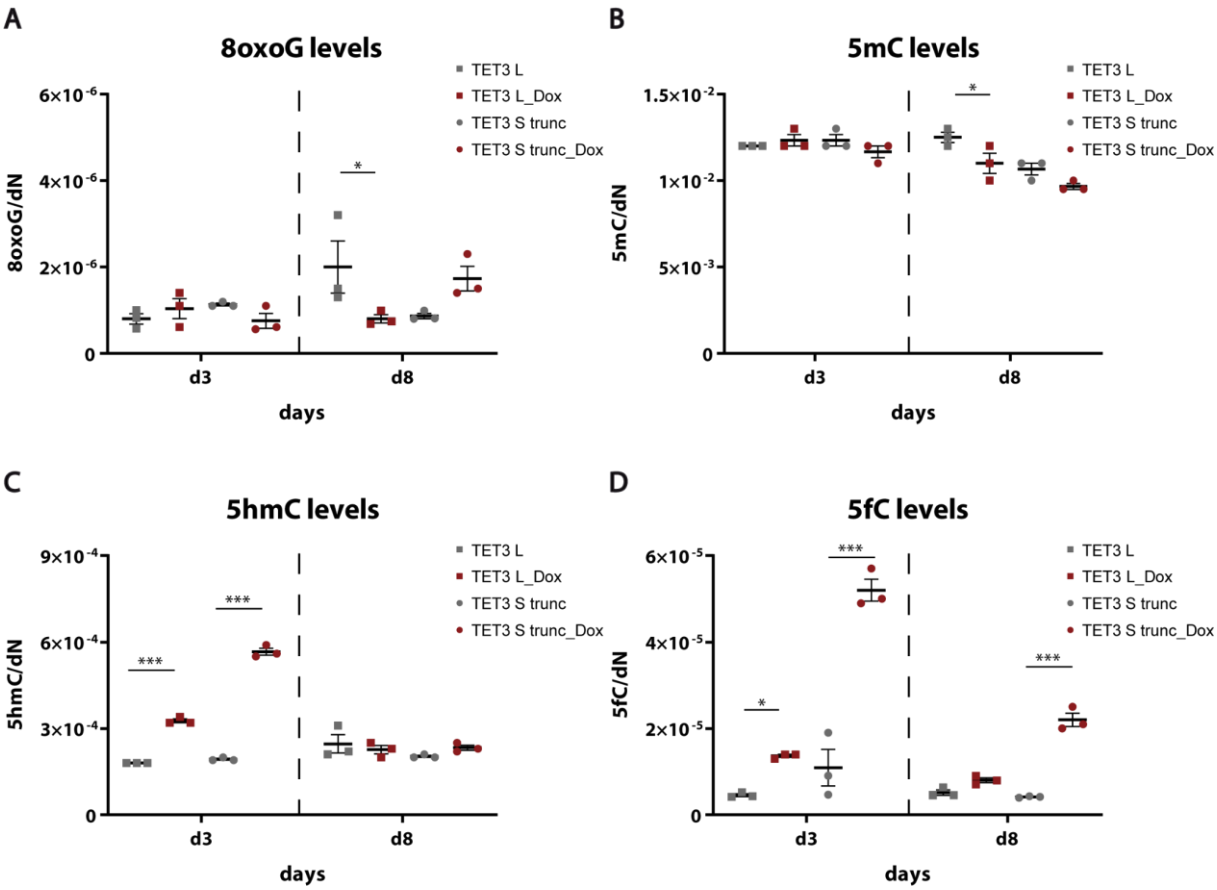

Figure 46: Quantification of global cytosine modification levels

Global 8oxoG **(A)**, 5mC **(B)**, 5hmC **(C)** and 5fC **(D)** levels were measured by UHPLC-MS/MS in gDNA samples of TET3 L and TET3 S trunc overexpressing PGP1 cells harvested at d3 and d8 of DOX incubation. Statistics: Error bars (SEM) are shown. * $p \leq 0.05$, (Two-way ANOVA with Sidak´s multiple comparisons test), n = 3.

To conclude, the data confirm that the generation of 5hmC and 5fC is dependent on TET3 levels. Overexpression of TET3 isoforms led to an increase in genomic 5hmC and 5fC levels. It seemed that the TET3 S trunc isoform has a higher impact on the global demethylation processes in PGP1 cells, as higher levels of 5hmC and 5fC were generated by TET3 S trunc than by TET3 L overexpression. In future experiments, more time points need to be analysed to fully understand the DNA demethylation processes in this system.

5 Discussion

5.1 5hmC dynamics in mouse hippocampus

5hmC is an important epigenetic mark in mammals. As an essential intermediate of the DNA demethylation pathway, 5hmC modulates several processes on DNA and chromatin level and, thereby, regulates gene expression (Cheng et al., 2015; Hashimoto et al., 2012). 5hmC is highly enriched in the brain (Globisch et al., 2010; Kriaucionis and Heintz, 2009; Münzel et al., 2010), where highest levels of 5hmC are detected in cerebral cortex and hippocampus (Münzel et al., 2010). As 5hmC is very abundant in the brain, it is suggested to be essential in brain development and function as well as in mechanisms causing neurodevelopmental and neurodegenerative diseases, such as Rett syndrome, schizophrenia and Alzheimer's disease (Cheng et al., 2015). Furthermore, it is reported to play an important role in acute stress and related diseases (Li et al., 2016b) as well as in synaptic plasticity and neuronal activity (Cortés-Mendoza et al., 2013).

In this study, activity-dependent changes of 5hmC levels in mouse hippocampal slices were investigated. As highest 5hmC levels are detected in the hippocampus (Münzel et al., 2010) and as activity-dependent synaptic plasticity is an essential feature of hippocampal synapses (Neves et al., 2008), the hippocampus is the most suitable brain region to investigate the influence of induced neuronal activity on DNA demethylation and related mechanisms. To determine changes in 5hmC levels in response to neuronal activity, acute mouse hippocampal slices were depolarized by applying 25 mM KCl solution for 6 h (Figure 14). After DNA and RNA isolation from slices of control and induced conditions, global 5mC and 5hmC levels were measured using UHPLC-MS/MS (Figure 15) as well as mRNA expression levels of different activity-dependent genes and Tet enzymes were quantified by qRT-PCR (Figure 16).

Depolarization of acute mouse hippocampal slices led to a clear and highly reproducible increase of 5hmC levels in comparison to the control condition (Figure 15). *Tet1*, *Tet2* and *Tet3* mRNA expression levels stayed stable after depolarization (Figure 16 - A), meaning that the effect of 5hmC increase does not depend on higher *Tet* transcript levels. Therefore, the increase of 5hmC after depolarization is best explained by increased Tet catalytic activity generating

more 5hmC in response to stimulation. Furthermore, Tet interaction partners as well as availability of co-factors and metabolites may play a role in this process. Kaas et al. disagrees with our finding that Tet levels remain stable after depolarization in the hippocampus. They report a significant decrease of *Tet1* transcript levels after depolarization using 25 mM KCl in primary hippocampal neurons (Kaas et al., 2013). The difference may be explained with the different tissue samples used in the experiments. In our setting, hippocampal slices were used, which consist not only of neurons but other cell types. Possibly, these other cell types contribute to remaining equal transcript levels of Tet enzymes or mask the effect in neurons.

Additionally, depolarization of acute mouse hippocampal slices resulted in more or less consistent changes of mRNA expression levels of activity-dependent genes, namely *Npas4*, *Bdnf* and *Arc* (Figure 16 - B). They all belong to the group of IEGs, which are rapidly and transiently activated by extracellular stimuli like neuronal activity or growth factors (Sun and Lin, 2016). Those activity-dependent genes display both demethylation and de novo methylation (Guo et al., 2011a). For example, transcription of *Bdnf* is increased by demethylation of the *Bdnf* promotor after depolarization in post-mitotic neurons (Martinowich et al., 2003), with Tet1 and Tet3 also being reported to regulate *Bdnf* expression by DNA demethylation (Guo et al., 2011b; Yu et al., 2015). Furthermore, Tet1 deficiency leads to a significant reduction of 5hmC levels and transcript levels of e.g. *Npas4* caused by hypermethylation of its promotor region (Rudenko et al., 2013).

Npas4 is only expressed in neurons and is only activated by neuronal activity (Sun and Lin, 2016), which fits to our results, as mRNA expression levels increased after depolarization of mouse hippocampal slices. *Npas4* is shown to be one of the most rapidly induced genes. *In vitro* studies with cultured neurons showed maximal *Npas4* mRNA expression levels 30 min to 1 h after stimulation (Lin et al., 2008). Moreover, *in vivo* studies with contextual fear conditioning of mice revealed maximal *Npas4* mRNA expression levels in hippocampus within 5 min, whereas other IEGs like *Arc* reached their peak after 30 min (Ramamoorthi et al., 2011). These reports match our results, as *Npas4* was upregulated after depolarizing mouse hippocampal slices for 6 h, whereas *Bdnf* and *Arc* only showed a moderate increase only in some biological

replicates. Those genes probably require longer incubation times or a higher KCl concentration in the used experimental setting. Lin et al. for instance used a KCl concentration of up to 55 mM to depolarize neurons (Lin et al., 2008). As a transcription factor, *Npas4* is reported to control the expression of several other activity-dependent genes, which are its downstream transcriptional targets (Sun and Lin, 2016). For example, the activity-dependent expression of *Bdnf* is directly regulated by *Npas4* binding to activity-dependent promotors of *Bdnf* (Lin et al., 2008). That fact may also explain why in our study *Bdnf* and probably also *Arc* mRNA expression levels increased less pronounced in comparison to *Npas4* mRNA expression levels. *Npas4* first needs to activate *Bdnf* expression and, thus, induction of *Bdnf* gene expression might have needed longer incubation times in our experiments.

To summarise, the study shows activity-dependent changes of 5hmC levels and mRNA expression levels of IEGs in mouse hippocampal slices. It suggests 5hmC not only as an intermediate of the DNA demethylation pathway but also as an important epigenetic marker, which is involved in gene regulation, neuronal activity, stress response, synaptic homeostasis, learning and memory formation. However, gene-specific sequencing of 5hmC would be necessary to confirm this assumption. Nevertheless, the study confirms the relevance of epigenetic markers and mechanisms involved in many processes of the mammalian organism and their importance to fully understand physiological as well as pathophysiological mechanisms in mammals.

5.2 Tet3 L2 + Nestin Cre mouse model

Tet3 KO mouse models are key to investigate the role and function of Tet3 in biological systems. Since a general Tet3 KO is embryonically lethal (Gu et al., 2011), only mouse models can be used, in which the KO of Tet3 is limited to specific cell types or specific regions of the body.

To generate the Tet3 L2 + Nestin Cre mouse line based on the Cre/loxP site recombination system, a conditional Tet3 KO mouse line (Amouroux et al., 2016) and a Nestin Cre mouse line (Tronche et al., 1999) were crossed (Figure 12). Thus, exon 8 and 9 of the *Tet3* gene, which are flanked by loxP sites, are excised in those cells of the mouse body, in which Nestin Cre recombinase is expressed. According to the Nestin expression pattern within the nervous

system, a Tet3 KO is reached in cells of the CNS and PNS of the Tet3 L2 + Nestin Cre mouse model enabling the investigation of Tet3 function in the brain.

The Nestin Cre mouse line used for the conditional KO itself shows mild growth retardation, impaired fear response and metabolic alterations, which results from a human growth hormone minigene in the transgenic construct downstream of Cre recombinase (Declercq et al., 2015). This phenotype must be considered as "background phenotype" when analysing the generated Tet3 L2 + Nestin Cre mouse model. Therefore, the genotype (Tet3 WT, Nestin Cre positive) was preferred as control group for all experiments in contrast to Tet3 L2 homozygous, Nestin Cre negative mice.

Alternatively, a Nestin Cre/ERT2 transgenic mouse line, which expresses a tamoxifen inducible Cre recombinase under the control of the Nestin promotor, could be used. With such an approach, Cre recombinase activity could be precisely controlled by tamoxifen application and induced at any time point after E11, when Nestin is expressed. For example, a functional Tet3 KO can be induced by application of tamoxifen during postnatal or even adult stages. In this way, effects already arising during development and contributing to altered phenotype formation may be excluded. Furthermore, a possible toxic effect of Cre recombinase itself could be reduced to a minimum by controlling the induction of Cre activity (McLellan et al., 2017).

The Tet3 deletion was confirmed on mRNA level by qRT-PCR (Figure 20) using an assay specific for the deleted part of the *Tet3* gene. *Total Tet3* mRNA expression was still detectable in bulk RNA samples from all analysed tissues. Immunohistochemical analysis showed Tet3 protein signal in different areas of mouse brain sections (Figure 18). Thus, no obvious differences were detected between cKO and CTR brain regarding *Tet3* transcript and Tet3 protein levels. To be able to show a depletion of Tet3 protein for example in Western Blot, one would need to isolate only Nestin Cre positive cells from the tissue using a specific protocol, which effectively excludes Nestin Cre negative and thus Tet3 CTR cells from the analysis.

Furthermore, a dominant negative effect can be discussed in context of the KO principle. The observed changes in cKO animals may be the results of such an effect of the mutation, which means that a mutation within the gene negatively affects the WT gene product and blocks or

interferes with its functions, but does not change its expression and interactions. This assumption of a dominant negative effect in context of the observed abnormalities as a result of *Tet3* deficiency fits to the report about first human patients with *TET3* mutations, which describes mono-allelic mutations having activating or dominant negative effects and bi-allelic mutations leading to loss of function of TET3 (Beck et al., 2020).

5.2.1 Characterization of the Tet3 L2 + Nestin Cre mouse model

In this study, analysis of the Tet3 L2 + Nestin Cre mouse model revealed an abnormal phenotype regarding body size, brain size and brain morphology (Figure 17). Observation of CTR and cKO animals over a period of at least 28 days revealed significant growth abnormalities in cKO mice (Figure 17 - B). Furthermore, while the overall size of brains of cKO animals was smaller than in CTR, the brains appeared to be bigger relative to the body weight, which revealed a relative macroencephaly with respect to their body size in cKO animals (Figure 17 - C). These phenotypic features were also observed in human patients with *TET3* mutations (Beck et al., 2020). Beck et al. identified and characterized eleven patients in eight different families with mutations in *TET3* and phenotypic features of intellectual disability and global developmental delay, hypotonia, autistic traits, movement disorders, growth abnormalities, and facial dysmorphism overlapping with those of many other Mendelian disorders of the epigenetic machinery. In line with the observation of macroencephaly in mice, in human patients macro- as well as microcephaly were reported. Interestingly, Beck et al. reported that monoallelic *TET3* mutations already cause mild phenotypic features in humans, whereas in mice, no differences were detected between CTR and heterozygous animals concerning body size and weight (data not shown). Concerning the observed growth abnormalities in cKO animals, olfactory dysfunction can be discussed, as there are reports about delayed body development in *Cngb1* (cyclic nucleotide-gated channel beta 1) KO pups in connection to olfactory deficits interfering with nursing and food take (Michalakis et al., 2006). *Cngb1* KO mice reach the body weight of their WT siblings later. In contrast, Tet3 cKO animals increase in body weight, but do not reach the weight of their CTR siblings during adolescence. Therefore, olfactory deficits because of Tet3 KO can be involved in causing growth abnormalities but may

be only one of several issues of a complex network contributing to the pathological phenotype formation. Underlying mechanisms need to be further investigated.

In addition to reduced weight and macroencephaly, morphological analysis of the brain seemed to indicate smaller size of lateral ventricles in brains of cKO in comparison to CTR animals, which needs to be further assessed quantitatively. A Nissl staining, which is generally used to visualise morphology and pathology of neural tissue (Kádár et al., 2009), did not reveal any gross morphological differences in neurons of cKO and CTR animals (Figure 17 - D). Importantly, similar section levels of brain slices from CTR and cKO animals are required to compare brain and neural morphology and size of specific brain regions as well as to quantify differences in size. As it is difficult to cut different mouse brains in the exact same way and therefore to get directly comparable sections of both genotypes, Nissl staining only serves as orientation and first detection method of morphological abnormalities like a small lateral ventricle. To solve the issue of section comparability, tissue clearing protocols in connection with specific imaging and quantification methods can be used to analyse whole brains and to measure the size of the lateral ventricles, respectively (Ertürk et al., 2014; Ueda et al., 2020). Furthermore, magnetic resonance imaging (MRI) can be performed to analysis size and volume of different brain regions.

Since in this study a Nestin Cre driver line was used for the conditional cell-specific Tet3 KO and Nestin expression was detected in ependymocytes (Korzhevskii et al., 2015; Matsuda et al., 2013), the observed small ventricles in Tet3 cKO animals might relate to impairment of ependymocytes. In general, a layer of ependymocytes lines the wall of brain ventricles in adult mammals, being essential for brain homeostasis and for the transport of cerebrospinal fluid (CSF) through the ventricular system by its cilia (Del Bigio, 1995; Del Bigio, 2010; Spassky et al., 2005). The CSF itself is produced by ependymal cells covering the surface of the choroid plexus, located in the ventricle (Péraldi-Roux et al., 1990). Ependymocytes are generated during development between embryonic day E14 and E16, do not divide in normal adult mouse brain and complete their differentiation to multiciliated ependymal cells during the first postnatal week (Spassky et al., 2005). Possibly, functional Tet3 KO might affect the production of ependymocytes during development leading to impaired wall thickness and reduced size of the

lateral ventricles remaining in adult Tet3 cKO animals. To understand the underlying mechanisms causing this defect, examination of embryonic stages or early postnatal stages (P0 or P1) of Tet3 cKO animals may be necessary. Since ependymocytes of the choroid plexus produce the CSF filling the lateral ventricles, another possibility causing the observed alterations may be that not the function of ependymocytes per se, but rather CSF production is impaired by Tet3 deficiency leading to less CSF volume and / or altered CSF composition and, consequently, to smaller lateral ventricles. This assumption regarding impaired CSF production by ependymocytes of the choroid plexus resulting in smaller brain ventricles is supported by a report about Slc4a10 (solute carrier family 4 member 10) KO mice (Jacobs et al., 2008). The Na^+-dependent Cl^--HCO_3^--exchanger Slc4a10 is expressed within the basolateral membrane of ependymocytes of the choroid plexus and is shown to be involved in CSF production (Jacobs et al., 2008). Jacobs et al. suggested that a Slc4a10 KO cause a failure in the CSF production resulting in the collapse of brain ventricles in mice. Another publication reports about brain morphological abnormalities, including small lateral ventricles, as well as impaired behaviour in a *Tspyl2* (testis specific protein, Y-encoded-like 2) loss-of-function mouse model (Li et al., 2016a). Being expressed during brain during developmental as well as adult stage, Tspyl2 regulates the expression of genes encoding glutamate receptors and is involved in cell proliferation and synaptic function (Li et al., 2016a).

As Antunes et al. described increasing anxiety-like behaviour and regulation of cognitive function in mice by Tet3 ablation (Antunes et al., 2020), behavioural tests like open-field-test, elevated plus maze or Morris water maze need to be performed to additionally analyse the consequences of the Tet3 deletion on behaviour in our Tet3 L2 + Nestin Cre mouse model, in particular since the Nestin Cre mouse line itself shows an impaired fear response. In their study, Antunes et al. used a different Tet3 L2/L2 mouse line, in which Exon 7 of *Tet3* is flanked by loxP sites, and a Camk2a (calcium/calmodulin-dependent protein kinase II alpha)-CreERT2 mouse line, which expresses a tamoxifen-inducible Cre recombinase under the control of the mouse Camk2a promotor region. By mating these mouse lines, they reached a *Tet3* deletion in mature forebrain glutamatergic neurons after tamoxifen application. Here, deletion of exon 7

resulted in *Tet3* gene disruption and in a truncated Tet3 protein, which lacks the catalytic domain (Antunes et al., 2020).

5.2.2 Effects of the Tet3 KO on mRNA expression, DNA and protein levels

To validate the mouse model, Tet3 protein was first detected by immunohistochemical analysis using a Tet3 antibody, recognizing the common C-terminal part of the Tet3 protein. Tet3 signal was detected in mouse brain slices of both CTR and cKO animals (Figure 18). To exclude possible non-specificity of Tet3 antibodies, RNAscope® technology based *in situ* hybridisation probes were established to visualise and localise *Tet3* mRNA localisation. The specific Tet3 probe binds the *Tet3* mRNA part encoded by exon 3. Since this region is upstream of the knocked-out region, this probe is equally well suited to detect WT and cKO transcripts. Confocal images showed *Tet3* localisation in a dotty, for RNAscope® technology typical way, but did not reveal obvious differences between CTR and cKO tissue (Figure 19). Future experiments with co-stainings with e.g. 5hmC are needed to inform about the exact localisation of the *Tet3* mRNA.

To quantify mRNA expression levels of *Tet* enzymes and *Npas4*, qRT-PCR experiments, summarised in Figure 20 - C, were performed with samples from different brain regions (cerebral cortex, cerebellum, hippocampus, olfactory bulb) of adult CTR and cKO animals. In all analysed tissue samples, mRNA levels of *total Tet3* transcript did not change in CTR and cKO animals, whereas mRNA levels of *Tet3 del* were significantly reduced in cKO animals. This indicates that, on the one hand, the excision of the loxP flanked Tet3 sequence by Nestin Cre recombinase was successful, and, on the other hand, that *Tet3* transcript was still abundantly expressed. One reason could be that the Nestin promotor does not drive Cre recombinase activity in all cells within the analysed neuronal tissues and therefore not all cells are affected by the KO. Furthermore, it may suggest that the excision of exon 8 and 9 of the *Tet3* gene by Cre recombinase does not lead to a detectable decrease in *Tet3* transcript due to a lack of nonsense-mediated mRNA decay. The cKO revealed some compensational effects on the mRNA expression of the other *Tet* isoforms. While *Tet1* transcript levels did not change in all analysed tissues, *Tet2* mRNA expression levels increased slightly but significantly in cerebellum und

olfactory bulb tissue of cKO animals and at least showed a slight increasing tendency in cKO cerebral cortex tissue, suggesting *Tet2* specific upregulation and compensation mechanisms in response to the Tet3 cKO. Additionally, Tet3 cKO seemed to affect expression of some IEGs at least to some extent. Due to high variability, *Npas4* transcript levels did not show significant changes between cKO and CTR animals in all analysed tissues, but an increasing tendency was observed, in line with findings by Antunes et al., who showed an significant upregulation of *Npas4* as well as *c-Fos* in the hippocampus of Tet3 L2 + Camka2a-CrERT2 mice, suggesting regulation of IEGs by Tet3 (Antunes et al., 2020).

Furthermore, levels of cytosine modifications were analysed in Tet3 cKO and CTR animals by IHC (Figure 21) and UHLPC-MS/MS (Figure 22). 5mC and 5hmC were detected in mouse brain sagittal slices of both CTR and cKO animals. As IHC is not a quantitative method, a conclusion about different levels in tissues of CTR and cKO animal cannot be drawn. Therefore, global levels of 5mC and 5hmC levels in gDNA samples of mouse hippocampus, cerebral cortex, cerebellum and olfactory bulb tissue of CTR and Tet3 cKO animals were quantified by UHPLC-MS/MS analysis to assess, if a Tet3 KO in Nestin Cre positive cells influences 5mC oxidation and 5hmC generation in those tissues. 5mC levels in all analysed tissues were not affected by Tet3 depletion, indicating that depletion of Tet3 did not influence global 5mC levels and 5mC oxidation. 5hmC levels significantly decreased in cerebellum samples of cKO animals, whereas in hippocampus, cerebral cortex and olfactory bulb tissue, 5hmC levels did not differ between CTR and cKO animals. This leads to the conclusion that, in cKO animals, reduced Tet3 activity in cerebellum led to a decrease in 5hmC levels. The reason for these region-specific effects of the cKO on genomic 5hmC levels in unclear. Generally, the cerebellum tissue displays the lowest 5hmC levels within the brain. Possibly, the method is more sensitive at these levels, which is the reason, why significant changes were detected for cerebellum, but not for the other investigated brain regions. In hippocampus, cerebral cortex and olfactory bulb samples, 5hmC levels did not change, which is in line with Antunes et al., who did not detect changes in global 5hmC levels in different forebrain regions like prefrontal cortex, hippocampus and amygdala (Antunes et al., 2020), suggesting compensation by *Tet1* and *Tet2* action, as their transcript levels are even increased in case of *Tet2* in some tissue types after Tet3 deletion.

Next, the proteome of cerebral cortex, cerebellum, hippocampus and olfactory bulb tissue of CTR and Tet3 cKO animals was analysed by mass spectrometry (Figure 23). Proteome analysis revealed no major differences between cKO and CTR animals regarding the proteome in any of the analysed tissues, suggesting only specific effects of Tet3 depletion on protein expression.

In all analysed tissue samples, RNA-binding protein 3 (Rbm3) was significantly enriched in cKO animals in comparison to CTR animals. Interestingly, Rbm3, a cold-inducible RNA-binding protein, is reported to be involved in neurodegeneration, cell spreading and migration as well as neurogenesis (Jackson et al., 2015; Yan et al., 2019; Zhu et al., 2016; Zhu et al., 2019). Furthermore, in cerebellum samples, cold-inducible RNA-binding protein (Cirbp) was enriched in cKO animals in comparison to CTR animals. Interestingly, Rbm3 and Cirbp are reported as a unique couple of RNA-binding proteins, which are transcriptionally upregulated in response to cold (Zhu et al., 2016). Both proteins show many similarities and specific differences concerning the regulation of several molecular and cellular processes (Zhu et al., 2016). For example, Rbm3 and Cirbp are both key factors during early development. In addition to their upregulation and functions during hypothermia, they both adopt important roles in cell protection under general stress conditions. The biggest difference in this context is that Rbm3 only has neuroprotective effects, whereas Cirbp can either be involved in cell protection or lead to the induction of neuronal cell death by influencing neuroinflammation processes. The fact that both Rbm3 and Cirbp are enriched in the proteome analysis of cKO tissue leads to the assumption that mechanisms causing upregulation of these two proteins or the two proteins themselves may contribute to the formation of the observed abnormal phenotypes.

Moreover, long-chain acyl-CoA dehydrogenase (Acdal), a mitochondrial protein and a member of the acyl-CoA dehydrogenase family, was significantly depleted in cKO animals compared to CTR animals in all analysed tissues. Its main function is the β-oxidation of fatty acids within the mitochondria, which is also connected to thermogenesis. Acdal deficient mice are sensitive to cold and hypothermia, as a reduction of fatty acid oxidation leads to lower heat generation in the body. (Guerra et al., 1998; Schuler and Wood, 2002). Because of this reported cold sensitivity in response to Acdal deletion, a connection between Acadl and Rbm3 may be suggested. Deletion of Tet3 in the Tet3 L2 + Nestin Cre mouse model might have caused a

depletion of Acdal in all analysed tissues, which in turn leads to a dysregulated thermogenesis and cold sensitivity of cells, resulting in an upregulation of cold-inducible Rbm3. Follow-up analysis of thermoregulation in cKO mice is needed to test this hypothesis.

Furthermore, especially in cerebellum samples, proteins related to metabolism were significantly enriched or depleted. Those were Vdac2 and Vdac3 (voltage dependent anion-selective channel 2 and 3) contributing to oxidative metabolism in mitochondria (Naghdi and Hajnóczky, 2016), Cox7c (cytochrome c oxidase subunit 7C) involved in mitochondrial respiratory chain, and Ndufa5, a subunit of NADH dehydrogenase located in the mitochondrial inner membrane. Moreover, other proteins were significantly depleted in all tissue samples, e.g. Timm10 (translocase of inner mitochondrial membrane 10), Mpc2 (mitochondrial pyruvate carrier 2) and Atp2a (sarcoplasmic/endoplasmic reticulum calcium ATPase 1). These findings of enriched and depleted proteins involved in several mitochondrial and metabolic processes suggest a connection of Tet3 to cell metabolism, which confirms unpublished data from a collaboration project with the Carell group (LMU Munich), to which I contributed physiological data on acute hippocampal slice experiments combined with confocal imaging of various immunohistochemical and immunocytochemical experiments. In that project, the basic aim was to analyse how metabolic processes control and influence Tet3 activity, since Tet3 oxidation requires α-ketoglutarate (αKG) as a cofactor, which is one of the key metabolites of the organism. The central question was how the required supply of Tet3 with αKG needed for the oxidation of 5mC is achieved and which consequences result from that on the general oxidation mechanism. The interaction between Tet3 and glutamate dehydrogenase 1 (Glud1), which converts glutamate directly into αKG enabling a citric acid independent αKG supply, was investigated in detail. Interestingly, Glud1 activity was found to be essential for the control of Tet activity during neuronal activation. In further experiments, we revealed that global metabolic changes affect Tet activity, which is increased under glycolytic conditions and decreased under non-glycolytic conditions. Additionally, the NAD^+/NADH machinery as well as other metabolites may also play a role, which needs to be further investigated. The study is in line with several reports about impairment of Tet activity by αKG analogues and citric acid cycle intermediates like fumarate ad succinate (Koivunen and Laukka, 2018; Laukka et al., 2016;

Xiao et al., 2012). Furthermore, Tet3 is reported to be involved in causing metabolic diseases such as type-2 diabetes (Da et al., 2020). In conclusion, there is growing evidence suggesting an important role of Tet3 in energy metabolism and vice versa. Detailed follow-up experiments are needed to clarify the exact mechanisms and consequences for neuronal function.

In cerebral cortex samples, additionally, Darpp32 (dopamine- and cAMP-regulated 32-kDa phosphoprotein), was found to be significantly enriched in cKO animals. Darpp32, a marker of mature striatal neurons, specifically for striatal medium-sized spiny neurons, is enriched in striatum and prefrontal cortex participating in dopamine and serotonin signalling pathways (Bibb et al., 2000; Jin et al., 2005). Additionally, it is reported to be expressed in striatal neurons newly formed after stroke induced ischemic lesion (Arvidsson et al., 2002; Lindvall and Kokaia, 2015). Analysis of bulk protein samples of cerebral cortex tissue revealed a significant enrichment of Darpp32 in cKO compared to CTR animals, suggesting altered cell type formation and neurogenesis, since Darpp32 expression is normally restricted to specific parts of the cerebral cortex. In line with this assumption, abnormal cell migration and proliferation in the dorsal SVZ was detected by IHC. Given that Darpp32 as well as Rbm3 and Cirbp were upregulated in the proteome of cKO animals, depletion of Tet3 in Nestin Cre positive cells might cause a stress condition in the Tet3 L2 + Nestin Cre mouse model similar to the one observed in stroke, ischemic lesions and hypoxia or hypothermia. Interestingly, Darpp32 also appeared to be differentially expressed in TET3 KO iNGNs in comparison to WT iNGNs, which further supports this hypothesis. Nevertheless, underlying mechanisms need to be further investigated in future experiments involving cellular stress models.

To conclude, while the proteomics dataset of bulk protein samples of different brain tissues did not reveal major changes, it does provide several indications for the involvement of Tet3 in cellular stress mechanisms, which might be involved in the developmental retardation phenotype observed in the Tet3 L2 + Nestin Cre mouse model.

5.2.3 Transcriptome analysis of sorted cortical neurons and astrocytes

To specifically investigate the consequences of Tet3 depletion on neurons and astrocytes, cell sorting from cerebral cortex tissue followed by transcriptome analysis using RNA sequencing was performed. Cerebral cortex was dissected from CTR and cKO animals and dissociated via a Papain digest. After Myelin removal and staining with surface marker specific antibodies, different cell fractions were sorted using FACS (Figure 24). Sample preparation and FACS procedure were successfully established. FACS gating strategy was confirmed and validated by an additional sorting experiment using different cell specific antibodies (Figure 25) and qRT-PCR analysis of mRNA expression of cell type specific markers in the obtained populations (Figure 26).

Transcriptomic analysis revealed significant differences between cortical astrocytes and neurons of cKO and CTR animals (Figure 27, Figure 28), as it was expected due to cell type specific transcriptomes. Furthermore, the data suggests that Tet3 does not seem to play a major role in astrocytes, because no differences regarding their transcriptome were detected between cKO and CTR astrocyte samples. This finding is further supported by Antunes et al., who showed that in adult mouse cortex and hippocampus Tet3 is present in mature neurons and oligodentrocytes, but not in astrocytes (Antunes et al., 2020). In contrast, the comparison of neurons from cKO vs. CTR animals showed many significant differences between the two groups (Figure 29 - A), suggesting a major role of Tet3 in neurons. Four times more transcripts are downregulated than upregulated in cKO neurons compared to CTR, indicating that a depletion of Tet3 function in neurons influences neuronal gene expression patterns and, preferentially, leads to a suppression of gene expression. A regulatory function of Tet3 in gene expression has been frequently reported. For example, Tet function was shown to be important for gene transcription during cell activation and specification, summarised in (Lio and Rao, 2019). Besides, the genome-wide distribution of 5hmC underlines the involvement of Tet enzymes in gene expression, as it is enriched at gene bodies and enhancers of highly transcribed genes (Lio and Rao, 2019). Furthermore, in the retina, Tet3 was shown to activate gene expression by interacting with the transcriptional factor REST and inducing H3K36 trimethylation (Perera et al., 2015).

GO analysis revealed an association of upregulated genes in cKO neurons with chromosome and chromatin organization as well as cell cycle processes (Figure 29 - B), suggesting a dependency on Tet3 function, matching the fact that Tet-mediated DNA demethylation is essential to model the epigenetic landscape and chromatin accessibility (Fang et al., 2019). Downregulated genes in cKO neurons were associated with immune response and connected signalling pathways, indicating an involvement of Tet3 in these processes and supporting several publications, reviewed by Lio and Rao, which describe the roles of Tet proteins in regulating the adaptive and innate immune systems (Lio and Rao, 2019).

Unfortunately, the obtained transcriptomic data for both astrocyte and neuron fractions was not optimal, with the data quality of astrocyte samples being slightly higher.

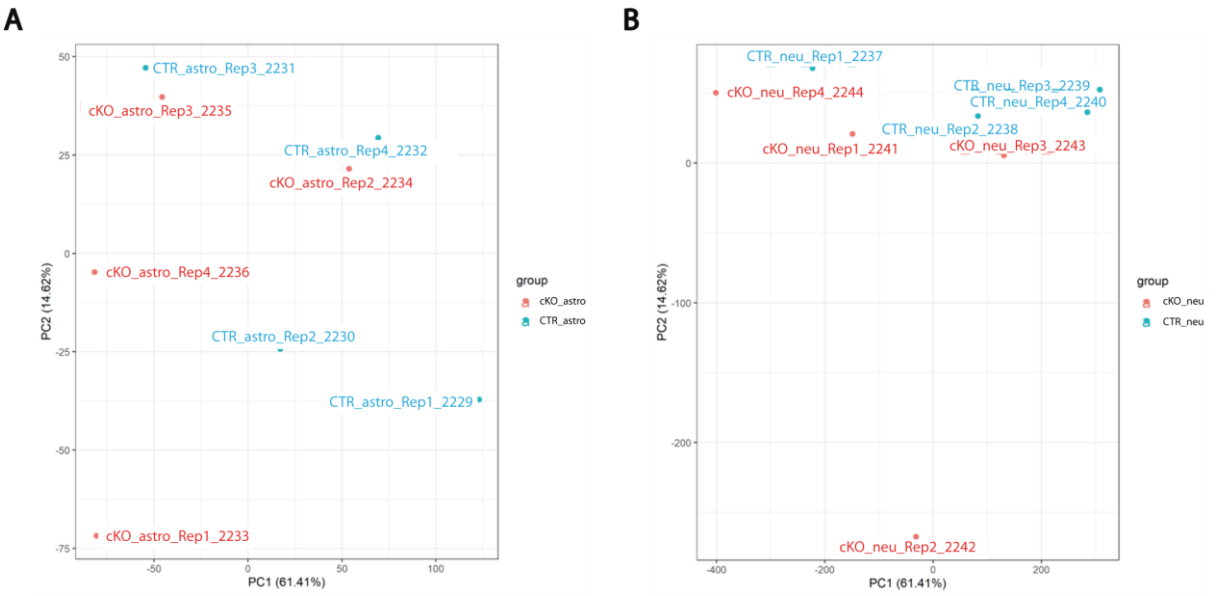

Figure 47: Principal component analysis of replicates

Principle component analysis of astrocyte **(A)** as well as neuron **(B)** samples of CTR and cKO replicates shows their variable distribution, indicating low RNA sequencing data quality.

The principal component analysis (Figure 47) shows that not all replicates of the same genotype clustered together, which optimally should be the case. In this context, it can be discussed, if only those replicates shall be considered for analysis, which cluster together and show the least variability in the PCA plots. For example, regarding neuron samples, CTR replicates 3 and 4 as

well as cKO replicates 1, 2 and 3 could be chosen. With that approach, effects, which base on low data quality, may be excluded from the further analysis.

Several reasons for the low data quality can be discussed. On the one hand, the sample preparation procedure from tissue dissociation to FACS and finally RNA isolation can impact the RNA and, consequently, the transcriptomic data quality. Here, total duration of the procedure as well as disruption and disintegration of cells, generating cells of different sizes and leading to a loss of cytosol and RNA, may result in decreased quality of RNA and data. On the other hand, biological reasons concerning RNA stability in general need to be considered. Moreover, especially regarding the low number of neurons obtained with the applied FACS protocol, it might be that the harvested cell population might reflect only a small subpopulation of the more stable neurons. Considering that all samples were equally processed, sorted populations of all replicates should be fully comparable, however, one can never be completely sure about the actual sample composition.

Another technical option may be sorting of neuronal and astrocyte nuclei instead of using surface antigens to isolate the entire cell. However, such a procedure would not exclude general FACS-related RNA stability issues and requires rather harsh tissue dissociation and preparation steps, which cause cell disruption and does not shorten the isolation procedure.

To sum up, the data meets the expectations concerning general differences between astrocytes and neurons, but, unfortunately due to quality issues, it is not optimally suited to draw solid conclusions on consequences of Tet3 deletion on the transcriptomic level. Biological as well as technical problems may underly low RNA quality, but there seem to be not many options for optimization of the preparation procedure. For that reason, RNA from whole cerebral cortex and cerebellum of CTR and cKO animals will be analysed in the future. However, the results of this RNA sequencing experiment will represent bulk instead of cell type specific analysis, matching the proteomics data.

5.2.4 Analysis of adult neurogenesis

Due to the observed pathological phenotype of cKO animals regarding body and brain size as well as the widespread distribution of Nestin within the nervous system, alterations in

neurogenesis may be expected in Tet3 cKO animals compared to CTR. Therefore, neuroblast migration starting in the SVZ was analysed by IHC (Figure 31, Figure 32). During adult neurogenesis, neuroblast normally migrate in organized chains unidirectionally along the RMS towards the olfactory bulb. Immunohistochemical analysis of Dcx and Ki67, typical markers for neuroblast migration and cell proliferation, in mouse brain sagittal slices revealed a disorganization of the neuroblast chains in the RMS (Figure 31) as well as migrating and proliferating cells in the dorsal SVZ of cKO compared to CTR animals (Figure 32). These alterations concerning neurogenesis were detected in multiple immunohistochemical experiments of different replicates, revealing a novel link between Tet3 depletion in specific cell types and misdirected neurogenesis.

Several publications already assumed an involvement of Tet3 in other neurogenesis-related aspects. For example, Montalbán-Loro et al. recently suggest a role of the non-catalytic form of Tet3 in the maintenance of adult NSC state by a mechanism involving direct binding and repression of Tet3 to the imprinted gene *Snrpn* (Montalbán-Loro et al., 2019). A non-catalytic form of Tet3 could also be responsible for the observed abnormal phenotype formation in our study, as the design of the genetic deletion is still compatible with expression of a - catalytically inactive though - Tet3 protein, which could still support non-catalytic Tet3 function. Li et al. showed a critical role of Tet3 in NPC maintenance as well as terminal differentiation of neurons. In their study, Tet3 deficiency caused apoptotic cell death in cultured NPCs, resulting in decreased neuron generation (Li et al., 2015). Furthermore, Tet1 KO mice displayed altered hippocampal neurogenesis and cognition (Zhang et al., 2013). Transferring these findings to the pathological phenotype observed in the Tet3 L2 + Nestin Cre mouse model, Tet3 deficiency may not cause apoptosis, but stress conditions, which lead to impaired neurogenesis in the SVZ neurogenic niche. Moreover, misplaced Ki67 and Dcx positive cells in the dorsal lateral ventricle (Figure 32) might indicate problems in corticogenesis during embryonic development caused by deletion of Tet3 in Nestin Cre positive cells, which remain in the adult. Taken together, this suggests a role of Tet3 in embryonic development, but requires studies in embryos of cKO and CTR animals for further clarification.

Ependymocytes serve several essential functions including brain homeostasis as well as CSF production and transport (Del Bigio, 1995; Del Bigio, 2010; Spassky et al., 2005). In addition, they sense secreted molecules from the CSF through their cilia to regulate NSC proliferation and differentiation in the adult SVZ and facilitate CSF flow, which is important for neuroblast migration from the SVZ to the olfactory bulb (Del Bigio, 1995; Del Bigio, 2010; Kyrousi et al., 2015). Finally, ependymocytes display a functional role in adult neurogenesis and regeneration after injury following e.g. stroke, producing neuroblasts and astrocytes (Carlén et al., 2009; Kyrousi et al., 2015). It is tempting to speculate that Tet3 depletion in the Tet3 L2 + Nestin Cre mouse model might have affected ependymocyte function leading to a defective regulation of NSC proliferation and differentiation in the SVZ as well as of neuroblast migration from the SVZ to the olfactory bulb. Moreover, Tet3 deficiency might have caused injury-like conditions triggering ependymocytes to produce neuroblasts in a diffuse way in respective brain regions.

To summarise, depletion of Tet3 in Nestin Cre positive cells of the Tet2 L2 + Nestin Cre mouse brain affects energy metabolism and leads to conditions similar to those caused by different forms of stress such as stroke, ischemic lesions and hypoxia or hypothermia as well as impaired neurogenesis. Underlying mechanisms, probably starting during embryonic development, need to be further investigated.

In this context, it needs to be mentioned that the selection of matching levels of histological tissue sections from cKO animals for comparative analysis with CTR is hampered by their small brain volume size. The lateral ventricles, often used for orientation, are smaller in cKO animals, which complicates the choice of similar histological tissue sections. As already mentioned, the Nestin Cre line, used in this study, itself shows similar, but milder alterations. In some rare Nestin Cre positive brain sections, a mild disorder concerning neurogenesis was also detected, which needs to be considered.

To visualise cell migration *ex vivo* and to further analyse the alterations regarding adult neurogenesis and neuroblast migration from the SVZ to the olfactory bulb, SVZ explants were successfully established in the laboratory (Figure 33). The SVZ is carefully removed from the brain to maintain its cellular structure and brought into culture, where its cells continue

developing and migrating *ex vivo*. Validation experiments using IHC (Figure 34) showed the successful establishment and reproducibility of the method, which is a valuable tool e.g. for quantitative analysis of neuroblast migration starting in the SVZ and heading towards the olfactory bulb. Explant cultures in general have several advantages (JoVE Science Education Database, 2020a; JoVE Science Education Database, 2020b). For example, they enable the observation and manipulation of developing tissues in ways, which are hardly possible *in vivo*. Explant cultures can be used to test effects of specific compounds on tissue development, as the composition of the culture medium can be modified in multiple ways. Nevertheless, explants require special treatment after being removed from the organism. Culture medium as well as extracellular matrix used in an explant experiment need to imitate the natural conditions (JoVE Science Education Database, 2020a; JoVE Science Education Database, 2020b). Another option for *in vitro* analysis of neuroblast migration are neurosphere cultures, which were implemented in the lab, but still need some optimization.

SVZ explants of CTR and cKO (Figure 35) showed differences in neuroblast migration starting in the SVZ and confirmed obtained data from immunohistochemical experiments of brain sagittal sections (Figure 31). Tet3 cKO explants showed diffuse neuroblast migration leading into different directions and starting from several sides of the explant without forming the typical chains. This suggests an impaired neuroblast migration from the SVZ to the olfactory bulb by Tet3 deletion.

To conclude, SVZ explants are a valuable tool to investigate neuroblast migration in CTR and Tet3 cKO animals. Finally, some options for quantitative analysis are suggested for further experiments (Figure 48).

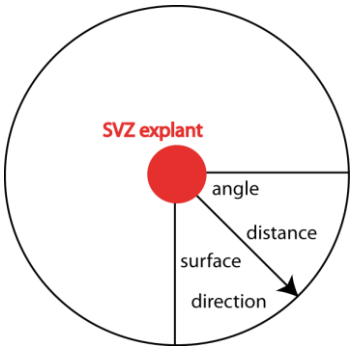

Figure 48: Quantitative analysis of neuroblast migration in SVZ explants

Neuroblast migration direction and distance as well as the occupied surface by migrating neuroblasts can be determined in SVZ explants of different genotypes using ImageJ software.

In addition to migration direction, the distance of migration can be measured and compared in SVZ explants of different genotypes requiring definition of specific starting and end points of the measurement in the ImageJ software. Furthermore, the surface occupied by migrating neuroblasts can be calculated. These parameters allow quantitative conclusions and comparisons of neuroblast migration in SVZ explants between different genotypes.

5.2.5 Conclusion

To conclude, the basic characterization of the Tet3 L2 + Nestin Cre mouse model revealed growth retardation, macroencephaly and a small lateral ventricle size in cKO animals in comparison to CTR animals, which complement the report about first identified *TET3* deficient human patients. The discovered abnormalities in the Tet3 L2 + Nestin Cre mouse model in addition to the mentioned reports about human *TET3* deficient patients confirms *Tet3* in being a candidate epigenetic machinery disease gene. Additionally, alterations regarding adult neurogenesis in the SVZ including diffuse neuroblast migration via the RMS to the olfactory bulb as well as proliferation in the dorsal SVZ were detected in the Tet3 L2 + Nestin Cre mouse model. Depletion of catalytically active Tet3 in Nestin Cre positive cells in the mouse brain leads to changes related to Tet3 function in energy metabolism of cells and to conditions similar to those caused by different forms of stress such as stroke, ischemic lesions and hypoxia or hypothermia, finally causing the observed pathological phenotype. Underlying mechanisms, probably starting in embryonic development, need to be further investigated. Furthermore, behavioural tests need to be performed to analyse behaviour in the Tet3 L2 + Nestin Cre mouse

model. Unfortunately, transcriptomic analysis of sorted cortical neurons and astrocytes does not allow much conclusion about consequences of Tet3 deletion on the transcriptomic level because of data quality issues.

5.3 Analysis of Tet3 isoforms

5.3.1 Tet3 L KO and Tet3 S KO mouse models

To investigate different functions of Tet3 isoforms *in vivo*, the aim was to generate mouse lines, which specifically lack either Tet3 L or Tet3 S isoforms.

The strategy for the generation of the Tet3 L KO mouse line was based on specific sgRNAs flanking, and thus deleting, the exon encoding the CXXC domain, which is specific for the Tet3 L isoforms, and the corresponding upstream promotor (Figure 49 - A). The procedure yielded a single mouse with the desired genetic deletion which was identified by a specifically designed genotyping assay. For the generation of the Tet3 S KO mouse line, the alternative promotor located upstream of exon 1, which is unique for Tet3 S, and exon 1 itself were deleted using specific sgRNAs (Figure 50 - A). Here, four mice with a successful deletion were identified by genotyping. In contrast to only two sgRNAs used to generate the Tet3 L KO mouse line, four sgRNAs were utilised to generate the Tet3 S KO mouse model, which might have increased the probability of successful deletion and possibly resulting in different deletion sizes, since more than one combination of sgRNAs may enable the deletion of the target region. Sanger sequencing revealed three different genomic deletions of different sizes in the Tet3 S KO founder lines. All four Tet3 S KO founder lines were analysed and compared in first validation experiments to detect possible differences.

For designing the KO approach for both mouse lines, the Eukaryotic Promotor Database (EPD) was screened for typical eukaryotic promotor elements such as TATA, GC and CCAAT boxes in the respective promotor regions of Tet3 L and Tet3 S. Whereas TATA boxes, generally part of the core promoter, regulate the site of transcription initiation, CCAAT and GC boxes bind transcription factors and influence the frequency of gene transcription by the polymerase (Karp, 2010).

Those typical promotor motifs were visualised in relation to the TSS (Figure 49 - B, Figure 50 - B). The high number of promotor motifs in the sgRNAs flanked part confirmed the assumption of the promotor localisation and the KO strategy for both Tet3 L KO and Tet3 S KO mouse models.

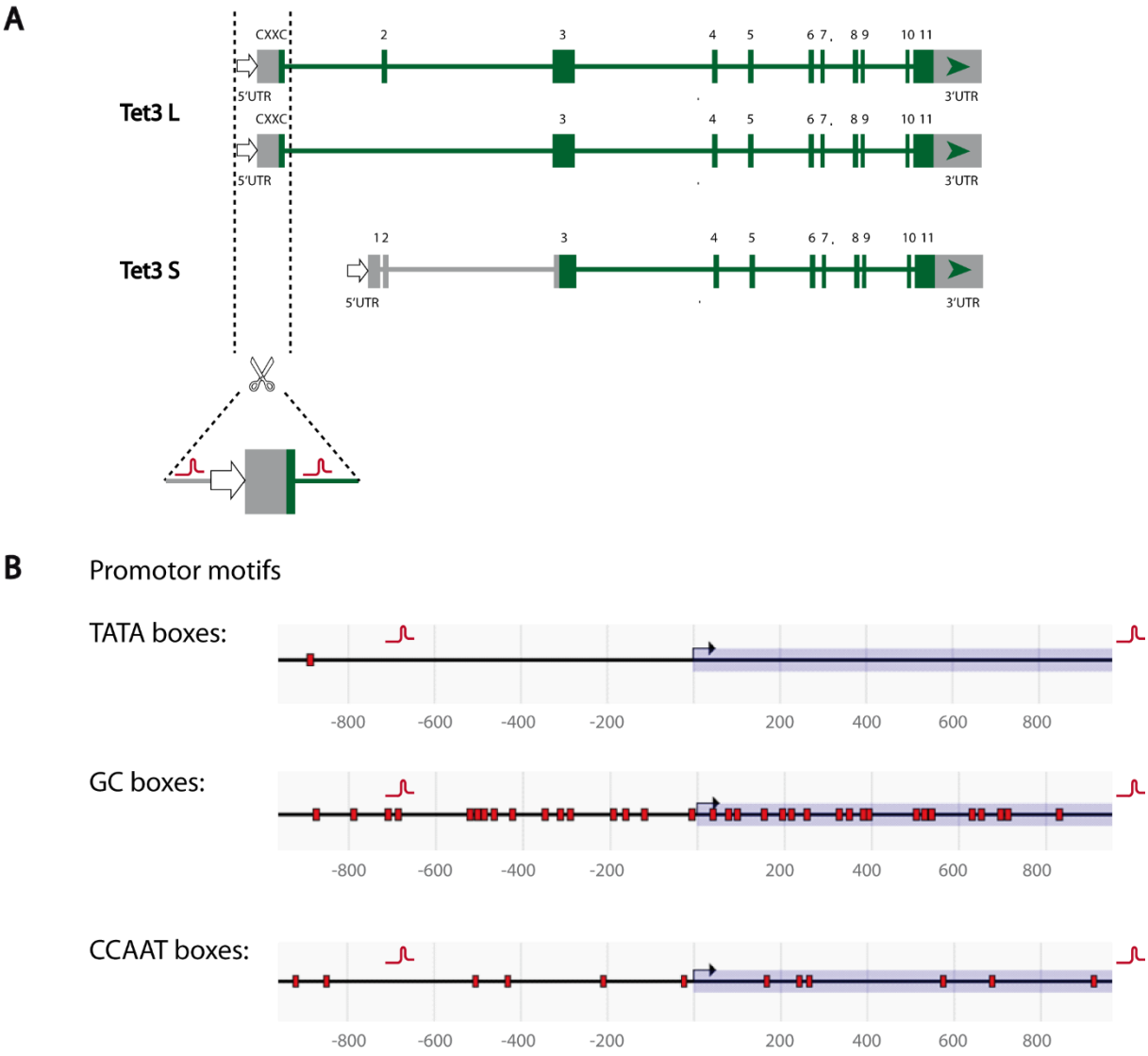

Figure 49: Localisation of promotor motifs - Tet3 L KO

(A) To generate the Tet3 L KO mouse line, the specific exon of Tet3 L isoforms encoding the CXXC domain and the corresponding promotor were deleted using CRISPR-Cas9 technology. **(B)** The Eukaryotic Promotor Database (EPD) was screened for typical promotor elements in the assumed region of the Tet3 L promotor with a cut-off p-value of 0.01 (p = 0.01). TATA boxes, GC boxes and CCAAT boxes are shown in relation to the TSS. The approximate positions of the used sgRNAs are marked.

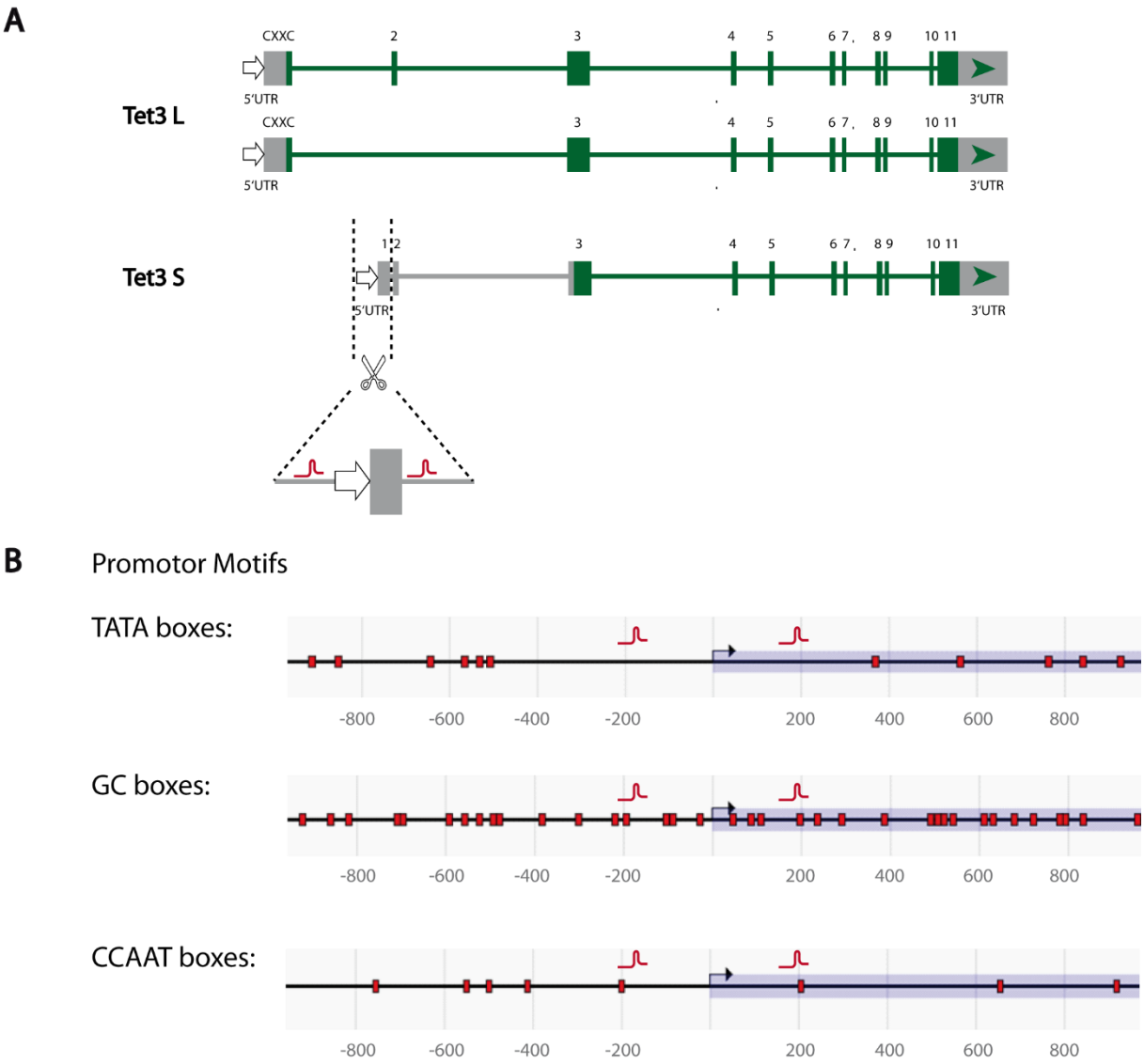

Figure 50: Localisation of promotor motifs - Tet3 S KO

(A) To generate the Tet3 S KO mouse line, the alternative promotor located next to exon 1, which is unique for the Tet3 S isoform, and exon 1 itself, were deleted using CRISPR-Cas9 technology. **(B)** The Eukaryotic Promotor Database (EPD) was screened for typical promotor elements in the assumed region of the Tet3 S promotor with a cut-off p-value of 0.01 (p = 0.01). TATA boxes, GC boxes and CCAAT boxes are shown in relation to the TSS. The approximate positions of the used sgRNAs are marked.

The first step to validate the generated mouse lines was to examine possible off-target effects of the used CRISPR-Cas9 system (Table 8). As frequently reported, Cas9 endonuclease can cleave off-target DNA sequences in the genome leading to uncontrolled genome modifications, which can be highly problematic especially when applying CRISPR-Cas9 technology in clinical therapy (Zhang et al., 2015). Several factors are discussed to contribute to off-target effect formation. For example, the sgRNA, consisting of a non-seed and a seed sequence, impacts the

formation of off-target effects (Cong et al., 2013; Zhang et al., 2015). Furthermore, the PAM sequence is relevant for Cas9 activity (Duan et al., 2014; Zhang et al., 2015). For those reasons, the choice of sgRNAs requires careful design for each specific approach. Here, the CRISPOR website with a 20 bp-NGG PAM setting for *Sp*Cas9 and a specificity score lower than 50 for the sgRNA elimination was used to predict the most specific sgRNA sequences in the target region. In this study, the predicted five most probable exonic off-target regions in the Tet3 L KO and Tet3 S KO mouse genome per used sgRNA were analysed to investigate potential mutations resulting from Cas9-mediated DSB generation and incorrect repair. For both Tet3 L KO and Tet3 S KO mouse lines, all tested loci did not show any differences in the off-target sequence compared to the mouse reference genome indicating low off-target activity of the used Cas9 RNP complexes. However, NGS techniques are necessary to make an absolute and final statement about the absence of off-target effects in the generated mouse lines. Moreover, it was discovered that complex genome rearrangements and extensive on-target effects such as deletions of up to several kb can occur using the CRISPR-Cas9 system, which cannot be detected using short range PCR assays (Kosicki et al., 2018). Since PCR assays with specific primer pairs flanking the sgRNA binding sites were used to determine the deletion size caused by the system in the different obtained mouse lines, larger deletions would not have been detected. As in the first founder mice also WT bands were detected, assuming heterozygosity for the KO allele, larger deletions are quite unlikely, because of diploidy. On top of that, PCR amplification followed by Sanger sequencing was also used to investigate possible off-target effects, yielding product bands of around 600 to 900 bp. Here, larger deletions might not be detected.

To further validate the generated mouse lines was to analyse mRNA expression levels of *total Tet3* and *Tet3* isoforms in retina and brain tissue of 4-week-old mice by qRT-PCR (Figure 38). *Total Tet3* transcript levels in retina showed a slight decrease in Tet3 L KO animals and were even significantly reduced in all Tet3 S KO founder lines, confirming that Tet3 S plays a major role in the retina. In contrast, no significant differences in *total Tet3* mRNA expression levels in cerebral cortex in Tet3 L KO and Tet3 S KO mouse lines in comparison to WT were detected, suggesting compensation mechanism between the isoforms. This assumption was confirmed by separately analysing transcript levels of *Tet3 L* and *Tet3 S*. On the one hand, mRNA

expression levels of *Tet3 L* isoforms significantly increased in all Tet3 S KO founder lines in retina and cerebral cortex in comparison to WT, whereas they were not detectable in Tet3 L KO animals. On the other hand, *Tet3 S* transcript was not detectable in all Tet3 S KO founder lines, whereas it was detectable in WT and Tet3 L KO animals in retina and cortex. Moreover, in Tet3 L KO animals, *Tet3 S* transcript levels significantly increased in cortex compared to WT, whereas they did not increase in retina. This suggests that Tet3 L isoforms do not play a major role in retina, already shown by (Perera et al., 2015), as their KO does not cause compensation by Tet3 S, indicating that differences in *Tet3 L* transcript levels do not affect the system. To conclude, the results of qRT-PCR analysis of *total Tet3*, *Tet3 L* and *Tet3 S* transcript levels confirms the respective deletion of specific regions of the *Tet3* gene and additionally suggests compensation between the different Tet3 isoforms. This finding matches reports about compensation mechanisms by increased expression or increased activity of remaining Tet enzymes in some cases after deletion of one or several Tet family members (Lio and Rao, 2019; Rasmussen and Helin, 2016).

Further validation of the generated mouse lines was performed by IHC (Figure 39) using specific antibodies for either the N-terminal or C-terminal part of the Tet3 protein. The C-terminus specific antibody (Tet3 #54) should recognize all Tet3 isoforms, because this part is common for all Tet3 isoforms. In contrast, the N-terminus specific antibody (Tet3 #55) should only recognize Tet3 L, because this CXXC domain containing part is specific for Tet3 L isoforms. Consequently, an absence of Tet3 S isoform cannot be visualised using these antibodies. Tet3 protein signal was detected in mouse retina as well as brain slices of WT, Tet3 L KO and Tet3 S KO animals using both antibodies. Surprisingly, in Tet3 L KO retina and brain slices, Tet3 L signal appeared not to be different than in the control and Tet3 S KO slices. In those samples, the N-terminal specific antibody should not bind any protein in principle, questioning the success of the KO strategy in general, but also questioning the specificity of the antibodies. To fully understand whether deletion of putative promotor regions and unique exons really abolishes transcriptome of Tet3 L and Tet3 S isoforms, a 5' RACE (rapid amplification of cDNA ends) needs to be performed to analyse the 5' sequence of all existing transcripts in Tet3 L and Tet3 S KO mouse lines.

Furthermore, cytosine modifications were detected in Tet3 L KO, Tet3 S KO and WT animals by IHC (Figure 40, Figure 41) and UHLPC-MS/MS (Figure 42). As IHC is not a quantitative method, global levels of 5mC and 5hmC in gDNA samples of retina and different brain regions of WT as well as Tet3 L KO and Tet3 S KO animals were quantified by UHPLC-MS/MS analysis. 5mC levels did not differ significantly in retina tissue between WT, Tet3 L KO and Tet3 S KO animals. 5hmC levels decreased significantly in retina samples of all Tet3 S KO founder lines, whereas there was no significant change in 5hmC levels of Tet3 L KO animals in comparison to WT, indicating again the major role of the Tet3 S isoform in the retina. Both 5mC and 5hmC levels did not change significantly in cerebral cortex samples between all analysed genotypes, which was also observed for hippocampus und cerebellum tissue samples. To conclude, data obtained from the quantification of global 5mC and 5hmC levels in retina and different brain tissues fits to the results of the qRT-PCR experiments. In Tet3 S KO retina, the general activity of Tet3 is reduced and therefore less 5hmC is produced, confirming that the Tet3 S isoform is the major Tet3 isoform in the retina and compensation by Tet3 L isoforms is not enough to balance 5hmC levels. In cerebral cortex and other brain regions, *total Tet3* levels as well as 5hmC levels did not change in all analysed genotypes, underlining the compensation mechanism between the different Tet3 isoforms.

Lastly, the proteome of whole brain and retina of WT, Tet3 L KO and Tet3 S KO animals was analysed by mass spectrometry (Figure 43). Comparisons for Tet3 L KO or Tet3 S KO vs. WT retina and brain tissue revealed a few differences between the genotypes. Significantly enriched or depleted histones, crystallins and keratins were considered as non-specific impurities and excluded from the analysis. A diversity of different proteins was detected, ranging from proteins involved in translation initiation, significantly depleted in both Tet3 L and Tet3 S KO retina compared to WT, to chromatin organizers for proper RGC function, significantly enriched in Tet3 L KO retina tissue, or to proteins playing a role in degeneration of RGCs and photoreceptors, significantly enriched in Tet3 S KO retina. Furthermore, in brain tissue, proteins involved in cancer development, significantly depleted in both Tet3 L KO and Tet3 S KO, or proteins important for cytoplasmic mRNA transport, significantly enriched in Tet3 L KO tissue, as well as proteins critical for sperm mitochondrial function, significantly

enriched in Tet3 S KO, were detected. Due to the low number and diversity of the finding, no conclusion can be drawn to connect Tet3 isoforms with specific enriched or depleted proteins and further with biological processes or disease mechanisms. Other more specific and sensitive approaches, e.g. transcriptome analysis of sorted cell populations, are required to assess the role of Tet3 isoforms in the organisms.

Importantly, Tet3 L KO as well as Tet3 S KO mouse lines did not show an abnormal phenotype regarding e.g. body size and weight as the Tet3 L2 + Nestin Cre mouse model. Further characterization of morphology and structural integrity of retina and brain by IHC, RNA sequencing, ophthalmic examinations like optical coherence tomography (OCT) and electroretinography (ERG) to assess the impact of Tet3 L and Tet3 S KO on vision as well as behavioural tests are necessary. Furthermore, examinations of earlier time points and even of embryonic stages need to be considered, since in adult mice compensation mechanisms between the Tet3 isoforms seem to hide or balance any possible effect, maybe occurring during development as a result of Tet3 isoform KO.

As on molecular level, no differences were detected between the different Tet3 S KO founder lines, further analysis could focus on only one founder line to make a large-scale characterization feasible. Tet3 S KO founder line 4 shows the biggest deletion in comparison to the others, which is associated with the highest probability of successful Tet3 S KO.

To sum up, the generation of Tet3 L and Tet3 S KO mouse lines was successful, which first validation by genotyping and qRT-PCR experiments showed. After the crucial analysis of existing transcripts via 5' RACE and further validation, the two generated KO models can serve as a promising starting point to investigate the different roles of Tet3 isoforms *in vivo*.

5.3.2 TET3 isoform overexpressing cell lines

To have a complementary *in vitro* model to the Tet3 L KO and Tet3 S KO mouse lines, TET3 isoform overexpressing human iPS cell lines (PGP1 and iNGN cells) were generated by inserting the coding sequences of TET3 isoforms into the iPS cell genome using PiggyBac transposon technology (Figure 13, Figure 44). Overexpression of TET3 isoforms is induced by DOX addition to the cells. Since iNGNs contain a DOX inducible neurogenin cassette in the

genome, neuronal differentiation as well as TET3 isoform overexpression is simultaneously induced by DOX application.

TET3 S trunc is a shortened version of TET3 S, lacking the exon, which is specific for the TET3 S isoform. The inserted coding sequence starts within exon 3 of the *TET3* gene, which is common for all TET3 isoforms. TET3 S trunc shows normal catalytic activity but does not represent the occurring TET3 S isoform. For that reason, findings of experiments with TET3 S trunc overexpression cannot be fully transferred to TET3 S isoform action.

After adding DOX to the respective systems, different phenomena were observed in PGP1 and iNGN cell lines (Figure 44). TET3 isoforms overexpressing PGP1 cells showed normal growth and development (Figure 44 - C), whereas simultaneous induction of TET3 isoform overexpression and neuronal differentiation in iNGNs led to cell death (Figure 44 - B). This interesting finding shows the relevance of TET3 in neuronal differentiation independently from isoforms, since cell death was observed in TET3 L as well as TET3 S trunc overexpressing iNGNs. The involvement of TET3 in cell differentiation processes was already reported in numerous publications and reviews (Koivunen and Laukka, 2018; Li et al., 2015; Lio and Rao, 2019; Wu and Zhang, 2017). Furthermore, several reports showed cell death phenomena in the context of overexpression of TET enzymes. For example, overexpression of Tet1 was demonstrated to increase cell apoptosis and to inhibit cell growth in osteosarcoma cells (Teng et al., 2019). Moreover, TET3 overexpression was reported to impair and reduce cell growth and tumour formation glioblastoma cells (Carella et al., 2020).

TET3 L and TET3 S trunc overexpressing PGP1 cells were analysed by qRT-PCR to determine mRNA expression levels of *TET1*, *TET2* and *TET3* at d3 and d8 after DOX addition (Figure 45). Transcript levels of *TET3 S* isoform cannot be determined because the unique exon for *TET3 S* is missing in the *TET3 S trunc* version. Therefore, mRNA levels of *total TET3* represent levels of *TET3 S trunc* in addition to native *total TET3* levels of the cells. Expression levels of *total TET3* increased in both TET3 L and TET3 S trunc overexpressing cell lines after DOX application, confirming that the DOX-inducible *TET3* gene expression cassettes were successfully integrated into the PGP1 genome and functional. In addition to that, mRNA

expression levels of *TET3 L* increased in TET3 L overexpressing cells, whereas transcript levels of *TET3 L* did not increase in TET3 S trunc overexpressing cells, meeting the expectations and additionally confirming the successful generation of the cell lines. On d3 of DOX incubation, a higher increase in *total TET3* and *TET3 L* mRNA expression levels was detected in comparison to d8 of DOX incubation. Regarding this finding, several reasons can be discussed. On the one hand, toxic effects of TET3 overexpression may cause cell death leading to lower numbers of cells expressing TET3 L and TET3 S trunc isoforms and in consequence to lower mRNA expression levels of *total TET3* and *TET3 L*. On the other hand, feedback mechanisms may play a role in the system. Reaching a certain expression level may lead to depressing effects on TET3 expression, preventing the cells from possible toxic effects of too high levels. Regarding expression levels of *TET1* and *TET2* transcripts, no significant changes were detected, indicating that overexpression of TET3 L and TET3 S trunc isoforms does not influence mRNA expression levels of *TET1* and *TET2*.

Next, global levels of 5mC, 5hmC and 5fC in TET3 L and TET3 S trunc overexpressing PGP1 cells at d3 and d8 after DOX addition were analysed by UHPLC-MS/MS (Figure 46). In contrast to other experiments, 5fC levels were measurable in all conditions (Figure 46 - D). The detectable 5fC levels in the TET3 isoform overexpressing PGP1 cells can be explained by higher cytosine modification levels in iPS cell lines in comparison to e.g. different mouse brain regions. For that reason, 5fC levels in this study exceeded the detection limit of the method, whereas in mouse brain tissues the limit was not reached. 5mC levels did not change significantly in TET3 L and TET3 S trunc overexpressing cells at d3 of DOX incubation, whereas they significantly decreased for TET3 L overexpressing cells in comparison to the control at d8 of DOX incubation. Here, a reason may be again a toxic effect of TET3 isoform overexpression causing cell death and, consequently, lower 5mC levels. 5hmC levels significantly increase for TET3 L and TET3 S trunc overexpressing cells in comparison to control at d3 of DOX incubation, displaying the catalytic activity of TET3 L and TET3 S trunc isoforms to generate 5hmC by 5mC oxidation. In contrast, no changes in 5hmC levels were detectable in cells harvested at d8 of DOX incubation. Toxic effects may also play a role regarding 5hmC levels. Additionally, feedback mechanism may lead to decreasing 5hmC generation or to an increased

5hmC oxidation to 5fC and following products. 5fC levels significantly increased for TET3 L and TET3 S trunc overexpressing cells in comparison to control at d3 and d8 of DOX incubation. With regard to the whole demethylation process during the eight days of DOX incubation of TET3 isoform overexpressing PGP1 cells, it can be assumed that an extensive oxidation of 5mC to 5hmC and further to 5fC is in process at d3 of DOX incubation, explaining the high levels of 5hmC and 5fC at this time point. In comparison to 5hmC and 5fC levels, 5mC levels did not change significantly. Only a tendency to decrease was observed for 5mC levels in TET3 S trunc overexpressing cells. Probably, this is due to the sensitivity of the method and higher 5mC levels per dN in the gDNA compared to 5hmC and 5fC. Until d8 of DOX incubation, all newly generated 5hmC and 5fC molecules may have been converted into unmodified cytosines, explaining levels equal to control. However, 5mC levels finally displayed a statistically significant decrease as a consequence of the extensive demethylation processes caused by TET3 overexpression. Nevertheless, more time points during the DOX incubation period need to be analysed to fully understand the DNA demethylation processes in this system. As the 8oxoG levels stayed under a biological relevant number in all conditions during the whole experiment ($< 5 \cdot 10^{-6}$ 8oxoG/dN), an influence of other than TET3-mediated oxidation processes on cytosine modification levels can be excluded. The slightly increased 8oxoG levels of the TET3 L control condition at d8 may be explained by more DNA damages during sample preparation in comparison to the other conditions.

To conclude, the data confirm that the generation of 5hmC and 5fC is dependent on TET3 levels. Overexpression of TET3 L and TET3 S trunc isoforms leads to an increase of 5hmC and 5fC generation. It seems that overexpression of TET3 S trunc isoform has a higher impact on the oxidation processes, as in this cell line, higher levels of 5hmC and 5fC were detected than in TET3 L isoform overexpressing PGP1 cells. This suggests that N-terminal domains in TET3 L limit and / or inhibit TET3 catalytic activity e.g. by limiting its activity to specific genomic sites through protein-DNA or protein-protein interactions. Differences between d3 and d8 conditions were observed in both qRT-PCR and UHPLC-MS/MS experiments, which might be best explained by toxic effects and feedback mechanisms occurring in the cells in response to TET3 isoform overexpression.

In conclusion, the generation of TET3 isoform overexpressing cell lines was successful. After further validation, they display a good basis for *in vitro* models such as organoids and for further investigations of cell differentiation, cell metabolism or cell cycle and their dependency on TET3 isoforms. In this context, the finding of cell death as a consequence of simultaneous induction of TET3 isoform overexpression and cell differentiation opens opportunities to investigate cell death.

5.4 Summary

Taken together, the present dissertation shows successfully generated mouse and cell culture models to investigate multifaceted roles of Tet3 in neurons, additionally forming a promising basis for future analyses of Tet3 involvement in disease mechanisms.

Whereas characterization of the Tet3 L2 + Nestin Cre mouse model revealed a pathological phenotype including growth abnormalities, impaired brain size and altered adult neurogenesis in cKO animals, complementing the report about first identified *TET3* mutant human patients, the specific KO of Tet3 L and Tet3 S isoforms, respectively, appeared not to cause similar disorders. Possibly, compensation mechanisms between the Tet3 isoforms prevent abnormal phenotype formation in Tet3 L KO and Tet3 S KO mouse lines, whereas, in the Tet3 L2 + Nestin Cre mouse model, Tet1 and Tet2 seem not to be able to compensate loss of catalytically active Tet3. Nevertheless, overexpression of TET3 in human iPS cells indicates possible toxic effects on cell growth, suggesting that both Tet3 depletion and overexpression impact neuronal processes. In addition, the study demonstrated that altered neuronal activity in the brain leads to impaired Tet3 action and 5hmC patterns in genes related to diseases, possibly offering new options for therapeutic interventions.

6 Appendix

6.1 Primers

Table 11: Primer sequences used for genotyping

Name		Sequence
Tet3 S KO	forward	5‘- ATACCCACATACTGCCGCTC -3‘
	reverse 1	5’- GCCGGGCCTCCCATTATC -3’
	reverse 2	5’- GACAGTCGCCCCTTGTG -3’
Tet3 L KO	forward	5’- TGGGTTGTGACCCTCATGC -3’
	reverse 1	5’- CAGCCCAAGCTGTCGAGG -3’
	reverse 2	5’- ATGCAAGAACAGGAGCCCAC -3’
RD8 mCrb1	forward 1	5’- GTGAAGACAGCTACAGTTCTGATG -3’
	forward 2	5’- GCCCCTGTTTGCATGGAGGAAACTTGGAAGACAGCT ACAGTTCTT -3’
	reverse	5’- GCCCCATTTGCACACTGATGAC -3’
Tet3 L2	forward 1	5’- CAGACAGTGGCATAGCAGTGG -3’
	forward 2	5’- TGAGTAAGAGCAGGCAGGGAG -3’
	reverse	5’- CTAGCACCTCAGTCTGGGACC -3’
Cre	forward	5’- GCAGAACCTGAAGATGTTCGC -3’
	reverse	5’- ACACCAGAGACGGAAATCCAT -3’
Nestin Cre	forward 1	5’- TTGCTAAAGCGCTACATAGGA -3’
	forward 2	5’- CCTTCCTGAAGCAGTAGAGCA -3’
	reverse	5’- GCCTTATTGTGGAAGGACTG -3’

Table 12: Primer sequences used for qRT-PCR

* Primers were ordered from (Eagle-I Network, 2011; Hasel et al., 2017; Ma et al., 2009; Ramamoorthi et al., 2011).

Name		Sequence
mAlas	forward	5’- TCGCCGATGCCCATTCTTATC -3’
	reverse	5’- GGCCCCAACTTCCATCATCT -3’
Total mTet3	forward	5’- GAGCACGCCAGAGAAGATCAA -3’
	reverse	5’- CAGGCTTTGCTGGGACAATC -3’
Tet3 del	forward	5’- GGTCACAGCCTGCATGGACT -3’
	reverse	5’- AGCGATTGTCTTCCTTGGTCAG -3′
mTet3 L	forward	5’- ATCGTCGCACACACCAGATC -3’
	reverse	5’- TCCTTCACGAGCATTTATTTCCA -3’
mTet3 S	forward	5’- GCGGCCGATGCAGTAGTG -3’
	reverse	5’- ATCAACTGGGCTGAGCTCTGA -3’

mTet1	forward	5’- TGAAGCTCAAACATCAAGCA -3’
	reverse	5’- GTACCTCCATCACAGTCAC -3’
mTet2	forward	5’- AGCGGAGCCCAAGAAAGCCA -3’
	reverse	5’- GCAAAGCTGCGGTTGTGCTGT -3’
mArc *	forward	5’- TACCGTTAGCCCCTATGCCATC-3’
	reverse	5’- TGATATTGCTGAGCCTCAACTG-3’
mNPas4 *	forward	5’- CTGCATCTACACTCGCAAGG -3’
	reverse	5’- GCCACAATGTCTTCAAGCTCT -3’
mBdnf total *	forward	5’- GCCTTTGGAGCCTCCTCT -3’
	reverse	5’- CTGTCACACACGCTCAGCTC -3’
mGfap *	forward	5’- TCCTGGAACAGCAAAACAAG -3’
	reverse	5’- CAGCCTCAGGTTGGTTTCAT -3’
Total hTET3	forward	5’- GCAAGACACCTCGCAAGTTC -3’
	reverse	5’- CCTCGTTGGTCACCTGGTTC -3’
hTET3 L	forward	5’- CTGGAAAACTGTGGCGCTTG -3’
	reverse	5’-TTGACAGCCGCTCCTTGTCC -3’
hTET1	forward	5’- GCTCTCATGGGTGTCCAATTGCT -3’
	reverse	5’- ATGAGCACCACCATCACAGCAG -3’
hTET2	forward	5’- AAGGCTGAGGGACGAGAACGA -3’
	reverse	5’- TGAGCCCATCTCCTGCTTCCA -3’
hACTB	forward	5’- GCCGCCAGCTCACCAT -3’
	reverse	5’- CACGATGGAGGGGAAGACG -3’

Table 13: Primer sequences used for off-target analysis

Name		Sequence
intergenic Rpl31	forward	5’- AATGTGGTAACAGGCGCGTA -3’
	reverse	5’- AGCTGGGCCTGTAAAGAGTG -3’
exon Rpl31	forward	5’- CTCCACTGCTCAAGGCAGAT -3’
	reverse	5’- ACACACAACCACACCGGAAT -3’
intergenic Gm10974-Lrrk1	forward	5’- GGGTTCTAGCTCTGCACTCG -3’
	reverse	5’- CGTCTACCGAGGCACAAGAG -3’
intergenic Nfkb1-Gm9799	forward	5’- CAGTCAGTTTGGAGGCTGGG -3’
	reverse	5’- GGAATGCAGAGACACGGACT -3’
exon Kcnc3	forward	5’- GATTAGGGGAGGGAGAGCCA -3’
	reverse	5’- CCACCTAACCCAGTTCCC -3’
intergenic 1700021A07Rik-1700020N01Rik	forward	5’- TCAGAGCCCCTTGTGGAATG -3’
	reverse	5’- GCCATATCTGGAGTAGCGCA -3’
Intergenic Fau-ps1-Macrod2.a	forward	5’- GCTGAGGCTGGAGTTTGAGA -3’
	reverse	5’- TCAGGAGTTGCCTTTGCTGT -3’
intergenic Capn2-Capn8	forward	5’- AAGTGTTACCGGCAGACTGT -3’
	reverse	5’- TCACATTCGCCCCTACTTCC -3’

exon Agpat4	forward	5’- TAGGACTCTTCTGCGGGTGA -3’
	reverse	5’- AACTGACCACTGCTGCCTTC -3’
exon Caskin2	forward	5’- CTAGTGAAGGTGGCTCGGTG -3’
	reverse	5’- CTCGCCTCCTCACCTTTCAG -3’
intron A330033J07Rik	forward	5’- TTTGCTCTGAGGCAGAATGC -3’
	reverse	5’- CGAGGAAGCCAAGAGACCAG -3’
intergenic Gm20594-Gm4409	forward	5’- CCCACCTGATCCCTCTTGTT -3’
	reverse	5’- CATACAAAGGCCAGGGGTGT -3’
intergenic Gm13878-Gm13880	forward	5’- ACAGGCACAAAGCACACACA -3’
	reverse	5’- ACATGTGTGCCATAGCATAGTC -3’
exon Pard6a	forward	5’- GCCCCCAGGCTTTATGTTCT -3’
	reverse	5’- CAGGTCACTGCTGTCATCGT -3’
exon Kif3c	forward	5’- GGGTGGATTCCAGGCACTAC -3’
	reverse	5’- CAGGTACTGCTGGTTCTGGG -3’
exon Plekhh3	forward	5’- TATCCCCAAGCCTTACCCCA -3’
	reverse	5’- CAAGGCCATGGTTACTCCCA -3’
intron Zfp236	forward	5’- AAGGTGCGCTACAGATGACT -3’
	reverse	5’- CGTGCTGGCATTGTAGGTGT -3’
intron Txnrd3	forward	5’- CGACAACAAAGCCCTGGAGA -3’
	reverse	5’- TCCCTATTAGCCCCTCCCAC -3’
intron Abat	forward	5’- ATTGGGTGATGTGCAAAGAATGG -3’
	reverse	5’- TTGTCAGTAGGGTCTGCCTTG -3’
exon Bmp8a	forward	5’- GGATTTCACGCTGCATGTCG -3’
	reverse	5’- AGACACTACGGGTCCTACCG-3’
intergenic Gm17150 1700019N19Rik	forward	5’- CGGTGAATGTAGCAGCCCTT -3’
	reverse	5’- CACGTGGGATACTCTGGTGA -3’
intergenic 3110021A11Rik-Gm15532	forward	5’- CCGGACTTCAGTAAAACTTAATGCT -3’
	reverse	5’- CACGCTTGGAGACACTCACT -3’
intergenic Gm25261-Gm831	forward	5’- CCCACTGAGGTGTGTCAGAG -3’
	reverse	5’- AAGGGAAAACACCCAGCAGT -3’
exon Snx29	forward	5’- TCACCAGGGAAGAGTGCTTG -3’
	reverse	5’- ACGGGTAAGTTCCTCCCACT -3’
exon Ralb	forward	5’- TATGCTTGGATGCAGGTGCC -3’
	reverse	5’- AAATGGTGGAATAAGGCAGAACT -3’
intergenic Gm13658-Gm13660	forward	5’- CACGCAGAGTGAGCAAAGTC -3’
	reverse	5’- TTGCAGGGTTTCGCCTGATA -3’
intergenic Rpl28-ps4-Gm9946	forward	5’- TGAGCTATCTCCCACCCCTC -3’
	reverse	5’- CTGCGTCTTCCACGCAAATG -3’
intergenic Dnajb1-Gipc1	forward	5’- GAGGAGAAACAGAGGCAGCA -3’
	reverse	5’- TGTCCAGCTTTTTCTGGGGG -3’
exon Tcam1	forward	5’- AAGGCGGAGACAATGTGAGG -3’
	reverse	5’- GAGTGTGGCACCCTAAGACC -3’
exon Katnal1	forward	5’- TACCCCAAAGAGGCAGAAAGG -3’
	reverse	5’- AGAAGGTAGAAGCAGGGCGA -3’

Table 14: Cloning oligos and gene fragments used for cloning

Name		Sequence
TET3 L	forward	5'- ATAGCTAGCGCCACCATGGACTACAAGGACG -3'
	reverse	5'- ATAGCATTTAAAATCCCCAGCATGCCTGCTATTG -3'
TET3 S	forward	5'- CGGAGGACTCGACCCTCGCCCAAGCCCCGAT -3'
	reverse	5'-ACTTAGATTCAGCTGGATCCGATTTAAATTCCCCAGCATGCCT GCTATTG -3'
Tags - TET3 S (gene fragment)		5'- TTCCTACCCTCGTAAAGGTCTAGAGCTAGCGCCACCATGGAC TACAAGGACGACGATGACAAGCTCGATGGAGGATACCCCTACG ACGTGCCCGACTACGCCGGAGGACTCGACCCTCGCCCAAGCC -3'

6.2 Genotyping - PCR cycling parameters

Table 15: Tet3 L2 - PCR cycling parameter

The PCR protocol was obtained from Prof. Petra Hajkova's research group at the Imperial College in London.

Step	Temperature	Time	Number of cycles
Initial denaturation	94 °C	2 min	1
Denaturation	94 °C	45 s	40
Annealing	60 °C	45 s	
Extension	72 °C	1 min	
Final extension	72 °C	3 min	1
Soak	4 °C	indefinite	1

Table 16: Cre Recombinase - PCR cycling parameters

Step	Temperature	Time	Number of cycles
Initial denaturation	98 °C	2 min	1
Denaturation	98 °C	15 s	35
Annealing	58 °C	30 s	
Extension	72 °C	1 min	
Final extension	72 °C	10 min	1
Soak	4 °C	indefinite	1

Table 17: Nestin Cre - PCR cycling parameters

The PCR protocol is available from the genotyping protocol database of the Jackson Laboratory on https://www.jax.org/Protocol?stockNumber=003771&protocolID=31758.

Step	Temperature	Time	Number of cycles
Initial denaturation	94 °C	2 min	1
Denaturation	94 °C	20 s	10 (touchdown)
Annealing	65 °C (-0,5 °C per cycle)	15 s	
Annealing	68 °C	10 s	
Denaturation	94 °C	15 s	28
Annealing	60 °C	15s	
Extension	72 °C	10s	
Final extension	72 °C	2 min	1
Soak	4 °C	indefinite	1

Table 18: Tet3 S KO - PCR cycling parameters

Step	Temperature	Time	Number of cycles
Initial denaturation	95 °C	3 min	1
Denaturation	95 °C	30 s	40
Annealing	57 °C	45 s	
Extension	72 °C	30 s	
Final extension	72 °C	5 min	1
Soak	4 °C	indefinite	1

Table 19: Tet3 L KO - PCR cycling parameters

Step	Temperature	Time	Number of cycles
Initial denaturation	95 °C	3 min	1
Denaturation	95 °C	30 s	40
Annealing	55 °C	45 s	
Extension	72 °C	30 s	
Final extension	72 °C	5 min	1
Soak	4 °C	indefinite	1

6.3 Antibodies

Table 20: Antibodies used in immunocyto- and immunohistochemistry

* Those antibodies require a treatment with 2 N HCl for at least 20 min (5hmC antibodies) or 50 min (5mC antibody) followed by two washing steps with 0.1 M Tris-HCl pH = 8.5 for 5 - 10 min each before blocking. ** Those antibodies were generated in collaboration with Prof. Dr. med vet. Hermann Ammer, Faculty of Veterinary Medicine, Institute of Pharmacology, Toxicology and Pharmacy at LMU Munich.

Primary Antibodies				
Antibody	**Order no.**	**Company**	**Host**	**Dilution**
anti-5mC *	C15200081	Diagenode	mouse	1:300
anti-5hmC *	40000	Active Motif	mouse	1:1,000
anti-5hmC *	39769	Active Motif	rabbit	1:1,000
anti-Tet3 C-terminal	CT-5454	self-made **	rabbit	1:250 - 1:500
anti-Tet3 N-terminal	NT-5455	self-made **	rabbit	1:250 - 1:500
anti-Dcx	sc-271390	Santa Cruz	mouse	1:100
anti-Dcx	AB2253	Merck Millipore	guinea-pig	1:250
anti-Ki67	MA5-14520	Thermo Fisher Scientific	rabbit	1:250
anti-Gfap	Z033429-2	Agilent	rabbit	1:100
anti-Gfap-Cy3	C9205-2ML	Sigma Aldrich	mouse	1:1,000

Secondary Antibodies				
Antibody	**Order no.**	**Company**	**Host**	**Dilution**
Cy3 anti-rabbit	711-165-152	Jackson ImmunoResearch	donkey	1:400
Alexa 488 anti-rabbit	4412S	Cell Signaling	goat	1:400
Alexa 647 anti-rabbit	A21443	Life Technologies	chicken	1:400
Cy3 anti-mouse	715-165-150	Jackson ImmunoResearch	donkey	1:400
Alexa 488 anti-mouse	A-11001	Thermo Fisher Scientific	goat	1:800
Cy2 anti-guinea pig	706-225-148	Jackson ImmunoResearch	donkey	1:200
Cy3 anti-guinea pig	706-165-148	Jackson ImmunoResearch	donkey	1:400
Alexa 594 anti-guinea pig	A-11076	Thermo Fisher Scientific	goat	1:400

Table 21: Antibodies used for FACS

Antibody	Order no.	Company	Host	Dilution
anti-ACSA-2-PE	130-116-244	Miltenyi	mouse	1:50
anti-CD90.2-APC	130-120-898	Miltenyi	mouse	1:50
anti-CD11b-PE-Cy7™	552850	BD Biosciences	rat	1:500
anti-Gfap	Z033429-2	Agilent	rabbit	1:100
Alexa 488 anti-rabbit	4412S	Cell Signaling	goat	1:500
anti-NeuN-Alexa 488	MAB377X	Millipore	mouse	1:100

Table 22: Antibodies used for Western Blot

Antibody	Order no.	Company	Host	Dilution
anti-GFP	632380	Clontech, Takara	mouse	1:2000
HRP-conjugated anti-rabbit IgG	A0545	Sigma-Aldrich	goat	1:5000
HRP-conjugated anti-mouse IgG	2031	Santa Cruz	goat	1:2000

6.4 Supplemental data

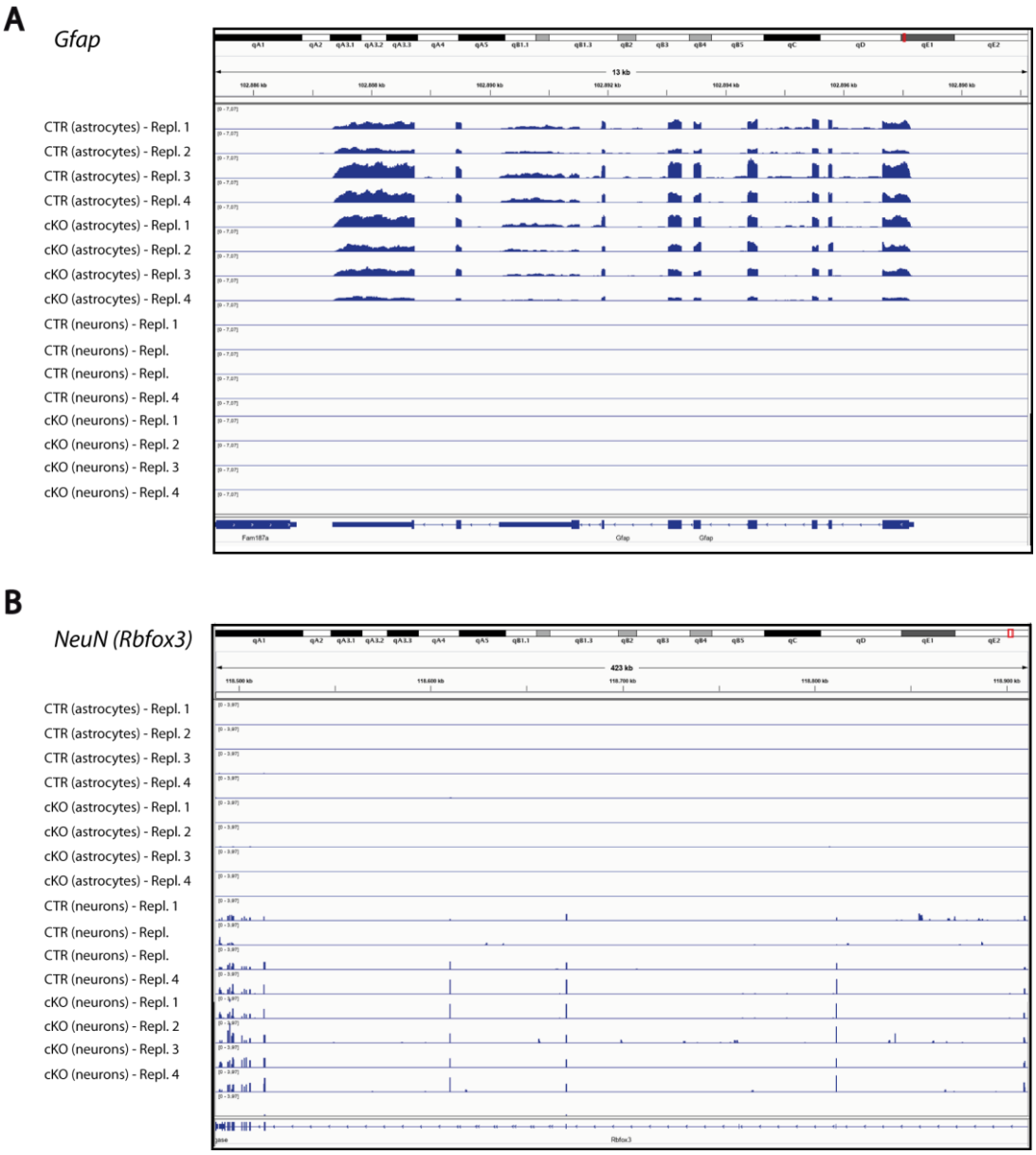

Figure 51: *Gfap* and *NeuN* transcript in sorted cortical astrocytes and neurons

Gfap and *NeuN* (*Rbfox3*) transcripts in cortical astrocytes and neurons of cKO and WT animals were visualised using IGV software, additionally confirming the purity of the obtained sorted cell populations.

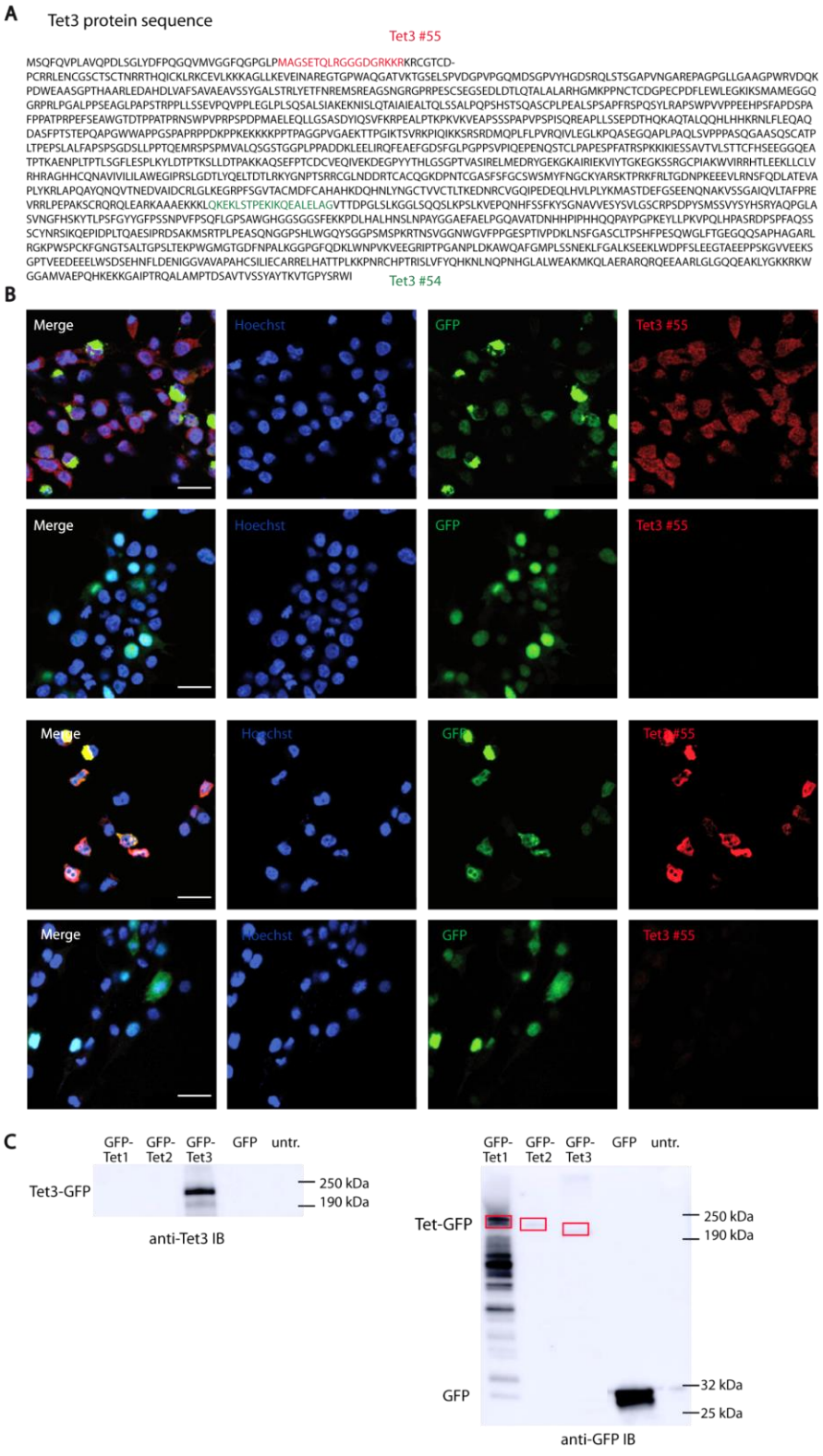

Figure 52: Tet3 isoform-specific antibodies

(A) Tet3 protein sequence. Binding positions of Tet3 #54 and Tet3 #55 antibodies are marked in colour. **(B)** Immunocytochemistry of HEK293T cells transfected with Tet3-GFP (rows 1 + 3) and GFP-constructs (rows 2 + 4): Hoechst (blue), GFP (green), Tet3 (red). Images were taken using a confocal microscope. Scale bar 50 µm. **(C)** Anti-Tet3 #54 and anti-GFP immuno blots (IB) using whole lysate from cells transfected with Tet1-GFP, Tet2-GFP, Tet3-GFP as well as GFP constructs and an untransfected control.

7 References

Abidi, A., Mignon-Ravix, C., Cacciagli, P., Girard, N., Milh, M. and Villard, L. (2016). "Early-onset epileptic encephalopathy as the initial clinical presentation of WDR45 deletion in a male patient." European journal of human genetics : EJHG **24**(4): 615-618.

ACD (Biotechne) (2017). "RNAscope® Multiplex Fluorescent Reagent Kit v2 Assay - User Manual." 2020, from https://ruo.mbl.co.jp/bio/product/epigenetics/images/rnascope/USM-323100_MultiplexFluorescent_v2_UserManual_Support_04032017.pdf.

Alkozi, H. A., Franco, R. and Pintor, J. J. (2017). "Epigenetics in the Eye: An Overview of the Most Relevant Ocular Diseases." Frontiers in genetics **8**: 144-144.

Allfrey, V. G., Faulkner, R. and Mirsky, A. E. (1964). "Acetylation and methylation of histones and their possible role in the regulation of RNA synthesis." Proceedings of the National Academy of Sciences of the United States of America **51**(5): 786-794.

Amouroux, R., Nashun, B., Shirane, K., Nakagawa, S., Hill, P. W. S., D'Souza, Z., Nakayama, M., Matsuda, M., Turp, A., Ndjetehe, E., Encheva, V., Kudo, N. R., Koseki, H., Sasaki, H. and Hajkova, P. (2016). "De novo DNA methylation drives 5hmC accumulation in mouse zygotes." Nature Cell Biology **18**(2): 225-233.

An, W. (2007). Histone Acetylation And Methylation. Chromatin and Disease. T. K. Kundu, R. Bittman, D. Dasgupta et al. Dordrecht, Springer Netherlands**:** 355-374.

Anderson, K. W., Chen, J., Wang, M., Mast, N., Pikuleva, I. A. and Turko, I. V. (2015). "Quantification of histone deacetylase isoforms in human frontal cortex, human retina, and mouse brain." PLOS ONE **10**(5): e0126592-e0126592.

Andrade, N., Komnenovic, V., Blake, S. M., Jossin, Y., Howell, B., Goffinet, A., Schneider, W. J. and Nimpf, J. (2007). "ApoER2/VLDL receptor and Dab1 in the rostral migratory stream function in postnatal neuronal migration independently of Reelin." Proceedings of the National Academy of Sciences **104**(20): 8508.

Antunes, C., Da Silva, J. D., Guerra-Gomes, S., Alves, N. D., Ferreira, F., Loureiro-Campos, E., Branco, M. R., Sousa, N., Reik, W., Pinto, L. and Marques, C. J. (2020). "Tet3 ablation in adult brain neurons increases anxiety-like behavior and regulates cognitive function in mice." Molecular Psychiatry.

Arvidsson, A., Collin, T., Kirik, D., Kokaia, Z. and Lindvall, O. (2002). "Neuronal replacement from endogenous precursors in the adult brain after stroke." Nature Medicine **8**(9): 963-970.

Bagci, H. and Fisher, Amanda G. (2013). "DNA Demethylation in Pluripotency and Reprogramming: The Role of Tet Proteins and Cell Division." Cell Stem Cell **13**(3): 265-269.

Bannister, A. J. and Kouzarides, T. (2011). "Regulation of chromatin by histone modifications." Cell research **21**(3): 381-395.

Barreto, G., Schäfer, A., Marhold, J., Stach, D., Swaminathan, S. K., Handa, V., Döderlein, G., Maltry, N., Wu, W., Lyko, F. and Niehrs, C. (2007). "Gadd45a promotes epigenetic gene activation by repair-mediated DNA demethylation." Nature **445**(7128): 671-675.

Bassett, E. A. and Wallace, V. A. (2012). "Cell fate determination in the vertebrate retina." Trends in Neurosciences **35**(9): 565-573.

Bear, M. F., Connors, B. W. and Paradiso, M. A. (2016). Neuroscience - Exploring the Brain. China, Wolters Kluwer.

Beck, D. B., Petracovici, A., He, C., Moore, H. W., Louie, R. J., Ansar, M., Douzgou, S., Sithambaram, S., Cottrell, T., Santos-Cortez, R. L. P., Prijoles, E. J., Bend, R., Keren, B., Mignot, C., Nougues, M.-C., Õunap, K., Reimand, T., Pajusalu, S., Zahid, M., Saqib, M. A. N., Buratti, J., Seaby, E. G., McWalter, K., Telegrafi, A., Baldridge, D., Shinawi, M., Leal, S. M., Schaefer, G. B., Stevenson, R. E., Banka, S., Bonasio, R. and Fahrner, J. A. (2020). "Delineation of a Human Mendelian Disorder of the DNA Demethylation Machinery: TET3 Deficiency." The American Journal of Human Genetics **106**(2): 234-245.

Bednar, J., Horowitz, R. A., Grigoryev, S. A., Carruthers, L. M., Hansen, J. C., Koster, A. J. and Woodcock, C. L. (1998). "Nucleosomes, linker DNA, and linker histone form a unique structural motif that directs the higher-order folding and compaction of chromatin." Proceedings of the National Academy of Sciences of the United States of America **95**(24): 14173-14178.

Benayoun, B. A., Pollina, E. A. and Brunet, A. (2015). "Epigenetic regulation of ageing: linking environmental inputs to genomic stability." Nature reviews. Molecular cell biology **16**(10): 593-610.

Berger, S. L., Kouzarides, T., Shiekhattar, R. and Shilatifard, A. (2009). "An operational definition of epigenetics." Genes & development **23**(7): 781-783.

Bhaya, D., Davison, M. and Barrangou, R. (2011). "CRISPR-Cas Systems in Bacteria and Archaea: Versatile Small RNAs for Adaptive Defense and Regulation." Annual Review of Genetics **45**(1): 273-297.

Bibb, J. A., Yan, Z., Svenningsson, P., Snyder, G. L., Pieribone, V. A., Horiuchi, A., Nairn, A. C., Messer, A. and Greengard, P. (2000). "Severe deficiencies in dopamine signaling in presymptomatic Huntington's disease mice." Proceedings of the National Academy of Sciences of the United States of America **97**(12): 6809-6814.

Bostick, M., Kim, J. K., Estève, P.-O., Clark, A., Pradhan, S. and Jacobsen, S. E. (2007). "UHRF1 Plays a Role in Maintaining DNA Methylation in Mammalian Cells." Science **317**(5845): 1760.

Bowman, R. L. and Levine, R. L. (2017). "TET2 in Normal and Malignant Hematopoiesis." Cold Spring Harbor perspectives in medicine **7**(8): a026518.

Braun, S. M. G. and Jessberger, S. (2014). "Adult neurogenesis: mechanisms and functional significance." Development **141**(10): 1983.

Busanello, A., Santucci, D., Bonini, S. and Micera, A. (2017). "Review: Environmental impact on ocular surface disorders: Possible epigenetic mechanism modulation and potential biomarkers." The Ocular Surface **15**(4): 680-687.

Busskamp, V., Lewis, N. E., Guye, P., Ng, A. H. M., Shipman, S. L., Byrne, S. M., Sanjana, N. E., Murn, J., Li, Y., Li, S., Stadler, M., Weiss, R. and Church, G. M. (2014). "Rapid neurogenesis through transcriptional activation in human stem cells." Molecular systems biology **10**(11): 760-760.

Candelaria, M., Burgos, S., Ponce, M., Espinoza, R. and Dueñas-Gonzalez, A. (2017). "Encouraging results with the compassionate use of hydralazine/valproate (TRANSKRIP™) as epigenetic treatment for myelodysplastic syndrome (MDS)." Annals of Hematology **96**(11): 1825-1832.

Carella, A., Tejedor, J. R., García, M. G., Urdinguio, R. G., Bayón, G. F., Sierra, M., López, V., García-Toraño, E., Santamarina-Ojeda, P., Pérez, R. F., Bigot, T., Mangas, C., Corte-Torres, M. D., Sáenz-de-Santa-María, I., Mollejo, M., Meléndez, B., Astudillo, A., Chiara, M. D., Fernández, A. F. and Fraga, M. F. (2020). "Epigenetic downregulation of TET3 reduces genome-wide 5hmC levels and promotes glioblastoma tumorigenesis." International Journal of Cancer **146**(2): 373-387.

Carlén, M., Meletis, K., Göritz, C., Darsalia, V., Evergren, E., Tanigaki, K., Amendola, M., Barnabé-Heider, F., Yeung, M. S. Y., Naldini, L., Honjo, T., Kokaia, Z., Shupliakov, O., Cassidy, R. M., Lindvall, O. and Frisén, J. (2009). "Forebrain ependymal cells are Notch-dependent and generate neuroblasts and astrocytes after stroke." Nature Neuroscience **12**(3): 259-267.

Carroll, D. (2011). "Genome engineering with zinc-finger nucleases." Genetics **188**(4): 773-782.

Chen, J., Boyle, S., Zhao, M., Su, W., Takahashi, K., Davis, L., DeCaestecker, M., Takahashi, T., Breyer, M. D. and Hao, C.-M. (2006). "Differential Expression of the Intermediate Filament Protein Nestin during Renal Development and Its Localization in Adult Podocytes." Journal of the American Society of Nephrology **17**(5): 1283.

Cheng, Y., Bernstein, A., Chen, D. and Jin, P. (2015). "5-Hydroxymethylcytosine: A new player in brain disorders?" Experimental Neurology **268**: 3-9.

Choudhuri, S., Cui, Y. and Klaassen, C. D. (2010). "Molecular targets of epigenetic regulation and effectors of environmental influences." Toxicology and applied pharmacology **245**(3): 378-393.

Colquitt, B. M., Allen, W. E., Barnea, G. and Lomvardas, S. (2013). "Alteration of genic 5-hydroxymethylcytosine patterning in olfactory neurons correlates with changes in gene expression and cell identity." Proceedings of the National Academy of Sciences of the United States of America **110**(36): 14682-14687.

Cong, L., Ran, F. A., Cox, D., Lin, S., Barretto, R., Habib, N., Hsu, P. D., Wu, X., Jiang, W., Marraffini, L. A. and Zhang, F. (2013). "Multiplex genome engineering using CRISPR/Cas systems." Science (New York, N.Y.) **339**(6121): 819-823.

Constantinides, P. G., Jones, P. A. and Gevers, W. (1977). "Functional striated muscle cells from non-myoblast precursors following 5-azacytidine treatment." Nature **267**(5609): 364-366.

Cooper, G. M. (2000). The Cell: A Molecular Approach. Chromosomes and Chromatin, Sunderland (MA): Sinauer Associates. **2**.

Copeland, R. A., Solomon, M. E. and Richon, V. M. (2009). "Protein methyltransferases as a target class for drug discovery." Nature Reviews Drug Discovery **8**(9): 724-732.

Corso-Díaz, X., Jaeger, C., Chaitankar, V. and Swaroop, A. (2018). "Epigenetic control of gene regulation during development and disease: A view from the retina." Progress in retinal and eye research **65**: 1-27.

Cortés-Mendoza, J., Díaz de León-Guerrero, S., Pedraza-Alva, G. and Pérez-Martínez, L. (2013). "Shaping synaptic plasticity: The role of activity-mediated epigenetic regulation on gene transcription." International Journal of Developmental Neuroscience **31**(6): 359-369.

Cosloy, S. D. and Oishi, M. (1973). "Genetic transformation in Escherichia coli K12." Proceedings of the National Academy of Sciences of the United States of America **70**(1): 84-87.

Cruickshank, M. N., Besant, P. and Ulgiati, D. (2010). "The impact of histone post-translational modifications on developmental gene regulation." Amino Acids **39**(5): 1087-1105.

Da, L., Cao, T., Sun, X., Jin, S., Di, X., Huang, X., Yang, X., Carmichael, G. G., Taylor, H. S., Diano, S. and Huang, Y. (2020). "Hepatic TET3 contributes to type-2 diabetes by inducing the HNF4α fetal isoform." Nature communications **11**(1): 342-342.

Declercq, J., Brouwers, B., Pruniau, V. P. E. G., Stijnen, P., de Faudeur, G., Tuand, K., Meulemans, S., Serneels, L., Schraenen, A., Schuit, F. and Creemers, J. W. M. (2015). "Metabolic and Behavioural Phenotypes in Nestin-Cre Mice Are Caused by Hypothalamic Expression of Human Growth Hormone." PLOS ONE **10**(8): e0135502-e0135502.

Del Bigio, M. R. (1995). "The ependyma: A protective barrier between brain and cerebrospinal fluid." Glia **14**(1): 1-13.

Del Bigio, M. R. (2010). "Ependymal cells: biology and pathology." Acta Neuropathologica **119**(1): 55-73.

Deng, W., Aimone, J. B. and Gage, F. H. (2010). "New neurons and new memories: how does adult hippocampal neurogenesis affect learning and memory?" Nature Reviews Neuroscience **11**(5): 339-350.

Dieni, S., Matsumoto, T., Dekkers, M., Rauskolb, S., Ionescu, M. S., Deogracias, R., Gundelfinger, E. D., Kojima, M., Nestel, S., Frotscher, M. and Barde, Y.-A. (2012). "BDNF and its pro-peptide are stored in presynaptic dense core vesicles in brain neurons." The Journal of cell biology **196**(6): 775-788.

Dobin, A., Davis, C. A., Schlesinger, F., Drenkow, J., Zaleski, C., Jha, S., Batut, P., Chaisson, M. and Gingeras, T. R. (2013). "STAR: ultrafast universal RNA-seq aligner." Bioinformatics (Oxford, England) **29**(1): 15-21.

Doench, J. G., Fusi, N., Sullender, M., Hegde, M., Vaimberg, E. W., Donovan, K. F., Smith, I., Tothova, Z., Wilen, C., Orchard, R., Virgin, H. W., Listgarten, J. and Root, D. E. (2016). "Optimized sgRNA design to maximize activity and minimize off-target effects of CRISPR-Cas9." Nature Biotechnology **34**(2): 184-191.

Doyle, A., McGarry, M. P., Lee, N. A. and Lee, J. J. (2012). "The construction of transgenic and gene knockout/knockin mouse models of human disease." Transgenic research **21**(2): 327-349.

Duan, J., Lu, G., Xie, Z., Lou, M., Luo, J., Guo, L. and Zhang, Y. (2014). "Genome-wide identification of CRISPR/Cas9 off-targets in human genome." Cell research **24**(8): 1009-1012.

Eagle-I Network (2011). "Mouse GFAP qPCR Primer set." 2018, from https://harvard.eagle-i.net/i/0000012d-a530-bd64-4882-b08d80000000.

Egger, G., Liang, G., Aparicio, A. and Jones, P. A. (2004). "Epigenetics in human disease and prospects for epigenetic therapy." Nature **429**(6990): 457-463.

Ehrlich, M., Buchanan, K. L., Tsien, F., Jiang, G., Sun, B., Uicker, W., Weemaes, C. M. R., Smeets, D., Sperling, K., Belohradsky, B. H., Tommerup, N., Misek, D. E., Rouillard, J.-M., Kuick, R. and Hanash, S. M. (2001). "DNA methyltransferase 3B mutations linked to the ICF syndrome cause dysregulation of lymphogenesis genes." Human molecular genetics **10**(25): 2917-2931.

Ericsson, A. C., Crim, M. J. and Franklin, C. L. (2013). "A brief history of animal modeling." Missouri medicine **110**(3): 201-205.

Ertürk, A., Lafkas, D. and Chalouni, C. (2014). "Imaging cleared intact biological systems at a cellular level by 3DISCO." Journal of visualized experiments : JoVE(89): 51382.

Esteller, M. (2008). "Epigenetics in Cancer." New England Journal of Medicine **358**(11): 1148-1159.

Esvelt, K. M., Mali, P., Braff, J. L., Moosburner, M., Yaung, S. J. and Church, G. M. (2013). "Orthogonal Cas9 proteins for RNA-guided gene regulation and editing." Nature Methods **10**(11): 1116-1121.

Euroform Healthcare (2020, 19.01.2020). "Function of the Dorsal Lateral Geniculate Nucleus of the Thalamus." 2020, from https://www.euroformhealthcare.biz/medical-physiology/function-of-the-dorsal-lateral-geniculate-nucleus-of-the-thalamus.html.

European Medicines Agency (EMA) (2009). "Vidaza (Azacitidine)." EPAR summary for the public. 2020, from https://www.ema.europa.eu/en/medicines/human/EPAR/vidaza#authorisation-details-section.

European Medicines Agency (EMA) (2015). "Farydak (Panobinostat)." EPAR - Summary for the public. 2020, from https://www.ema.europa.eu/en/medicines/human/EPAR/farydak.

European Medicines Agency (EMA) (2019). "Dacogen (Decitabine)." EPAR summary for the public. 2020, from https://www.ema.europa.eu/en/medicines/human/EPAR/dacogen.

Fahrner, J. A. and Bjornsson, H. T. (2014). "Mendelian Disorders of the Epigenetic Machinery: Tipping the Balance of Chromatin States." Annual Review of Genomics and Human Genetics **15**(1): 269-293.

Fang, S., Li, J., Xiao, Y., Lee, M., Guo, L., Han, W., Li, T., Hill, M. C., Hong, T., Mo, W., Xu, R., Zhang, P., Wang, F., Chang, J., Zhou, Y., Sun, D., Martin, J. F. and Huang, Y. (2019). "Tet inactivation disrupts YY1 binding and long-range chromatin interactions during embryonic heart development." Nature communications **10**(1): 4297.

Faulk, C. and Dolinoy, D. C. (2011). "Timing is everything: the when and how of environmentally induced changes in the epigenome of animals." Epigenetics **6**(7): 791-797.

Feinberg, A. P. and Vogelstein, B. (1983). "Hypomethylation distinguishes genes of some human cancers from their normal counterparts." Nature **301**(5895): 89-92.

Feng, Y., Li, X., Cassady, K., Zou, Z. and Zhang, X. (2019). "TET2 Function in Hematopoietic Malignancies, Immune Regulation, and DNA Repair." Frontiers in Oncology **9**: 210.

Fernandes, K. A., Mitchell, K. L., Patel, A., Marola, O. J., Shrager, P., Zack, D. J., Libby, R. T. and Welsbie, D. S. (2018). "Role of SARM1 and DR6 in retinal ganglion cell axonal and somal degeneration following axonal injury." Experimental eye research **171**: 54-61.

Figueroa, M. E., Lugthart, S., Li, Y., Erpelinck-Verschueren, C., Deng, X., Christos, P. J., Schifano, E., Booth, J., van Putten, W., Skrabanek, L., Campagne, F., Mazumdar, M., Greally, J. M., Valk, P. J. M., Löwenberg, B., Delwel, R. and Melnick, A. (2010). "DNA Methylation Signatures Identify Biologically Distinct Subtypes in Acute Myeloid Leukemia." Cancer Cell **17**(1): 13-27.

Fischle, W., Wang, Y. and David Allis, C. (2003). "Binary switches and modification cassettes in histone biology and beyond." Nature **425**(6957): 475-479.

Frauer, C., Rottach, A., Meilinger, D., Bultmann, S., Fellinger, K., Hasenöder, S., Wang, M., Qin, W., Söding, J., Spada, F. and Leonhardt, H. (2011). "Different binding properties and function of CXXC zinc finger domains in Dnmt1 and Tet1." PLOS ONE **6**(2): e16627-e16627.

Gao, Y., Yan, Y. and Huang, T. (2015). "Human age-related cataracts: Epigenetic suppression of the nuclear factor erythroid 2-related factor 2-mediated antioxidant system." Molecular Medicine Reports **11**(2).

García-Giménez, J. L., Seco-Cervera, M., Tollefsbol, T. O., Romá-Mateo, C., Peiró-Chova, L., Lapunzina, P. and Pallardó, F. V. (2017). "Epigenetic biomarkers: Current strategies and future challenges for their use in the clinical laboratory." Critical reviews in clinical laboratory sciences **54**(7-8): 529-550.

Garneau, J. E., Dupuis, M.-È., Villion, M., Romero, D. A., Barrangou, R., Boyaval, P., Fremaux, C., Horvath, P., Magadán, A. H. and Moineau, S. (2010). "The CRISPR/Cas bacterial immune system cleaves bacteriophage and plasmid DNA." Nature **468**(7320): 67-71.

Gasiunas, G., Barrangou, R., Horvath, P. and Siksnys, V. (2012). "Cas9-crRNA ribonucleoprotein complex mediates specific DNA cleavage for adaptive immunity in bacteria." Proceedings of the National Academy of Sciences of the United States of America **109**(39): E2579-E2586.

Gibson, D. G., Young, L., Chuang, R.-Y., Venter, J. C., Hutchison, C. A. and Smith, H. O. (2009). "Enzymatic assembly of DNA molecules up to several hundred kilobases." Nature Methods **6**(5): 343-345.

Gleeson, J. G., Lin, P. T., Flanagan, L. A. and Walsh, C. A. (1999). "Doublecortin Is a Microtubule-Associated Protein and Is Expressed Widely by Migrating Neurons." Neuron **23**(2): 257-271.

Globisch, D., Munzel, M., Muller, M., Michalakis, S., Wagner, M., Koch, S., Bruckl, T., Biel, M. and Carell, T. (2010). "Tissue distribution of 5-hydroxymethylcytosine and search for active demethylation intermediates." PLOS ONE **5**(12): e15367.

Goldman, D. (2014). "Müller glial cell reprogramming and retina regeneration." Nature reviews. Neuroscience **15**(7): 431-442.

Gontier, G., Iyer, M., Shea, J. M., Bieri, G., Wheatley, E. G., Ramalho-Santos, M. and Villeda, S. A. (2018). "Tet2 Rescues Age-Related Regenerative Decline and Enhances Cognitive Function in the Adult Mouse Brain." Cell Reports **22**(8): 1974-1981.

Gordon, J. W. and Ruddle, F. H. (1981). "Integration and stable germ line transmission of genes injected into mouse pronuclei." Science **214**(4526): 1244.

Gordon, J. W., Scangos, G. A., Plotkin, D. J., Barbosa, J. A. and Ruddle, F. H. (1980). "Genetic transformation of mouse embryos by microinjection of purified DNA." Proceedings of the National Academy of Sciences of the United States of America **77**(12): 7380-7384.

Greenberg, M. V. C. and Bourc'his, D. (2019). "The diverse roles of DNA methylation in mammalian development and disease." Nature Reviews Molecular Cell Biology **20**(10): 590-607.

Grosche, A., Hauser, A., Lepper, M. F., Mayo, R., von Toerne, C., Merl-Pham, J. and Hauck, S. M. (2016). "The Proteome of Native Adult Müller Glial Cells From Murine Retina." Molecular & cellular proteomics : MCP **15**(2): 462-480.

Grunstein, M. (1997). "Histone acetylation in chromatin structure and transcription." Nature **389**(6649): 349-352.

Gu, T.-P., Guo, F., Yang, H., Wu, H.-P., Xu, G.-F., Liu, W., Xie, Z.-G., Shi, L., He, X., Jin, S.-g., Iqbal, K., Shi, Y. G., Deng, Z., Szabó, P. E., Pfeifer, G. P., Li, J. and Xu, G.-L. (2011). "The role of Tet3 DNA dioxygenase in epigenetic reprogramming by oocytes." Nature **477**(7366): 606-610.

Guerra, C., Koza, R. A., Walsh, K., Kurtz, D. M., Wood, P. A. and Kozak, L. P. (1998). "Abnormal nonshivering thermogenesis in mice with inherited defects of fatty acid oxidation." The Journal of clinical investigation **102**(9): 1724-1731.

Guo, J. U., Ma, D. K., Mo, H., Ball, M. P., Jang, M.-H., Bonaguidi, M. A., Balazer, J. A., Eaves, H. L., Xie, B., Ford, E., Zhang, K., Ming, G.-l., Gao, Y. and Song, H. (2011a). "Neuronal activity modifies the DNA methylation landscape in the adult brain." Nature Neuroscience **14**(10): 1345-1351.

Guo, J. U., Su, Y., Zhong, C., Ming, G.-l. and Song, H. (2011b). "Hydroxylation of 5-methylcytosine by TET1 promotes active DNA demethylation in the adult brain." Cell **145**(3): 423-434.

Gurumurthy, C. B. and Lloyd, K. C. K. (2019). "Generating mouse models for biomedical research: technological advances." Disease models & mechanisms **12**(1): dmm029462.

Haeussler, M., Schönig, K., Eckert, H., Eschstruth, A., Mianné, J., Renaud, J.-B., Schneider-Maunoury, S., Shkumatava, A., Teboul, L., Kent, J., Joly, J.-S. and Concordet, J.-P. (2016). "Evaluation of off-target and on-target scoring algorithms and integration into the guide RNA selection tool CRISPOR." Genome Biology **17**(1): 148.

Hahn, Maria A., Qiu, R., Wu, X., Li, Arthur X., Zhang, H., Wang, J., Jui, J., Jin, S.-G., Jiang, Y., Pfeifer, Gerd P. and Lu, Q. (2013). "Dynamics of 5-Hydroxymethylcytosine and Chromatin Marks in Mammalian Neurogenesis." Cell Reports **3**(2): 291-300.

Hall, B., Limaye, A. and Kulkarni, A. B. (2009). "Overview: generation of gene knockout mice." Current protocols in cell biology **Chapter 19**: Unit-19.12.17.

Hasel, P., Dando, O., Jiwaji, Z., Baxter, P., Todd, A. C., Heron, S., Márkus, N. M., McQueen, J., Hampton, D. W., Torvell, M., Tiwari, S. S., McKay, S., Eraso-Pichot, A., Zorzano, A., Masgrau, R., Galea, E., Chandran, S., Wyllie, D. J. A., Simpson, T. I. and Hardingham, G. E. (2017). "Neurons and neuronal activity control gene expression in astrocytes to regulate their development and metabolism." Nature communications **8**(1): 15132.

Hashimoto, H., Liu, Y., Upadhyay, A. K., Chang, Y., Howerton, S. B., Vertino, P. M., Zhang, X. and Cheng, X. (2012). "Recognition and potential mechanisms for replication and erasure of cytosine hydroxymethylation." Nucleic acids research **40**(11): 4841-4849.

Hermann, A., Goyal, R. and Jeltsch, A. (2004). "The Dnmt1 DNA-(cytosine-C5)-methyltransferase Methylates DNA Processively with High Preference for Hemimethylated Target Sites." Journal of Biological Chemistry **279**: 48350-48359.

Hewitt, A. W., Januar, V., Sexton-Oates, A., Joo, J. E., Franchina, M., Wang, J. J., Liang, H., Craig, J. E. and Saffery, R. (2017). "DNA methylation landscape of ocular tissue relative to matched peripheral blood." Scientific Reports **7**(1): 46330.

Holliday, R. and Pugh, J. E. (1975). "DNA modification mechanisms and gene activity during development." Science **187**(4173): 226.

Horii, T. and Hatada, I. (2014). "Genome engineering using the CRISPR/Cas system." World Journal of Medical Genetics **4**(3): 69-76.

Horvath, P. and Barrangou, R. (2010). "CRISPR/Cas, the Immune System of Bacteria and Archaea." Science **327**(5962): 167.

Hsu, P. D., Scott, D. A., Weinstein, J. A., Ran, F. A., Konermann, S., Agarwala, V., Li, Y., Fine, E. J., Wu, X., Shalem, O., Cradick, T. J., Marraffini, L. A., Bao, G. and Zhang, F. (2013). "DNA targeting specificity of RNA-guided Cas9 nucleases." Nature Biotechnology **31**(9): 827-832.

Huang, Y., Chavez, L., Chang, X., Wang, X., Pastor, W., Kang, J., Zepeda-Martínez, J., Pape, U., Jacobsen, S., Peters, B. and Rao, A. (2014). "Distinct roles of the methylcytosine oxidases Tet1 and Tet2 in mouse embryonic stem cells." Proceedings of the National Academy of Sciences of the United States of America **111**: 1361-1366.

Hutchinson, J. N., Fagerness, J., Kirby, A., Reynolds, R., Zak, A., Gimelbrant, A., Plenge, R., Daly, M., Chess, A. and Seddon, J. M. (2014). "(Epi)Genetic analyses of age-related macular degeneration: case-control and discordant twin studies." Human heredity **78**(2): 59-72.

Iqbal, K., Jin, S.-G., Pfeifer, G. P. and Szabó, P. E. (2011). "Reprogramming of the paternal genome upon fertilization involves genome-wide oxidation of 5-methylcytosine." Proceedings of the National Academy of Sciences **108**(9): 3642.

Ito, S., D'Alessio, A. C., Taranova, O. V., Hong, K., Sowers, L. C. and Zhang, Y. (2010). "Role of Tet proteins in 5mC to 5hmC conversion, ES-cell self-renewal and inner cell mass specification." Nature **466**(7310): 1129-1133.

Ito, S., Shen, L., Dai, Q., Wu, S. C., Collins, L. B., Swenberg, J. A., He, C. and Zhang, Y. (2011). "Tet Proteins Can Convert 5-Methylcytosine to 5-Formylcytosine and 5-Carboxylcytosine." Science **333**(6047): 1300.

Ivanova, E., Hwang, G. S. and Pan, Z. H. (2010). "Characterization of transgenic mouse lines expressing Cre recombinase in the retina." Neuroscience **165**(1): 233-243.

Iwan, K., Rahimoff, R., Kirchner, A., Spada, F., Schröder, A. S., Kosmatchev, O., Ferizaj, S., Steinbacher, J., Parsa, E., Müller, M. and Carell, T. (2018). "5-Formylcytosine to cytosine conversion by C–C bond cleavage in vivo." Nature Chemical Biology **14**(1): 72-78.

Iyer, L. M., Tahiliani, M., Rao, A. and Aravind, L. (2009). "Prediction of novel families of enzymes involved in oxidative and other complex modifications of bases in nucleic acids." Cell cycle (Georgetown, Tex.) **8**(11): 1698-1710.

Jackson, T. C., Manole, M. D., Kotermanski, S. E., Jackson, E. K., Clark, R. S. B. and Kochanek, P. M. (2015). "Cold stress protein RBM3 responds to temperature change in an ultra-sensitive manner in young neurons." Neuroscience **305**: 268-278.

Jacobs, S., Ruusuvuori, E., Sipilä, S. T., Haapanen, A., Damkier, H. H., Kurth, I., Hentschke, M., Schweizer, M., Rudhard, Y., Laatikainen, L. M., Tyynelä, J., Praetorius, J., Voipio, J. and Hübner, C. A. (2008). "Mice with targeted *Slc4a10* gene disruption have small brain ventricles and show reduced neuronal excitability." Proceedings of the National Academy of Sciences **105**(1): 311.

Jenuwein, T. and Allis, C. D. (2001). "Translating the Histone Code." Science **293**(5532): 1074.

Jin, K., LaFevre-Bernt, M., Sun, Y., Chen, S., Gafni, J., Crippen, D., Logvinova, A., Ross, C. A., Greenberg, D. A. and Ellerby, L. M. (2005). "FGF-2 promotes neurogenesis and neuroprotection and prolongs survival in a transgenic mouse model of Huntington's disease." Proceedings of the National Academy of Sciences of the United States of America **102**(50): 18189-18194.

Jin, S.-G., Zhang, Z.-M., Dunwell, Thomas L., Harter, Matthew R., Wu, X., Johnson, J., Li, Z., Liu, J., Szabó, Piroska E., Lu, Q., Xu, G.-l., Song, J. and Pfeifer, Gerd P. (2016). "Tet3 Reads 5-Carboxylcytosine through Its CXXC Domain and Is a Potential Guardian against Neurodegeneration." Cell Reports **14**(3): 493-505.

Jin, S. L., Zhang Y Fau - Chen, Z. H., Chen Zh Fau - Qian, D. W., Qian Dw Fau - Qine, Y. J., Qine Yj Fau - Yongjie, Q., Yongjie Q Fau - He, S. K., He Sk Fau - Guo, H. K. and Guo, H. K. (2015). "Epigenetic changes of the Klotho gene in age-related cataracts." European Review for Medical and Pharmacological Sciences **19**(14): 2544-2553.

Jinek, M., Chylinski, K., Fonfara, I., Hauer, M., Doudna, J. A. and Charpentier, E. (2012). "A programmable dual-RNA-guided DNA endonuclease in adaptive bacterial immunity." Science (New York, N.Y.) **337**(6096): 816-821.

Jobe, E. M., Gao, Y., Eisinger, B. E., Mladucky, J. K., Giuliani, C. C., Kelnhofer, L. E. and Zhao, X. (2017). "Methyl-CpG-Binding Protein MBD1 Regulates Neuronal Lineage Commitment through Maintaining Adult Neural Stem Cell Identity." The Journal of neuroscience : the official journal of the Society for Neuroscience **37**(3): 523-536.

Jones, P. A. and Baylin, S. B. (2002). "The fundamental role of epigenetic events in cancer." Nature Reviews Genetics **3**(6): 415-428.

Jones, P. A. and Baylin, S. B. (2007). "The epigenomics of cancer." Cell **128**(4): 683-692.

Jones, P. A. and Taylor, S. M. (1980). "Cellular differentiation, cytidine analogs and DNA methylation." Cell **20**(1): 85-93.

JoVE Science Education Database (2020a). "Developmental Biology. Explant Culture for Developmental Studies.".

JoVE Science Education Database (2020b). "Neuroscience. Explant Culture of Neural Tissue."

Justice, M. J. and Dhillon, P. (2016). "Using the mouse to model human disease: increasing validity and reproducibility." Disease models & mechanisms **9**(2): 101.

Justice, M. J., Siracusa, L. D. and Stewart, A. F. (2011). "Technical approaches for mouse models of human disease." Disease models & mechanisms **4**(3): 305-310.

Kaas, G. A., Zhong, C., Eason, D. E., Ross, D. L., Vachhani, R. V., Ming, G.-L., King, J. R., Song, H. and Sweatt, J. D. (2013). "TET1 controls CNS 5-methylcytosine hydroxylation, active DNA demethylation, gene transcription, and memory formation." Neuron **79**(6): 1086-1093.

Kachinsky, A. M., Dominov, J. A. and Miller, J. B. (1995). "Intermediate filaments in cardiac myogenesis: nestin in the developing mouse heart." Journal of Histochemistry & Cytochemistry **43**(8): 843-847.

Kádár, A., Wittmann, G., Liposits, Z. and Fekete, C. (2009). "Improved method for combination of immunocytochemistry and Nissl staining." Journal of Neuroscience Methods **184**(1): 115-118.

Kadiyala, C. S. R., Zheng, L., Du, Y., Yohannes, E., Kao, H.-Y., Miyagi, M. and Kern, T. S. (2012). "Acetylation of retinal histones in diabetes increases inflammatory proteins: effects of minocycline and manipulation of histone acetyltransferase (HAT) and histone deacetylase (HDAC)." The Journal of biological chemistry **287**(31): 25869-25880.

Kaelin, W. G., Jr. and McKnight, S. L. (2013). "Influence of metabolism on epigenetics and disease." Cell **153**(1): 56-69.

Kaneko, N., Sawada, M. and Sawamoto, K. (2017). "Mechanisms of neuronal migration in the adult brain." Journal of Neurochemistry **141**(6): 835-847.

Karp, G. C. (2010). Cell and Molecular Biology - Concepts and Experiments. USA, John Wiley & Sons, Inc.

Karpova, N. N., Sales, A. J. and Joca, S. R. (2017). "Epigenetic Basis of Neuronal and Synaptic Plasticity." Current Topics in Medicinal Chemistry **17**(7): 771-793.

Kee, N., Sivalingam, S., Boonstra, R. and Wojtowicz, J. M. (2002). "The utility of Ki-67 and BrdU as proliferative markers of adult neurogenesis." Journal of Neuroscience Methods **115**(1): 97-105.

Kempermann, G. (2015). "Adult Neurogenesis: An Evolutionary Perspective." Cold Spring Harbor perspectives in biology **8**(2): a018986-a018986.

Kempermann, G., Song, H. and Gage, F. H. (2015). "Neurogenesis in the Adult Hippocampus." Cold Spring Harbor perspectives in biology **7**(9): a018812-a018812.

Kerschensteiner, D. and Guido, W. (2017). "Organization of the dorsal lateral geniculate nucleus in the mouse." Visual neuroscience **34**: E008-E008.

Kim, H., Kim, M., Im, S.-K. and Fang, S. (2018). "Mouse Cre-LoxP system: general principles to determine tissue-specific roles of target genes." Laboratory animal research **34**(4): 147-159.

Kleppisch, T., Pfeifer, A., Klatt, P., Ruth, P., Montkowski, A., Fässler, R. and Hofmann, F. (1999). "Long-Term Potentiation in the Hippocampal CA1 Region of Mice Lacking cGMP-Dependent Kinases Is Normal and Susceptible to Inhibition of Nitric Oxide Synthase." The Journal of Neuroscience **19**(1): 48.

Knierim, J. (1997). "Chapter 5: Cerebellum." Neuroscience online, Section 3: Motor systems. 2020, from https://nba.uth.tmc.edu/neuroscience/m/s3/chapter05.html.

Ko, M., An, J., Bandukwala, H. S., Chavez, L., Äijö, T., Pastor, W. A., Segal, M. F., Li, H., Koh, K. P., Lähdesmäki, H., Hogan, P. G., Aravind, L. and Rao, A. (2013). "Modulation of TET2 expression and 5-methylcytosine oxidation by the CXXC domain protein IDAX." Nature **497**(7447): 122-126.

Koivunen, P. and Laukka, T. (2018). "The TET enzymes." Cellular and Molecular Life Sciences **75**(8): 1339-1348.

Kornberg, R. D. (1974). "Chromatin Structure: A Repeating Unit of Histones and DNA." Science **184**(4139): 868.

Kornberg, R. D. and Thonmas, J. O. (1974). "Chromatin Structure: Oligomers of the Histones." Science **184**(4139): 865.

Korzhevskii, D. E., Kirik, O. V. and Alekseeva, O. S. (2015). "Nestin Expression in the Ependymal Cells of the Lateral Ventricles of the Rat Brain during Aging." Neuroscience and Behavioral Physiology **45**(8): 882-883.

Kosicki, M., Tomberg, K. and Bradley, A. (2018). "Repair of double-strand breaks induced by CRISPR-Cas9 leads to large deletions and complex rearrangements." Nature Biotechnology **36**(8): 765-771.

Kouzarides, T. (2007). "Chromatin Modifications and Their Function." Cell **128**(4): 693-705.

Kowluru, R. A. (2017). "Diabetic retinopathy, metabolic memory and epigenetic modifications." Vision Research **139**: 30-38.

Kowluru, R. A., Kowluru, A., Mishra, M. and Kumar, B. (2015). "Oxidative stress and epigenetic modifications in the pathogenesis of diabetic retinopathy." Progress in retinal and eye research **48**: 40-61.

Kriaucionis, S. and Heintz, N. (2009). "The nuclear DNA base 5-hydroxymethylcytosine is present in Purkinje neurons and the brain." Science (New York, N.Y.) **324**(5929): 929-930.

Kyrousi, C., Arbi, M., Pilz, G.-A., Pefani, D.-E., Lalioti, M.-E., Ninkovic, J., Götz, M., Lygerou, Z. and Taraviras, S. (2015). "Mcidas and GemC1 are key regulators for the generation of multiciliated ependymal cells in the adult neurogenic niche." Development **142**(21): 3661.

Langedijk, J., Mantel-Teeuwisse, A. K., Slijkerman, D. S. and Schutjens, M.-H. D. B. (2015). "Drug repositioning and repurposing: terminology and definitions in literature." Drug Discovery Today **20**(8): 1027-1034.

Larizza, L. and Finelli, P. (2019). "Developmental disorders with intellectual disability driven by chromatin dysregulation: Clinical overlaps and molecular mechanisms." Clinical Genetics **95**(2): 231-240.

Laukka, T., Mariani, C. J., Ihantola, T., Cao, J. Z., Hokkanen, J., Kaelin, W. G., Jr., Godley, L. A. and Koivunen, P. (2016). "Fumarate and Succinate Regulate Expression of Hypoxia-inducible Genes via TET Enzymes." The Journal of biological chemistry **291**(8): 4256-4265.

Lee, H.-Z., Kwitkowski, V. E., Del Valle, P. L., Ricci, M. S., Saber, H., Habtemariam, B. A., Bullock, J., Bloomquist, E., Li Shen, Y., Chen, X.-H., Brown, J., Mehrotra, N., Dorff, S., Charlab, R., Kane, R. C., Kaminskas, E., Justice, R., Farrell, A. T. and Pazdur, R. (2015). "FDA Approval: Belinostat for the Treatment of Patients with Relapsed or Refractory Peripheral T-cell Lymphoma." Clinical Cancer Research **21**(12): 2666.

Lee, M., Bryan, K., Peipei, L., Elizabeth, E., Katie, L., Wei, C., Noah, L., Matthew, W., Juozas, G., Gerhard A, C., Stefan, J. and Viviane, L. (2019). "Epigenomic analysis of Parkinson's disease neurons identifies *Tet2* loss as neuroprotective." bioRxiv: 779785.

Lendahl, U., Zimmerman, L. B. and McKay, R. D. G. (1990). "CNS stem cells express a new class of intermediate filament protein." Cell **60**(4): 585-595.

Li, B. and Dewey, C. N. (2011). "RSEM: accurate transcript quantification from RNA-Seq data with or without a reference genome." BMC bioinformatics **12**: 323-323.

Li, E., Bestor, T. H. and Jaenisch, R. (1992). "Targeted mutation of the DNA methyltransferase gene results in embryonic lethality." Cell **69**(6): 915-926.

Li, E. and Zhang, Y. (2014). "DNA methylation in mammals." Cold Spring Harbor perspectives in biology **6**(5): a019133-a019133.

Li, Q., Chan, S. Y., Wong, K. K., Wei, R., Leung, Y. O., Ding, A. Y., Hui, T. C. K., Cheung, C., Chua, S. E., Sham, P. C., Wu, E. X. and McAlonan, G. M. (2016a). "Tspyl2 Loss-of-Function Causes Neurodevelopmental Brain and Behavior Abnormalities in Mice." Behavior Genetics **46**(4): 529-537.

Li, S., Papale, L. A., Zhang, Q., Madrid, A., Chen, L., Chopra, P., Keleş, S., Jin, P. and Alisch, R. S. (2016b). "Genome-wide alterations in hippocampal 5-hydroxymethylcytosine links plasticity genes to acute stress." Neurobiology of disease **86**: 99-108.

Li, T., Yang, D., Li, J., Tang, Y., Yang, J. and Le, W. (2015). "Critical Role of Tet3 in Neural Progenitor Cell Maintenance and Terminal Differentiation." Molecular Neurobiology **51**(1): 142-154.

Lim, D. A. and Alvarez-Buylla, A. (2016). "The Adult Ventricular-Subventricular Zone (V-SVZ) and Olfactory Bulb (OB) Neurogenesis." Cold Spring Harbor perspectives in biology **8**(5): a018820.

Lin, Y., Bloodgood, B. L., Hauser, J. L., Lapan, A. D., Koon, A. C., Kim, T.-K., Hu, L. S., Malik, A. N. and Greenberg, M. E. (2008). "Activity-dependent regulation of inhibitory synapse development by Npas4." Nature **455**(7217): 1198-1204.

Lindvall, O. and Kokaia, Z. (2015). "Neurogenesis following Stroke Affecting the Adult Brain." Cold Spring Harbor perspectives in biology **7**(11): a019034.

Lio, C.-W. J. and Rao, A. (2019). "TET Enzymes and 5hmC in Adaptive and Innate Immune Systems." Frontiers in immunology **10**: 210-210.

Liu, N., Wang, M., Deng, W., Schmidt, C. S., Qin, W., Leonhardt, H. and Spada, F. (2013). "Intrinsic and Extrinsic Connections of Tet3 Dioxygenase with CXXC Zinc Finger Modules." PLOS ONE **8**(5): e62755.

Lois, C. and Alvarez-Buylla, A. (1994). "Long-distance neuronal migration in the adult mammalian brain." Science **264**(5162): 1145.

Lois, C., García-Verdugo, J.-M. and Alvarez-Buylla, A. (1996). "Chain Migration of Neuronal Precursors." Science **271**(5251): 978.

Love, M. I., Huber, W. and Anders, S. (2014). "Moderated estimation of fold change and dispersion for RNA-seq data with DESeq2." Genome Biology **15**(12): 550-550.

Lu, X., Zhao, B. S. and He, C. (2015). "TET family proteins: oxidation activity, interacting molecules, and functions in diseases." Chemical Reviews **115**(6): 2225-2239.

Lu, Y., Krishnan, A., Brommer, B., Tian, X., Meer, M., Vera, D. L., Wang, C., Zeng, Q., Yu, D., Bonkowski, M. S., Yang, J.-H., Hoffmann, E. M., Zhou, S., Korobkina, E., Davidsohn, N., Schultz, M. B., Chwalek, K., Rajman, L. A., Church, G. M., Hochedlinger, K., Gladyshev, V. N., Horvath, S., Gregory-Ksander, M. S., Ksander, B. R., He, Z. and Sinclair, D. A. (2019). "Reversal of ageing- and injury-induced vision loss by Tet-dependent epigenetic reprogramming." bioRxiv: 710210.

Luebbert, M. (2016). "Study of Sensitization of Non-M3 AML Blasts to ATRA by Epigenetic Treatment With Tranylcypromine (TCP) (TRANSATRA)." 2020, from https://clinicaltrials.gov/ct2/show/NCT02717884.

Luger, K., Mäder, A. W., Richmond, R. K., Sargent, D. F. and Richmond, T. J. (1997). "Crystal structure of the nucleosome core particle at 2.8 Å resolution." Nature **389**(6648): 251-260.

Ma, D. K., Jang, M.-H., Guo, J. U., Kitabatake, Y., Chang, M.-l., Pow-anpongkul, N., Flavell, R. A., Lu, B., Ming, G.-l. and Song, H. (2009). "Neuronal Activity–Induced Gadd45b Promotes Epigenetic DNA Demethylation and Adult Neurogenesis." Science **323**(5917): 1074.

Makarova, K. S., Haft, D. H., Barrangou, R., Brouns, S. J. J., Charpentier, E., Horvath, P., Moineau, S., Mojica, F. J. M., Wolf, Y. I., Yakunin, A. F., van der Oost, J. and Koonin, E. V. (2011). "Evolution and classification of the CRISPR-Cas systems." Nature reviews. Microbiology **9**(6): 467-477.

Mali, P., Yang, L., Esvelt, K. M., Aach, J., Guell, M., DiCarlo, J. E., Norville, J. E. and Church, G. M. (2013). "RNA-guided human genome engineering via Cas9." Science (New York, N.Y.) **339**(6121): 823-826.

Mandel, M. and Higa, A. (1970). "Calcium-dependent bacteriophage DNA infection." Journal of Molecular Biology **53**(1): 159-162.

Mann, B. S., Johnson, J. R., Cohen, M. H., Justice, R. and Pazdur, R. (2007). "FDA Approval Summary: Vorinostat for Treatment of Advanced Primary Cutaneous T-Cell Lymphoma." The Oncologist **12**(10): 1247-1252.

Marks, P. A., Miller, T. and Richon, V. M. (2003). "Histone deacetylases." Current Opinion in Pharmacology **3**(4): 344-351.

Marks, P. A., Richon, V. M. and Rifkind, R. A. (2000). "Histone Deacetylase Inhibitors: Inducers of Differentiation or Apoptosis of Transformed Cells." JNCI: Journal of the National Cancer Institute **92**(15): 1210-1216.

Martinowich, K., Hattori, D., Wu, H., Fouse, S., He, F., Hu, Y., Fan, G. and Sun, Y. E. (2003). "DNA Methylation-Related Chromatin Remodeling in Activity-Dependent BDNF Gene Regulation." Science **302**(5646): 890.

Matsuda, Y., Yoshimura, H., Suzuki, T. and Ishiwata, T. (2013). "Nestin: Neural Stem/Progenitor Cell Marker in Brain Tumors, Evolution of the Molecular Biology of Brain Tumors and the Therapeutic Implications." Terry Lichtor, IntechOpen, DOI: 10.5772/52634. 2020, from https://www.intechopen.com/books/evolution-of-the-molecular-biology-of-brain-tumors-and-the-therapeutic-implications/nestin-neural-stem-progenitor-cell-marker-in-brain-tumors.

McGhee, J. D. and Felsenfeld, G. (1980). "Nucleosome Structure." Annual Review of Biochemistry **49**(1): 1115-1156.

McLellan, M. A., Rosenthal, N. A. and Pinto, A. R. (2017). "Cre-loxP-Mediated Recombination: General Principles and Experimental Considerations." Current Protocols in Mouse Biology **7**(1): 1-12.

Mehravar, M., Shirazi, A., Nazari, M. and Banan, M. (2019). "Mosaicism in CRISPR/Cas9-mediated genome editing." Developmental Biology **445**(2): 156-162.

Meinke, G., Bohm, A., Hauber, J., Pisabarro, M. T. and Buchholz, F. (2016). "Cre Recombinase and Other Tyrosine Recombinases." Chemical Reviews **116**(20): 12785-12820.

Melamed, P., Yosefzon, Y., David, C., Tsukerman, A. and Pnueli, L. (2018). "Tet Enzymes, Variants, and Differential Effects on Function." Frontiers in Cell and Developmental Biology **6**: 22-22.

Metzger, D. and Chambon, P. (2001). "Site- and Time-Specific Gene Targeting in the Mouse." Methods **24**(1): 71-80.

Mi, Y., Shi, Z. and Li, J. (2015). "Spata19 is critical for sperm mitochondrial function and male fertility." Molecular Reproduction and Development **82**(11): 907-913.

Michalakis, S., Kleppisch, T., Polta, S. A., Wotjak, C. T., Koch, S., Rammes, G., Matt, L., Becirovic, E. and Biel, M. (2011). "Altered synaptic plasticity and behavioral abnormalities in CNGA3-deficient mice." Genes Brain Behav **10**(2): 137-148.

Michalakis, S., Reisert, J., Geiger, H., Wetzel, C., Zong, X., Bradley, J., Spehr, M., Hüttl, S., Gerstner, A., Pfeifer, A., Hatt, H., Yau, K.-W. and Biel, M. (2006). "Loss of CNGB1 protein leads to olfactory dysfunction and subciliary cyclic nucleotide-gated channel trapping." The Journal of biological chemistry **281**(46): 35156-35166.

Mnatzakanian, G. N., Lohi, H., Munteanu, I., Alfred, S. E., Yamada, T., MacLeod, P. J. M., Jones, J. R., Scherer, S. W., Schanen, N. C., Friez, M. J., Vincent, J. B. and Minassian, B. A. (2004). "A previously unidentified MECP2 open reading frame defines a new protein isoform relevant to Rett syndrome." Nature Genetics **36**(4): 339-341.

Montalbán-Loro, R., Lozano-Ureña, A., Ito, M., Krueger, C., Reik, W., Ferguson-Smith, A. C. and Ferrón, S. R. (2019). "TET3 prevents terminal differentiation of adult NSCs by a non-catalytic action at Snrpn." Nature communications **10**(1): 1726.

Moran-Crusio, K., Reavie, L., Shih, A., Abdel-Wahab, O., Ndiaye-Lobry, D., Lobry, C., Figueroa, Maria E., Vasanthakumar, A., Patel, J., Zhao, X., Perna, F., Pandey, S., Madzo, J., Song, C., Dai, Q., He, C., Ibrahim, S., Beran, M., Zavadil, J., Nimer, Stephen D., Melnick, A., Godley, Lucy A., Aifantis, I. and Levine, Ross L. (2011). "Tet2 Loss Leads to Increased Hematopoietic Stem Cell Self-Renewal and Myeloid Transformation." Cancer Cell **20**(1): 11-24.

Mulvihill, M. M., Benjamin, D. I., Ji, X., Le Scolan, E., Louie, S. M., Shieh, A., Green, M., Narasimhalu, T., Morris, P. J., Luo, K. and Nomura, D. K. (2014). "Metabolic profiling reveals PAFAH1B3 as a critical driver of breast cancer pathogenicity." Chemistry & biology **21**(7): 831-840.

Münzel, M., Globisch, D., Brückl, T., Wagner, M., Welzmiller, V., Michalakis, S., Müller, M., Biel, M. and Carell, T. (2010). "Quantification of the Sixth DNA Base Hydroxymethylcytosine in the Brain." Angewandte Chemie International Edition **49**(31): 5375-5377.

Naghdi, S. and Hajnóczky, G. (2016). "VDAC2-specific cellular functions and the underlying structure." Biochimica et biophysica acta **1863**(10): 2503-2514.

Nagy, A. (2000). "Cre recombinase: The universal reagent for genome tailoring." genesis **26**(2): 99-109.

Nam, S. C., Kim, Y., Dryanovski, D., Walker, A., Goings, G., Woolfrey, K., Kang, S. S., Chu, C., Chenn, A., Erdelyi, F., Szabo, G., Hockberger, P. and Szele, F. G. (2007). "Dynamic features of postnatal subventricular zone cell motility: A two-photon time-lapse study." Journal of Comparative Neurology **505**(2): 190-208.

Neves, G., Cooke, S. F. and Bliss, T. V. P. (2008). "Synaptic plasticity, memory and the hippocampus: a neural network approach to causality." Nature Reviews Neuroscience **9**(1): 65-75.

Oh, S. W., Harris, J. A., Ng, L., Winslow, B., Cain, N., Mihalas, S., Wang, Q., Lau, C., Kuan, L., Henry, A. M., Mortrud, M. T., Ouellette, B., Nguyen, T. N., Sorensen, S. A., Slaughterbeck, C. R., Wakeman, W., Li, Y., Feng, D., Ho, A., Nicholas, E., Hirokawa, K. E., Bohn, P., Joines, K. M., Peng, H., Hawrylycz, M. J., Phillips, J. W., Hohmann, J. G., Wohnoutka, P., Gerfen, C. R., Koch, C., Bernard, A., Dang, C., Jones, A. R. and Zeng, H. (2014). "A mesoscale connectome of the mouse brain." Nature **508**(7495): 207-214.

Okano, M., Bell, D. W., Haber, D. A. and Li, E. (1999). "DNA Methyltransferases Dnmt3a and Dnmt3b Are Essential for De Novo Methylation and Mammalian Development." Cell **99**(3): 247-257.

Ozaki, E., Gibbons, L., Neto, N. G. B., Kenna, P., Carty, M., Humphries, M., Humphries, P., Campbell, M., Monaghan, M., Bowie, A. and Doyle, S. L. (2020). "SARM1 deficiency promotes rod and cone photoreceptor cell survival in a model of retinal degeneration." Life Science Alliance **3**(5): e201900618.

Pal, S. and Tyler, J. K. (2016). "Epigenetics and aging." Science advances **2**(7): e1600584-e1600584.

Palmiter, R. D. and Brinster, R. L. (1985). "Transgenic mice." Cell **41**(2): 343-345.

Palmiter, R. D., Brinster, R. L., Hammer, R. E., Trumbauer, M. E., Rosenfeld, M. G., Birnberg, N. C. and Evans, R. M. (1982). "Dramatic growth of mice that develop from eggs microinjected with metallothionein-growth hormone fusion genes." Nature **300**(5893): 611-615.

Parent, J. M. and Murphy, G. G. (2008). "Mechanisms and functional significance of aberrant seizure-induced hippocampal neurogenesis." Epilepsia **49**(s5): 19-25.

Parent, J. M., Vexler, Z. S., Gong, C., Derugin, N. and Ferriero, D. M. (2002). "Rat forebrain neurogenesis and striatal neuron replacement after focal stroke." Annals of Neurology **52**(6): 802-813.

Payne, K. K., Stephen, T. L., Chaurio, R. A., Allegrezza, M. J., Zhu, H., Perez-Sanz, J., Perales-Puchalt, A., Nguyen, J. M., Vara-Ailor, A., Eruslanov, E. B., Borowsky, M. E., Zhang, R., Laufer, T. M. and Conejo-Garcia, J. R. (2017). "The chromatin organizer SATB1 governs the epigenetic repression of the co-inhibitory receptor PD-1 in T cells." The Journal of Immunology **198**(1 Supplement): 56.58.

Peng, Y.-R., Tran, N. M., Krishnaswamy, A., Kostadinov, D., Martersteck, E. M. and Sanes, J. R. (2017). "Satb1 Regulates Contactin 5 to Pattern Dendrites of a Mammalian Retinal Ganglion Cell." Neuron **95**(4): 869-883.e866.

Péraldi-Roux, S., Dao, B. N.-T., Hirn, M. and Gabrion, J. (1990). "Choroidal ependymocytes in culture: Expression of markers of polarity and function." International Journal of Developmental Neuroscience **8**(5): 575-583.

Perera, A., Eisen, D., Wagner, M., Laube, Silvia K., Künzel, Andrea F., Koch, S., Steinbacher, J., Schulze, E., Splith, V., Mittermeier, N., Müller, M., Biel, M., Carell, T. and Michalakis, S. (2015). "TET3 Is Recruited by REST for Context-Specific Hydroxymethylation and Induction of Gene Expression." Cell Reports **11**(2): 283-294.

Petricca, S. (2015). "Transcription factor Pax6 regulates cell cycle progression and cell fate determination: the modular logic of complex transcriptional control." Dissertation, LMU München: Graduate School of Systemic Neurosciences (GSN)

Pfaffl, M. W. (2001). "A new mathematical model for relative quantification in real-time RT-PCR." Nucleic acids research **29**(9): e45-e45.

Pfaffl, M. W., Horgan, G. W. and Dempfle, L. (2002). "Relative expression software tool (REST) for group-wise comparison and statistical analysis of relative expression results in real-time PCR." Nucleic acids research **30**(9): e36-e36.

Pfenninger, C. V., Roschupkina, T., Hertwig, F., Kottwitz, D., Englund, E., Bengzon, J., Jacobsen, S. E. and Nuber, U. A. (2007). "CD133 Is Not Present on Neurogenic Astrocytes in the Adult Subventricular Zone, but on Embryonic Neural Stem Cells, Ependymal Cells, and Glioblastoma Cells." Cancer Research **67**(12): 5727.

Picelli, S., Björklund, Å. K., Faridani, O. R., Sagasser, S., Winberg, G. and Sandberg, R. (2013). "Smart-seq2 for sensitive full-length transcriptome profiling in single cells." Nature Methods **10**(11): 1096-1098.

Preibisch, S., Saalfeld, S. and Tomancak, P. (2009). "Globally optimal stitching of tiled 3D microscopic image acquisitions." Bioinformatics (Oxford, England) **25**(11): 1463-1465.

Purves, D., Augustine, G. J., Fitzpatrick, D., Katz, L. C., LaMantia, A.-S., McNamara, J. O. and Williams., S. M. (2001a). Chapter: Central Projections of Retinal Ganglion Cells. Neuroscience. 2nd Edition, Sunderland (MA): Sinauer Associates.

Purves, D., Augustine, G. J., Fitzpatrick, D., Katz, L. C., LaMantia, A.-S., McNamara, J. O. and Williams., S. M. (2001b). Chapter: Phototransduction. Neuroscience. 2nd edition., Sunderland (MA): Sinauer Associates.

Purves, D., Augustine, G. J., Fitzpatrick, D., Katz, L. C., LaMantia, A.-S., McNamara, J. O. and Williams., S. M. (2001c). Chapter: The Retina. Neuroscience. 2nd edition., Sunderland (MA): Sinauer Associates.

Pushpakom, S., Iorio, F., Eyers, P. A., Escott, K. J., Hopper, S., Wells, A., Doig, A., Guilliams, T., Latimer, J., McNamee, C., Norris, A., Sanseau, P., Cavalla, D. and Pirmohamed, M. (2019). "Drug repurposing: progress, challenges and recommendations." Nature Reviews Drug Discovery **18**(1): 41-58.

Rakyan, V. K., Down, T. A., Balding, D. J. and Beck, S. (2011). "Epigenome-wide association studies for common human diseases." Nature reviews. Genetics **12**(8): 529-541.

Ramamoorthi, K., Fropf, R., Belfort, G. M., Fitzmaurice, H. L., McKinney, R. M., Neve, R. L., Otto, T. and Lin, Y. (2011). "Npas4 Regulates a Transcriptional Program in CA3 Required for Contextual Memory Formation." Science **334**(6063): 1669.

Ran, F. A., Cong, L., Yan, W. X., Scott, D. A., Gootenberg, J. S., Kriz, A. J., Zetsche, B., Shalem, O., Wu, X., Makarova, K. S., Koonin, E. V., Sharp, P. A. and Zhang, F. (2015). "In vivo genome editing using Staphylococcus aureus Cas9." Nature **520**(7546): 186-191.

Ran, F. A., Hsu, P. D., Wright, J., Agarwala, V., Scott, D. A. and Zhang, F. (2013). "Genome engineering using the CRISPR-Cas9 system." Nature Protocols **8**(11): 2281-2308.

Rasmussen, K. D. and Helin, K. (2016). "Role of TET enzymes in DNA methylation, development, and cancer." Genes & development **30**(7): 733-750.

Richards, C. L., Bossdorf, O. and Pigliucci, M. (2010). "What Role Does Heritable Epigenetic Variation Play in Phenotypic Evolution?" BioScience **60**(3): 232-237.

Riggs, A. D. (1975). "X inactivation, differentiation, and DNA methylation." Cytogenetics and Cell Genetics **14**: 9-25.

Rosenthal, N. and Brown, S. (2007). "The mouse ascending: perspectives for human-disease models." Nature Cell Biology **9**(9): 993-999.

Rouet, P., Smih, F. and Jasin, M. (1994). "Expression of a site-specific endonuclease stimulates homologous recombination in mammalian cells." Proceedings of the National Academy of Sciences of the United States of America **91**(13): 6064-6068.

Rudenko, A., Dawlaty, M. M., Seo, J., Cheng, A. W., Meng, J., Le, T., Faull, K. F., Jaenisch, R. and Tsai, L.-H. (2013). "Tet1 is critical for neuronal activity-regulated gene expression and memory extinction." Neuron **79**(6): 1109-1122.

Sahay, A. and Hen, R. (2007). "Adult hippocampal neurogenesis in depression." Nature Neuroscience **10**(9): 1110-1115.

Sander, J. D. and Joung, J. K. (2014). "CRISPR-Cas systems for editing, regulating and targeting genomes." Nature Biotechnology **32**(4): 347-355.

Sandoval, J., Peiró-Chova, L., Pallardó, F. V. and García-Giménez, J. L. (2013). "Epigenetic biomarkers in laboratory diagnostics: emerging approaches and opportunities." Expert Review of Molecular Diagnostics **13**(5): 457-471.

Santiago, M., Antunes, C., Guedes, M., Iacovino, M., Kyba, M., Reik, W., Sousa, N., Pinto, L., Branco, M. R. and Marques, C. J. (2019). "Tet3 regulates cellular identity and DNA methylation in neural progenitor cells." Cellular and Molecular Life Sciences.

Santiago, M., Antunes, C., Guedes, M., Sousa, N. and Marques, C. J. (2014). "TET enzymes and DNA hydroxymethylation in neural development and function — How critical are they?" Genomics **104**(5): 334-340.

Sauer, B. (1998). "Inducible Gene Targeting in Mice Using the Cre/loxSystem." Methods **14**(4): 381-392.

Sauer, B. and Henderson, N. (1988). "Site-specific DNA recombination in mammalian cells by the Cre recombinase of bacteriophage P1." Proceedings of the National Academy of Sciences of the United States of America **85**(14): 5166-5170.

Scharfman, H. E. and Hen, R. (2007). "Neuroscience. Is more neurogenesis always better?" Science (New York, N.Y.) **315**(5810): 336-338.

Schindelin, J., Arganda-Carreras, I., Frise, E., Kaynig, V., Longair, M., Pietzsch, T., Preibisch, S., Rueden, C., Saalfeld, S., Schmid, B., Tinevez, J.-Y., White, D. J., Hartenstein, V., Eliceiri, K., Tomancak, P. and Cardona, A. (2012). "Fiji: an open-source platform for biological-image analysis." Nature Methods **9**(7): 676-682.

Schröder, H., Moser, N. and Huggenberger, S. (2020a). The Mouse Cerebellum. Neuroanatomy of the Mouse: An Introduction. H. Schröder, N. Moser and S. Huggenberger. Cham, Springer International Publishing**:** 153-170.

Schröder, H., Moser, N. and Huggenberger, S. (2020b). The Mouse Cerebral Cortex. Neuroanatomy of the Mouse: An Introduction. H. Schröder, N. Moser and S. Huggenberger. Cham, Springer International Publishing**:** 231-265.

Schröder, H., Moser, N. and Huggenberger, S. (2020c). The Mouse Hippocampus. Neuroanatomy of the Mouse: An Introduction. H. Schröder, N. Moser and S. Huggenberger. Cham, Springer International Publishing**:** 267-288.

Schröder, H., Moser, N. and Huggenberger, S. (2020d). The Mouse Olfactory System. Neuroanatomy of the Mouse: An Introduction. H. Schröder, N. Moser and S. Huggenberger. Cham, Springer International Publishing**:** 319-331.

Schübeler, D. (2015). "Function and information content of DNA methylation." Nature **517**(7534): 321-326.

Schuler, A. M. and Wood, P. A. (2002). "Mouse Models for Disorders of Mitochondrial Fatty Acid β-Oxidation." ILAR Journal **43**(2): 57-65.

Scott, J. W., Wellis, D. P., Riggott, M. J. and Buonviso, N. (1993). "Functional organization of the main olfactory bulb." Microscopy Research and Technique **24**(2): 142-156.

Sharif, J., Muto, M., Takebayashi, S.-i., Suetake, I., Iwamatsu, A., Endo, T. A., Shinga, J., Mizutani-Koseki, Y., Toyoda, T., Okamura, K., Tajima, S., Mitsuya, K., Okano, M. and Koseki, H. (2007). "The SRA protein Np95 mediates epigenetic inheritance by recruiting Dnmt1 to methylated DNA." Nature **450**(7171): 908-912.

Sharma, S., Kelly, T. K. and Jones, P. A. (2010). "Epigenetics in cancer." Carcinogenesis **31**(1): 27-36.

Shen, B., Zhang, J., Wu, H., Wang, J., Ma, K., Li, Z., Zhang, X., Zhang, P. and Huang, X. (2013). "Generation of gene-modified mice via Cas9/RNA-mediated gene targeting." Cell research **23**(5): 720-723.

Shi, M. and Shen, L. (2017). The Molecular Basis of DNA Demethylation. DNA and Histone Methyalation as Cancer Targets. A. Kaneda and Y.-i. Tsukada, Humana Press (Springer Nature).

Simons, M. and Trotter, J. (2007). "Wrapping it up: the cell biology of myelination." Current Opinion in Neurobiology **17**(5): 533-540.

Sina, A. A. I., Carrascosa, L. G., Liang, Z., Grewal, Y. S., Wardiana, A., Shiddiky, M. J. A., Gardiner, R. A., Samaratunga, H., Gandhi, M. K., Scott, R. J., Korbie, D. and Trau, M. (2018). "Epigenetically reprogrammed methylation landscape drives the DNA self-assembly and serves as a universal cancer biomarker." Nature communications **9**(1): 4915.

Singh, A. K., Zhao, B., Liu, X., Wang, X., Li, H., Qin, H., Wu, X., Ma, Y., Horne, D. and Yu, X. (2020). "Selective targeting of TET catalytic domain promotes somatic cell reprogramming." Proceedings of the National Academy of Sciences **117**(7): 3621.

Smith, Z. D. and Meissner, A. (2013). "DNA methylation: roles in mammalian development." Nature Reviews Genetics **14**(3): 204-220.

Šorm, F., Píškala, A., Čihák, A. and Veselý, J. (1964). "5-Azacytidine, a new, highly effective cancerostatic." Experientia **20**(4): 202-203.

Spassky, N., Merkle, F. T., Flames, N., Tramontin, A. D., García-Verdugo, J. M. and Alvarez-Buylla, A. (2005). "Adult ependymal cells are postmitotic and are derived from radial glial cells during embryogenesis." The Journal of neuroscience : the official journal of the Society for Neuroscience **25**(1): 10-18.

Spruijt, Cornelia G., Gnerlich, F., Smits, Arne H., Pfaffeneder, T., Jansen, Pascal W. T. C., Bauer, C., Münzel, M., Wagner, M., Müller, M., Khan, F., Eberl, H. C., Mensinga, A., Brinkman, Arie B., Lephikov, K., Müller, U., Walter, J., Boelens, R., van Ingen, H., Leonhardt, H., Carell, T. and Vermeulen, M. (2013). "Dynamic Readers for 5-(Hydroxy)Methylcytosine and Its Oxidized Derivatives." Cell **152**(5): 1146-1159.

Strahl, B. D. and Allis, C. D. (2000). "The language of covalent histone modifications." Nature **403**(6765): 41-45.

Sun, W., Kim, H. and Moon, Y. (2010). "Control of neuronal migration through rostral migration stream in mice." Anatomy & cell biology **43**(4): 269-279.

Sun, X. and Lin, Y. (2016). "Npas4: Linking Neuronal Activity to Memory." Trends in Neurosciences **39**(4): 264-275.

Sung, Y. H., Baek, I.-J., Kim, D. H., Jeon, J., Lee, J., Lee, K., Jeong, D., Kim, J.-S. and Lee, H.-W. (2013). "Knockout mice created by TALEN-mediated gene targeting." Nature Biotechnology **31**(1): 23-24.

Suzuki, M. M. and Bird, A. (2008). "DNA methylation landscapes: provocative insights from epigenomics." Nature Reviews Genetics **9**(6): 465-476.

Swenson, R. S. (2006). "Review of clinical and functional neuroscience: Chapter 11 - The Cerebral Cortex." 2020, from https://www.dartmouth.edu/~rswenson/NeuroSci/chapter_11.html.

Szyf, M. (2009). "The early life environment and the epigenome." Biochimica et Biophysica Acta (BBA) - General Subjects **1790**(9): 878-885.

Tahiliani, M., Koh, K. P., Shen, Y., Pastor, W. A., Bandukwala, H., Brudno, Y., Agarwal, S., Iyer, L. M., Liu, D. R., Aravind, L. and Rao, A. (2009). "Conversion of 5-methylcytosine to 5-hydroxymethylcytosine in mammalian DNA by MLL partner TET1." Science (New York, N.Y.) **324**(5929): 930-935.

Tatton-Brown, K., Seal, S., Ruark, E., Harmer, J., Ramsay, E., del Vecchio Duarte, S., Zachariou, A., Hanks, S., O'Brien, E., Aksglaede, L., Baralle, D., Dabir, T., Gener, B., Goudie, D., Homfray, T., Kumar, A., Pilz, D. T., Selicorni, A., Temple, I. K., Van Maldergem, L., Yachelevich, N., van Montfort, R., Rahman, N. and Childhood Overgrowth, C. (2014). "Mutations in the DNA methyltransferase gene DNMT3A cause an overgrowth syndrome with intellectual disability." Nature Genetics **46**(4): 385-388.

Teng, S., Ma, C., Yu, Y. and Yi, C. (2019). "Hydroxyurea promotes TET1 expression and induces apoptosis in osteosarcoma cells." Bioscience reports **39**(5): BSR20190456.

Tham, C.-S., Lin, F.-F., Rao, T. S., Yu, N. and Webb, M. (2003). "Microglial activation state and lysophospholipid acid receptor expression." International Journal of Developmental Neuroscience **21**(8): 431-443.

Tiosano, D., Baris, H. N., Chen, A., Hitzert, M. M., Schueler, M., Gulluni, F., Wiesener, A., Bergua, A., Mory, A., Copeland, B., Gleeson, J. G., Rump, P., van Meer, H., Sival, D. A., Haucke, V., Kriwinsky, J., Knaup, K. X., Reis, A., Hauer, N. N., Hirsch, E., Roepman, R., Pfundt, R., Thiel, C. T., Wiesener, M. S., Aslanyan, M. G. and Buchner, D. A. (2019). "Mutations in PIK3C2A cause syndromic short stature, skeletal abnormalities, and cataracts associated with ciliary dysfunction." PLOS Genetics **15**(4): e1008088.

Tran, H., Brunet, A., Grenier, J. M., Datta, S. R., Fornace, A. J., DiStefano, P. S., Chiang, L. W. and Greenberg, M. E. (2002). "DNA Repair Pathway Stimulated by the Forkhead Transcription Factor FOXO3a Through the Gadd45 Protein." Science **296**(5567): 530.

Traube, F. R., Schiffers, S., Iwan, K., Kellner, S., Spada, F., Muller, M. and Carell, T. (2019). "Isotope-dilution mass spectrometry for exact quantification of noncanonical DNA nucleosides." Nat Protoc **14**(1): 283-312.

Tronche, F., Kellendonk, C., Kretz, O., Gass, P., Anlag, K., Orban, P. C., Bock, R., Klein, R. and Schütz, G. (1999). "Disruption of the glucocorticoid receptor gene in the nervous system results in reduced anxiety." Nature Genetics **23**(1): 99-103.

Ueda, H. R., Ertürk, A., Chung, K., Gradinaru, V., Chédotal, A., Tomancak, P. and Keller, P. J. (2020). "Tissue clearing and its applications in neuroscience." Nature Reviews Neuroscience **21**(2): 61-79.

Upadhyay, A. K. and Cheng, X. (2011). "Dynamics of histone lysine methylation: structures of methyl writers and erasers." Progress in drug research. Fortschritte der Arzneimittelforschung. Progres des recherches pharmaceutiques **67**: 107-124.

Urnov, F. D., Rebar, E. J., Holmes, M. C., Zhang, H. S. and Gregory, P. D. (2010). "Genome editing with engineered zinc finger nucleases." Nature Reviews Genetics **11**(9): 636-646.

Vanmarsenille, L., Verbeeck, J., Belet, S., Roebroek, A. J., Van de Putte, T., Nevelsteen, J., Callaerts-Vegh, Z., D'Hooge, R., Marynen, P. and Froyen, G. (2013). "Generation and Characterization of an Nxf7 Knockout Mouse to Study NXF5 Deficiency in a Patient with Intellectual Disability." PLOS ONE **8**(5): e64144.

Villota-Salazar, N. A., Mendoza-Mendoza, A. and González-Prieto, J. M. (2016). "Epigenetics: from the past to the present." Frontiers in Life Science **9**(4): 347-370.

von Bernhardi, R., Bernhardi, L. E. and Eugenín, J. (2017). "What Is Neural Plasticity?". The Plastic Brain. Advances in Experimental Medicine and Biology. von Bernhardi R., Eugenín J. and Muller K., Spinger, Cham. **1015**.

Waddington, C. H. (1939). "An introduction to modern genetics." The MacMillan Company, New York.

Waddington, C. H. (1942). "The Epigenotype." Endeavour **1**: 18-20.

Wagner, M., Steinbacher, J., Kraus, T. F., Michalakis, S., Hackner, B., Pfaffeneder, T., Perera, A., Muller, M., Giese, A., Kretzschmar, H. A. and Carell, T. (2015). "Age-dependent levels of 5-methyl-, 5-hydroxymethyl-, and 5-formylcytosine in human and mouse brain tissues." Angew Chem Int Ed Engl **54**(42): 12511-12514.

Wan, H., Wang, Q., Chen, X., Zeng, Q., Shao, Y., Fang, H., Liao, X., Li, H.-S., Liu, M.-G., Xu, T.-L., Diao, M., Li, D., Meng, B., Tang, B., Zhang, Z. and Liao, L. (2020). "WDR45 contributes to neurodegeneration through regulation of ER homeostasis and neuronal death." Autophagy **16**(3): 531-547.

Wang, H., Yang, H., Shivalila, C. S., Dawlaty, M. M., Cheng, A. W., Zhang, F. and Jaenisch, R. (2013). "One-step generation of mice carrying mutations in multiple genes by CRISPR/Cas-mediated genome engineering." Cell **153**(4): 910-918.

Wei, L., Liu, B., Tuo, J., Shen, D., Chen, P., Li, Z., Liu, X., Ni, J., Dagur, P., Sen, H. N., Jawad, S., Ling, D., Park, S., Chakrabarty, S., Meyerle, C., Agron, E., Ferris, F. L., 3rd, Chew, E. Y., McCoy, J. P., Blum, E., Francis, P. J., Klein, M. L., Guymer, R. H., Baird, P. N., Chan, C.-C. and Nussenblatt, R. B. (2012). "Hypomethylation of the IL17RC promoter associates with age-related macular degeneration." Cell Reports **2**(5): 1151-1158.

Weinhold, B. (2006). "Epigenetics: the science of change." Environmental health perspectives **114**(3): A160-A167.

Wenzler, S. and Jung, M. (2017). "Lesezeichen im Buch des Lebens." Deutsche Apotheker Zeitung **44**: 60-66.

Widom, J. (1989). "Toward a Unified Model of Chromatin Folding." Annual Review of Biophysics and Biophysical Chemistry **18**(1): 365-395.

Wilhelmsson, U., Lebkuechner, I., Leke, R., Marasek, P., Yang, X., Antfolk, D., Chen, M., Mohseni, P., Lasič, E., Bobnar, S. T., Stenovec, M., Zorec, R., Nagy, A., Sahlgren, C., Pekna, M. and Pekny, M. (2019). "Nestin Regulates Neurogenesis in Mice Through Notch Signaling From Astrocytes to Neural Stem Cells." Cerebral Cortex **29**(10): 4050-4066.

World Health Organization (WHO). "Causes for Blindness and vision impairment: Priority eye diseases." 2020, from https://www.who.int/blindness/causes/priority/en/index1.html.

Wossidlo, M., Nakamura, T., Lepikhov, K., Marques, C. J., Zakhartchenko, V., Boiani, M., Arand, J., Nakano, T., Reik, W. and Walter, J. (2011). "5-Hydroxymethylcytosine in the mammalian zygote is linked with epigenetic reprogramming." Nature communications **2**(1): 241.

Wu, H. and Zhang, Y. (2014). "Reversing DNA methylation: mechanisms, genomics, and biological functions." Cell **156**(1-2): 45-68.

Wu, N., Yang, M., Gaur, U., Xu, H., Yao, Y. and Li, D. (2016a). "Alpha-Ketoglutarate: Physiological Functions and Applications." Biomolecules & therapeutics **24**(1): 1-8.

Wu, T. P., Wang, T., Seetin, M. G., Lai, Y., Zhu, S., Lin, K., Liu, Y., Byrum, S. D., Mackintosh, S. G., Zhong, M., Tackett, A., Wang, G., Hon, L. S., Fang, G., Swenberg, J. A. and Xiao, A. Z. (2016b). "DNA methylation on N(6)-adenine in mammalian embryonic stem cells." Nature **532**(7599): 329-333.

Wu, X. and Zhang, Y. (2017). "TET-mediated active DNA demethylation: mechanism, function and beyond." Nature Reviews Genetics **18**(9): 517-534.

Xiao, H., Hasegawa, T. and Isobe, K.-i. (1999). "Both Sp1 and Sp3 are responsible for p21waf1 promoter activity induced by histone deacetylase inhibitor in NIH3T3 cells." Journal of Cellular Biochemistry **73**(3): 291-302.

Xiao, M., Yang, H., Xu, W., Ma, S., Lin, H., Zhu, H., Liu, L., Liu, Y., Yang, C., Xu, Y., Zhao, S., Ye, D., Xiong, Y. and Guan, K.-L. (2012). "Inhibition of α-KG-dependent histone and DNA demethylases by fumarate and succinate that are accumulated in mutations of FH and SDH tumor suppressors." Genes & development **26**(12): 1326-1338.

Xu, Y., Wu, F., Tan, L., Kong, L., Xiong, L., Deng, J., Barbera, A. J., Zheng, L., Zhang, H., Huang, S., Min, J., Nicholson, T., Chen, T., Xu, G., Shi, Y., Zhang, K. and Shi, Yujiang G. (2011). "Genome-wide Regulation of 5hmC, 5mC, and Gene Expression by Tet1 Hydroxylase in Mouse Embryonic Stem Cells." Molecular Cell **42**(4): 451-464.

Xu, Y., Xu, C., Kato, A., Tempel, W., Abreu, Jose G., Bian, C., Hu, Y., Hu, D., Zhao, B., Cerovina, T., Diao, J., Wu, F., He, Housheng H., Cui, Q., Clark, E., Ma, C., Barbara, A., Veenstra, Gert Jan C., Xu, G., Kaiser, Ursula B., Liu, X. S., Sugrue, Stephen P., He, X., Min, J., Kato, Y. and Shi, Yujiang G. (2012). "Tet3 CXXC Domain and Dioxygenase Activity Cooperatively Regulate Key Genes for *Xenopus* Eye and Neural Development." Cell **151**(6): 1200-1213.

Yan, J., Goerne, T., Zelmer, A., Guzman, R., Kapfhammer, J. P., Wellmann, S. and Zhu, X. (2019). "The RNA-Binding Protein RBM3 Promotes Neural Stem Cell (NSC) Proliferation Under Hypoxia." Frontiers in Cell and Developmental Biology **7**(288).

Yang, Q., Liang, X., Sun, X., Zhang, L., Fu, X., Rogers, Carl J., Berim, A., Zhang, S., Wang, S., Wang, B., Foretz, M., Viollet, B., Gang, David R., Rodgers, Buel D., Zhu, M.-J. and Du, M. (2016). "AMPK/alpha-Ketoglutarate Axis Dynamically Mediates DNA Demethylation in the Prdm16 Promoter and Brown Adipogenesis." Cell Metabolism **24**(4): 542-554.

Yang, X. J. and Seto, E. (2007). "HATs and HDACs: from structure, function and regulation to novel strategies for therapy and prevention." Oncogene **26**(37): 5310-5318.

Yen, S.-T., Zhang, M., Deng, J. M., Usman, S. J., Smith, C. N., Parker-Thornburg, J., Swinton, P. G., Martin, J. F. and Behringer, R. R. (2014). "Somatic mosaicism and allele complexity induced by CRISPR/Cas9 RNA injections in mouse zygotes." Developmental Biology **393**(1): 3-9.

Yu, H., Su, Y., Shin, J., Zhong, C., Guo, J. U., Weng, Y.-L., Gao, F., Geschwind, D. H., Coppola, G., Ming, G.-l. and Song, H. (2015). "Tet3 regulates synaptic transmission and homeostatic plasticity via DNA oxidation and repair." Nature Neuroscience **18**(6): 836-843.

Zhang, B., Pan, X., Cobb, G. P. and Anderson, T. A. (2007). "microRNAs as oncogenes and tumor suppressors." Developmental Biology **302**(1): 1-12.

Zhang, R.-R., Cui, Q.-Y., Murai, K., Lim, Yen C., Smith, Zachary D., Jin, S., Ye, P., Rosa, L., Lee, Yew K., Wu, H.-P., Liu, W., Xu, Z.-M., Yang, L., Ding, Y.-Q., Tang, F., Meissner, A., Ding, C., Shi, Y. and Xu, G.-L. (2013). "Tet1 Regulates Adult Hippocampal Neurogenesis and Cognition." Cell Stem Cell **13**(2): 237-245.

Zhang, X.-H., Tee, L. Y., Wang, X.-G., Huang, Q.-S. and Yang, S.-H. (2015). "Off-target Effects in CRISPR/Cas9-mediated Genome Engineering." Molecular therapy. Nucleic acids **4**(11): e264-e264.

Zhao, C., Deng, W. and Gage, F. H. (2008). "Mechanisms and Functional Implications of Adult Neurogenesis." Cell **132**(4): 645-660.

Zhao, X., Ueba, T., Christie, B. R., Barkho, B., McConnell, M. J., Nakashima, K., Lein, E. S., Eadie, B. D., Willhoite, A. R., Muotri, A. R., Summers, R. G., Chun, J., Lee, K.-F. and Gage, F. H. (2003). "Mice lacking methyl-CpG binding protein 1 have deficits in adult neurogenesis and hippocampal function." Proceedings of the National Academy of Sciences **100**(11): 6777.

Zhong, Q. and Kowluru, R. A. (2010). "Role of histone acetylation in the development of diabetic retinopathy and the metabolic memory phenomenon." Journal of Cellular Biochemistry **110**(6): 1306-1313.

Zhou, P., Luo, Y., Liu, X., Fan, L. and Lu, Y. (2012a). "Down-regulation and CpG island hypermethylation of CRYAA in age-related nuclear cataract." FASEB journal : official publication of the Federation of American Societies for Experimental Biology **26**(12): 4897-4902.

Zhou, P., Ye, H.-F., Jiang, Y.-X., Yang, J., Zhu, X.-J., Sun, X.-H., Luo, Y., Dou, G.-R., Wang, Y.-S. and Lu, Y. (2012b). "αA crystallin may protect against geographic atrophy-meta-analysis of cataract vs. cataract surgery for geographic atrophy and experimental studies." PLOS ONE **7**(8): e43173-e43173.

Zhu, X., Bührer, C. and Wellmann, S. (2016). "Cold-inducible proteins CIRP and RBM3, a unique couple with activities far beyond the cold." Cellular and molecular life sciences : CMLS **73**(20): 3839-3859.

Zhu, X., Yan, J., Bregere, C., Zelmer, A., Goerne, T., Kapfhammer, J. P., Guzman, R. and Wellmann, S. (2019). "RBM3 promotes neurogenesis in a niche-dependent manner via IMP2-IGF2 signaling pathway after hypoxic-ischemic brain injury." Nature communications **10**(1): 3983.

8 List of publications

Thumbs, P.*, Ensfelder, T.T.*, Hillmeier, M.*, Wagner, M.*, Heiss, M., **Scheel, C.**, Schön, A., Müller, M., Michalakis, S., Kellner, S. and Carell, T. (2020). "Synthesis of galactosyl-queuosine and distribution of hypermodified Q-nucleosides in mouse tissues." Angewandte Chemie International Edition (published online 11/03/2020).

Traube, F. R.*, Özdemir, D., Glück, A. F., **Scheel, C.**, Geserich, A. S., Iwan, K., Hammelmann, V., Rahimoff, R., Müller, M., Spada, F., Cox, J., Biel, M., Michalakis, S. and Carell, T. (2020). ”Gdh interacts with Tet3 to supply α-ketoglutarate, linking 5mdC oxidation to neuronal function and metabolic state.” (in preparation)

Traube, F. R.*, Splith, V.*, **Scheel, C.***, Geserich, A. S., Gasparoni, G., Stadlmeier, M., Özdemir, D., Runtsch, L., Nordström, K. J, V., Hammelmann, V., Giorgio, G., Walter, J., Carell, T., Michalakis, S. (2020). "Functional interaction between TET3 and MECP2 - Novel insights into epigenetic mechanisms in neuronal differentiation". (in preparation)

* first author(s)

9 Author contributions

Tet3 S KO and Tet3 L KO mouse lines were generated by Dr. Florian Giesert (Wurst group, Helmholtz Zentrum Munich) by microinjection of CRISPR-Cas9 components into one-cell embryos and subsequent transfer of zygotes into pseudo-pregnant female mice. Quantification of cytosine modifications in all mouse tissue and cell samples was performed by Dr. Franziska Traube (Carell group, LMU Munich), who also helped to isolate DNA, RNA and proteins from mouse tissue and cell samples. Proteomics analysis of all mouse tissue samples was conducted by Dr. Michael Stadlmeier (Carell group, LMU Munich). RNA sequencing of sorted mouse cortical neurons and astrocytes was performed by Dr. Gilles Gasparoni (Walter group, Saarland University). FACS experiments were performed by Dr. Lisa Richter (Core Facility Flow Cytometry at the Biomedical Center, LMU Munich). Specific Tet3 antibodies were generated by Prof. Dr. med. vet. Hermann Ammer (Faculty of Veterinary Medicine, Institute of Pharmacology, Toxicology and Pharmacy, LMU Munich). Dr. Elisa Murenu supported the study with suggestions concerning SVZ explants, FACS and immunohistochemistry. Grazia Giorgio helped in establishing RNAscope® technology and FACS procedure. Dr. Victoria Splith supported the study with suggestions for the generation of mouse and cell lines.

10 Acknowledgements

Zuallererst möchte ich mich bei **Herrn Prof. Dr. Stylianos Michalakis** bedanken, dass er mich in seine Arbeitsgruppe aufgenommen und es mir ermöglicht hat, diese Dissertation zu verwirklichen. Vielen Dank, Stelio, für das entgegengebrachte Vertrauen, die vielen Ideen und Diskussionen sowie die ein oder andere herausfordernde Aufgabe.

Ein großer Dank gilt auch **Herrn Prof. Dr. Martin Biel** für die Aufnahme in seinen Arbeitskreis, für seine stetige Unterstützung als eines meiner TAC-Mitglieder und für die Übernahme des Zweitgutachtens dieser Dissertation.

Ich möchte mich außerdem bei **Dr. Fabio Spada** bedanken, der als Mitglied meines TAC-Komitees seine Erfahrung und Ideen in meine Projekte miteinbrachte.

Der **Graduate School Life Science Munich (LSM)** danke ich für die Möglichkeit an ihrem Promotionsprogramm teilzunehmen, für die Unterstützung während meiner Promotion sowie für die vielen neuen Bekanntschaften aus aller Welt und die Möglichkeit in jeglicher Hinsicht den Horizont zu erweitern.

Bedanken möchte ich mich herzlich bei **Herrn Prof. Dr. Thomas Carell** und seiner Arbeitsgruppe für die gute Zusammenarbeit bei den gemeinsamen Projekten während meiner Promotion. Ein großer Dank geht hier an **Dr. Franziska Traube** und **Dilara Özdemir**. Vielen Dank, **Franzi**, für deine Unterstützung und dein Vertrauen in all den Jahren. Es war mir eine große Freude, mit dir die unzähligen Experimente gemacht zu haben. **Dilara**, die vielen gemeinsamen Stunden am Konfokalmikroskop werde ich in sehr guter Erinnerung behalten.

Außerdem bedanke ich mich herzlich bei **Herrn Prof. Dr. Jörn Walter** und seinen Mitarbeitern aus Saarbrücken für die gute Kollaboration. Ein großer Dank geht hier an **Dr. Gilles Gasparoni**, der sehr viele Proben von uns bearbeitet und analysiert hat.

Ein großer Dank geht auch an **Dr. Verena Mehlfeld**, die immer ein offenes Ohr für mich hatte und mir viele Methoden und Sachverhalte mit ihrer geduldigen und gutmütigen Art nähergebracht hat. Ich habe sehr viel von dir gelernt, **Verena**!

Weiterhin möchte ich **Dr. Elisa Murenu** für die Unterstützung und die vielen Ideen, die sie in meine Projekte eingebracht hat, danken. Bedanken möchte ich mich auch bei **Grazia Giorgio** für die sehr gute und produktive Zusammenarbeit bei den Tet3-Projekten.

Vielen Dank an all meine lieben Kolleginnen und Kollegen im Labor. Ohne euch, die gemeinsamen Aktivitäten und das gute Miteinander wäre alles sehr viel schwieriger gewesen. Besonders hervorheben möchte ich dabei **Dr. Anna Geserich, Johanna Wagner, Kerstin Skokann, Dr. Lisa Riedmayr, Manuela Brümmer, Marina Pavlou, Dr. Sybille Böhm und Dr. Victoria Splith**, die nicht nur großartige Kolleginnen, sondern auch gute Freundinnen geworden sind. Vielen Dank, **Anna**, für deine große Unterstützung vor allem in meiner Anfangszeit und die schönen gemeinsamen Abende mit Ed Sheeran, Raclette oder Spaghetti Bolognese. Vielen Dank, **Johanna,** für die unzähligen gemeinsamen Stunden im Labor, aber auch darüber hinaus, für die Kaffee- und Zitrone-Ingwer-Tee-Pausen, für dein immer offenes Ohr und deine optimistische Art. Vielen Dank, **Vicky**, für deine große Unterstützung und Geduld bei größeren und kleineren Problemen im Labor, aber auch außerhalb, für die Motivation in der ein oder anderen schwierigen Phase und für deine Freundschaft. **Kerstin**, bei dir möchte ich mich ganz herzlich für die gemeinsame Zeit als Schreibtisch-Nachbarinnen und das gegenseitige Gut-zu-Reden in allen Lebens- und Laborlagen bedanken. Es sollte wohl so sein.

Der größte Dank geht an meine **Eltern** und **Großeltern**, die immer an mich geglaubt, mich unterstützt und ermutigt haben, weiterzumachen. Ich weiß, dass ich immer auf euch zählen kann. **Opa**, dir hätte ich gerne diese Arbeit noch gezeigt.

Zu guter Letzt möchte ich mich bei der wichtigsten Person in meinem Leben bedanken. **Fabian**, du hast mir den Rücken freigehalten, alles mitgemacht, immer an mich geglaubt und mich niemals aufgegeben. Du bist mein Ruhepol, der immer für mich da ist und auf den ich mich immer verlassen kann. Ich freue mich auf alles, was die Zukunft für uns bereithält.